Loughborough University

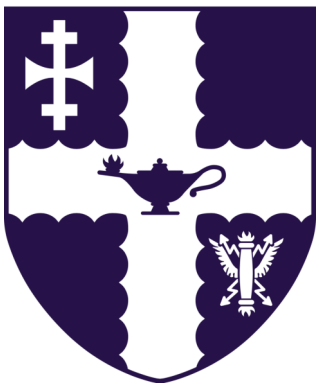

Doctoral Thesis

Visualization of Atomic and Molecular Systems Using Phase-Space Methods

Benjamin Ian Davies
Department of Physics,
School of Science

Submitted in partial fulfilment of the requirements for the award of Doctor of Philosophy of Loughborough University

23 November 2021

Visualization of atomic and molecular systems using phase-space methods

B I Davies

(Dated: 23 November 2021)

Acknowledgements

I would like to to thank my supervisors who helped make this thesis a reality. Mark for his assistance and direction throughout my Ph.D., both personally and professionally, Vince for helping me with ideas and tests as well as spending extended time debugging with me and always providing an ear for my latest dilemma and, finally, John for his guidance and support throughout. Further, I would like to thank Russell Rundle for being a great sounding board and of immense help whenever called for; keeping me sane was not an easy task at times.

Thankfully, my experience has also been made immeasurably more enjoyable due to the friendships created with those in the QSERG including Todd, Kieran, Joe and Will. Finally, I would like to thank all those in my personal life who somehow manage to put up with me and have always remained supportive.

Abstract

The application of phase-space methods, in particular the Wigner function, to visualziation techniques as a way of gaining deeper insight to quantum systems has found extensive use in areas such as quantum optics. The ability to create visualizations within other fields that better characterize and identify quantum states and correlations is also becoming more prominent. In part, this is due to having to consider quantum correlations across large systems in order to explain physical process such as bond formation and haemoglobin transfer, and to characterize information exchange such as that within quantum information systems. Recently, developments in the generalization of the Wigner function, expressed in a displaced parity form, has provided opportunity for phase-space visualzizations to be extended.

Using these techniques, it will be shown how a visualization tool can be created to explore the internal correlations of atomic systems and fully reconstruct a non-trivially correlated state. Applying this tool to quantum chemistry simulation software will highlight how the visualization tool can be applied to the backend of existing systems and provide great utility in subsequent analysis. Further, application to the area of quantum information explores how this visualization technique can help better characterize states and identify signatures that reveal information exchange within quantum systems. This work demonstrates how phase-space visualizations, applied in different ways, can give insight previously unavailable. This insight comes from the treatment of heterogeneous systems, systems with both discrete and continuous variables, allowing for spin-spatial entanglement to be visualized. It will also be seen later (see §3.5) why a spinor representation is insufficient for displaying spin-spin entanglement.

Contents

List of Figures

Chapter 1

Introduction

At the turn of the twentieth century, phenomena yet to be explained included the UV catastrophe, the double-slit experiment, and the photo-electric effect. Despite a general confidence that these were mere technicalities that would be solved before physics could pack up forever; explanations were not forthcoming. In the early part of the new century, on the back of the work of several physicists, maybe most notably Max Planck, a different perspective began to arise; there was more to physics than the classical view.

To explain these phenomena quantum theory was developed and it was quickly noticed that many of the consequences of such a theory were as yet untested. For instance, it introduced a significant departure from the deterministic foundation of classical mechanics, especially in the introduction of new phenomena such as entanglement. The realization that physics needed quantum theory, and that it could not be accepted within the current framework, took time but is now largely agreed.

One consequence of this shift, moving from deterministic classical mechanics to a probabilistic quantum mechanics, was a new wave of interest in statistical physics. Certain areas, such as thermodynamics, had found great utility in statistical approaches to physics and many of the ideas would soon be needed to help describe quantum theory. A major part of statistical physics, is the concept of phase space. A discussion of phase space shall be the basis of Chapter 2, but one consequence

of phase space is the ability to represent, sometimes in a visual way, every possible state of the system. In this respect, quantum theory, as it stood, would not play so nicely.

The visualization of quantum states is of great interest in many different fields. This is because being able to model the evolution of these states ought to allow a cheaper and more efficient method of designing technology [1, 2]. However, it is not just technology from a quantum technology point of view, that is to say, quantum computers, SQUIDs and so on, but also including drug simulations, protein folding simulations and material design [3, 4]. All of these provide huge potential in terms of the change that they could have on society, if realized.

Visualizations have the ability to add a level of intuition to these abstract subjects that can not be gained elsewhere. A long term problem has been the inclusion of non-linear dynamics and environmental interactions to quantum systems explored in theories such as quantum jumps, or quantum state diffusion among others [5, 6]. Secondly, there is a fundamental problem in the visualization of quantum states, long before evolution would even be considered, due to the often very large dimensionality of the system itself. So, although it is necessary to solve both issues, the visualization is the problem to be focused upon in this work. In essence, the standard visualization techniques have proven inadequate in displaying the full quantum information; so it is necessary to find a new method of visualizing states [7–10].

An area which offers such opportunity is that of the generalized Wigner function (after a long history this work builds on the general form presented in Ref. [11]). This is because the phase-space representation can be easily understood for the one-dimensional system, and also for the three-dimensional system. However, it should be noted that the Wigner function for a three-dimensional system is a six-dimensional function, due the phase space nature, and therefore in general must be reduced via integration [12–14]. Marginals, which are Wigner function representations arranged over some subspace, can be recovered by the integration of particular states forming the overall system or indeed a particular dimension of the system [15].

The key benefit of such an approach though, is that when spin (or another particle) is added to such a system the only difference is in the dimensionality. The objective therefore, is to find a way of visualizing the important features of a high dimensional function in three dimensions, or four with the addition of time or colour, in a way that can be easily understood given the context of current representations.

The area of interest leads most of this research is quantum chemistry. This is because there are a number of problems that such a technique could aid in understanding such as visualizing the formation of chemical bonds or perhaps explaining why the reaction rates observed may be lower across a material surface, than those obtained from computer simulations, due to the ability to represent entanglement in an accessible way [16, 17]. Some work has already been done on combining the advances in physics with chemistry, for instance, the inclusion of spin in the model of the atom [8]. Efforts have also come in the form of visualizations [7,18–24]. These generally use position space representations and contour maps to demonstrate the features of different states. However, the problem with many of these techniques is that understanding the pictures is non-trivial. This means that the effort put into understanding the pictures can be higher than the insight gained, *i.e.*, there is little value in using them.

Recently, the phase-space representation of quantum mechanics has been used to characterize quantum states and to develop complete mathematical description in line with the state vector and matrix representations [11, 12, 25–32]. Although originally developed in 1932 as a mechanism for linking thermodynamics to quantum mechanics, a formalized version linking to statistical mechanics was developed by Moyal, simultaneously with Groenewold, some years later [12,33,34]. This made the phase-space representation a powerful tool for describing the evolution of quantum mechanics. Using such a technique is not without problems and for quantum systems one property of standard probability distribution functions must be removed leading to its description through the use of a quasi-probability distribution function. The Wigner function removes positive-definiteness which although conceptually difficult

is not without resolutions and is not an issue for this work [30–32, 34–36]. In fact, the negativity of the Wigner function is one of the features that enables the creation of such an informative visualization as presented in this thesis.

Subsequent developments, including the introduction of the displacement operator as a mechanism for creating coherent states in the development of the P-function and the formulation of the kernel for generating a quasi-probability distribution function through a group action, have increased the utility of the phase-space representation [37–39]. Further, reframing the Wigner function in terms of a displaced parity allowed for measurements of quantum mechanics in phase space where the Wigner function proves to be particularly good at revealing coherences and correlations, such as squeezing and superposition [40]. It is this utility that has made it an invaluable tool in the identification, and characterization, of quantum states such as Schrödinger cat states [41–43]. This success, particularly in quantum optics, may have been the impetus for the development of intracules as a tool for understanding quantum chemistry [15, 18–22, 44, 45].

Historically, there have been a number of attempts to improve the visualization of quantum states such as the Husimi Q-function [46]. Usually, these have been applied to quantum technologies and have a firm grounding in quantum information and/or quantum computing. In the development of a method for better modelling atomic systems, a significant visualization was introduced. Using a fully quantum mechanical technique, the construction of intracules has lead to investigations that provide deeper insight to the structure of molecules [22]. A consequence of this technique is a series of visualizations of different aspects of the state. For instance, there is a position intracule, a momentum intracule, an action intracule and many others. Each of these gives the reader a different insight into the information contained within a state and information on the correlations between each subsystem. To do this, intracules make use of the Wigner function and the phase-space representation of quantum mechanics [22].

Intracules were developed as a quantum mechanical tool, distinct from Hartree-

Fock and density functional theory methods, for calculating electron correlation densities [22]. Although the focus was not on the visualization, the concern was largely as a tool for calculating energies, a consequence was the creation of visualizations of the properties of quantum states [18, 21]. Visualizations of systems often have one of two issues; either they do not display enough information to be useful individually or they contain too much information to be comprehensible. The situation of intracules is a good example of the first issue.

In isolation the intracules are not particularly useful but combining different intracules together, reveals significant information about the system. An issue with such a tool, is that each intracule must be understood independently before the full information can be obtained. Further, each intracule needs different knowledge to distil information from it, *i.e.*, there is an overhead on the ability to pull out useful information. Of course this will be true of any visualization technique as the nature of matter cannot, unfortunately, be obtained without a certain amount of overhead. The key focus when visualizing a particular system, should be to reduce this overhead as much as possible. This work uses phase space to produce a visualization that should not require much extra effort to understand. It also produces pictures which follow a consistent style and, although at times a set of figures are required to study the system, each picture is of a similar style without need for extra knowledge to interpret.

However, these concerns aside, the development of intracules demonstrated an accessible way of using phase-space techniques to provide deeper insight to chemical systems. Addressing real problems over the energies of certain systems, usually due to the lack of quantum mechanical considerations, their work attempted to address inadequacies in the simulation techniques [22]. The current work attempts to use the example of intracules, mainly by considering similar states, to demonstrate that a visualization using the same phase-space methods may be more useful at highlighting problems within the simulations. Key to this approach is the acknowledgement of the benefits of phase-space methods for exploring quantum systems and the inad-

equacies of current chemistry simulations with regards to consideration of quantum correlations. The development of phase-space methods for describing spin systems has also proven to be historically difficult.

The first description of a two-level atom, in the phase-space framework, was produced by Stratonovich based upon Moyal's formalisms [47]. However, there was little progress in this area until new formulations were produced, most notably by Wootters, with the aim of representing qubits [48, 49]. The distinction between Wootters' formulation and that of Stratonovich is the nature of the degrees of freedom. The goal of Wootters, was to describe a discrete two-level system, whereas Stratonovich was aiming for a continuous set of degrees of freedom, similar to the concept of the Bloch sphere. Although different in this regard, they are both valid methods for developing a Wigner function and can be used in different ways to achieve different aims. For instance, Wooters' method has achieved success in the field of quantum information where it has demonstrated how the negativity in the Wigner function can be used to help describe computational processes [50–52].

As described above, visualizations are very tricky things to get right and make intuitive. The Bloch sphere is a sphere whose poles represent orthogonal states and the surface of which contains all the pure states formed of those two states. Each of these states can then be reduced to an arrow pointing from the centre to the surface. This results in a spin state having an arrow representation pointing in the direction intuition would dictate, *i.e.*, spin-up points 'up'. It is with this in mind that the technique used here develops the method used by Stratonovich. This is in part due to the similarity of the method with the Bloch sphere and leads to a visualization similar to those already used within quantum information. The development of Stratonovich's method into the Moyal representation builds on work considering spin coherent states, which has made the technique much more accessible [53–55]. Examples of how useful this method has been can be seen in Refs. [56–61] and has recently been extended in Ref. [11,62]. Each of these pull together different examples of visualizing systems and begin to introduce a useful method of visualizing spin.

However, most systems are spatially interesting and in many cases have spin-spatial entanglement as well as spin-spin entanglement. Being able to use a visualization to describe the spin-spin entanglement is best achieved by having a catalogue of known states, but including the spatial-spin entanglement proves more challenging. To be able to fully characterize a state, it is necessary to have some way of gaining insight of the spatial-spin entanglement. For instance, spin-orbit coupling in catalysts is an area where understanding the correlations between spatial and spin degrees of freedom is very important [63,64]. Currently, a reliable and intuitive method for visualizing these systems for analysis is not in common use.

This work develops a tool that can be used for visualizing generic systems regardless of the origin of entanglement thereby allowing analysis of all types of quantum correlations. To demonstrate the power of such a technique, the initial part of this thesis deals with an application to chemistry using a similar approach to that of intracules. This uses model atoms to develop an accessible introduction to the visualization technique and demonstrates the use of the images to understand and analyze quantum correlations within a system. It is important to understand how this method works for very simple systems so that key signatures can be identified and applied in subsequent situations.

Another reason for beginning with simple model atom approximations, is because the applications of this tool are potentially wide. One area that is of great interest is that of ion traps and quantum dots. Both these areas are based around models using the harmonic oscillator and, therefore, the full quantum chemistry wavefunction would be unnecessary for a visualization tool. To demonstrate the application of this method, the next part of this thesis deals with extending the visualization technique as a tool for processing simulation output data. This demonstrates how processing the output of quantum chemistry simulations can be connected to the process that produces visualizations. The method for doing this allows a choice of different images to be produced extending the additional avenues of analysis. The potential demonstrated here could prove to be of great value and the idea could be

extended to more specific software in the future.

It should be stressed, however, that chemistry is not the only area of interest. Being able to visualize entanglement across atomic systems, or potentially molecular systems, would be of huge value in many fields. For instance, 'quantum biology' has open problems including the strong dependence of photosynthesis processes and haemoglobin activity centres upon entanglement, where such a technique could be of utility [65–70]. To demonstrate this, the final part of this thesis deals with an example case in the area of state verification. Here, the ability to distinguish similar states is vital to understanding a system's behaviour. Previous techniques have been demonstrated to be inadequate, such as the use of the reduced Wigner function, where specific degrees of freedom are integrated out, which loses key quantum correlations. These are lost due to the integration over correlated degrees of freedom. This increases the need for more reliable tools. Also demonstrated here, is the potential application to larger systems where the spatial-spin correlations become even more important due to the information which can be shared between a large number of subsystems.

Each part of this thesis deals with a different area of the overall problem of visualizing quantum correlations in a consistent and reliable manner. First, the technique is developed and key examples given to aid future analysis. The technique is then applied to the output of 'real' quantum chemistry simulations in order to analyze the same systems in a more realistic setting. This demonstrates the ability to apply this technique to the backend of software used for modelling any system and also the reliability of the visualization tool. Finally, the technique is applied to a system from a different field to demonstrate how the tool can provide deeper insight than current methods. These areas need a more reliable tool for visualizing quantum correlations in order to ensure success in the field. For chemistry, this tool can provide potential routes for better analyzing bond creation, reaction rates and entanglement in quantum biological systems. For quantum information, the ability to characterize states within technology development will be key to producing

reliable quantum devices.

Visualization should not be underestimated in its power to reveal information. For example, the use of a qubit coupled with a field mode is often used as a toy model for decoherence. Without a visualization technique this would not be as successful as the way that information is lost to the environment would not be as accessible. Further, coupling together multiple qubits to understand the mechanism of a quantum process, which relies upon entanglement, is more easily understood through visualizations that demonstrate how the entanglement is passed around. It is therefore reasonable to suggest that the missing spatial-spin effects in atoms and molecules, which affect energy levels and therefore bond formation, would also benefit from visualizations that display those correlations in an accessible way. Due to the success in other fields, it is also reasonable to suggest that such a route to this type of visualization is through the use of phase-space methods.

Given the wide audience that may be interested in this area, efforts have been made to include as much overview of general areas as necessary to fully appreciate the content. This at times may seem unnecessary, but given the cross-disciplinary nature of this work it is probably wise to be as transparent as possible about how all this work fits together. By using the framework presented in Ref. [62] a visualization technique is created for different quantum systems. The technique relies upon building a catalogue of known states that allow analysis of more complicated states by inspection. In practice, this reduces the overhead in understanding the visualization and allows a substantial amount of information to be displayed. It will be shown that for model systems, this technique can be highly informative, in terms of revealing the information contained within a state, as well as identifying the features of chemical simulation software. Finally, the ability to add extra information to such a visualization is discussed with consideration of the different systems that can be subsequently explored.

Chapter 2

Phase-Space Methods

Over the past century, a considerable amount of effort has gone into developing frameworks in order to understand quantum mechanics. The use of state vectors or matrices as the mathematical description is all too familiar to the practising physicist. However, the consequences of quantum mechanics are much more complex and are far harder to interpret or understand. Given the success of phase-space methods in other areas of physics, attempts have been made to explore quantum systems in this way and to develop visualizations [12, 25–29, 31, 32, 36, 39, 46, 48, 53, 57, 71–75]. Although these attempts proved somewhat fruitful, it was only recently that a complete, and general framework, was created [11, 62, 76].

Phase-space methods were first developed by Weyl and Wigner, culminating in a phase-space (Wigner) function that described the quantum state [12, 77]. The generalization of the Wigner function for an arbitrary operator was developed by Moyal, and independently by Groenewold, in an attempt to build a statistical theory which described quantum mechanics [33, 34]. This established a framework for describing the evolution of a quantum state purely in phase space. One component of this framework is considered in the rest of this work; the quasi-probability distribution, the Wigner function. The reasons for the *quasi*-probability aspect is due to the abandonment of positive-definiteness which occurs on extension into the quantum realm. Negativity of the Wigner function has been widely discussed but is not in general a problem [32, 34]. In fact, it may be argued that the negativity

in the Wigner function is the direct manifestation of quantum correlations and, by extension, entanglement [30, 31, 35, 36].

Consideration was given to other quasi-probability functions, or distributions, for representing quantum states. These include the Husimi-Kano Q-function and the Glauber-Sudarshan P-function [37, 46, 78]. These distributions are related to the Wigner function by Gaussian convolution and do have visualizations already. However, the failure of these methods to produce a revealing and simple visualization means that looking at the Wigner function is preferable. This chapter begins by introducing phase space in a classical sense then adapting the formalism for quantum systems. The Wigner function is then introduced for both spatial- and spin-dependent only systems and a general form is developed for spin-1/2 systems.

2.1 Phase Space

In statistical physics, phase-space is often used to display the allowed states, and their probabilities in an understandable way. For instance, in classical mechanics, statistical physics is employed in the Hamiltonian representation. Here, the particles in the system are given a set of positions, each denoted by an x_i, and momenta, denoted by a p_i, where i denotes the particle. Over time, these points then form trajectories in an abstraction called phase space [79].

A phase space, is a space in which all the degrees of freedom of a system are described. For a one dimensional particle this can simply be reduced to the position and momentum, x and p_x respectively. In this space every state of the system is uniquely defined, *i.e.*, objects with identical phase-space descriptions are identical states of the system. At least that is true for classical mechanics.

Although it may seem obvious, it is worth highlighting just how informative the phase-space is in classical mechanics. It is useful to consider a simple example, so the example of the one dimensional simple harmonic oscillator shall now be presented.

2.1.1 Classical Harmonic Oscillator

A system that is often studied in phase space is the simple harmonic oscillator (SHO). Consider for a moment the non-phase-space visualization of this system. It would probably be a video, a picture would not be of any use, of a pendulum swinging or a spring bouncing. The problem is that although these two videos would be very different, the actual systems, from a physical view, are rather similar.

The phase-space visualization displays this similarity by reducing the system down to its degrees of freedom. The first common figure subsequently produced is what will be called a 'slice' of the phase space. By this, all that is meant is that it is a reduction of the full phase-space function by certain degrees of freedom, *i.e.*, if the full phase-space function is $f(x, p_x, t)$ there are a number of slices $f(x, t)$, $f(x, p_x)$, $f(p_x, t)$, and all the single variable functions. This slicing approach leads to the popular textbook picture of a swinging pendulum as two sine waves, see Fig. 2.1 (a).

To understand the system though, the two pictures must be studied together. One showing the position of the pendulum, the other the momentum of the pendulum with respect to time. There is a phase difference between the two functions from which the physics of the system can be deduced [79]. It can be very hard to see whether there is a subtle damping in the system or if there is any driving force. In isolation they are of limited use but when combined, they produce significantly more information. Further, by comparison with visualizations of known systems, different features in an unknown system can be pulled out meaning that the physics can be better described. Essentially, signatures that identify certain types of physics can be applied across a range of states.

With some thought of where this is heading, it should be pointed out that these slices are created from the full phase space. For instance the position-time slice is created by integrating out the momentum;

$$\int_{-\infty}^{\infty} f(x, p_x, t)\ \mathrm{d}p_x. \tag{2.1}$$

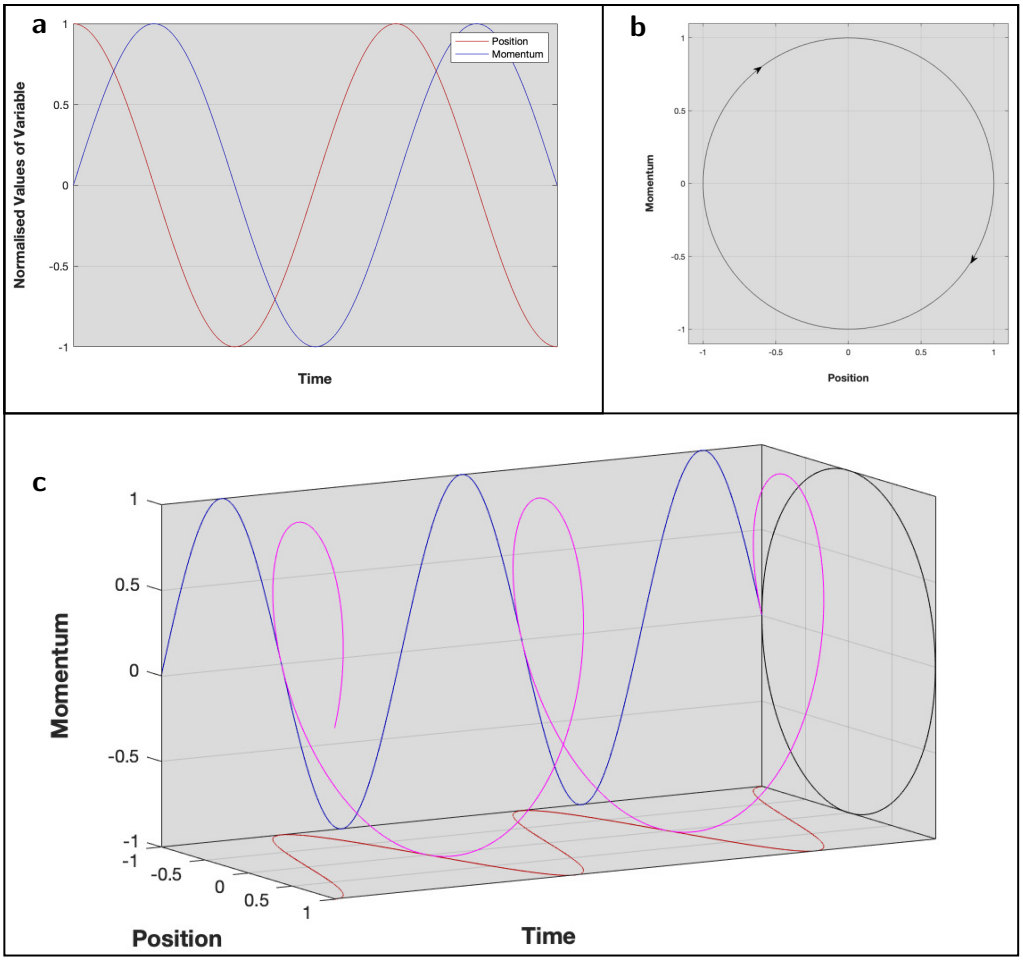

Figure 2.1: This figure displays several depictions of the simple harmonic oscillator in phase space. (a) shows the evolution of the position and momentum values of the oscillator, normalized to unity. As can be seen they follow a cosine and sine function respectively. (b) is the normalized phase space representation of the motion of the oscillator. It forms a circle that rotates anticlockwise as the system evolves. Finally in (c), is a representation of how all these images fit together. This figure essentially demonstrates three different ways of displaying the information about the harmonic oscillator using different phase-space slices.

A similar approach is used for the momentum-time slice and the position-momentum slice. Throughout the rest of this work 'integrating out' will refer to the process of removing a degree of freedom from a function to obtain a slice of that function (or a reduced function).

The position-momentum slice, Fig. 2.1 (b), is somewhat easier to understand – a point following a circular path. Often this picture is displayed as a circle with arrows indicating the direction that the point rotates in (an indication of the involvement of time in the full Wigner function). This single picture allows a substantial amount

of information about the state to be deduced. Further, it is much easier to see slight changes that could be brought in by damping or driving forces (in these cases the picture would begin to spiral inwards or outwards respectively).

Equally, combining all this information into one plot (the full phase-space slice being the spiral), as in Fig. 2.1 (c), it can become somewhat overwhelming. The information is now hard to pull out and the utility of a phase-space visualization has been lost. The line between good and bad is very thin for visualizations and somewhat subjective. This work has been motivated by the desire to produce an easily understandable visualization, that has the power, impact and utility of the phase-space visualization of the harmonic oscillator.

2.1.2 Formalized Classical Phase Space

Before considering the methods that will be used throughout this work, it is useful to formalize the classical phase space. As discussed in § 2.1 the key advantage of phase space is that it provides a convenient visualization of the state. Although other techniques exist of visualizing the state, most prove to be inadequate for studying quantum correlations [18–22, 57, 73].

Classical statistical physics introduces the ensemble in phase space with an associated probability function. The expectation value of a quantity Q can be found using its associated function $Q(\Omega)$ using

$$\langle Q \rangle = \int Q(\Omega)\, P(\Omega)\, \mathrm{d}\Omega, \tag{2.2}$$

where Ω is an appropriate parametrization of the space. Here, $P(\Omega)$ is the probability density function of the phase space, parametrized over Ω. P has many similarities to the wavefunction in quantum mechanics, in that it contains sufficient information to fully describe the state, but it is not immediately obvious how to extend this to the quantum realm.

However, when considering the expectation values of quantum operators a route

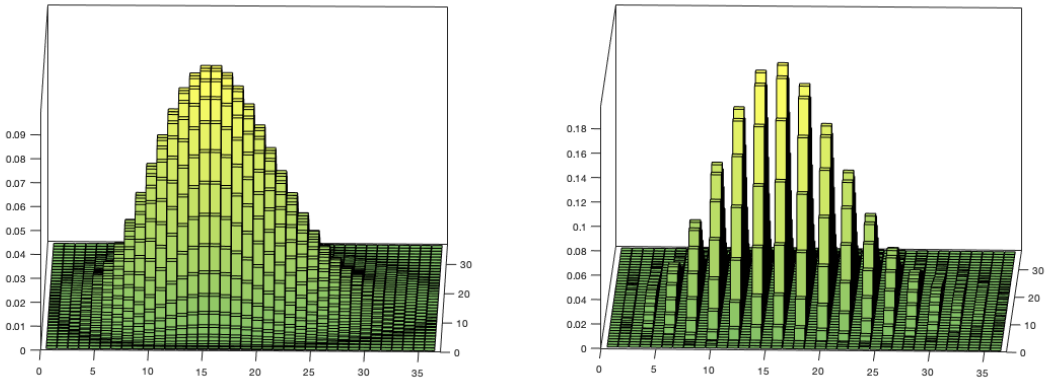

Figure 2.2: Here are examples of a visualization of the density matrix for two different states. On the left is a coherent state $|\alpha\rangle$ with $\alpha = 4$ and appears as a Gaussian whilst the one on the right is the equal superposition of $|\alpha\rangle$ and $|-\alpha\rangle$. Noticeably, this superposition eliminates half the terms from the density matrix and it becomes clear that the two states can be distinguished. Note the vertical axis indicates the value in the matrix and the other axes represent the number states that form the basis and therefore the position of the value in the matrix.

of application can be found. A similar notation is used for the expectation value of an arbitrary operator $\hat{A}(\Omega)$ that describes a quantity A such that

$$\langle A \rangle = \mathrm{Tr}\left[\hat{A}\hat{\rho}\right] \tag{2.3}$$

where $\hat{\rho}$ is the density operator. The time evolution of the distribution function, the function that describes the positions and velocities of the particles, in classical phase space can be described by use of the Liouville equation [79]. This helps motivate the use of the Wigner function because in the classical limit, the evolution of the Wigner function is analogous to the Lioville equation and the Wigner function itself reduces to the Liouville probability density function [80].

The density operator is most commonly given in matrix form and has been used to visualize quantum states [38]. For instance, if we consider two different states (the exact form of which are discussed later), in this case the coherent state $|\alpha\rangle$ with $\alpha = 4$ and a Schrödinger's cat state made of an equal superposition of $|\alpha\rangle$ and $|-\alpha\rangle$, then visualizing the density matrix immediately highlights the difference. As seen in Fig. 2.2, the coherent state appears as almost Gaussian whereas the superposition

has half the elements missing. It is features like this that could be used to develop signatures for identifying commonality between states. Although able to distinguish between the states, the visualization offers little extra information about the exact nature of the state.

2.1.3 Quantum Phase Space

In classical phase space, each point is uniquely identified as a state of the system with an exact position and momentum. When transferring this into the quantum realm a clear problem arises. The Heisenberg uncertainty relation essentially quantifies the extent to which two operators do not commute within an inner product space. It states the lack of commutation in terms of the dispersion, standard deviation, of the operators. For the special case of position-momentum phase space (where the relevant commutation relation is $[\hat{q}, \hat{p}] = \mathrm{i}\hbar$) this can be written as

$$\left\langle (\Delta\hat{q})^2 \right\rangle \left\langle (\Delta\hat{p})^2 \right\rangle \geq \left(\frac{\hbar}{2}\right)^2, \tag{2.4}$$

or more commonly,

$$\Delta\hat{q}\Delta\hat{p} \geq \frac{\hbar}{2}. \tag{2.5}$$

Here $\Delta\hat{q}$ and $\Delta\hat{p}$ are the dispersion, or uncertainty, of the position and momentum operators respectively [81].

Although commonly misstated as a consequence of measurement, it is important to impress that the Heisenberg uncertainty principle is simply a consequence of mathematics [82]. The discussion often fails to separate the violable Heisenberg measurement-disturbance relationship and the inviolable uncertainty principle [83]. Due to the fact that the uncertainty principle is a strict, rigorous mathematical theorem, independent of quantum mechanics, or any other physical theory, measurement has no bearing. Given this fact, a phase space representation is directly affected by the uncertainty principle.

In classical physics, the fact that position and momentum can have absolute

values at all times means that elements in phase space are infinitesimal. However, in the quantum theory, where the commutation relation between position and momentum operators in non-zero, there is a finite size to such an element. The smallest element therefore is of size $(\hbar/2)^n$ where n is the number of non-commuting degrees of freedom in the phase space [15]. This means a state can no longer be represented by a point in the phase space and translating the classical phase space into the quantum realm becomes problematic.

2.2 The Wigner Function

An attempt to align classical statistical mechanics with the new quantum theory, led to the development of, what is now called, the Wigner function [12,25,33,39,84]. The Wigner function is a quasi-probability distribution developed in an attempt to express the wavefunction in terms of its statistical distribution in phase space. Introduced in 1932 by Eugene Wigner, it has since had few modifications, but many extensions have opened up its utility within physics [12]. It is important to note that Moyal and Groenewold separately and independently derived the Wigner function, applying it more directly to quantum mechanics and the relationship of expectation values and phase-space [33,34]. First, we shall explore the links between the Wigner function and classical mechanics to provide the motivation for the work that follows. We will then consider how this allows us to produce a Wigner function that can be used for describing an arbitrary quantum system. Finishing with the practicalities of implementing such an analysis.

The Wigner function is a quasi-probability distribution, as it contains negative values which can potentially indicate quantum correlations, that links the wavefunction of a quantum state, the standard representation of the state, with phase space [25,33,84–88]. It converts the wavefunction vector into a probability distribution, in the sense that it is normalized to have an area less than unity, and allows a different analysis of the quantum interactions within a state [33, 86, 88]. Although there has been concern over the appearance of negative probabilities, it is now gen-

erally agreed that due to the restriction of the region size, in accordance with $\hbar$, these disappear in the classical limit and therefore remains physical [35, 89]. This is because any measurement, and therefore probability, is taken over a quadrature, due to the uncertainty, and therefore always results in a non-negative value.

This means that the value of the Wigner function at a point in phase space is related to the probability that the particle will appear in that state. Initially, it would be easy to believe that this means that there are regions where this takes a negative probability and there is then an issue about what exactly this means. By considering the fact that the probability of a measurement is determined by averaging over a quadrature, and therefore the negative values are simply constituents of a larger sum which will always result in a non-negative value, they are not problematic. Instead, they are likely to be the result of quantum correlations or interference, *e.g.*, by putting two coherent states into a superposition they interfere with each other producing oscillations of negative and positive values. Equally, it can be stated that the negativity is a consequence of the non-Gaussian nature of the Wigner function known as Hudson's theorem [35].

Due to the success of the Wigner function in other fields, particularly in quantum optics, it seems reasonable to believe that it may well be useful in visualizing the entanglement that exists within atoms and molecules [15, 44]. A full history of the Wigner function is unnecessary for this work and would inevitably miss out individuals who have contributed in various ways. Instead, the key features of the mathematical framework are presented with explanations where necessary. For a more complete treatment see Refs. [62, 76, 88]. Note that the following introduction follows Ref. [90] closely.

2.2.1 Spatial Wigner Functions

The Wigner function is the quasi-probability distribution that defines the state of the system through the system's degrees of freedom [62, 76, 88]. For a single particle,

the Wigner function can be written as

$$W_{\hat{\rho}}(q,p) = \int_{-\infty}^{\infty} \left\langle q - \frac{\xi}{2}\middle|\hat{\rho}\middle|q + \frac{\xi}{2}\right\rangle \exp(\mathrm{i}\, p\xi)\ \mathrm{d}\xi, \tag{2.6}$$

where $\hat{\rho}$ is the density operator for the state [15]. This form can be extended to any operator, $W_{\hat{A}}$ and to the Fock basis, the set of states that arise from the SHO.

An operator can be introduced that displaces the vacuum state to some new point in phase space. This displacement operator $\hat{D}(\alpha) = \exp(\alpha\hat{a}^\dagger - \alpha^*\hat{a})$ where α is related to position and momentum through the form $(1/\sqrt{2})(q + \mathrm{i}\, p)$ for unit mass and resonant frequency and $\hat{a}^\dagger$ and $\hat{a}$ are the creation and annihilation operators respectively [37]. Relating this form to the Wigner function, *via* a Fourier transform, allows the Wigner function to be written in terms of a group action [34, 38]

$$W(\alpha) = \mathrm{Tr}\left[2\hat{\rho}\hat{D}(\alpha)\,\hat{\Pi}\hat{D}^\dagger(\alpha)\right], \tag{2.7}$$

$$= \mathrm{Tr}\left[\hat{\rho}\hat{\Pi}(\alpha)\right]. \tag{2.8}$$

Here $\hat{\Pi}$ is the standard parity operator that reflects the state through the origin. This means that $\hat{\Pi}(\alpha)$ reflects the state through the origin and displaces it by some amount and is therefore called the displaced parity operator. It is this displaced parity operator, or kernel, that is the basis for the general form presented in Ref. [62].

As an example of this, some states are presented in Fig. 2.3 and Fig. 2.4. Each of these states demonstrates different features of this formulation ensuring that all elements of the kernel are correctly computed, even though only the trace of the resultant matrix is used.

The states in Fig. 2.3 are a series of Fock states which appear as oscillations, related to the order of the state, in phase space with an intensity of $1/\pi$, due to normalization, centred at the origin. The key signature of the Wigner function, with regards to Fock states, is the increase in negative regions, forming rings around the origin, as n increases.

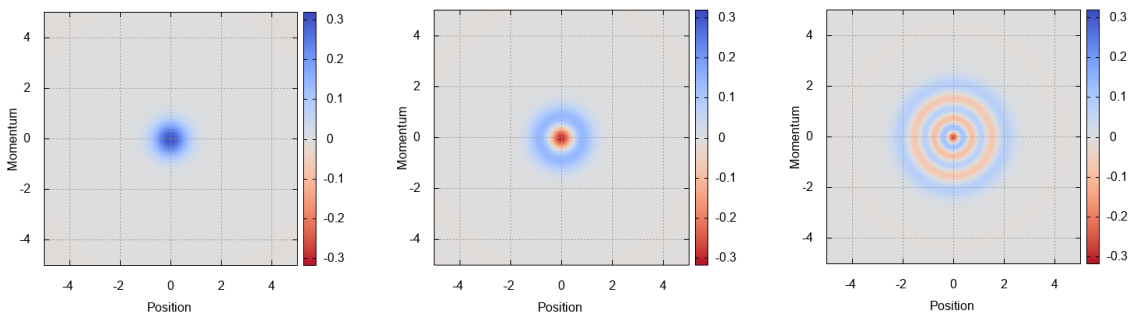

Figure 2.3: The $n = 0$, 1 and 5 Fock states plotted in phase space. They are normalized and show the increase of negative regions in the Wigner function as n increases.

Using the Fock states as a basis allows the consideration of coherent states. Due to the oscillatory nature of the Fock states, the coherent states appear as Gaussians in phase-space. Their origin is determined by the amount of displacement occurring and the standard method of labelling the state, is such that a state displaced by some amount α is denoted as the coherent state $|\alpha\rangle$. The relationship between the coherent states and the Fock states can be expressed as [91]

$$|\alpha\rangle = \exp\left(-\frac{|\alpha|^2}{2}\right) \sum_{n=0}^{\infty} \frac{\alpha^n}{\sqrt{n!}} |n\rangle \,. \tag{2.9}$$

Further, due to the well localized nature of coherent states, the negativity disappears.

These states are often used to showcase a particular feature of the Wigner function, shown to have been useful in many areas such as quantum optics, the appearance of interference terms [15]. Combining these coherent states into a superposition produces a Schrödinger's cat state, both odd and even forms are plotted in Fig. 2.4. The difference between the two cases being that one has a central negative peak in the interference terms and the other has a positive peak. It is important to be able to distinguish these because compositions of more complex states can be affected to a high degree if the interference contributions are not correct, due to superposition. This interference term signature is an obvious feature that can be utilized when analyzing a state. To demonstrate this a number of cat states have also been plotted.

These also provide an example of the difference between quantum and classical

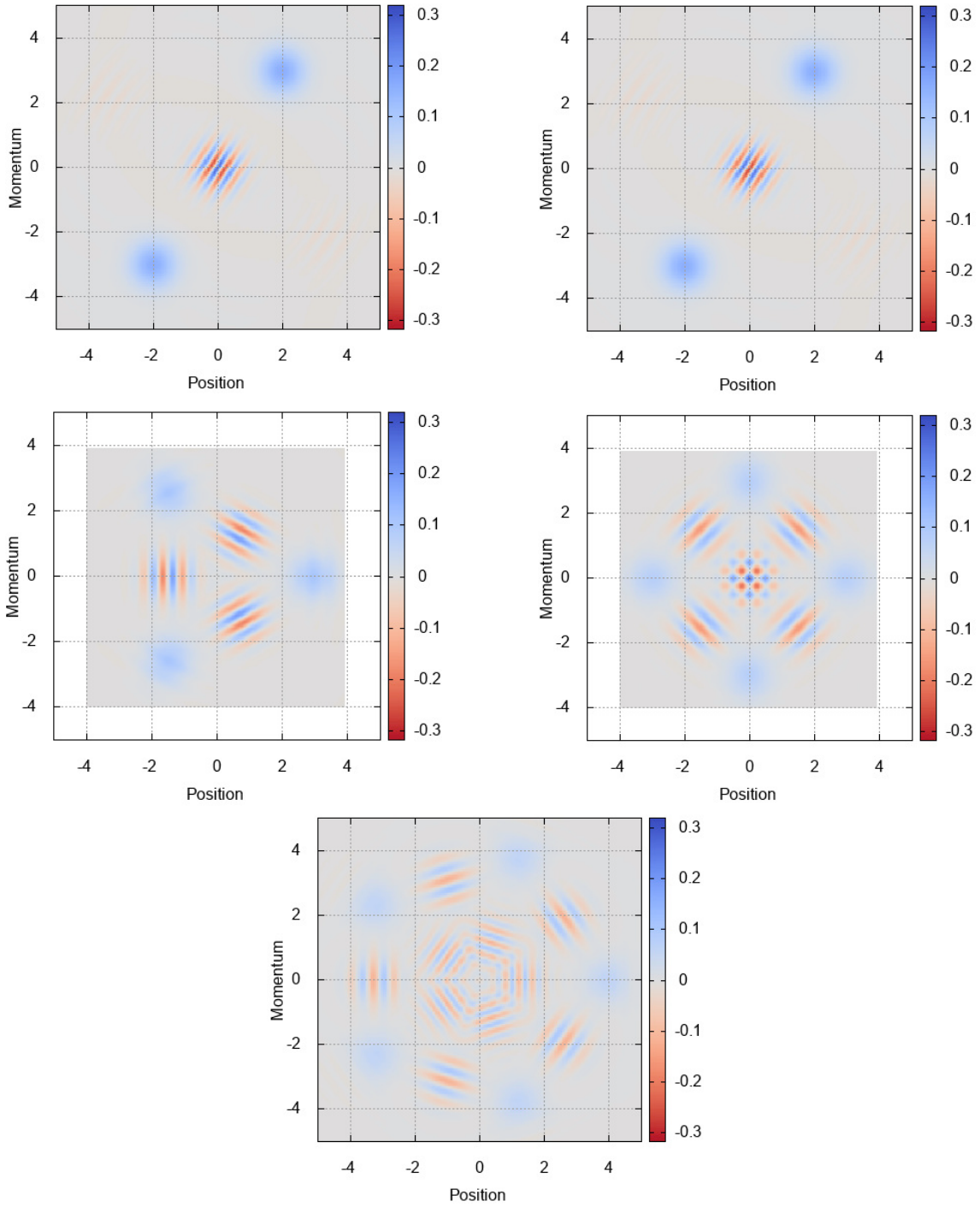

Figure 2.4: A collection of Schrödinger's cat state plots to demonstrate the key features of coherent states and the interference terms that arise due to superposition. From left to right, top to bottom are the states: $\alpha = 2 + 2\,\mathrm{i}$, the even superposition; $\alpha = 2 - 2\,\mathrm{i}$, the odd superposition; the cube roots of unity, rescaled for clarity, as the values of α in a three state superposition; the fourth roots of unity, rescaled for clarity, as the values for α in a four state superposition; and the fifth roots of unity, rescaled for clarity, as the values for α in a five state superposition.

correlations discussed later. The interference terms are a signature of quantum correlations, that is, they appear in a Schrödinger's cat state due to the quantum

nature of the state. If the interference terms were not there, there would still be correlations between the two coherent states but this would be purely classical. For instance, in the classical only situation there is an equal probability of the object being found in either one state or the other but in a quantum situation it can also be found in the region of the interference terms.

2.2.2 Spin Wigner Function

For an electron, the full Wigner function is formed of both spin and spatial degrees of freedom. Having established the Wigner function for the spatial components, we must also now introduce the spin component. It was shown in Ref. [76] how to develop the framework for the Wigner function of a spin-half particle. The phase space of such a system is plotted on the surface of a sphere, the displacement operator is instead replaced with the rotation operator

$$\hat{U}(\theta,\phi,\Phi) = \exp(\mathrm{i}\,\hat{\sigma}_z\phi)\exp(\mathrm{i}\,\hat{\sigma}_y\theta)\exp(\mathrm{i}\,\hat{\sigma}_z\Phi) \tag{2.10}$$

where $0 \leq \theta \leq \pi/2$, $0 \leq \phi \leq \pi$, and $0 \leq \Phi \leq 2\pi$ and the operators $\hat{\sigma}_y$ and $\hat{\sigma}_z$ are the standard Pauli matrices. Note, this operator is not a unique choice but is most suitable for this work. As we shall find shortly, the third angle Φ cancels and plays no part in the Wigner function.

The spin parity chosen here satisfies the Stratonovich-Weyl correspondence and is given as

$$\hat{\pi} = \frac{1}{2}\left(\mathbb{1} + \sqrt{3}\sigma_z\right). \tag{2.11}$$

See Ref. [76] for a full discussion on the choosing of the spin parity. A different sign convention is used for $\hat{U}(\theta,\phi,\Phi)$ and $\hat{\pi}$ to that used in Refs. [11, 62, 76] so that the Wigner function for the state $|\uparrow\rangle$, corresponding to the $+1$ eigenvalue of $\hat{\sigma}_z$, *i.e.*, spin up, points up. This is done so that the visualization is more intuitive.

In the same way as for the spatial Wigner function, the final form is the expect-

ation value of the displaced parity;

$$W(\Omega) = \mathrm{Tr}\Big[2\hat{\rho}\hat{U}(\Omega)\,\hat{\pi}\hat{U}^{\dagger}(\Omega)\Big]\,, \tag{2.12}$$

$$= \mathrm{Tr}\Big[\hat{\rho}\hat{\Pi}(\Omega)\Big]\,, \tag{2.13}$$

where $\hat{\Pi}(\Omega)$ is the displaced spin parity. From Eq. (2.10) and (2.11), noticing that $\exp(-\mathrm{i}\,\sigma_z\Phi)\hat{\pi}\exp(\mathrm{i}\,\sigma_z\Phi) = \hat{\pi}$, it is clear that there is no dependence of the Wigner function on Φ.

2.2.3 Composite Systems

The spatial and spin Wigner functions are both important for different systems. There is much utility in exploring both of these in an independent manner. However, for the purpose of dealing with quantum chemistry, or rather with atomic level reactions, it is more useful to combine them. That is to say that we create a Wigner function for the entire system, coupling spin with spatial degrees of freedom. Fortunately, the Wigner function has the nice property that the composite system is formed by taking expectation values of the tensor product of each constituent part. That is to say, that the spatial and spin displaced parities are created separately and then the tensor product is taken.

In the case of the hydrogen atom, if the nucleus is neglected, the electron needs a spatial displaced parity and a spin displaced parity with the final Wigner function being the expectation value of the tensor product of them;

$$W(\alpha,\Omega) = \mathrm{Tr}\Big[\hat{\rho}\left(\hat{\Pi}(\alpha)\otimes\hat{\Pi}(\Omega)\right)\Big]\,. \tag{2.14}$$

Instead, if a number of different spins are combined, then the Wigner function becomes;

$$W(\Omega_1,\Omega_2,\ldots) = \mathrm{Tr}\Big[\hat{\rho}\left(\hat{\Pi}(\Omega_1)\otimes\hat{\Pi}(\Omega_2)\otimes\ldots\right)\Big]\,. \tag{2.15}$$

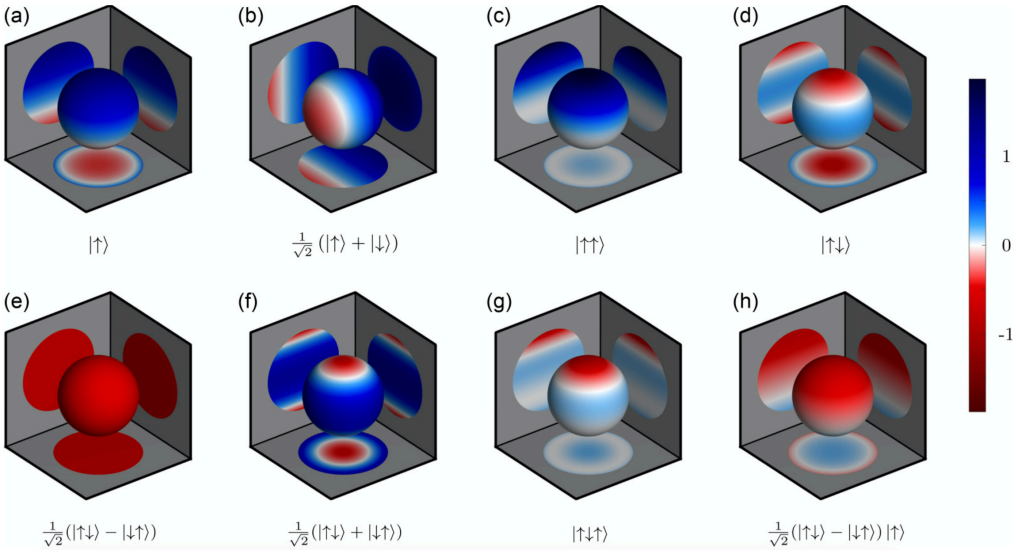

Figure 2.5: A set of example plots of spin Wigner functions that are also used to aid interpretation of the results presented later in this work. The state vectors for each Wigner function are given under each image. Multi-spin states have been plotted on the equal angle slice, *i.e.*, $\theta_i = \theta$ and $\phi_i = \phi$ for all i. Note that (c) is the product of two states which individually are the same as (a), (g) is the product of (a) and (d), and (h) is the product of (a) and (e). These states are discussed in greater detail later but also see Ref. [76] for a full discussion.

A set of examples of such states are presented in Fig. 2.5 which itself is a reference set of states for later discussion. The key feature to notice is the ability to distinguish of the singlet state, not standard for other techniques, as well as the ability to discern each triplet state with little effort. Note that the states with multiple spins are plotted on the equal-angle slice, *i.e.*, $\theta_i = \theta$ and $\phi_i = \phi$ for all i. This is motivated by the fact that as outlined in Ref. [92], a significant amount of the total information is contained on this slice. Further, the equal-angle slice produces a uniquely identifiable singlet state which is necessary for the following work. Although other slices, *i.e.*, those where the values of θs and ϕs differ, could be taken, the work within this thesis does not require them.

Moving beyond hydrogen, the number of electrons in the system will go up. The displaced parity for each electron is formed in the same way and the total displaced parity is the tensor product of those belonging to each electron. For N electrons,

the model of an atom excluding the nucleus, the Wigner function is

$$W(\alpha_1, \ldots, \Omega_1, \ldots) = \mathrm{Tr}\left[\hat{\rho}\,\left(\hat{\Pi}(\alpha_1) \otimes \ldots \otimes \hat{\Pi}(\Omega_1) \otimes \ldots\right)\right], \tag{2.16}$$

$$= \mathrm{Tr}\left[\hat{\rho} \bigotimes_{i=1}^{N} \hat{\Pi}_i^{\mathrm{e}^-}(\alpha_i, \Omega_i)\right], \tag{2.17}$$

$$= \mathrm{Tr}\left[\hat{\rho} \bigotimes_{i=1}^{N} \hat{\Pi}_i^{\mathrm{e}^-}(\mathbf{q}_i, \mathbf{p}_i, \theta_i, \phi_i)\right], \tag{2.18}$$

$$W(\mathbf{q}_1, \mathbf{p}_1, \theta_1, \phi_1, \ldots) = \mathrm{Tr}\left[\hat{\rho}\hat{\Pi}(\mathbf{q}_1, \mathbf{p}_1, \theta_1, \phi_1, \ldots)\right]. \tag{2.19}$$

Notice that the α variable is converted to the position and momentum of the electron and Ω expands to just θ and ϕ as Φ cancels out in the Wigner function. This means that each electron provides three position degrees of freedom, three concomitant momentum degrees of freedom and two spin degrees of freedom. The Wigner function, or displaced parity, for a single electron is eight dimensional. This means that the Wigner function for an N-electron atom is $8N$ dimensional.

2.2.4 Marginals

There are a number of techniques that can be used to reduce the number of degrees of freedom in the system. Having demonstrated that even a simple hydrogen system, approximated as an electron in a central potential, is eight dimensional, the question is how to reduce it. Thankfully, due to the way in which the Wigner function has been developed, the method is the same as for those appearing in quantum optics. For instance, the Wigner function of a one-dimensional Fock states has both position and momentum marginals (more in the case of increased dimensionality of the system). A marginal is therefore a reduced form of the full state focusing on a subset of the degrees of freedom. However, it is common to also look at just the position space, or the momentum space depending upon the system's properties, and characterize the features using a reduced Wigner function. This is done by integrating over all the degrees of freedom that are to be removed, commonly called integrating out.

For instance, the Wigner function for the one-dimensional Fock state is a function of both position and momentum; $W(q,p)$. The position marginal, also in this case the position probability density function, for the n^{th} Fock state is

$$\psi(q) = |\langle q|n\rangle|^2 \,, \tag{2.20}$$

$$= \frac{1}{\sqrt{2\pi}} \int_{-\infty}^{\infty} W_n(q,p)\ \mathrm{d}p, \tag{2.21}$$

$$= W_n(q)\,. \tag{2.22}$$

Similarly, the same thing could be done for the momentum degree of freedom producing a different marginal. For higher dimensional systems, this principle of integrating out degrees of freedom still holds. This means even in the case of a spin-spatial system, spin degrees of freedom or spatial degrees of freedom or momentum degrees of freedom can individually, or collectively, be integrated out to produce a number of reduced Wigner functions. Further, each marginal may require a different procedure in order to be analyzed.

This is the format that intracules utilizes, *i.e.*, they build a collection of marginals to characterize the state. Although helpful in a number of situations, it fails when the system gets complicated because the number of marginals that must be considered increases dramatically. A method for solving this problem is to produce a visualization where different marginals display information in the same way. These marginals can then be used to probe the system further so that features that are relevant to the problem can be identified. Although, as there is no easy way of determining which marginals must be used, a method for exploring as many as possible, in as easier way as possible, is necessary.

2.3 General Form for Spin-Half Particles

To demonstrate the ability with which the Wigner function can be used, it is useful to consider the case of a spin-half particle in three dimensions $\boldsymbol{q}$. This of course is

analogous to the electron. The wavefunction of the pure state is

$$\psi = \begin{pmatrix} u(\boldsymbol{q}) \\ v(\boldsymbol{q}) \end{pmatrix}, \tag{2.23}$$

such that the density matrix is

$$\hat{\rho} = \begin{pmatrix} u(\boldsymbol{q})\, u^*(\boldsymbol{q}') & u(\boldsymbol{q})\, v^*(\boldsymbol{q}') \\ v(\boldsymbol{q})\, u^*(\boldsymbol{q}') & v(\boldsymbol{q})\, v^*(\boldsymbol{q}') \end{pmatrix}. \tag{2.24}$$

Now, the Wigner function is a function of position, momentum and spin degrees of freedom;

$$W(\boldsymbol{q},\boldsymbol{p},\boldsymbol{e}) = \frac{1}{\pi^3}\,\mathrm{Tr}\left[\hat{\Delta}(\boldsymbol{e}) \int_{-\infty}^{\infty} \hat{\rho}(\boldsymbol{q}-\boldsymbol{\xi},\boldsymbol{q}+\boldsymbol{\xi}) \exp(-2\,\mathrm{i}\,\boldsymbol{p}\cdot\boldsymbol{\xi})\ \mathrm{d}^3\boldsymbol{\xi}\right], \tag{2.25}$$

$$= \frac{1}{\pi^3}\,\mathrm{Tr}\left[\frac{1+\sqrt{3}\,(\boldsymbol{e}\cdot\boldsymbol{\sigma})}{2} \int_{-\infty}^{\infty} \hat{\rho}(\boldsymbol{q}-\boldsymbol{\xi},\boldsymbol{q}+\boldsymbol{\xi}) \exp(-2\,\mathrm{i}\,\boldsymbol{p}\cdot\boldsymbol{\xi})\ \mathrm{d}^3\boldsymbol{\xi}\right], \tag{2.26}$$

taking $\hbar = 1$ and where $\boldsymbol{e} = (\sin\theta\cos\phi, \sin\theta\sin\phi, \cos\theta)$ and $\hat{\Delta}(\boldsymbol{e})$ is the kernel associated with θ and ϕ [62].

Consider the position-spin marginal, that is the full Wigner function integrated over all momentum degrees of freedom only, then using the fact that the integrand only has a p dependence in the exponential, which will evaluate to $\pi^3\delta(\boldsymbol{\xi})$ then

$$W(\boldsymbol{q},\boldsymbol{e}) = \mathrm{Tr}\Big[\hat{\Delta}(\boldsymbol{e})\,\hat{\rho}(\boldsymbol{q})\Big], \tag{2.27}$$

$$= \mathrm{Tr}\left[\frac{1}{2}\begin{pmatrix} 1+\sqrt{3}\cos\theta & \sqrt{3}\sin\theta\,\mathrm{e}^{-\mathrm{i}\,\varphi} \\ \sqrt{3}\sin\theta\,\mathrm{e}^{\mathrm{i}\,\varphi} & 1-\sqrt{3}\cos\theta \end{pmatrix} \begin{pmatrix} |u(\boldsymbol{q})|^2 & u(\boldsymbol{q})\,v^*(\boldsymbol{q}) \\ v(\boldsymbol{q})\,u^*(\boldsymbol{q}) & |v(\boldsymbol{q})|^2 \end{pmatrix}\right], \tag{2.28}$$

$$= \frac{|u(\boldsymbol{q})\,|^2 + |v(\boldsymbol{q})\,|^2}{2} + \frac{\sqrt{3}\left[\sin\theta\left(u(\boldsymbol{q})\,v^*(\boldsymbol{q})\,\mathrm{e}^{\mathrm{i}\,\phi} + u^*(\boldsymbol{q})\,v(\boldsymbol{q})\,\mathrm{e}^{-\mathrm{i}\,\phi}\right) + (|u(\boldsymbol{q})\,|^2 - |v(\boldsymbol{q})\,|^2)\cos\theta\right]}{2}, \tag{2.29}$$

$$\begin{aligned} = \frac{|u(\boldsymbol{q})\,|^2 + |v(\boldsymbol{q})\,|^2}{2} &+ \sqrt{3}\left[\Re(u^*(\boldsymbol{q})\,v(\boldsymbol{q}))\sin\theta\cos\phi + \Im(u(\boldsymbol{q})\,v^*(\boldsymbol{q}))\sin\theta\sin\phi\right] \\ &+ \frac{\sqrt{3}}{2}(|u(\boldsymbol{q})\,|^2 - |v(\boldsymbol{q})\,|^2)\cos\theta. \end{aligned} \tag{2.30}$$

As discussed earlier, this formulation is analogous to having the continuous variables on the surface of the Bloch sphere. In essence, at each point in space a pure state Wigner function exists pointing in some direction, position dependent unless the state is separable, scaled by the factor $|u|^2 + |v|^2$. This means that the total Wigner function encodes the local charge and spin density for all points in space. Essentially, the Wigner function is able to display information about the state of the electron at all points in space such that information about overall magnetization or charge can be distilled. This is the basis of subsequent discussions, especially in relation to the lithium atom.

Chapter 3

Theoretical Atoms

Being able to discuss chemistry, in particular the reason atoms and molecules form in the way they do, often requires some visualization. The Rutherford atom, now synonymous with physics for the vast majority of people, is rather unphysical and not appropriate for modern application but provides a useful visual tool for discussion. The assumptions of the model are also far too restrictive to obtain any real insight at a quantum level. This chapter discusses the development of a visualization that can be used to explore some of the features of atomic systems relevant to both quantum chemistry and technologies. It closely follows the work I did set out in Ref. [90].

Traditionally, atomic and molecular orbitals are visualized using the 90-percentile function. This is the surface that contains 90 percent of the probability density of the associated quantum-mechanical energy eigenstate, with particular bounds determining its construction [93]. Although useful for low-level systems, the lack of spin information in the visualization is a barrier to understanding states in quantum chemistry. The lack of spin information means that correlation information within atoms is lost and molecular spin information fails to fully account for interactions between electrons. Spin-spatial and spin-spin correlations help determine the way in which atoms may react, including how bonds may form [17, 94–97]. This is largely due to the fact that certain spin states can reduce energies, yet the traditional 90-percentile visualization lacks any of this insight. Further, although intracules provides some extra detail, the accessibility is low and not all correlations are present.

The fact that spin affects the arrangement of atoms is not unfamiliar. It has already been empirically studied by chemists, seen through the formulation of the Aufbau Principle and Hund's Rules [93]. These rules, although associated with spin pairing energies, say little about the effect that the spin state has across a molecule [98]. As atomic level chemistry becomes more dependent upon quantum effects, the need to better explain subtle quantum effects, such as electron entanglement across a molecular structure, and properties becomes more important. The need for a visualization tool capable of describing such processes (and modern quantum-chemistry numerical simulations which include spin and entanglement) is increased [99–102]. Further, work studying chemical reactions such as those in Refs. [103–105], suggest that such tools are lacking from the analysis. The visualization, if it is to be able to capture all quantum correlations, must therefore contain the spin information as well as the spatial degrees of freedom in the system.

There have been a number of attempts made to visualize atoms and molecules in a more complete way [18–22, 48, 53, 57, 60, 61, 73, 87]. Due to the strong entanglement relationships between all of the degrees of freedom in certain systems none of these is particularly satisfactory. Given that a Wigner function (if constructed correctly) is informationally-complete, it would seem an obvious candidate for such visualizations. This would allow the system to be represented as a quasi-probability density function as outlined in the previous chapter.

The Husimi-Q function, reduced Wigner function and other techniques that currently exist for visualizing quantum states consider spatial and spin degrees of freedom separately. These methods therefore consider different homogeneous frameworks for visualizing their systems, *i.e.*, the systems have only one phase-space representation. By extension, a heterogeneous system is one which combines differing phase-space representations. The necessary framework for representing a heterogeneous system is presented originally in Refs. [11, 62]. Prior to this work, there was only one significant consideration of such a system. A response to the generalization of the Wigner function presented in Refs. [11], it considers the use of the

negative volume of Wigner functions as an entanglement witness for hybrid bipartite states [36]. The result of their consideration is a more 'convenient tool' for the experimental verification of such states. This problem has been pursued because as the quantum correlations within a system become more important, the ability to visualize them becomes more necessary in order to fully characterize the state.

The visualization of the Wigner function is very much application dependent. Due to the construction of the Wigner function, as outlined in the previous chapter, it is clear that in the case where momentum is more important momentum-space can be readily chosen as a subspace for exploring the physics. For instance, an electron in a periodic lattice would have well-defined momentum states therefore integrating out the spatial degrees of freedom would be a sensible choice. Similarly, an electron in a potential that is periodic in one dimension and quadratic in those perpendicular, integration of the spatial component in the periodic dimension and the momentum components in the others would be more appropriate.

The position representation is the usual route for describing an atom, as spatial degrees of freedom are often more significant than momentum degrees of freedom in chemical analysis. This is not least because the 'shape' of the atom is of relevance to they way in which bonds can form and molecules react. The method of using the position representation in atomic visualizations have become a staple of most chemistry textbooks. Notably, these are created by use of the 90-percentile and are coloured to indicate the sign of the wavefunction at that point. In an attempt to create visualizations of atoms that are familiar, and thereby easier to interpret, the position space has been used here. Although momentum space could be chosen it is not the most intuitive to begin this analysis. The effect of this choice, is to produce visualizations that have the same structure as those that are prevalent within textbooks and immediately recognizable to the community. This chapter introduces the visualization and the discusses its application to a number of different atomic states.

3.1 Theory

To begin the construction of the visualization, it is important to understand the theoretical framework of the system. Due to the fact that previous visualizations have had simplifications and assumptions within them that compromise the method, it is necessary to be explicit about the method used here. The chemistry behind the method may be unfamiliar so a short introduction, highlighting the important features, is presented. Note that the visualization is not contingent upon the construction of states in this way, as will be explored later in this thesis, it is simply an accessible way of introducing the technique. The following section follows standard chemistry textbook derivations such as those found in Refs. [93, 98, 106–108].

3.1.1 Classical Energy

To be able to describe a molecule is to be able to specify the relative positions and angles of all the constituent atoms. But to do this a thorough understanding of the shapes of the atoms is therefore needed. Beginning with a single-electron system, we shall only consider hydrogen, but it should be noted that an ion with one nucleus and one electron, *e.g.* He^+, would be equivalent, where the energy is given to the first approximation as

$$E = \mathcal{T}_n + \mathcal{T}_e + \mathcal{V}(\boldsymbol{r}), \tag{3.1}$$

$$\begin{aligned} &= \frac{1}{2} M_n \left[\left(\frac{\mathrm{d}x_n}{\mathrm{d}t} \right)^2 + \left(\frac{\mathrm{d}y_n}{\mathrm{d}t} \right)^2 + \left(\frac{\mathrm{d}z_n}{\mathrm{d}t} \right)^2 \right] \\ &\quad + \frac{1}{2} m_e \left[\left(\frac{\mathrm{d}x_e}{\mathrm{d}t} \right)^2 + \left(\frac{\mathrm{d}y_e}{\mathrm{d}t} \right)^2 + \left(\frac{\mathrm{d}z_e}{\mathrm{d}t} \right)^2 \right] - \frac{e^2}{4\pi\varepsilon_0 r}. \end{aligned} \tag{3.2}$$

Values sub-scripted n are co-ordinates associated with the nucleus and with e for the electron with r the distance of separation [93]. This energy takes account only of the kinetic energies of the electron and nucleus and the electrostatic potential energy neglecting spin and other relativistic effects. Instead of this form, it is more

common for standard chemistry to use the electronic energy of the atom, the energy of a bound atomic state, using the reduced electron mass

$$E = \frac{1}{2}\mu_e \left[\left(\frac{\mathrm{d}x}{\mathrm{d}t}\right)^2 + \left(\frac{\mathrm{d}y}{\mathrm{d}t}\right)^2 + \left(\frac{\mathrm{d}z}{\mathrm{d}t}\right)^2 \right] - \frac{Ze^2}{4\pi\varepsilon_0 r}, \tag{3.3}$$

with $\mu_e = (M_n m_e)/(M_n + m_e)$ [98]. Here, Z indicates the nuclear charge. This separates out the relative motion of the electron and nucleus from the motion of the atom as a whole. Classically, the maximum separation is given by solving

$$E = -\frac{Ze^2}{4\pi\varepsilon_0 r_{\mathrm{max.}}}. \tag{3.4}$$

Although this is simple classical chemistry, it begins to expose the main problem with modelling chemical systems; the exponential complexity added by degrees of freedom. As the system grows interactions between each of the particles must be considered in order to fully approximate the energy of the system [91].

3.1.2 Hamiltonian Formulation of Single-Electron Atoms

For the same single-electron atom, the quantum mechanical form of the energy is given by the Hamiltonian [93]

$$\mathcal{H} = -\frac{h^2}{8\pi^2\mu_e}\nabla^2 - \frac{Ze^2}{4\pi\varepsilon_0 r}. \tag{3.5}$$

In the case of atoms in a stationary state, the electron wavefunctions Ψ can be found by solving the time independent Schrödinger equation (TISE),

$$\mathcal{H}\Psi(x,y,z) = E\Psi(x,y,z). \tag{3.6}$$

Solving this equation gives continuous results if E is ≥ 0 but only for discrete values below zero. These wavefunctions are the only allowed bound states of the electron and are denoted atomic orbitals (AO) with corresponding energy referred

to as orbital energy.

Note that the Bohr radius is defined as

$$a_0 = \frac{\varepsilon_0 h^2}{\pi m_e e^2}, \tag{3.7}$$

the atomic unit of length, and similarly the Rydberg energy,

$$\mathcal{R} = \frac{m_e e^4}{8\varepsilon_0 h^2} = \frac{e^2}{9\pi\varepsilon_0 a_0}, \tag{3.8}$$

with the Hartree, $2\mathcal{R}$, an atomic unit for energy [98]. The Hartree also allows a measure of accuracy with regards to modelling to be formed, with the standard chemical tolerance being 1.6×10^{-3} Hartree [109]. In the context of subtle quantum correlations that can affect energy levels, this is a rather large tolerance.

For a one electron atom, the bound electronic energies of the system are given by

$$E_n = \frac{-Z^2\mathcal{R}}{n^2}, \tag{3.9}$$

with principal quantum number n. The ground state corresponds with $n = 1$ and states are described as excited otherwise. It is worth reiterating that so far relativistic effects and spin contributions have been completely neglected. For hydrogen this has little effect on the energy but as the number of electrons increases, these effects will become increasingly important due to the increase of correlations. Note, although the energy is not affected too much the internal structure of hydrogen is. It should also be noted that the p-orbitals ($n = 2$) appear degenerate using these classical equations due to the neglect of spin-orbit coupling; this is because of the difference in spin orientation [93].

3.1.3 Ground State Single-Electron Atom

By considering the radial and the angular parts individually, the wavefunction of the single-electron atom is, in polar co-ordinates (r, θ, ϕ),

$$\Psi_{n,l,m}(r, \theta, \phi) = R_{n,l}(r)\, Y_{l,m}(\theta, \phi), \tag{3.10}$$

where n is the principal quantum number, l the angular quantum number, m the magnetic quantum number and $Y_{l,m}$ the corresponding spherical harmonic. Note that the polar co-ordinates are given as:

$$z = r\cos\theta, \tag{3.11}$$

$$y = r\sin\theta\sin\phi, \tag{3.12}$$

$$x = r\sin\theta\cos\phi. \tag{3.13}$$

For the $1s$ orbital ($n = 1$), there is only one wavefunction,

$$\Psi_{1s} = 2\left(\frac{Z}{a_0}\right)^{\frac{3}{2}} \exp\left(\frac{-Zr}{a_0}\right)\left(\frac{1}{4\pi}\right)^{\frac{1}{2}}. \tag{3.14}$$

The r-dependent component is the exponential, whilst the remaining constants appear in order to ensure normalization. Note that this is one solution to the TISE and is not unique in form, however all other forms describe the same state and it is thus sufficient to only list one [93].

The traditional visualizations of the single-electron atom though are of the probability density for the electron. Its associated probability density, the square of the wavefunction, is therefore a function of the probability of finding the electron in a specific volume of space. It is this that leads to the visualizations now common in textbooks and the description of the electron as a 'cloud'. This is the model of the atom commonly used but, as it has been pointed out before, is insufficient for accounting for the spin of the electron. This should emphasize that if the final

visualization is to contain spin information, the traditional model must be adapted.

The probability density, in this case only, is interchangeable with the electron density and is why the product of the electron density with the electronic charge results in the charge density. The probability density of the $1s$ orbital then is [98]

$$\Psi_{1s}^2 = \frac{1}{\pi}\left(\frac{Z}{a_0}\right)^3 \exp\left(\frac{-2Zr}{a_0}\right). \tag{3.15}$$

From classical physics it can be stated that the point at which the kinetic energy is zero, the potential and electronic energies are equal. This gives a maximum radius to the system. However, Eq. (3.15) demonstrates there is a finite probability that the electron can be found beyond the radius set by classical physics, *i.e.*, the probability is non-zero for any arbitrary distance due to quantum tunnelling [93]. Also, as the electron is found with equal probability at equal distance from the nucleus, the ground state is often represented as a sphere. More traditionally a sphere with a surface at a distance where 90 % of the time, the electron will be measured as inside the sphere; the 90-percentile surface.

3.1.4 Quantum Numbers

It is important to now clarify the use of quantum numbers in Eq. (3.10). The energy level associated with an orbital is given by the principal quantum number n and is therefore the number that distinguishes energetic states. Those states with equivalent n values but differing l and/or m, are denoted as being energetically degenerate. However, there are constraints upon the allowed values for l and m; [91]

$$l = 0, 1, 2, \ldots, n-1 \quad \text{and} \quad |m| \leq l. \tag{3.16}$$

This means that the lowest-energy state, $n = 1$, $m = l = 0$, is non-degenerate and is referred to as an s-orbital. The letter notation, coming from atomic spectroscopy, is associated with the quantum number l and denotes any state with $l = 0$ as an s-orbital.

To distinguish between different energy orbitals the principal quantum number is used such that the lowest-energy state is the $1s$. For the first-excited state $n = 2$ giving the following states;

$$n = 2, \begin{cases} l = 0, m = 0, \\ l = 1, \begin{cases} m = -1, \\ m = 0, \\ m = 1, \end{cases} \end{cases} \tag{3.17}$$

which are denoted $2s$, $2p_{-1}$, $2p_0$, and $2p_1$ from top to bottom. The letter notation is a mechanism for indicating the quantum number l and the subscript indicates the values of m. In general, the number of degenerate states for an energy level n is n^2. Further, because of this degeneracy there is a choice about the forms that can be chosen. Unlike for the $1s$-orbital, which can be determined to a form that only differs in phase, the $n = 2$ degenerate state has different spatial forms [91].

3.1.5 First Excited State Single-Electron Atom

Assuming the breakdown of quantum numbers in Eq. (3.17) holds, the first excited state, $n = 1$, actually comprises of four distinct states. There is the s-orbital ($l = 0$) and the three p-orbitals ($l = 1, m = -1, 0, 1$) as stated above. Considering the wavefunction for the $2s$-orbital,

$$\psi_{2s} = \frac{1}{4\sqrt{2\pi}} \left(\frac{Z}{a_0}\right)^{\frac{3}{2}} \left(2 - \frac{Zr}{a_0}\right) \exp\left(\frac{-Zr}{2a_0}\right), \tag{3.18}$$

which like the $1s$ is a spherically symmetric function, and, as can be seen in Fig. 3.1, are all s-orbitals. This is clearly seen from the fact that the only dependence in all s-orbitals is on the radial distance r. For other orbitals, there is a dependence upon other spatial degrees of freedom (θ and ϕ).

It is worth spending a little time analyzing this function as it will be of benefit

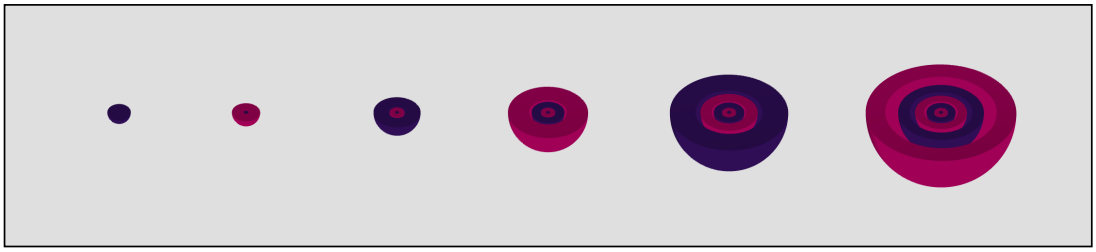

Figure 3.1: The 90-percentile plots of the s-orbitals in order from $n = 1$ to $n = 7$ in terms of the energy levels. It is clear how the radius of the probability density has increased, but this also means that the electron density is far more diffuse. It is also easy to spot how the number of times that the wavefunction oscillates from positive to negative increases. The radial nodes occur on the boundary of these oscillations, *cf.* the Fock states. These plots were made using Orbital Viewer.

when it is used later. First, note that because of the form of the exponent the $2s$-orbital is more spread out than the $1s$. This means that the electron density is more diffuse within such an orbital and as such is referred to as an 'outer' electron as compared to 'inner' electrons such as those in a $1s$-orbital, though not always strictly outer electrons [93]. Of course this usage of words very quickly becomes rather useless due to the size of systems and the rate at which they increase in complexity. However, as we remain relatively small throughout this thesis, it is a good way of distinguishing levels. Note, as will be discussed later, that the ability to identify a specific electron disappears in the true quantum situation.

In addition, the pre-factor $(2 - Zr/a_0)$ has a significant effect upon the form of the orbital. For sufficiently small values of r, it is clear that this term is positive and as $r \to 0$, $(2 - Zr/a_0) \to 2$. Similarly, for larger r, it behaves as $-Zr/a_0$, therefore the function must have a region where the function is close to zero. This is because the function is smooth and therefore lacks a discontinuity. Such a region is referred to as a spherical radial node. This means that there is a region of the $2s$-orbital where the probability of finding the electron at these points is zero. In fact this analysis can subsequently be extended to higher energy s-orbitals where we see that there are $(n - 1)$ nodes for the ns-orbital.

Next, considering the $2p$-orbitals, the wavefunctions are

$$\psi_{2p_0}(r, \theta, \phi) = \frac{1}{4\sqrt{2\pi}} \left(\frac{Z}{a_0}\right)^{\frac{3}{2}} \left(\frac{Zr}{a_0}\right) \exp\left(\frac{-Zr}{2a_0}\right) \cos\theta, \tag{3.19}$$

$$\psi_{2p_{\pm1}}(r,\theta,\phi) = \mp\frac{1}{8\sqrt{\pi}}\left(\frac{Z}{a_0}\right)^{\frac{3}{2}}\left(\frac{Zr}{a_0}\right)\exp\left(\frac{-Zr}{2a_0}\right)\sin\theta\exp\left(\pm\mathrm{i}\,\varphi\right), \tag{3.20}$$

where the spherical harmonics $Y_{1,0} = \sqrt{3/4\pi}\cos\theta$ and $Y_{1,\pm1} = \mp\sqrt{3/8\pi}\sin\theta\exp(\pm\mathrm{i}\,\phi)$ have been used. Comparing with the $2s$-orbital, the exponential decay is equivalent and so the radial size will be about equal, meaning these would also be considered outer orbitals for small systems such as the ones in this thesis. However the pre-factor, analogous to the one discussed for the $2s$, results in the function vanishing only at the nucleus rather than any other point meaning a lack of radial nodes [93]. The angular dependence in these orbitals makes them significantly different from the s-orbitals. It means that the orbitals have a directional property.

As the $2p_{\pm1}$-orbitals are complex it easier to infer the shape through logical considerations. The probability densities of both functions are equivalent and differ only in angular dependence to the p_0-orbital. The p_0-orbital has a $\cos^2\theta$ dependence as opposed to a $1/2\sin^2\theta$. However, due to trigonometric identities the sum of all the p-orbitals must be spherically symmetric with a node at the centre, as the angular dependence disappears. It turns out that the shape of each of these orbitals is a torus oriented in a different direction [98]. These states are eigenstates of the Hamiltonian with the same eigenvalue meaning that a linear superposition of these states is also an eigenstate. This allows us to produce an entirely real set of states denoted as the $2p_x$-, $2p_y$- and $2p_z$-orbitals.

Considering Eq. (3.19), and using the usual spherical co-ordinate relationships, it is seen that the directional property will occur in the z-direction. In fact it can be written better using mixed co-ordinates such that this directional property is emphasized [93],

$$\psi_{2p_z} = \frac{z}{4\sqrt{2\pi}}\left(\frac{Z}{a_0}\right)^{\frac{5}{2}}\exp\left(\frac{-Zr}{2a_0}\right). \tag{3.21}$$

This orbital is the $n = 2$, $l = 1$, $m = 0$ state and is comparatively easy to visualize. The wavefunction must be two lobes separated by an xy-plane node and superpositions of these states produce the torus form discussed earlier.

Similarly, it can be found

$$\psi_{2p_x} = \frac{1}{\sqrt{2}}\left(\psi_{2p_{-1}} - \psi_{2p_{+1}}\right) = \frac{1}{4\sqrt{2\pi}}\left(\frac{Z}{a_0}\right)^{\frac{3}{2}}\left(\frac{Zr}{a_0}\right)\exp\left(\frac{-Zr}{2a_0}\right)\sin\theta\cos\phi, \quad (3.22)$$

$$\psi_{2p_y} = \frac{\mathrm{i}}{\sqrt{2}}\left(\psi_{2p_{-1}} + \psi_{2p_{+1}}\right) = \frac{1}{4\sqrt{2\pi}}\left(\frac{Z}{a_0}\right)^{\frac{3}{2}}\left(\frac{Zr}{a_0}\right)\exp\left(\frac{-Zr}{2a_0}\right)\sin\theta\sin\phi. \quad (3.23)$$

By extension, the three $2p_q$-orbitals can be written in the form,

$$\psi_{2p_q} = \frac{q}{4\sqrt{2\pi}}\left(\frac{Z}{a_0}\right)^{\frac{5}{2}}\exp\left(\frac{-Zr}{2a_0}\right), \quad (3.24)$$

where $q = x$, y or z. The reason for doing this is that we now have a set of real, normalized wavefunctions for the $n = 2$ energy level [98]. Moreover, they are orthogonal to each other meaning

$$\int \psi_i(x,y,z)\,\psi_j(x,y,z)\,\mathrm{d}x\,\mathrm{d}y\,\mathrm{d}z = \delta_{i,j}, \quad (3.25)$$

and are also orthogonal to ψ_{1s}.

3.1.6 Higher Energy Levels of the Single-Electron Atom

Moving up another energy level becomes more problematic. Converting the process into one of logic, at the lowest energy level (the ground state) there is no ability to put in a node, and the level must be non-degenerate, to maintain orthogonality of states. However, when increasing the energy to $n = 2$ there is the ability to put in a single node, allowing the level to be degenerate. But, there are two ways of doing this, a radial node (corresponding to the $2s$) or a planar node (corresponding to the $2p_q$ orbitals.) A planar node can be added in three orthogonal ways ($x = 0$, $y = 0$ and $z = 0$), resulting in the degeneracy of the $2p_q$-orbital and also meaning that the states can be themselves be orthogonal [93].

Moving to the $n = 3$ energy level there are now two nodes to be placed. There can be two radial nodes, which can be done in only one way giving the $3s$, or there

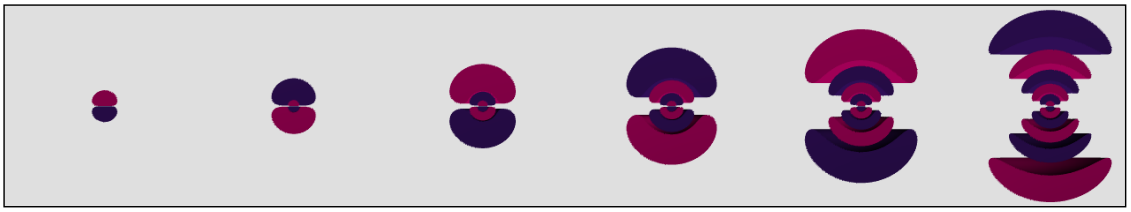

Figure 3.2: The 90-percentile plots of the p_z-orbitals in order from $n = 2$ to $n = 6$ in terms of the energy levels. The radius here has been stretched in the vertical axis so that the inner shells are made more obvious. The key thing to notice here is how the radial nodes increase with the energy level and occur very close to the nucleus of the atom. Remember also that these are only one of the possible three degenerate states for each energy level with $l = 1$.

could be one radial and one planar node. There is only one way of placing a radial node, but three orthogonal ways of placing the planar node again. This produces three different $3p$-orbitals, which look very similar to the $2p$-orbitals but with larger radius and a radial node. This means they effectively look like a $2p$-orbital nested inside a larger p-orbital, see Fig. 3.2

Finally, there could be two planar nodes, with each of the planes having three orthogonal placements producing six orbitals. Three of these are not linearly dependent and are reduced to only two independent, orthogonal states [93]. The point of this is so that the choice of states for each energy level n, are mutually orthogonal. This means that the real orthogonal states describing the $n = 3$ level are: $3s$, $3p_x$, $3p_y$, $3p_z$, $3d_{xy}$, $3d_{xz}$, $3d_{yz}$, $3d_{x^2-y^2}$, and $3d_{z^2}$.

At this point we have recovered the full standard visualization of atomic systems up to $n = 3$. Presented in Fig. 3.3 is a sub-set of the atomic orbitals discussed. In this visualization, there is no real consideration of many of the features that interest quantum chemists. They are so familiar, that they are very well understood by those who use them but are low-level in terms of the current theory. This form is useful for chemists and leads to natural descriptions of bond hybridization [59]. This visualization has also been used to introduce concepts to a wider audience by making the mechanism less abstract and more intuitive. However, the omission of spin means that using these to do the same for explaining spin-orbit coupling effects, such as those seen in catalysts, is not possible.

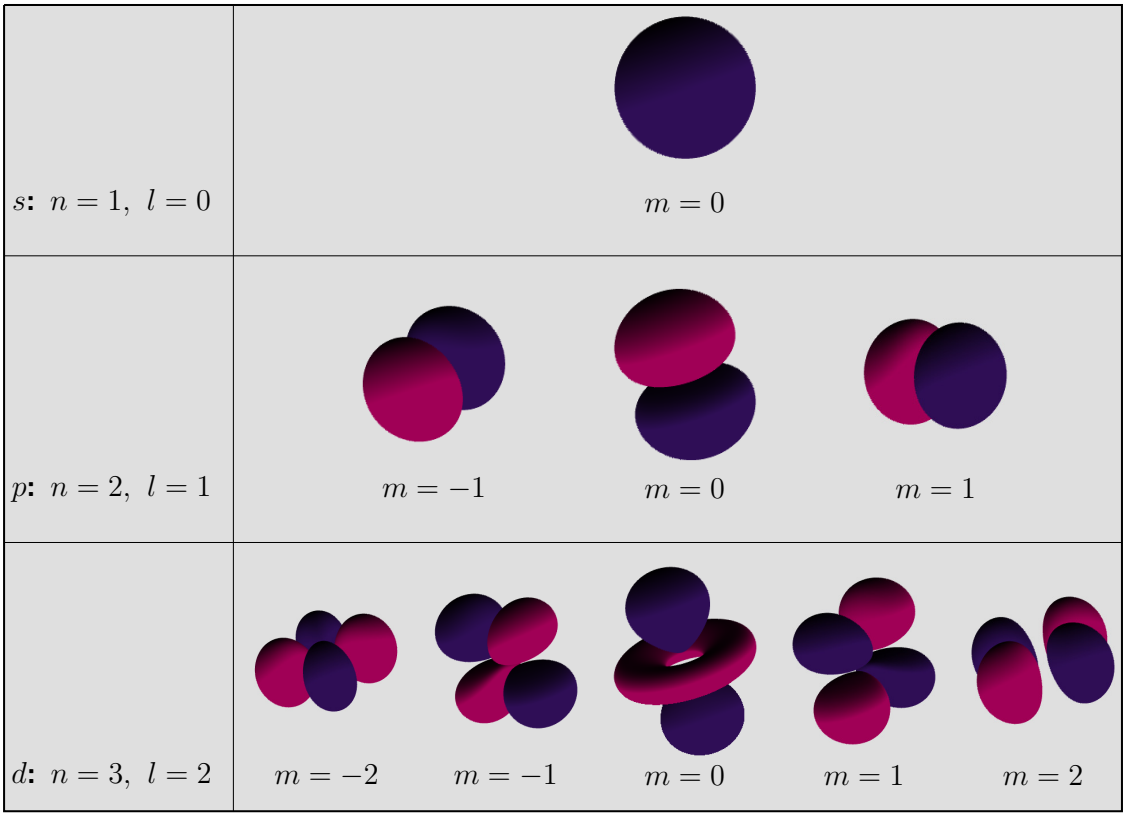

Figure 3.3: The common set of 90-percentile atomic orbitals upto the d orbital for a hydrogen atom. These are used throughout chemistry textbooks and are well understood. The order from top to bottom is associated with the principal quantum number n and azimuthal quantum number l, whilst from left to right the order is based upon the magnetic quantum number m.

3.1.7 Angular Momentum and Spin for the Single-Electron Atom

Although the visualizations take account of the theory only to this point, we can easily extend the theory to account for angular momentum and spin. The main points are that the total angular momentum of the atomic orbital allows us to properly define the azimuthal quantum number l;

$$\left|\boldsymbol{L}^2\right| = l\hbar^2\left(l+1\right) \tag{3.26}$$

and the angular momentum around the z-axis is

$$L_z = |m|\,\hbar \tag{3.27}$$

which introduces the magnetic quantum number [91]. Note that the choice of the z-axis is in line with convention and is not of physical significance.

This allows some insight to the atomic orbitals and their properties. It also means that the total angular momentum of an s-orbital is zero and so the electron must have an average trajectory equivalent to moving along a straight line through the nucleus. Due to symmetry this is an unknown line, producing the spherical probability density and the angular momentum in the z-direction is also zero [93]. The p-orbitals have an angular momentum component therefore they must always have some component of linear momentum that denotes motion about the nucleus. Although this is true of all p-orbitals, the direction of this component is different for each orbital with the same principal quantum number. The p_z-orbital has $m = 0$ so the angular momentum component in the z-direction is zero, recovering the planar node along the xy-plane. For the p_x- and p_y-orbitals, as $m = \pm 1$ the electron must rotate around the z-axis demonstrating how the orientation of the orbital must change. A similar discussion can be had for the d-orbitals but the focus of this discussion is the introduction of notation for molecules.

This magnetic quantum number allows the notation σ, π and δ to be used to denote the orbitals. These correspond to $|m| = 0$, 1, 2 respectively. The notation holds for the atomic orbitals, but for linear molecules the convention is to place all nuclei on the z-axis. The atomic orbitals are then easily assigned appropriate classification. Equally, for planar molecules the orbitals perpendicular to the plane are denoted π-orbitals and σ-orbitals when they lie in plane [98].

This is not the complete picture of a single-electron atom though, as we have neglected relativistic effects. When these are included the electron is found to have an inherent angular momentum of magnitude

$$|\boldsymbol{S}| = \sqrt{\frac{3}{4}}\hbar. \tag{3.28}$$

This is an addition to any other angular momentum the atom may have and is referred to as the spin of the electron [91]. There is agreement that only two spin

states exist with equal total angular momentum but different directions. The spin is commonly taken as about the z-axis and produces the two states

$$S_{\uparrow} = \frac{1}{2}\hbar, \tag{3.29}$$

$$S_{\downarrow} = -\frac{1}{2}\hbar. \tag{3.30}$$

These states will be represented as $|\uparrow\rangle$ (spin up) and $|\downarrow\rangle$ (spin down) respectively for the remainder of this thesis. The wavefunctions for the spin states are denoted as α and β respectively and are assumed to form an orthonormal basis.

The simplest way of including the spin is to take the product of the wavefunction as described above with the relevant spin wavefunction. These are referred to as spin orbitals demonstrating that the hydrogen ground state is doubly degenerate with one spin up and the other spin down [91]. Similarly, there a six p-orbitals, the three from before but both spin up and spin down variants.

Introducing the spin, means that the associated magnetic field, or more specifically the magnetic field produced by the electron orbit, must also be accounted for in the energy. This magnetic field affects the energies depending on whether it is parallel or anti-parallel to the total angular momentum. For the $2p$-orbitals, the six spin orbitals can be combined in such a way that this spin-orbit coupling is accounted for; four which have spin aligned with the orbital angular momentum and two where they are anti-parallel. This is done by making superpositions of the orbitals and is a demonstration of how new correlations begin to arise when better approximations are made. It is these correlations that are significant to our subsequent analysis.

3.2 The Model

While the hydrogenic orbitals are perhaps the most natural, they are not the most easy to use outside of atomic physics. They can cause extra difficulties that will distract from the main focus of this work and so, in line with other standards in the literature, a simpler basis is used. This is not least motivated by the subsequent

application of this method to quantum information systems where the Fock basis is the standard. All the discussions so far have included certain approximations in order to simplify the system being discussed. The most relevant model, for modelling the systems of interest here, that achieves simplification of the theory, but accuracy of energy, is the Moshinsky atom, similar to the Hooke atom [100–102, 110–112]. This model uses Gaussian wavefunctions to represent the atomic orbitals as laid out in Ref. [113]. This method has been developed and subsequently shown to be a very good approximation, in terms of calculating energies [114]. One concern is that the Gaussian wavefunctions do not account for the nucleus, however, in Ref. [114] it is also demonstrated that a δ-function can be included to account for the singularity at the nucleus. The model was further checked for accuracy in Ref. [115] motivated as an alternative to Slater-type orbitals. Another advantage of such a model is although the radial dependence at large distances is incorrect, linear combinations of such orbitals can be used to better model the systems without significant increase to complexity [115]. The model is greatly explored within nuclear physics, with subsequent applications to quantum chemistry, in Refs. [116,117]. Ref. [116] uses the harmonic oscillator states to develop a single-electron atom which is then extended to atoms with multiple electrons, whereas Ref. [117] extends this process to more general problems and demonstrates convergence to experiment for atomic systems with up to 112 electrons.

To introduce this visualization in the easiest possible way, a model similar to the Moshinsky atom, with the Coulomb confining potential being replaced with the three-dimensional harmonic oscillator, is used as in Ref. [82]. The key thing, as outlined for the Moshinsky atom, is that this approximation has no effect on the angular distribution of the eigenstates and can be used in a variational method to calculate accurate energies [91]. Further, this model, has the advantage that systems such as Compton scattering or atoms in periodic potentials, can easily be used to create a momentum-representation as in Refs. [118, 119].

3.2.1 Gaussian Wavefunction Representation

The atomic orbitals will be represented using Gaussian wavefunctions or more specifically the basis for the simple harmonic oscillator; the Fock states. The lowest s, p and d orbitals are analogous to the low energy Fock states of a three-dimensional simple harmonic oscillator. The states for an oscillator of mass $m = 1$ and frequency $\omega = 1$ are given as

$$\phi_{000} = \frac{\mathrm{e}^{-\mathbf{r}^2/2}}{\pi^{3/4}}, \tag{3.31}$$

$$\phi_{001} = \frac{\sqrt{2}\,\mathrm{e}^{-\mathbf{r}^2/2}}{\pi^{3/4}}\,(z)\,, \tag{3.32}$$

$$\phi_{002} = \frac{\mathrm{e}^{-\mathbf{r}^2/2}}{\pi^{3/4}}\left(2z^2 - 1\right), \tag{3.33}$$

$$\phi_{010} = \frac{\sqrt{2}\,\mathrm{e}^{-\mathbf{r}^2/2}}{\pi^{3/4}}\,(y)\,, \tag{3.34}$$

$$\phi_{011} = \frac{2\,\mathrm{e}^{-\mathbf{r}^2/2}}{\pi^{3/4}}\,(yz)\,, \tag{3.35}$$

$$\phi_{020} = \frac{\mathrm{e}^{-\mathbf{r}^2/2}}{\pi^{3/4}}\left(2y^2 - 1\right), \tag{3.36}$$

$$\phi_{100} = \frac{\sqrt{2}\,\mathrm{e}^{-\mathbf{r}^2/2}}{\pi^{3/4}}\,(x)\,, \tag{3.37}$$

$$\phi_{101} = \frac{2\,\mathrm{e}^{-\mathbf{r}^2/2}}{\pi^{3/4}}\,(xz)\,, \tag{3.38}$$

$$\phi_{110} = \frac{2\,\mathrm{e}^{-\mathbf{r}^2/2}}{\pi^{3/4}}\,(xy)\,, \tag{3.39}$$

$$\phi_{200} = \frac{\mathrm{e}^{-\mathbf{r}^2/2}}{\pi^{3/4}}\left(2x^2 - 1\right). \tag{3.40}$$

here the ϕ indices are n_x, n_y, n_z [91]. These create a complete basis from which all the lowest energy (s, p, d) orbitals can be created. Also, as it happens, the d-orbitals can be created due to the azimuthal quantum number being two.

Using the Fock states the orbitals for a single-electron atom can be written as [91]

$$s(\mathbf{r}) = \phi_{000} = \frac{\mathrm{e}^{-\mathbf{r}^2/2}}{\pi^{3/4}}, \tag{3.41}$$

$$p_x(\mathbf{r}) = \phi_{100} = \frac{\sqrt{2}\,\mathrm{e}^{-\mathbf{r}^2/2}}{\pi^{3/4}}x, \tag{3.42}$$

$$p_y(\mathbf{r}) = \phi_{010} = \frac{\sqrt{2}\,\mathrm{e}^{-\mathbf{r}^2/2}}{\pi^{3/4}}y, \tag{3.43}$$

$$p_z(\mathbf{r}) = \phi_{001} = \frac{\sqrt{2}\,\mathrm{e}^{-\mathbf{r}^2/2}}{\pi^{3/4}} z, \tag{3.44}$$

$$d_{xy} = \phi_{110} = \frac{2\,\mathrm{e}^{-\mathbf{r}^2/2}}{\pi^{3/4}} (xy)\,, \tag{3.45}$$

$$d_{yz} = \phi_{011} = \frac{2\,\mathrm{e}^{-\mathbf{r}^2/2}}{\pi^{3/4}} (yz)\,, \tag{3.46}$$

$$d_{z^2} = \sqrt{\frac{2}{3}} \left(\phi_{002} - \frac{1}{2}\phi_{200} - \frac{1}{2}\phi_{020} \right) = \frac{\mathrm{e}^{-\mathbf{r}^2/2}}{\sqrt{3}\pi^{3/4}} \left(2z^2 - x^2 - y^2\right), \tag{3.47}$$

$$d_{xz} = \phi_{101} = \frac{2\,\mathrm{e}^{-\mathbf{r}^2/2}}{\pi^{3/4}} (xz)\,, \tag{3.48}$$

$$d_{x^2-y^2} = \frac{1}{\sqrt{2}} (\phi_{200} - \phi_{020}) = \frac{\sqrt{2}\,\mathrm{e}^{-\mathbf{r}^2/2}}{\pi^{3/4}} \left(x^2 - y^2\right). \tag{3.49}$$

It is worth comparing these states to the functions with Eq. (3.14) and Eq. (3.24) to pull out the dependence on direction. The development of this theory and the similarity between the above functions and those that came out of the chemistry approach support this approximation.

Although, there are corrections that can be made, in terms of relativistic corrections and the fact that the nucleus is not a point source and therefore the potential is not quite equivalent, this approximation is sufficient at this stage to demonstrate the utility of our method. As it happens, due to the energy being low and the approximation being a reasonable one, when plotted the states here are almost identical in structure to the atomic orbitals.

3.2.2 Visualizing the States

As discussed, the problem that currently exists with the visualizations is the omission of spin information. The atomic orbitals presented in Fig. 3.3 are, to a good approximation, identical to the plots that would be made using the above. The first thing to note is that a three dimensional visualization is needed to fully appreciate the probability density. The second is that it should be stressed that these visualizations have been achieved by using the position representation. Finally, the colour of the probability density indicates the sign of the wavefunction. This information is not particularly informative though it can indicate the orientation and type of bonds

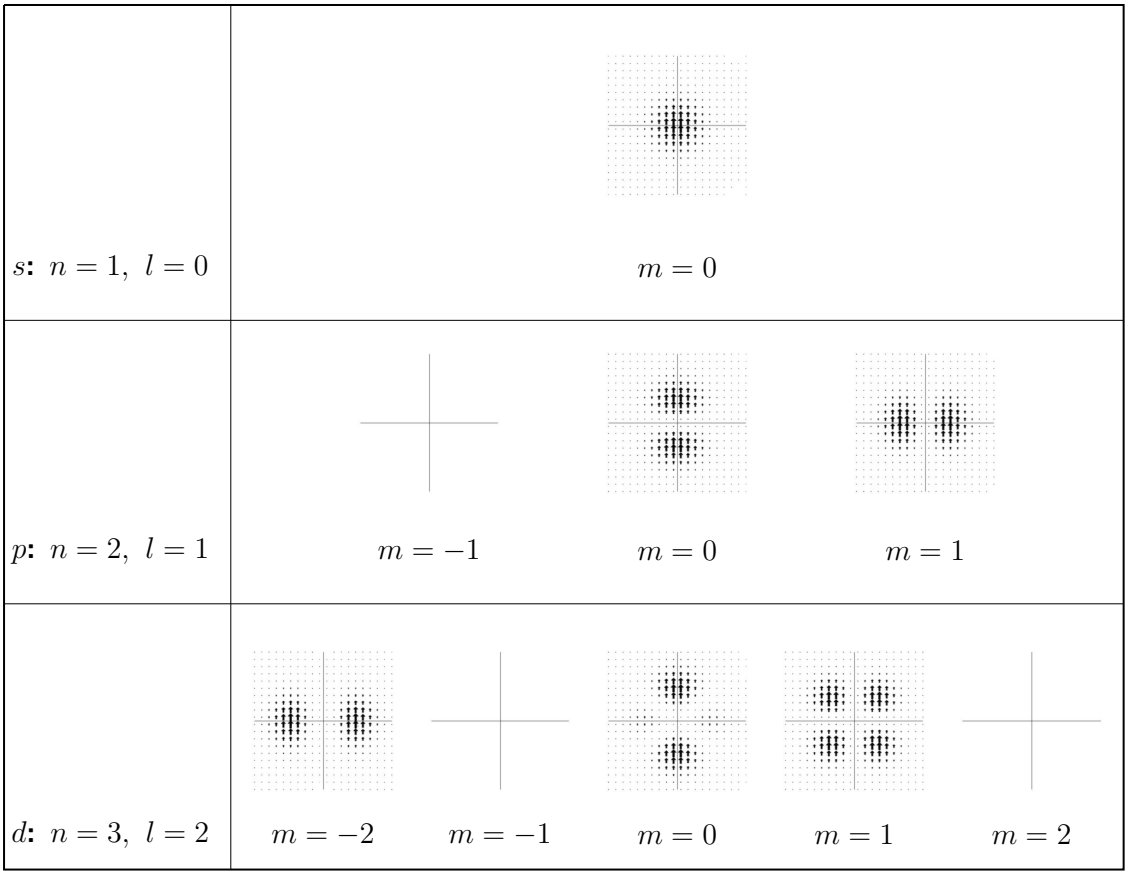

Figure 3.4: The set of orbitals to the d orbital for a hydrogen atom for the three-dimensional SHO basis. This is a close enough approximation that these orbitals are almost identical to the hydrogenic orbitals. For consistency across the thesis, all these plots have been taken in the xz-plane. As can be seen, three of the plots are blank as the wavefunction is zero in the plane being plotted. The reason for showing these is so that the reader can appreciate that the idea that all these orbitals can be reduced to a single common plane is not correct. These plots represent the start of including spin in the visualization of atomic orbitals. The magnitude of the arrows here represents the probability function of the orbital, in the case of an atom the charge density. The direction represents the spin. In all cases the spin chosen is in the z-direction and is in the ground state taken to be $|\uparrow\rangle$. The order from top to bottom is associated with the azimuthal quantum number whilst from left to right the order is based upon the magnetic quantum number.

that can form. Importantly, applying any spin information to this image would be difficult.

A more informative way of representing these figures is presented in Fig. 3.4. What happens in this situation is that a plane is chosen and, for a set of points in that plane, the Bloch vector is plotted. In this case the plane is the xz-plane and, for these states, the direction of the spin is always up (in the positive z-direction). The size of the arrow is then scaled according to the value of the probability density

at that point, with zero size producing no arrow. This method is problematic with it only being a two dimensional plane, but it can still be informative. Certainly, it could be argued that the state being visualized is far more certain than in the previous method as spin degeneracy is now clear.

Another issue with this method is that it makes the probability density hard to appreciate and does not extend to many electron systems. This is better demonstrated in the case of the zero planes where the lack of any information tells you nothing. This means to understand different states, one would have to pick and choose different planes to visualize the state. Without prior information of the state, it would be impossible to select a suitable plane. This is clearly not optimal, but could be automated. Also problematic is the issue with identical pictures. For instance the state $n = 3$, $l = 2$, $m = -2$ is identical to that in $n = 2$, $l = 1$, $m = 1$, although from Fig. 3.3 it is clear that these states are different.

It could be argued that one could avoid all these issues by taking a standard set of planes. Perhaps the experimenter would choose a random selection of planes that would be taken for every state being studied. As long as they were picked randomly and then consistently applied this would seem to resolve the issue. There is the problem that you may be unlucky and end up with a set of zero planes so the question arises as to how many planes should be picked for each state? This of course is a very difficult question to answer and so it seems more realistic to seek a more suitable visualization.

For reasons to be explored in greater detail later, instead of arrows being used, a reduced Wigner function, parameterized in the same way as the Bloch sphere, is placed at each point in space. This can seem a little unnecessary and, in some ways, a little cumbersome. However, its use is necessary to maintain as much information in the picture as possible. It should also be stressed here, as it will also be elsewhere, that on the Bloch sphere the colour scheme is red to blue moving from negative to positive with white being the zero point. Further, these colours are in no way related to the atomic orbitals in usual chemistry textbooks where the colour denotes the

sign of the wavefunction.

One last thing, before the introduction of the visualization, is the transformation of the atomic orbitals in Eqs. (3.41)–(3.49) into the angular momentum eigenstates. The purpose of this is for simplicity when the spin-orbit coupled states are being produced. For the s orbital, $l = 0$, the angular momentum eigenstate is equivalent to that described without the consideration [91]. For the p orbitals, $l = 1$,

$$p_{+1}(\mathbf{r}) = \frac{1}{\sqrt{2}}(p_x(\mathbf{r}) + \mathrm{i}\, p_y(\mathbf{r})) = \frac{\mathrm{e}^{-\mathbf{r}^2/2}}{\pi^{3/4}}\,(x + \mathrm{i}\, y)\,, \tag{3.50}$$

$$p_0(\mathbf{r}) = p_z(\mathbf{r}) = \frac{\sqrt{2}\,\mathrm{e}^{-\mathbf{r}^2/2}}{\pi^{3/4}} z, \tag{3.51}$$

$$p_{-1}(\mathbf{r}) = \frac{1}{\sqrt{2}}(p_x(\mathbf{r}) - \mathrm{i}\, p_y(\mathbf{r})) = \frac{\mathrm{e}^{-\mathbf{r}^2/2}}{\pi^{3/4}}\,(x - \mathrm{i}\, y)\,. \tag{3.52}$$

The angular momentum eigenstates for the d orbitals, $l = 2$,

$$d_{+2} = \frac{1}{\sqrt{2}}\,(d_{x^2-y^2} + \mathrm{i}\, d_{xy}) = \frac{\mathrm{e}^{-\mathbf{r}^2/2}}{\sqrt{2}\pi^{3/4}}\,(x + \mathrm{i}\, y)^2\,, \tag{3.53}$$

$$d_{+1} = \frac{1}{\sqrt{2}}\,(d_{xz} + \mathrm{i}\, d_{yz}) = -\frac{\sqrt{2}\,\mathrm{e}^{-\mathbf{r}^2/2}}{\pi^{3/4}}\,(x + \mathrm{i}\, y)\, z, \tag{3.54}$$

$$d_0 = d_{z^2} = \frac{\mathrm{e}^{-\mathbf{r}^2/2}}{\sqrt{3}\pi^{3/4}}\left(2z^2 - x^2 - y^2\right), \tag{3.55}$$

$$d_{-1} = \frac{1}{\sqrt{2}}\,(d_{xz} - \mathrm{i}\, d_{yz}) = \frac{\sqrt{2}\,\mathrm{e}^{-\mathbf{r}^2/2}}{\pi^{3/4}}\,(x - \mathrm{i}\, y)\, z, \tag{3.56}$$

$$d_{-2} = \frac{1}{\sqrt{2}}\,(d_{x^2-y^2} - \mathrm{i}\, d_{xy}) = \frac{\mathrm{e}^{-\mathbf{r}^2/2}}{\sqrt{2}\pi^{3/4}}\,(x - \mathrm{i}\, y)^2\,. \tag{3.57}$$

This concludes the framework of the initial states that will now be considered as the basis states for the remainder of this chapter.

3.3 Hydrogen

Hydrogen is the single-electron system that will be considered, or rather the three-dimensional harmonic oscillator version of a hydrogen atom. For simplicity, the state shall be referred to as hydrogen from now on. Even though there is only one electron in this system, the Wigner function is an eight dimensional function. It

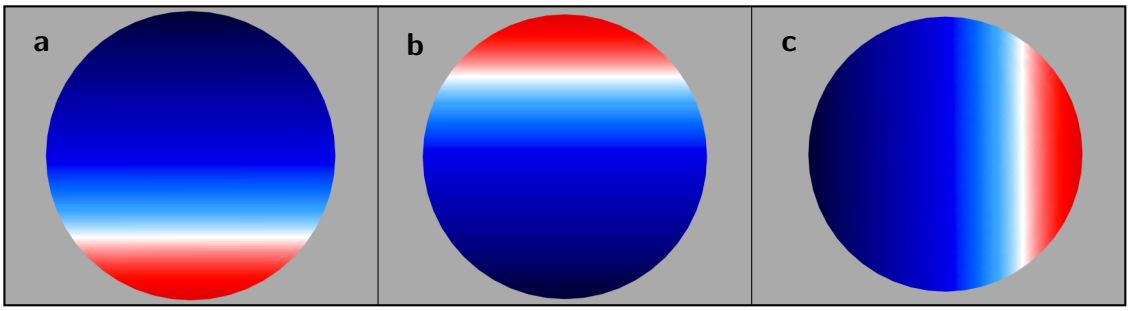

Figure 3.5: This is a set of Wigner functions for the spin states of a single electron that are relevant to the states considered in this section. The states shown are (a) $|\uparrow\rangle$, (b) $|\downarrow\rangle$ and (c) $(1/\sqrt{2})(|\uparrow\rangle + |\downarrow\rangle)$. Note that these are the z-component of spin and an unequal superposition of (a) and (b) would change the angle of rotation to that in (c). The z-axis is the vertical and the x-axis the horizontal; although this appears as a plane it is actually a sphere that has been plotted. Note that the zero point is indicate by the colour white with blue positive and red negative.

has three spatial $\boldsymbol{q}$ degrees of freedom, one each for x, y and z, three momentum $\boldsymbol{p}$ degrees of freedom, one each for p_x, p_y and p_z, and two spin degrees of freedom, θ and ϕ. Reproduced in Fig. 3.5, for the benefit of the reader, are the results of the spin Wigner function for the $|\uparrow\rangle$, $|\downarrow\rangle$ and $(1/\sqrt{2})(|\uparrow\rangle + |\downarrow\rangle)$ states. The final state visually means that the sphere rotates in plane depending on the contribution of $|\uparrow\rangle$ and $|\downarrow\rangle$, *i.e.*, when $|\uparrow\rangle$ dominates the blue region will be angled above the horizontal and when $|\downarrow\rangle$dominates the blue will be angled below the horizontal. Note that the zero point is indicated by the colour white with blue positive and red negative.

Considering the atomic orbitals already discussed, the aim is to produce something as similar as possible to what the textbooks already contain. To do this for hydrogen, the first thing is to integrate out the momentum degrees of freedom. For simplicity, the notation used is

$$W^{\mathrm{H}}(\boldsymbol{q},\theta,\phi) := \int W^{\mathrm{H}}(\boldsymbol{q},\boldsymbol{p},\theta,\phi)\,\mathrm{d}^3\boldsymbol{p}, \tag{3.58}$$

where the parameters not in the argument list have been integrated out. The use of marginals is a clear advantage to tracing components out as there is a reduction of complexity but it also ensures certain correlations are kept. Here, the momentum degrees of freedom have been removed leaving the position degrees of freedom, the

position representation as in the textbook examples, and the spin degrees of freedom; the full eight-dimensional function has been reduced to a function of three spatial degrees of freedom and two spatial.

Although, the ability to reduce the degrees of freedom is a useful one, there is still a problem of displaying this information. So far, the visualizations have built steadily towards pulling more information in and now, finally, the spin information can be included in full. It will not be until a two-electron atom is considered though that the benefits of this technique can be fully appreciated. To obtain the visualization a set of points is first chosen in the position space, initially a plane shall be chosen, though the problems outlined earlier still hold, but this can easily be extended to three dimensions. Note consideration of the type of 'packing' that should be used in these visualizations is more complex than first assumed as shall be discussed later. At each point then a sphere is plotted with an opacity α, where zero is fully transparent, according to

$$W^{\mathrm{H}}(\boldsymbol{q}) = \frac{2}{\pi}\int_0^{\pi/2}\mathrm{d}\theta\int_0^{\pi}\mathrm{d}\phi\,\sin(2\theta)\;W^{\mathrm{H}}(\boldsymbol{q},\theta,\phi), \tag{3.59}$$

with $\alpha = W^{\mathrm{H}}(\boldsymbol{q})/W^{\mathrm{H}}_{\mathrm{max}}(\boldsymbol{q})$. This reduced Wigner function, the position marginal, is simply the probability density function $|\psi^{\mathrm{H}}(\boldsymbol{q})|^2$ of the state. This in effect, is the 90-percentile surface of the orbitals shown earlier. However, in order to get sharper features, and compare more directly with these surfaces, all spheres with an opacity less than 0.1 have been omitted from the image.

Having plotted at each point a sphere, the textbook images have been recovered. The next step is to plot on the surface of each of these spheres the information about the spin of the electron if found at that point. To do this the reduced Wigner function $W^{\mathrm{H}}(\boldsymbol{q},\theta,\phi)$ is plotted on the sphere located at each $\boldsymbol{q}$. This in effect means that the image gives an indication of the probability of finding an electron at a given point with a given spin. A simple introduction to this is an s-orbital as presented in Fig. 3.6 which is as basic as can be made. It is a simple $1s$ orbital with the

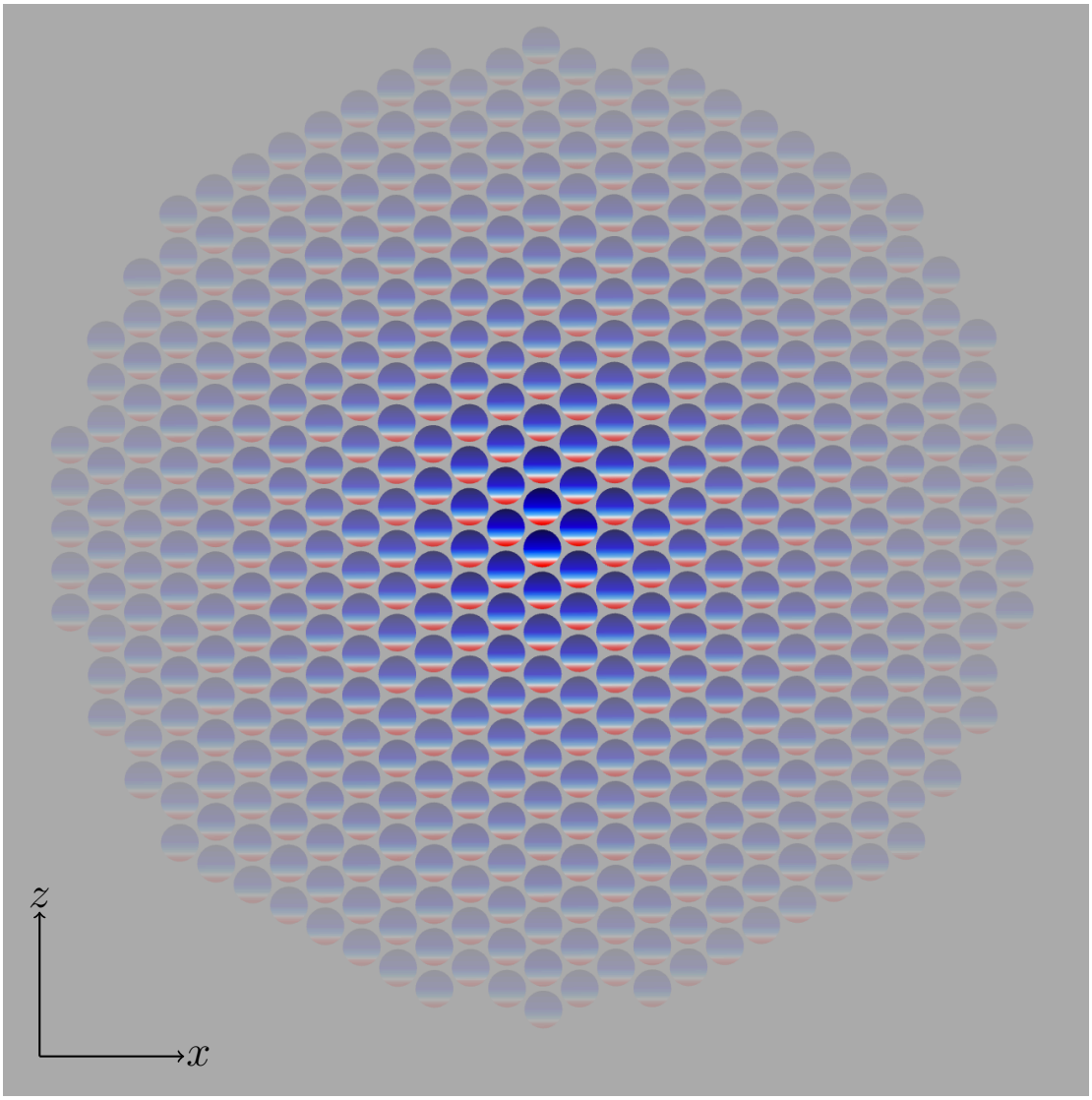

Figure 3.6: This figure displays the spin up $1s$ orbital for the three-dimensional harmonic oscillator, the model for a single-electron atom (hydrogen). The probability density function is the guide for the transparency of the spheres, *i.e.*, the more opaque a sphere the higher the probability of finding the electron there. The spheres then have the spin state of the electron plotted on the surface, this is $|\uparrow\rangle$ in every instance, giving a more informationally complete image of the state. Compare for instance with the standard textbook orbitals and with the spinor representation. It contains more information than the standard textbook image and is clearer in terms of the probability density than the spinor representation. Note that the zero point is indicate by the colour white with blue positive and red negative.

electron in the $|\uparrow\rangle$ state. This information is seen in the visualization from the fact that the shape is a circle, a sphere in the full position space, and at each point the electron is in a definite spin-up state.

Using only the image, and reference images, to guide the deduction it is also possible to fully understand one of these atomic orbitals. The state presented in Fig. 3.7 must be the $3d_{z^2}$-orbital of hydrogen, by comparison with Fig. 3.3, and again each point is clearly in the $|\uparrow\rangle$ state, by comparison with Fig. 3.5. Using this technique it has been possible to correctly infer that this is the $|3d_{z^2}, \uparrow\rangle$. As a comparison with standard textbook pictures, the degenerate spin states for the orbitals has been produced in Fig. 3.8.

However, the states that have so far been plotted are not realistic states for the reason set out in the theory, such as the omission of spin-orbit coupling. A lack of accounting for relativistic and other effects mean that they are not particularly physical. Before an explanation of the states though it is perhaps useful to try and deduce as much as possible from Fig. 3.9. Using the spin references in Fig. 3.5 it is possible to say that the spins are equivalent to a combination of $|\uparrow\rangle$ and $|\downarrow\rangle$ states in all cases. The more opaque spheres, therefore the ones in positions where the electron is most likely to be found, point along the positive z-axis. This indicates that there is an overall spin magnetic moment in the up-direction.

It is also clear that the spin direction of the electron depends upon where it is, *i.e.*, the spin direction is a function of position. As the displaced parity is formed *via* a tensor product, a pure separable state with density operator

$$\hat{\rho} = \hat{\rho}_{\text{spatial}} \otimes \hat{\rho}_{\text{spin}} \tag{3.60}$$

has a Wigner function

$$\begin{aligned} W(\boldsymbol{q}, \boldsymbol{p}, \theta, \phi) &= \text{Tr}[\hat{\rho}\, \Pi(\boldsymbol{q}, \boldsymbol{p}, \theta, \phi)]\,, & (3.61)\\ &= \text{Tr}[(\hat{\rho}_{\text{spatial}} \otimes \hat{\rho}_{\text{spin}})\, (\Pi_{\text{spatial}} \otimes \Pi_{\text{spin}})]\,, & (3.62)\\ &= \text{Tr}\left[(\hat{\rho}_{\text{spatial}} \Pi_{\text{spatial}}) \otimes (\hat{\rho}_{\text{spin}} \Pi_{\text{spin}})\right], & (3.63) \end{aligned}$$

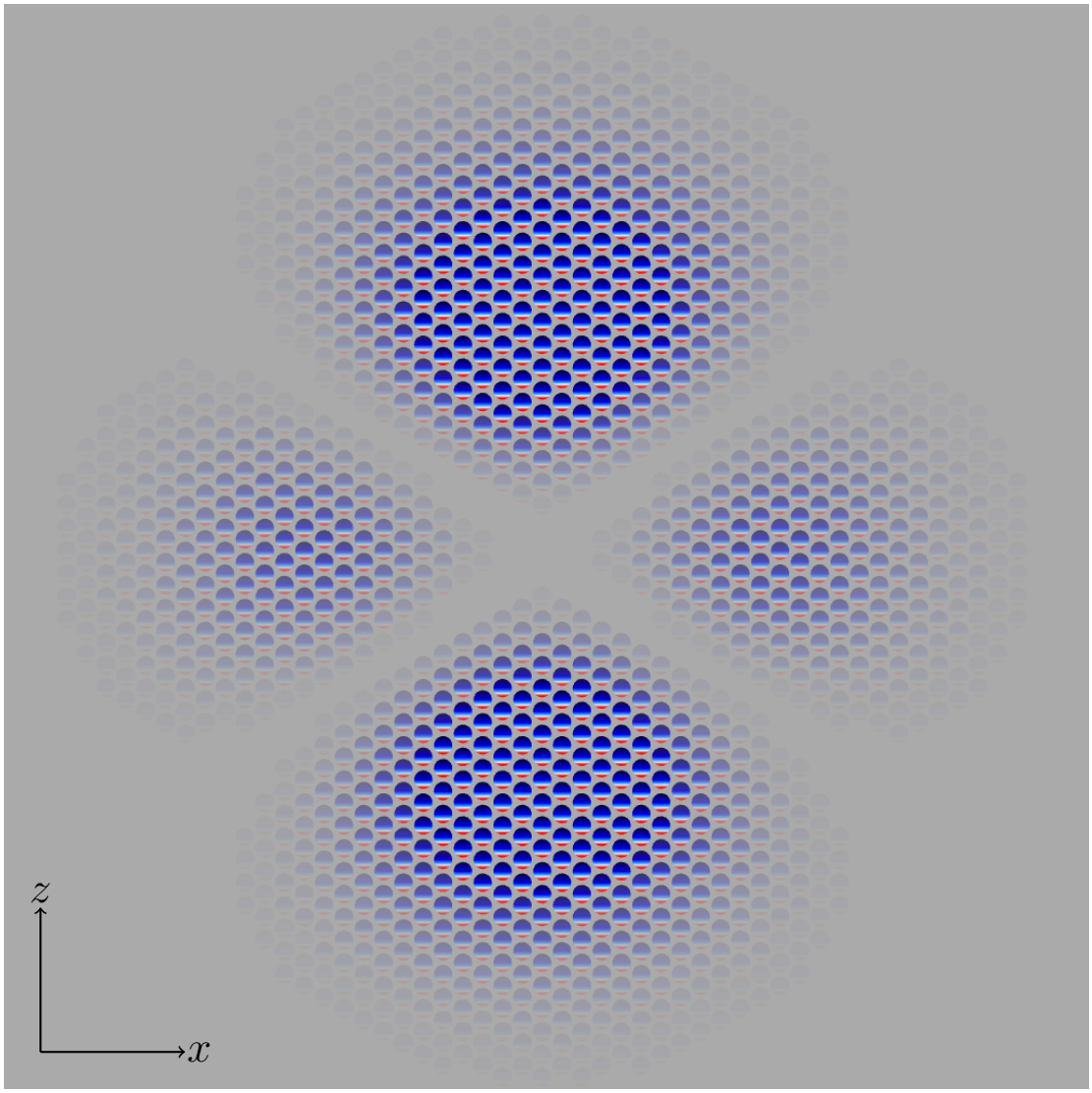

Figure 3.7: This figure displays the spin up $3d_{z^2}$ orbital for the three-dimensional harmonic oscillator. The Wigner function for this orbital has eight dimensions; the three spatial x, y, and z degrees of freedom, the momentum degrees of freedom associated with each spatial degree of freedom, and two spin degrees of freedom θ and ϕ. To obtain the familiar orbital structure, all momentum and spin degrees of freedom are integrated out to yield the probability density function in terms of position. These values are used to set the opacity (α) of each sphere, neglecting all points where $\alpha < 0.1$. At each point, $\boldsymbol{q}$, in the xz-plane the reduced Wigner function, $W^{\mathrm{H}}(\boldsymbol{q}, \theta, \phi)$, is plotted on a sphere. Each sphere can then be interpreted as an indication of the probability of finding the electron at $\boldsymbol{q}$ with a certain spin. In this plot, which has rotational symmetry about the z axis, the state of the system is of the same form as an $n = 3$, $l = 2$, $m = 0$ d-orbital of hydrogen with spin-up. Note that the zero point is indicate by the colour white with blue positive and red negative. Image and caption adapted from Ref. [90]

$$= \mathrm{Tr}\left[\hat{\rho}_{\mathrm{spatial}}\Pi_{\mathrm{spatial}}\right] \times \mathrm{Tr}\left[\hat{\rho}_{\mathrm{spin}}\Pi_{\mathrm{spin}}\right], \tag{3.64}$$

$$= W(\boldsymbol{q}, \boldsymbol{p}) \times W(\theta, \phi). \tag{3.65}$$

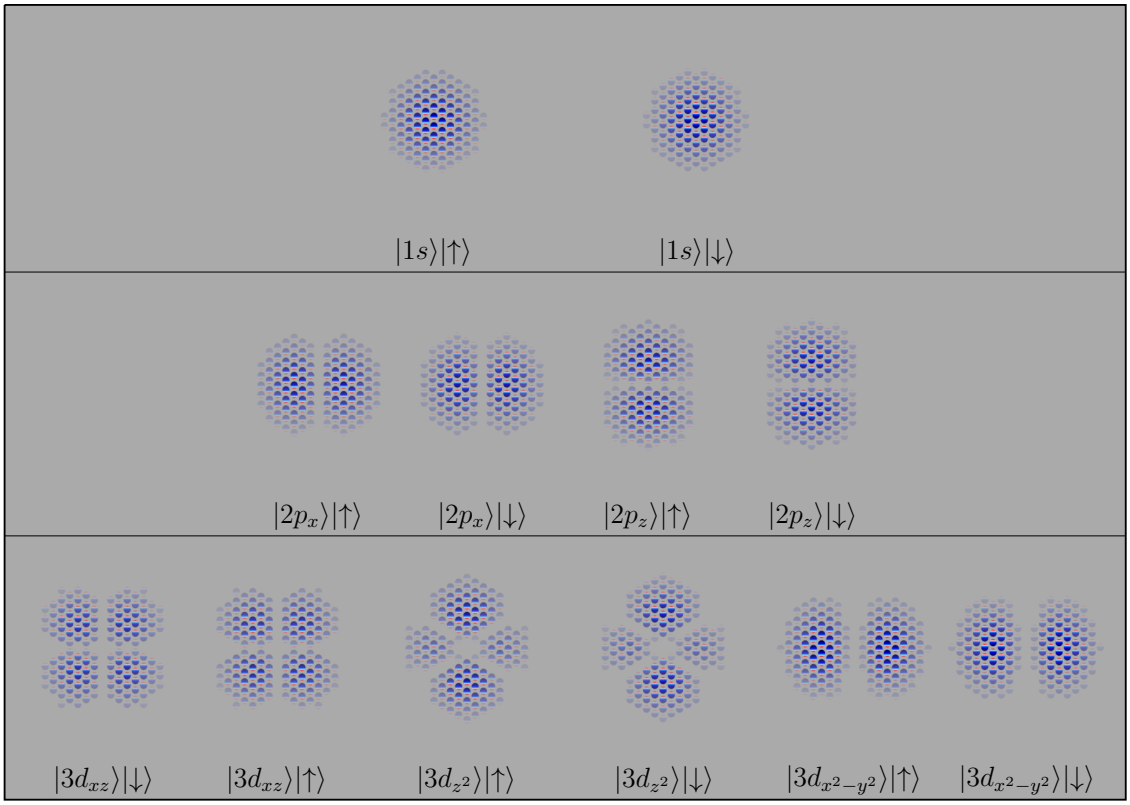

Figure 3.8: For completion of the progression of the textbook orbitals, the full set are produced here for both degenerate states of the electron. The key point is to notice that the two states are easily distinguished and that the states are readily understood. A visualization that is as familiar as this but containing the extra spin information is something that until these images has not been seen. Note that the sharp cut-offs in the spheres are due to size and resolution, in order to maintain a printer friendly image the number of points has been scaled back. Also the states that are zero in the xz-plane, the plane that is plotted here, have been omitted. Note that the zero point is indicate by the colour white with blue positive and red negative.

For different values of $\boldsymbol{q}$, the Wigner function in this case is the same state upto some scaling factor. This in effect means that the spin state must be equivalent everywhere and the probability density scales the values. If this separability is lacking then this decomposition does not work, and the spin being able to point in different directions becomes possible. As the state here is pure, the rotation in the spin state can only have arisen from the lack of separability, *i.e.*, entanglement. As a qualitative comparison, we can state that when the spin state at each point in phase-space is the same there is no entanglement and the state is separable. Equivalently, when the spin state is different, in this case when the spin state has rotated between

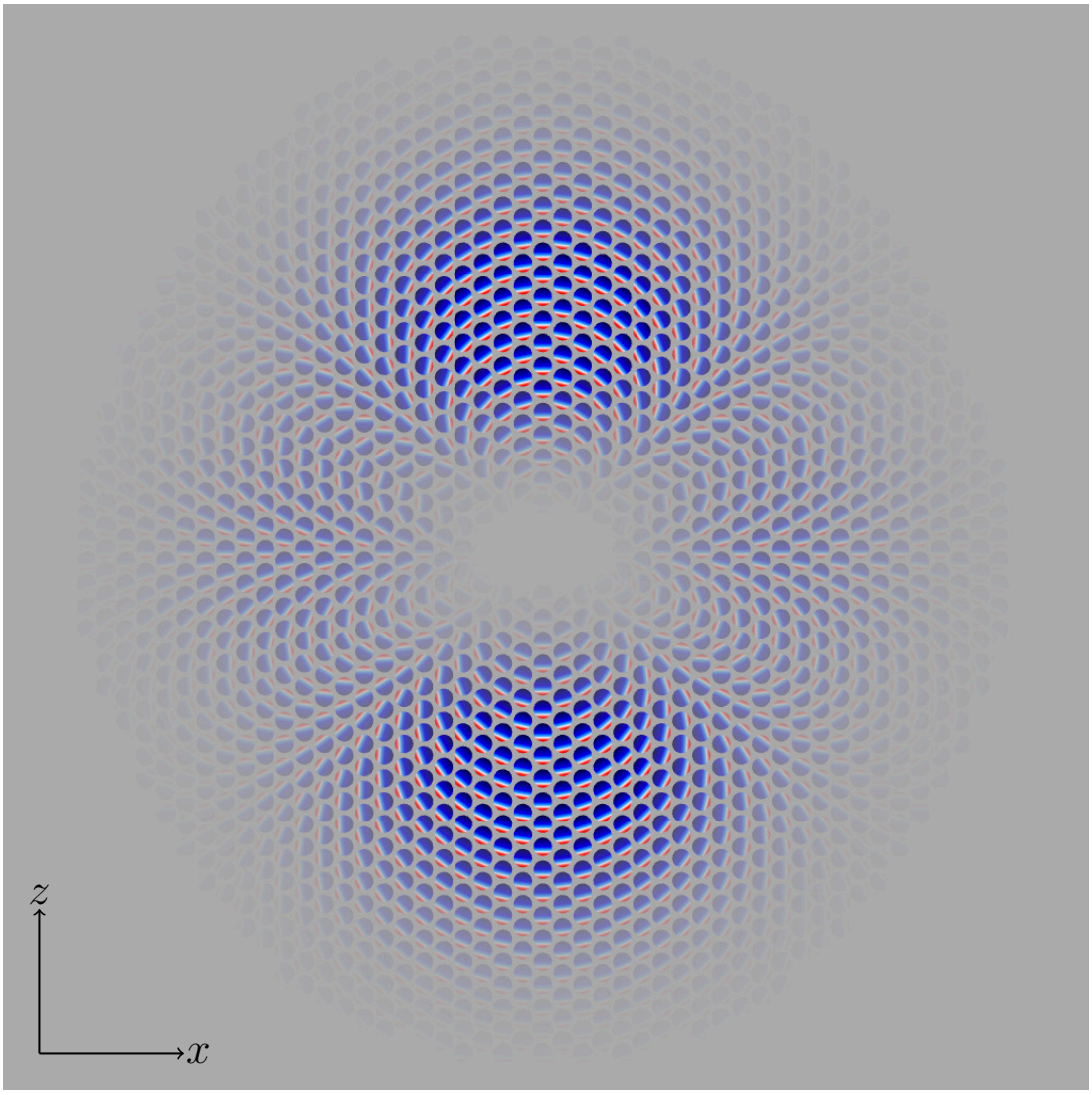

Figure 3.9: Due to relativistic effects in the Hamiltonian of real atomic hydrogen, states such as the one shown in Fig. 3.7 are not stationary. One of the most important corrections arises due to a coupling between spin and orbital angular momentum degrees of freedom. This affects every state, other than the s-orbitals, and the result is that the energy eigenstates have entangled spin and spatial degrees of freedom. Such entanglement cannot be made visible using conventional probability density plots. This figure uses the same technique outlined but for the $|j = 5/2, m = 1/2\rangle$ orbital; it is clear that there are correlations between the spin and spatial degrees of freedom. Note that the zero point is indicate by the colour white with blue positive and red negative. Image and caption adapted from Ref. [90]

different points in phase space, there is entanglement between the spin and spatial degrees of freedom.

Effectively, at this point, it is possible to pull out two pieces of information that are normally lost in the visualization. With this information, for the first time, it is possible to state, from one image, that this state is entangled. Real atomic hydrogen has a number of relativistic effects that affect the states total energy. The ability to subtly improve the model so as to account for these, and to obtain an accurate model, *i.e.*, correctly predict energy level structures, is necessary. The relativistic effect accounted for here is spin-orbit coupling, proportional to $\hat{\boldsymbol{L}}\cdot\hat{\boldsymbol{S}}$. To account for such effects in this system, there has been an addition of orbital angular momentum and spin. As explained earlier in this chapter, this is not trivial as the alignment of the components affects the energy of the state. But it can be shown that one state that takes account of this is

$$\left|j=\frac{5}{2},m=\frac{1}{2}\right\rangle=\sqrt{\frac{3}{5}}\left|d_{z^2}\right\rangle\left|\uparrow\right\rangle+\sqrt{\frac{1}{5}}(\left|d_{xz}\right\rangle+\mathrm{i}\left|d_{yz}\right\rangle)\left|\downarrow\right\rangle, \tag{3.66}$$

the state shown in Fig. 3.9. As deduced in the previous discussion, this state has a non-zero magnetization and strongly entangles spin and spatial degrees of freedom.[1]

It is useful to reproduce a number of states here that all take account of spin-orbit coupling terms. The eigenstates $|j,m\rangle$ are labelled by j the quantum number associated with $\hat{J}^2=(\hat{\boldsymbol{L}}+\hat{\boldsymbol{S}})^2$ and m the eigenvalue of $\hat{J}_z=\hat{L}_z+\hat{S}_z$ for orbital and spin angular momenta $\hat{\boldsymbol{L}}$ and $\hat{\boldsymbol{S}}$ respectively. For a full description of their determination see Ref. [91]. The $1s$-orbital is not affected by this coupling term, the $2p$-orbitals can be denoted $|J,M\rangle$ with $l=1$, $s=1/2$ and are [91]

$$\left|\frac{3}{2},\frac{3}{2}\right\rangle=p_{+1}\left|\uparrow\right\rangle=\pi^{-3/4}\,\mathrm{e}^{-r^2/2}\begin{pmatrix}x+\mathrm{i}\,y\\0\end{pmatrix}, \tag{3.67}$$

[1] To convince the reader, the entropy of entanglement is calculated as 0.971 bits [120]. If the state were pure the entropy of entanglement would be zero.

$$\left|\frac{3}{2},\frac{1}{2}\right\rangle = \frac{\sqrt{2}p_0\left|\uparrow\right\rangle + p_{+1}\left|\downarrow\right\rangle}{\sqrt{3}} = \frac{\pi^{-3/4}\,\mathrm{e}^{-r^2/2}}{\sqrt{3}}\begin{pmatrix} 2z \\ x+\mathrm{i}\,y \end{pmatrix}, \tag{3.68}$$

$$\left|\frac{3}{2},-\frac{1}{2}\right\rangle = \frac{p_{-1}\left|\uparrow\right\rangle + \sqrt{2}p_0\left|\downarrow\right\rangle}{\sqrt{3}} = \frac{\pi^{-3/4}\,\mathrm{e}^{-r^2/2}}{\sqrt{3}}\begin{pmatrix} x-\mathrm{i}\,y \\ 2z \end{pmatrix}, \tag{3.69}$$

$$\left|\frac{3}{2},-\frac{3}{2}\right\rangle = p_{-1}\left|\downarrow\right\rangle = \pi^{-3/4}\,\mathrm{e}^{-r^2/2}\begin{pmatrix} 0 \\ x-\mathrm{i}\,y \end{pmatrix}, \tag{3.70}$$

$$\left|\frac{1}{2},\frac{1}{2}\right\rangle = \frac{-p_0\left|\uparrow\right\rangle + \sqrt{2}p_{+1}\left|\downarrow\right\rangle}{\sqrt{3}} = \frac{\sqrt{2}\pi^{-3/4}\,\mathrm{e}^{-r^2/2}}{\sqrt{3}}\begin{pmatrix} -z \\ x+\mathrm{i}\,y \end{pmatrix}, \tag{3.71}$$

$$\left|\frac{1}{2},-\frac{1}{2}\right\rangle = \frac{-\sqrt{2}p_{-1}\left|\uparrow\right\rangle + p_0\left|\downarrow\right\rangle}{\sqrt{3}} = \frac{\pi^{-3/4}\,\mathrm{e}^{-r^2/2}}{\sqrt{3}}\begin{pmatrix} -x+\mathrm{i}\,y \\ z \end{pmatrix}. \tag{3.72}$$

The momentum-integrated Wigner functions for each of these states, using Eq. (2.30), are

$$\mathcal{W}_{\frac{3}{2},\frac{3}{2}}(\mathbf{r},\theta,\phi) = \frac{\mathrm{e}^{-\mathbf{r}^2}}{2\pi^{3/2}}(x^2+y^2)\left[1+\sqrt{3}\cos\theta\right] \tag{3.73}$$

$$\begin{aligned}\mathcal{W}_{\frac{3}{2},\frac{1}{2}}(\mathbf{r},\theta,\phi) = \frac{\mathrm{e}^{-\mathbf{r}^2}}{6\pi^{3/2}}\Big[&(4z^2+x^2+y^2)+\sqrt{3}\big(4zx\sin\theta\cos\phi+\\ &4zy\sin\theta\sin\phi+(4z^2-x^2-y^2)\cos\theta\big)\Big]\end{aligned} \tag{3.74}$$

$$\begin{aligned}\mathcal{W}_{\frac{3}{2},-\frac{1}{2}}(\mathbf{r},\theta,\phi) = \frac{\mathrm{e}^{-\mathbf{r}^2}}{6\pi^{3/2}}\Big[&(4z^2+x^2+y^2)+\sqrt{3}\big(4zx\sin\theta\cos\phi-\\ &4zy\sin\theta\sin\phi+(x^2+y^2-4z^2)\cos\theta\big)\Big]\end{aligned} \tag{3.75}$$

$$\mathcal{W}_{\frac{3}{2},-\frac{3}{2}}(\mathbf{r},\theta,\phi) = \frac{\mathrm{e}^{-\mathbf{r}^2}}{2\pi^{3/2}}(x^2+y^2)\left[1-\sqrt{3}\cos\theta\right] \tag{3.76}$$

$$\begin{aligned}\mathcal{W}_{\frac{1}{2},\frac{1}{2}}(\mathbf{r},\theta,\phi) = \frac{\mathrm{e}^{-\mathbf{r}^2}}{3\pi^{3/2}}\Big[&r^2+\sqrt{3}\big(-2zx\sin\theta\cos\phi-2zy\sin\theta\sin\phi+\\ &(z^2-x^2-y^2)\cos\theta\big)\Big]\end{aligned} \tag{3.77}$$

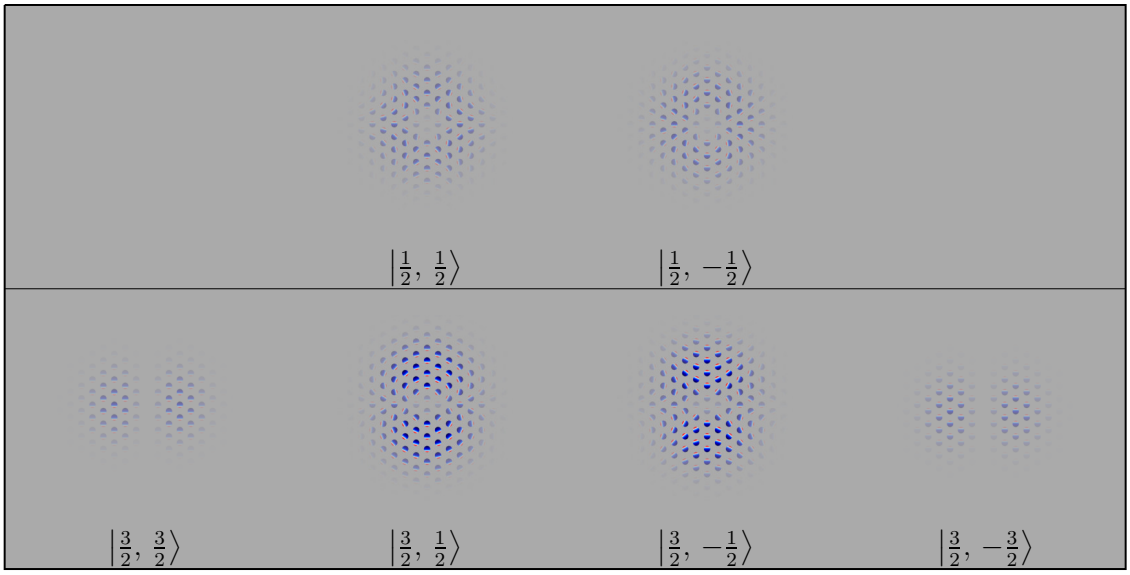

Figure 3.10: For completion, this is the full set of spin-orbit coupled states for $l = 1$, $s = 1/2$. They are plotted using the technique described for previous figures. The plane chosen is the xz-plane as most of the states are symmetrical about the z-axis spatially, and with regards to spin. Those states with spin-spatial entanglement are clearly different to those that are simply product states, *i.e.*, there is no entanglement. Note that the zero point is indicate by the colour white with blue positive and red negative.

$$\mathcal{W}_{\frac{1}{2},-\frac{1}{2}}(\mathbf{r},\theta,\phi) = \frac{\mathrm{e}^{-\mathbf{r}^2}}{3\pi^{3/2}}\Big[r^2 + \sqrt{3}\big(-2zx\sin\theta\cos\phi + 2zy\sin\theta\sin\phi + (x^2+y^2-z^2)\cos\theta\big)\Big] \tag{3.78}$$

Figure 3.10 shows these Wigner functions in the xz-plane. These are plotted using the technique just described, opacity related to probability density and spin mapped onto each sphere based on its position. This is a slice through the three-dimensional space but for most of the states there is rotational symmetry about the z-axis. However, this is not the case for both of the $m_j = -1/2$ states, where the yz-plane (not depicted) looks like the xz-plane of the corresponding $m_j = 1/2$ states but with the spin direction reversed. The spin-spatial entanglement is clear for the states $|3/2, \pm 1/2\rangle$ and $|1/2, \pm 1/2\rangle$, while $|3/2, \pm 3/2\rangle$ are product states.

As a check that these figures make sense, the reduced Wigner function which

integrates out the spatial degrees of freedom can be found;

$$w(\theta,\phi) = \int \mathcal{W}(\boldsymbol{r},\theta,\phi)\,\mathrm{d}^3\boldsymbol{r} \tag{3.79}$$

noting the relations such that

$$\int_{-\infty}^{\infty} \mathrm{e}^{-x^2}\,\mathrm{d}x = \sqrt{\pi} \quad \text{and} \quad \int_{-\infty}^{\infty} x^2\,\mathrm{e}^{-x^2}\,\mathrm{d}x = \frac{\sqrt{\pi}}{2}. \tag{3.80}$$

The spin-orbit states in Fig. 3.10 give

$$w_{\frac{3}{2}\frac{3}{2}}(\theta,\phi) = \frac{1}{2}\left(1+\sqrt{3}\cos\theta\right) \tag{3.81}$$

$$w_{\frac{3}{2}\frac{1}{2}}(\theta,\phi) = \frac{1}{2}\left(1+\frac{\sqrt{3}\cos\theta}{3}\right) \tag{3.82}$$

$$w_{\frac{3}{2}\frac{-1}{2}}(\theta,\phi) = \frac{1}{2}\left(1-\frac{\sqrt{3}\cos\theta}{3}\right) \tag{3.83}$$

$$w_{\frac{3}{2}\frac{-3}{2}}(\theta,\phi) = \frac{1}{2}\left(1-\sqrt{3}\cos\theta\right) \tag{3.84}$$

$$w_{\frac{1}{2}\frac{1}{2}}(\theta,\phi) = \frac{1}{2}\left(1-\frac{\sqrt{3}\cos\theta}{3}\right) \tag{3.85}$$

$$w_{\frac{1}{2}\frac{-1}{2}}(\theta,\phi) = \frac{1}{2}\left(1+\frac{\sqrt{3}\cos\theta}{3}\right) \tag{3.86}$$

The product states, $|3/2,\pm 3/2\rangle$, give a pure-state spin Wigner function, the others a mixed-state spin Wigner function. Note that for $j = 1/2$, $m_j = 1/2$ the spin is predominantly down and for $j = 1/2$, $m_j = -1/2$ the spin is predominantly up, as can be seen from the weighting of the Clebsch-Gordan coefficients in Eqs. (3.67)–(3.72).

This analysis is consistent with the images in Fig. 3.10 and can be easily pulled out of future visualizations. For instance, in the case of the $3d$-orbitals it is useful to perhaps analyze the figure first, pull out the features and then check against

the theory. This suggests that the interpretation of the visualizations is readily in agreement with the theory.

Similarly, the same can be done for the $3d$-orbitals, those with $l = 2$, $s = 1/2$;

$$\left|\frac{5}{2},\frac{5}{2}\right\rangle = d_{+2}\left|\uparrow\right\rangle = \frac{\mathrm{e}^{-\mathbf{r}^2/2}}{\sqrt{2}\pi^{3/4}}\begin{pmatrix}(x+\mathrm{i}\,y)^2\\0\end{pmatrix}, \tag{3.87}$$

$$\left|\frac{5}{2},\frac{3}{2}\right\rangle = \frac{2d_{+1}\left|\uparrow\right\rangle + d_{+2}\left|\downarrow\right\rangle}{\sqrt{5}} = \sqrt{\frac{2}{5}}\frac{\mathrm{e}^{-\mathbf{r}^2/2}}{\pi^{3/4}}\begin{pmatrix}-2\,(x+\mathrm{i}\,y)\,z\\\frac{1}{2}\,(x+\mathrm{i}\,y)^2\end{pmatrix}, \tag{3.88}$$

$$\left|\frac{5}{2},\frac{1}{2}\right\rangle = \frac{\sqrt{3}d_0\left|\uparrow\right\rangle + \sqrt{2}d_{+1}\left|\downarrow\right\rangle}{\sqrt{5}} = \frac{\mathrm{e}^{-\mathbf{r}^2/2}}{\sqrt{5}\pi^{3/4}}\begin{pmatrix}(2z^2-x^2-y^2)\\2\,(x+\mathrm{i}\,y)\,z\end{pmatrix}, \tag{3.89}$$

$$\left|\frac{5}{2},-\frac{1}{2}\right\rangle = \frac{\sqrt{2}d_{-1}\left|\uparrow\right\rangle + \sqrt{3}d_0\left|\downarrow\right\rangle}{\sqrt{5}} = \frac{\mathrm{e}^{-\mathbf{r}^2/2}}{\sqrt{5}\pi^{3/4}}\begin{pmatrix}2\,(x-\mathrm{i}\,y)\,z\\(2z^2-x^2-y^2)\end{pmatrix}, \tag{3.90}$$

$$\left|\frac{5}{2},-\frac{3}{2}\right\rangle = \frac{d_{-2}\left|\uparrow\right\rangle + 2d_{-1}\left|\downarrow\right\rangle}{\sqrt{5}} = \sqrt{\frac{2}{5}}\frac{\mathrm{e}^{-\mathbf{r}^2/2}}{\pi^{3/4}}\begin{pmatrix}\frac{1}{2}\,(x+\mathrm{i}\,y)^2\\2\,(x-\mathrm{i}\,y)\,z\end{pmatrix}, \tag{3.91}$$

$$\left|\frac{5}{2},-\frac{5}{2}\right\rangle = d_{-2}\left|\downarrow\right\rangle = \frac{\mathrm{e}^{-\mathbf{r}^2/2}}{\sqrt{2}\pi^{3/4}}\begin{pmatrix}0\\(x-\mathrm{i}\,y)^2\end{pmatrix}, \tag{3.92}$$

$$\left|\frac{3}{2},\frac{3}{2}\right\rangle = \frac{-d_{+1}\left|\uparrow\right\rangle + 2d_{+2}\left|\downarrow\right\rangle}{\sqrt{5}} = \sqrt{\frac{2}{5}}\frac{\mathrm{e}^{-\mathbf{r}^2/2}}{\pi^{3/4}}\begin{pmatrix}(x+\mathrm{i}\,y)\,z\\(x+\mathrm{i}\,y)^2\end{pmatrix}, \tag{3.93}$$

$$\left|\frac{3}{2},\frac{1}{2}\right\rangle = \frac{-\sqrt{2}d_0\left|\uparrow\right\rangle + \sqrt{3}d_{+1}\left|\downarrow\right\rangle}{\sqrt{5}} = \frac{\mathrm{e}^{-\mathbf{r}^2/2}}{\sqrt{5}\pi^{3/4}}\begin{pmatrix}\sqrt{\frac{2}{3}}\,(x^2+y^2-2z^2)\\-\sqrt{6}\,(x+\mathrm{i}\,y)\,z\end{pmatrix}, \tag{3.94}$$

$$\left|\frac{3}{2},-\frac{1}{2}\right\rangle = \frac{-\sqrt{3}d_{-1}\left|\uparrow\right\rangle + \sqrt{2}d_0\left|\downarrow\right\rangle}{\sqrt{5}} = \frac{\mathrm{e}^{-\mathbf{r}^2/2}}{\sqrt{5}\pi^{3/4}}\begin{pmatrix}-\sqrt{6}\,(x-\mathrm{i}\,y)\,z\\\sqrt{\frac{2}{3}}\,(2z^2-x^2-y^2)\end{pmatrix}, \tag{3.95}$$

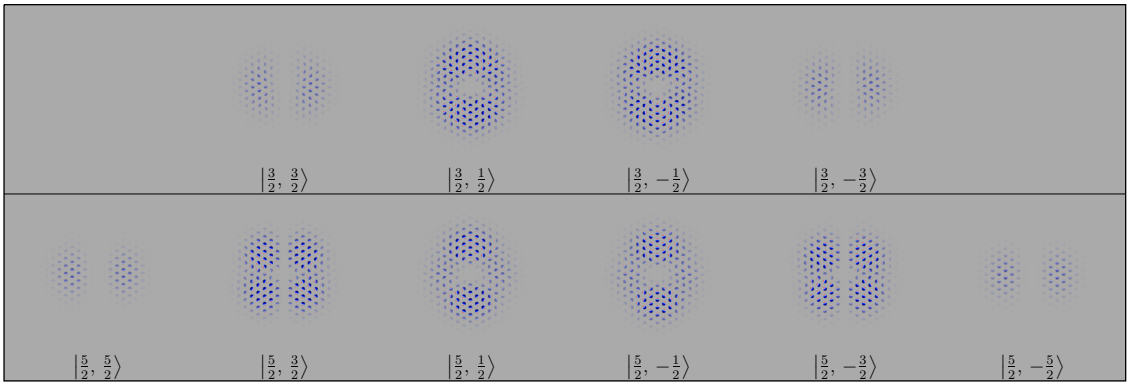

Figure 3.11: For completion, this is the full set of spin-orbit coupled states for $l = 2$, $s = 1/2$. They are plotted using the technique described for previous figures. The plane chosen is the xz-plane as most of the states are symmetrical about the z-axis spatially, and with regards to spin. Those states with spin-spatial entanglement are clearly different to those that are simply product states, *i.e.*, there is no entanglement. Note that the zero point is indicate by the colour white with blue positive and red negative.

$$\left|\frac{3}{2}, -\frac{3}{2}\right\rangle = \frac{-2d_{-2}\left|\uparrow\right\rangle + d_{-1}\left|\downarrow\right\rangle}{\sqrt{5}} = \sqrt{\frac{2}{5}}\frac{\mathrm{e}^{-\mathbf{r}^2/2}}{\pi^{3/4}}\begin{pmatrix} -\left(x - \mathrm{i}\, y\right)^2 \\ \left(x - \mathrm{i}\, y\right) z \end{pmatrix}. \tag{3.96}$$

These states are plotted in Fig. 3.11. The momentum integrated Wigner functions for these spin-orbit coupled states are:

$$D_{\frac{5}{2},\frac{5}{2}}(\mathbf{r}) = \frac{\mathrm{e}^{-\mathbf{r}^2}}{4\pi^{3/2}}\left(x^2 + y^2\right)^2\left[1 + \sqrt{3}\cos\theta\right], \tag{3.97}$$

$$D_{\frac{5}{2},\frac{3}{2}}(\mathbf{r}) = \frac{\mathrm{e}^{-\mathbf{r}^2}}{20\pi^{3/2}}\left(x^2 + y^2\right)\Big[x^2 + y^2 + 16z^2 - \sqrt{3}\big[8xz\sin\theta\cos\phi + 8yz\sin\theta\sin\phi + \left(x^2 + y^2 - 16z^2\right)\cos\theta\big]\Big], \tag{3.98}$$

$$D_{\frac{5}{2},\frac{1}{2}}(\mathbf{r}) = \frac{\mathrm{e}^{-\mathbf{r}^2}}{10\pi^{3/2}}\Big[\left(x^2 + y^2\right)^2 + 4z^4 - \sqrt{3}\big[4\left(x^2 + y^2 - 2z^2\right)\left(xz\sin\theta\cos\phi + yz\sin\theta\sin\phi\right) + \left(\left(8x^2 + 8y^2\right)z^2 - 4z^4 - \left(x^2 + y^2\right)^2\right)\cos\theta\big]\Big], \tag{3.99}$$

$$D_{\frac{5}{2},\frac{-1}{2}}(\mathbf{r}) = \frac{\mathrm{e}^{-\mathbf{r}^2}}{10\pi^{3/2}}\Big[\left(x^2+y^2\right)^2 + 4z^4 - \sqrt{3}\big[4\left(x^2+y^2-2z^2\right)\left(xz\sin\theta\cos\phi + yz\sin\theta\sin\phi\right) + \left(4z^4 - \left(8x^2+8y^2\right)z^2 + \left(x^2+y^2\right)^2\right)\cos\theta\big]\Big], \tag{3.100}$$

$$D_{\frac{5}{2},\frac{-3}{2}}(\mathbf{r}) = \frac{\mathrm{e}^{-\mathbf{r}^2}}{20\pi^{3/2}}\left(x^2+y^2\right)\Big[x^2+y^2+16z^2+\sqrt{3}\big[8xz\sin\theta\cos\phi + 8yz\sin\theta\sin\phi + \left(x^2+y^2-16z^2\right)\cos\theta\big]\Big], \tag{3.101}$$

$$D_{\frac{5}{2},\frac{-5}{2}}(\mathbf{r}) = \frac{\mathrm{e}^{-\mathbf{r}^2}}{4\pi^{3/2}}\left(x^2+y^2\right)^2\Big[1-\sqrt{3}\cos\theta\Big], \tag{3.102}$$

$$D_{\frac{3}{2},\frac{3}{2}}(\mathbf{r}) = \frac{\mathrm{e}^{-\mathbf{r}^2}}{5\pi^{3/2}}\left(x^2+y^2\right)\Big[x^2+y^2+z^2+\sqrt{3}\big[2xz\sin\theta\cos\phi + 2yz\sin\theta\sin\phi + \left(z^2-x^2-y^2\right)\cos\theta\big]\Big], \tag{3.103}$$

$$D_{\frac{3}{2},\frac{1}{2}}(\mathbf{r}) = \frac{\mathrm{e}^{-\mathbf{r}^2}}{15\pi^{3/2}}\Big[\left(x^2+y^2+4z^2\right)\left(x^2+y^2+z^2\right) - \sqrt{3}\big[6\left(x^2+y^2-2z^2\right)\left(xz\sin\theta\cos\phi + yz\sin\theta\sin\phi\right) + \left(\left(13x^2+13y^2\right)z^2 - \left(x^2+y^2\right)^2 - 4z^4\right)\cos\theta\big]\Big], \tag{3.104}$$

$$D_{\frac{3}{2},\frac{-1}{2}}(\mathbf{r}) = \frac{\mathrm{e}^{-\mathbf{r}^2}}{15\pi^{3/2}}\Big[\left(x^2+y^2+4z^2\right)\left(x^2+y^2+z^2\right) + \sqrt{3}\big[6\left(x^2+y^2-2z^2\right)\left(xz\sin\theta\cos\phi + yz\sin\theta\sin\phi\right) + \left(\left(13x^2+13y^2\right)z^2 - \left(x^2+y^2\right)^2 - 4z^4\right)\cos\theta\big]\Big], \tag{3.105}$$

$$D_{\frac{3}{2},\frac{3}{2}}(\mathbf{r}) = \frac{\mathrm{e}^{-\mathbf{r}^2}}{5\pi^{3/2}}\left(x^2+y^2\right)\Big[x^2+y^2+z^2-\sqrt{3}\big[2xz\sin\theta\cos\phi + 2yz\sin\theta\sin\phi + \left(z^2-x^2-y^2\right)\cos\theta\big]\Big]. \tag{3.106}$$

This visualization then, is not only able to distinguish between states with spin-orbit coupling and those without, but also make clear spin-spatial correlations. Figure 3.9 has different spin states of the electron at different positions, encapsulating the definition of pure state entanglement visually. That is, this is a direct manifestation of, and can be mapped back to, the fact that the spin of a particle cannot be

described independently of its position.

3.4 Helium

Having now introduced the visualization method, it is important to demonstrate why the spinor representation is insufficient. Although, at this point, the two visualizations are capable of displaying the same amount of information, for two spins this is not true. Consider the two-electron atom, helium, and its associated Wigner function. For the two electrons there are eight degrees of freedom each, three for the spatial components, three for the concomitant momenta and two for the spin components. Even after the momentum has been integrated out, the reduced Wigner function would be 10 dimensional. This, as will be seen later, can be reduced by another three dimensions, by considering the indistinguishability of electrons and their associated degrees of freedom. However, a seven dimensional function remains and their is no appropriate mechanism for the Bloch vector, the spinor representation, to display this information. But first it is useful to consider the model that is used for such a system.

3.4.1 Independent Particle Model

To emphasize certain assumptions made about atomic systems, the treatment of helium shall first be carried out in the simplest approximation. The analysis shall initially be only concerned with the orbital that the electrons are in, the spin is not considered. Most chemistry textbooks will begin with this introduction to helium, which is arguably no less difficult than the model used in this visualization. There is no electron-electron interaction in this approximation and electrons are considered individually as atomic orbitals.

For ground state helium the first concern is the lowest energy orbital, the $1s$ orbital. As helium is a two-electron atom, the lowest energy state is $1s(1)1s(2)$ more commonly written as $1s^2$. *N.B.* the notation used throughout this thesis will

tend to follow the first, *i.e.*, the orbital is notated followed by the electron number which that orbital is associated in brackets. This is of course an incorrect assignment, due to the Pauli exclusion principle, but it is easier for the case of discussion and is used for purely illustrative purposes. It could be assumed that when this level of discussion is being had, that the numbers indicate electrons as if the system has just been measured and the state been considered is given by the appropriate Slater determinant. The Slater determinant is a mechanism for determining an antisymmetric wavefunction to describe a system so that it complies with the Pauli exclusion principle. It labels electrons and orbitals which could be then assigned to a subsequent measurement. It will be introduced more formally later in this thesis.

The first excited state of helium is a little more interesting. One electron will remain in the lowest energy orbital and one will be promoted to a higher level. The electron would then be allowed in either a $2s$- or $2p$-orbital. However, this is a multi-electron system and the $2s$-orbital in a multi-electron system has a lower energy than the $2p$ [59]. The first excited state of helium then is $1s(1)2s(2)$ in this approximation. When spin is included however, it will be found that this prescriptive labelling is not entirely true. The overall point is that this initial approximation misses some very important contributions to energy and also produces an incorrect description of the atom.

It is easy to see the problem in the probability density of such an atom. Electrons are indistinguishable particles and as such the indices used to denote which electron is in which orbital is completely arbitrary. Therefore under permutations of electron indices, the probability density should remain unchanged; this is not true for this state. An attempt under this model is then made by looking for a state that enforces the condition that $|\psi_{12}|^2 = |\psi_{21}|^2$ with the only possible cases being when ψ is either symmetric or antisymmetric [98];

$$\psi_{\text{sym.}} = \frac{1}{\sqrt{2}}\left(1s(1)2s(2) + 1s(2)2s(1)\right) \tag{3.107}$$

$$\psi_{\text{ant.}} = \frac{1}{\sqrt{2}}\left(1s(1)2s(2) - 1s(2)2s(1)\right). \tag{3.108}$$

Both of these demonstrate a key consequence of quantum mechanics that is often omitted from discussions about the form of atoms. That is, that the electrons are not 'in' an orbital, they are in a superposition of all allowed orbitals with a probability of being found in any. In the case of helium, if an electron is measured as being in one of the orbitals then the other electron at that point in time must be in the other orbital, but that is all that can be said. Applying this amount of rigour to understanding the model will greatly help with the interpretation of the visualizations. This is because it will help us interpret what is happening in the Wigner function when an electron is at a specific position.

3.4.2 Moshinsky Atom

Due to the constraints of the above, we use a simpler but sufficient model for our calculations. The Moshinsky atom, as similarly discussed in Ref. [111], for the two-electron atom has Hamiltonian

$$\mathcal{H} = \frac{\hat{p}_1^2}{2m} + \frac{\hat{p}_2^2}{2m} + \frac{m\Omega^2}{2}\left[\hat{x}_1^2 + \hat{x}_2^2 + \kappa\left(\hat{x}_1^2 - \hat{x}_2^2\right)^2\right]. \tag{3.109}$$

Both particles are one-dimensional with mass m in an harmonic potential with frequency Ω and some interaction between the particles. This interaction in the term is scaled by κ and gives an approximation to the repulsion, when $-\frac{1}{2} < \kappa < 0$, between the electrons. Note that the interaction is attractive when $\kappa > 0$. Essentially, the trick to this model is replacing both the nuclear and electron-electron potentials with harmonic oscillators.

The Hamiltonian can then be rewritten in a separable form by use of the relative $(\hat{x},\, \hat{p})$ and centre-of-mass co-ordinates $(\hat{X},\, \hat{P})$,

$$\mathcal{H} = \frac{\hat{P}^2}{2m} + \frac{\hat{p}^2}{2m} + \frac{m\Omega^2}{2}\hat{X}^2 + \frac{m\omega^2}{2}\hat{x}^2, \tag{3.110}$$

with relative frequency $\omega = \sqrt{1+2\kappa}\Omega$ Ref. [111]. Here $\hat{X}$ is the position of the centre of mass and $\hat{P}$ is the momentum associated with the centre of mass of the

system. The energy levels of the Hamiltonian are given by

$$E_{N,n} = \hbar\Omega\left(N + \frac{1}{2}\right) + \hbar\omega\left(n + \frac{1}{2}\right), \tag{3.111}$$

where the 'uppercase' energy comes from the centre-of-mass co-ordinates and the 'lowercase' energy from the relative co-ordinates. The associated eigenfunctions of these energies are the standard harmonic oscillator wavefunctions

$$\psi_{N,n} = \sqrt{\frac{m^3\Omega\omega\sqrt{\Omega\omega}}{2^{N+n}N!n!\pi\hbar^3}}\exp\left(-\frac{m\left(\Omega^2X^2 - \omega^2x^2\right)}{2\hbar}\right)XxH_NH_n, \tag{3.112}$$

where H_i are the associated Hermite polynomials. *N.B.* for simplicity the prefactors to the individual eigenstates have been combined. This, using the standard Wigner functions of the harmonic oscillator, can be shown to have a Wigner function of

$$\begin{aligned} W_{N,n}(X,x,P,p) = {} & \frac{(-1)^{N+n}\left(2P^2 + 2m\Omega X^2\right)\left(2p^2 + 2m\omega x^2\right)}{m^2\pi^2\hbar^4\Omega\omega}\times \\ & \exp\left(-\frac{\Omega P^2 + \omega p^2 + m^2\Omega\omega\left(\omega x^2 + \Omega X^2\right)}{m\hbar\Omega\omega}\right)L_NL_n \end{aligned} \tag{3.113}$$

where L_i are the associated Laguerre polynomials.

If this Wigner function is then integrated over momentum degrees of freedom, it becomes the position-space probability density function as expected. Taking the ground state, if one of the remaining degrees of freedom is integrated out, due to identical particles it does not matter which, then the resulting reduced Wigner function is

$$\mathcal{W}(x) = \sqrt{\frac{2m\Omega\omega}{\pi\hbar\left(\Omega + \omega\right)}}\exp\left(-\frac{2m\Omega\omega x^2}{\hbar\left(\Omega + \omega\right)}\right). \tag{3.114}$$

This distribution broadens to infinity as the interaction becomes more repulsive, *i.e.*, $\kappa \to -\frac{1}{2}$, as would be expected. It also narrows if the interaction is attractive as expected too. This suggests that such a model is reasonable for describing the two-electron atom. This also holds for the higher energy levels though, as the model is

one dimensional, adding in spin-orbit coupling is not trivial. However, the spin-orbit coupled states of helium shall not be considered so this model remains reasonable.

3.4.3 Two-Electron Atom with Spin

As the electrons are identical particles, our particle distribution must be independent of the choice of labels. This means that the wavefunction must be symmetric, or antisymmetric, on the interchange of electron spatial and spin coordinates. In the case of a two-electron atom, the possible spin combinations are $|\uparrow_1\uparrow_2\rangle$, $|\uparrow_1\downarrow_2\rangle$, $|\downarrow_1\uparrow_2\rangle$, and $|\downarrow_1\downarrow_2\rangle$. Here the subscripts denote which electron is in which spin state, though of course the warnings given earlier apply. The first and last of these states are symmetric whilst the other two are antisymmetric. However, the two that are antisymmetric can be symmetrized by taking the sum and differences of the state products, *i.e.*, $|\uparrow_1\downarrow_2\rangle + |\downarrow_1\uparrow_2\rangle$ and $|\uparrow_1\downarrow_2\rangle - |\downarrow_1\uparrow_2\rangle$. This, when combined with the spatial co-ordinates, gives the four states [98];

$$1s(1)\,1s(2)\,|\uparrow_1\uparrow_2\rangle\,, \tag{3.115}$$

$$1s(1)\,1s(2)\,|\downarrow_1\downarrow_2\rangle\,, \tag{3.116}$$

$$1s(1)\,1s(2)\,|\uparrow_1\downarrow_2\rangle + |\downarrow_1\uparrow_2\rangle\,, \tag{3.117}$$

$$1s(1)\,1s(2)\,|\uparrow_1\downarrow_2\rangle - |\downarrow_1\uparrow_2\rangle\,. \tag{3.118}$$

The first three of these are all symmetric whilst the last is antisymmetric. Physically, the ground state of helium is a singlet, that is, there is only one state. This means that the wavefunction must be antisymmetric and leaves only the final state as having a physical meaning. Of course this is the Pauli exclusion principle; 'the only acceptable wavefunctions for an atom or molecule with two or more electrons are those for which the exchange of the positions and spins of any two electrons causes the value of the wavefunction to change its sign' [93].

Due to the way that this state has been formed, it is possible to use our Gaussian wavefunction basis to represent it. The Wigner function for a two-electron atom is

16-dimensional, three spatial, three momentum and two spin degrees of freedom for each electron. This increased dimensionality requires a different way of producing the visualization. In § 2.2.3, it was pointed out that the dimensionality of the Wigner function in atomic systems scales as $8N$. This is important because, unlike other methods, it is a linear scaling but also means that once the two-electron system has been visualized, the method remains the same. The reduced Wigner function is calculated by integrating over both sets of momenta and one set of spatial degrees of freedom; $W^{\mathrm{He}}(\boldsymbol{q}_1, \theta_1, \phi_1, \theta_2, \phi_2)$. As alluded to the indistinguishability of electrons means that it will not matter which one is chosen. As in the case of hydrogen, the function $W^{\mathrm{He}}(\boldsymbol{q}_1) = |\psi^{\mathrm{He}}(\boldsymbol{q}_1)|^2$, produced by integration over all spin degrees of freedom, is again used to set the intensity.

There is just one remaining difficulty in the visualization of the state; the fact that there are two spins. To resolve this, the sphere at each point in space is the equal-angle slice of the Wigner function for the spin degrees of freedom. This means that the function is evaluated only where $\theta_1 = \theta_2$ and $\phi_1 = \phi_2$. Given that great effort has been made to keep these images as familiar as possible, this slice has the advantage of keeping the figures similar to others in the literature, *e.g.*, the states found in Ref. [61]. An often underestimated advantage of the equal angle slice though, is that it also allows representation of the singlet state, a necessary requirement for atomic systems. Maintaining similarity to other representations and allowing the plotting of the singlet state, alongside the indistinguishability of the electrons, makes the equal angle slice a natural choice. The visualization therefore has the transparency set as before and a sphere at each point with the equal angle slice of the reduced Wigner function plotted on its surface. Figure 3.12 shows a number of relevant two-spin states. Note that Fig. 3.12 (a) is qualitatively the square of the Wigner function for the $|\uparrow\rangle$ state. Similarly, Fig. 3.12 (b) is the product of the $|\uparrow\rangle$ and $|\downarrow\rangle$ states, notice the comparatively larger negative regions on top and on the bottom as compared to a $|\uparrow\rangle$ or $|\downarrow\rangle$ state as well as two zero regions corresponding to those found in the $|\uparrow\rangle$ and $|\downarrow\rangle$ states.

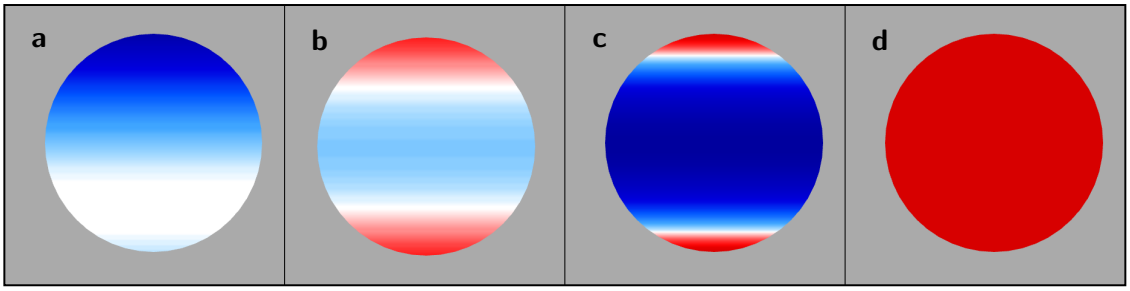

Figure 3.12: This is a set of reduced Wigner functions for spin states for the two-electron atom that are relevant to the states considered in this section. The states shown are (a) $|\uparrow\uparrow\rangle$, (b) $|\uparrow\downarrow\rangle$, (c) $|\uparrow\downarrow\rangle + |\downarrow\uparrow\rangle$ and (d) $|\uparrow\downarrow\rangle$ - $|\downarrow\uparrow\rangle$. The state $|\downarrow\downarrow\rangle$ is the flipped form of (a) but is not presented here. Note also that the first two states have no spin-spin entanglement whereas the second two do. Further, white is zero, blue positive and red negative.

In Fig. 3.13 we have plotted the ground state of helium. A number of things can be deduced from this. Firstly, each sphere is consistent with that of the two-spin singlet state as presented in Fig. 3.12 (d). This is more insightful than may first appear. A traditional way of introducing, or discussing, helium is that the ground state is formed of two electrons in the $1s$ shell. To account for the exclusion principle the spin of these electrons must be opposite to each other. Therefore, helium is a two-electron atom with one electron in the spin-up state and one in the spin-down state. Although, at first this may seem harmless it can cause discussions to very quickly leave out any spin-spin correlations. This is because the spin state that would conform to that description is in Fig. 3.12 (b), the state $|\uparrow\downarrow\rangle$, rather than the antisymmetric superposition of spin-up and spin-down. Even though those having the discussion often know that helium is actually a singlet state, it is not usually evidenced in a visualization. This method makes it an inescapable feature providing all the spin information and eliminating confusion.

Second, the intensity of this plot, as compared with Fig. 3.6, suggests that the spatial component is the product of two $1s$ orbitals. This is again consistent with the state and, though only apparent on comparison with a similar state, is not much of a step up from understanding traditional visualizations. Finally, the spatial and spin degrees of freedom are not correlated, *i.e.*, there is no entanglement, which is consistent with the ground state being a separable state. Again, from little more

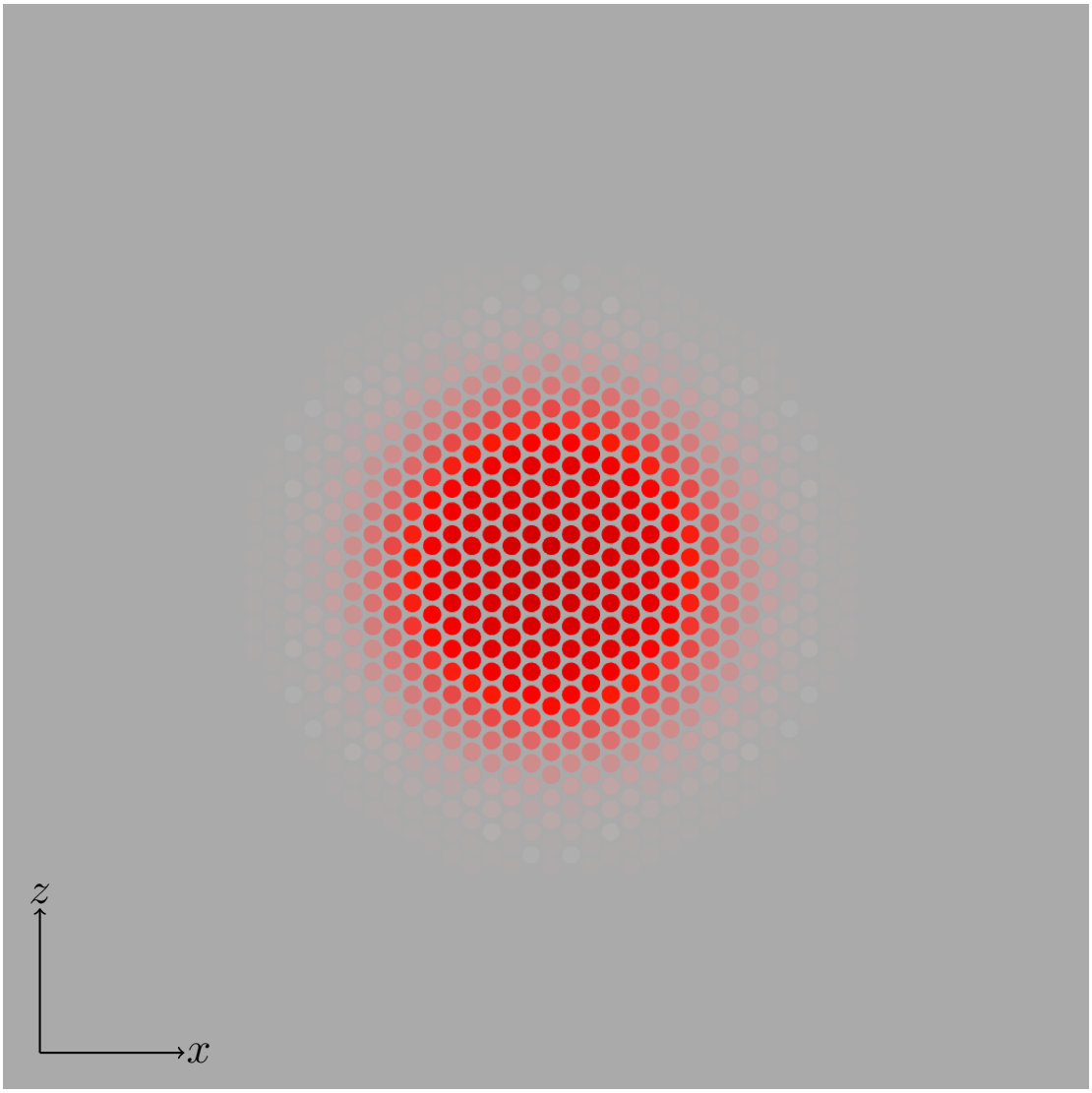

Figure 3.13: This shows the ground state of helium, $|1s(1)\,1s(2)\rangle\,|\uparrow_1\downarrow_2\rangle - |\downarrow_1\uparrow_2\rangle$. The opacity of the spheres indicates the probability of finding an electron at that point and the surface of the sphere shows the equal-angle slice, $\theta_1 = \theta_2 = \theta$ and $\phi_1 = \phi_2 = \phi$, of the Wigner function. Comparing the spin state with Fig. 3.12, the state corresponds to the entangled state Fig. 3.12 (d). The traditional way of introducing the helium atom, with one electron being spin-up and the other being spin-down, would produce the same picture but with the state in Fig. 3.12 (b) everywhere. This provides a visual compulsion to discuss the state as a singlet; a spin-spin entangled state. Effectively, it has been demonstrated that this technique not only visualizes spin-spatial entanglement (as in Fig. 3.9) but also spin-spin entanglement. Note that each sphere is entirely red with the same negative value at each point. Image and caption adapted from [90].

than the visualization, the entire state

$$\psi^{\text{He}}_{\text{grd.}} = \frac{1}{\sqrt{2}} \left|1s(1)1s(2)\right\rangle \left(\left|\uparrow_1\downarrow_2\right\rangle - \left|\downarrow_1\uparrow_2\right\rangle\right), \tag{3.119}$$

has been reconstructed, taking account of normalization after the fact.

3.4.4 The First Excited State of the Two-Electron Atom

Before adding in another electron, it is useful to consider the first excited state of helium. For the first excited state, one electron must remain in the $1s$ orbital whilst the other can be in the $2s$ or the $2p$ orbital [93]. Although these states share the same principal quantum number, they have differing energies due to the contributions of the differences in screening of nuclear charge [98]. For simplicity, the $1s2s$ configuration shall be chosen. If left in this form it is problematic for describing an atomic state because the wavefunction suggests two distances from the nucleus, violating the indistinguishability of the electrons. In essence, a wavefunction that did not attempt to resolve this would produce a prediction that is itself impossible to verify. This means the wavefunction for the spatial component must be independent of the labels assigned to the orbitals, *i.e.*,

$$\hat{\mathcal{P}}_{1,2}\psi_{1,2} = \psi_{2,1} = \pm\psi_{1,2}, \tag{3.120}$$

where $\hat{\mathcal{P}}_{1,2}$ is the operator that permutes the labels.

Two satisfactory solutions come as linear combinations of the eigenfunctions of the Hamiltonian, which must therefore be themselves eigenfunctions [98],

$$\psi_{\text{sym.}} = \frac{1}{\sqrt{2}} \left(\left|1s(1)\,2s(2)\right\rangle + \left|2s(1)\,1s(2)\right\rangle\right), \tag{3.121}$$

$$\psi_{\text{asym.}} = \frac{1}{\sqrt{2}} \left(\left|1s(1)\,2s(2)\right\rangle - \left|2s(1)\,1s(2)\right\rangle\right). \tag{3.122}$$

The first of these is the symmetric spatial wavefunction and the second the anti-symmetric spatial wavefunction. Overall, the wavefunction of the full state, when it

includes spin, must be antisymmetric. This can of course be achieved in two ways; by multiplying the symmetric spatial wavefunction by the antisymmetric spin wavefunction or *vice versa*. However, as demonstrated in Eqs. (3.115)–(3.118), there are four possible spin states; three are symmetric and one is antisymmetric. The wavefunctions each satisfy the exclusion principle and are linearly independent written out as [98]

$$\frac{1}{\sqrt{2}}\left(|1s(1)\,2s(2)\rangle + |2s(1)\,1s(2)\rangle\right)|\uparrow_1\uparrow_2\rangle\,, \tag{3.123}$$

$$\frac{1}{\sqrt{2}}\left(|1s(1)\,2s(2)\rangle - |2s(1)\,1s(2)\rangle\right)|\downarrow_1\downarrow_2\rangle\,, \tag{3.124}$$

$$\frac{1}{\sqrt{2}}\left(|1s(1)\,2s(2)\rangle + |2s(1)\,1s(2)\rangle\right)\left(|\uparrow_1\downarrow_2\rangle + |\downarrow_1\uparrow_2\rangle\right), \tag{3.125}$$

$$\frac{1}{\sqrt{2}}\left(|1s(1)\,2s(2)\rangle - |2s(1)\,1s(2)\rangle\right)\left(|\uparrow_1\downarrow_2\rangle - |\downarrow_1\uparrow_2\rangle\right). \tag{3.126}$$

The first three wavefunctions form the triplet states of excited helium whilst the last is the singlet excited state. Being able to distinguish between the singlet and the triplets is usually a simple task, but being able to distinguish the triplet states is not always trivial. All four of these states are distinct and physical and are presented in Fig. 3.14.

These images are on a different scale to previous ones and so it is not instantly recognizable that the radius of the probability density is larger. However, with a clear reference this would demonstrate that the state is a $2s$ and the transparency focused in the centre indicating a $1s$ contribution. The singlet state is instantly recognizable and each of the triplet states is too, *cf.* Fig. 3.12. This visualization can distinguish, in a rather natural way, each of the possible first excited stated in this given spatial configuration. Of course the $1s2p$ configuration would be distinguishable as well, but being able to instantly separate out the triplet states is a remarkable feature. This visualization contains a significant amount of spin information that is normally lost. With this in mind it is worth exploring what this information can allow us to do in a slightly more complicated situation.

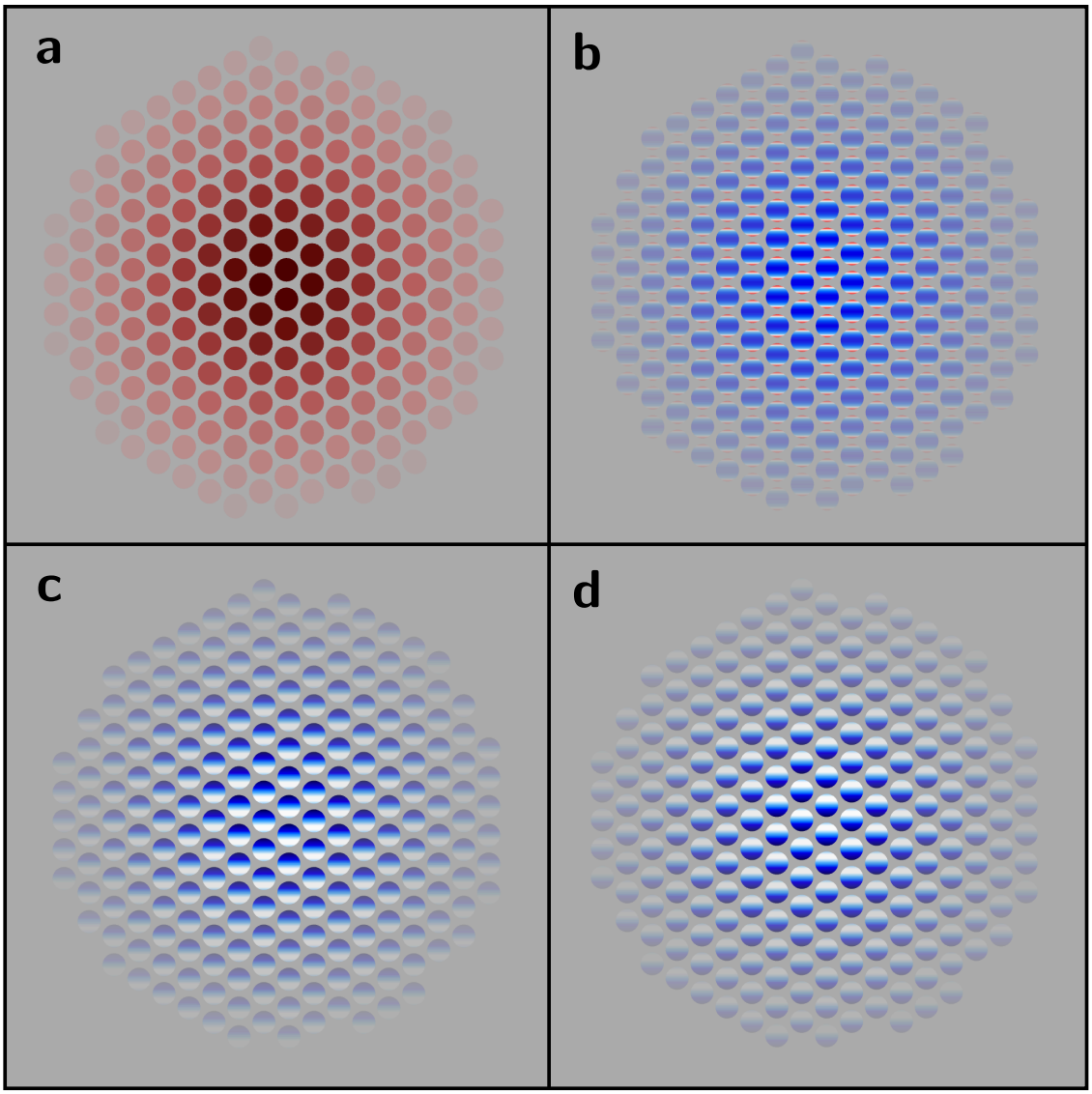

Figure 3.14: This figure shows the equal-angle slice, $\theta_1 = \theta_2 = \theta$ and $\phi_1 = \phi_2 = \phi$, of the Wigner function for the excited states of helium. (a) is the excited singlet state; (b) the first triplet state with magnetization quantum number $m = 0$; (c) the first triplet state with magnetization quantum number $m = 1$; (d) the first triplet state with magnetization quantum number $m = -1$. It is clear to see, with reference to Fig. 3.12 that there are spin-spin correlations here and it is easy to distinguish each of the triplet states with little effort. Note that white is zero, blue is positive and red is negative. Image and caption adapted from [90].

3.5 Lithium

Having established the use of this visualization in distinguishing states and getting spin-spin and spin-spatial degrees of freedom, it is useful to demonstrate what can be gained from an example. To do this the order of this section shall be reversed. Instead of starting at the theory, it begins with the image of a three-electron system (although arguably this is not a piece of information required to be able to make the following deductions). To aid analysis, the relevant three-spin states are presented in Fig. 3.15 and the system is presented in Fig. 3.16 across four different slices.

The reason that there are a number of images in this case, is that the system has more than two-electrons and therefore the structure will not be as simple as the cases so far considered. The technique outlined above is followed; the transparency of the figures is determined by the probability density function, for those that use transparency, and a sphere is then plotted at each point. On the surface of that sphere is plotted the equal angle slice, where appropriate, reduced Wigner function for the spin degrees of freedom.

In Fig. 3.16 (a) is the reduced Wigner function for only one set of spatial degrees

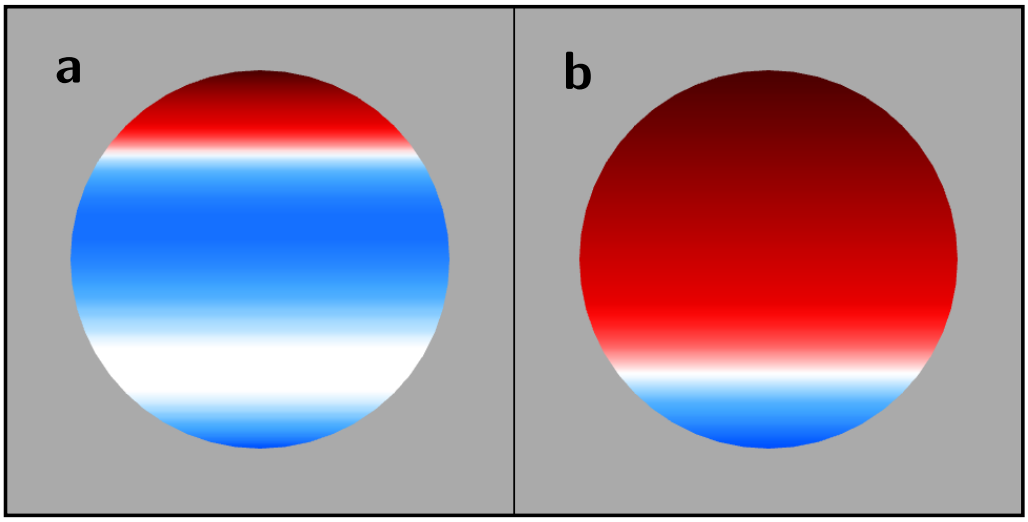

Figure 3.15: This is a set of reduced Wigner functions for the spin states for the three-electron atom that are relevant to the states considered in this section. The states shown are (a) $|\uparrow\downarrow\uparrow\rangle$ and (b) $|\uparrow\rangle(|\uparrow\downarrow\rangle$ - $|\downarrow\uparrow\rangle)$. Note that white is zero, blue is positive and red is negative.

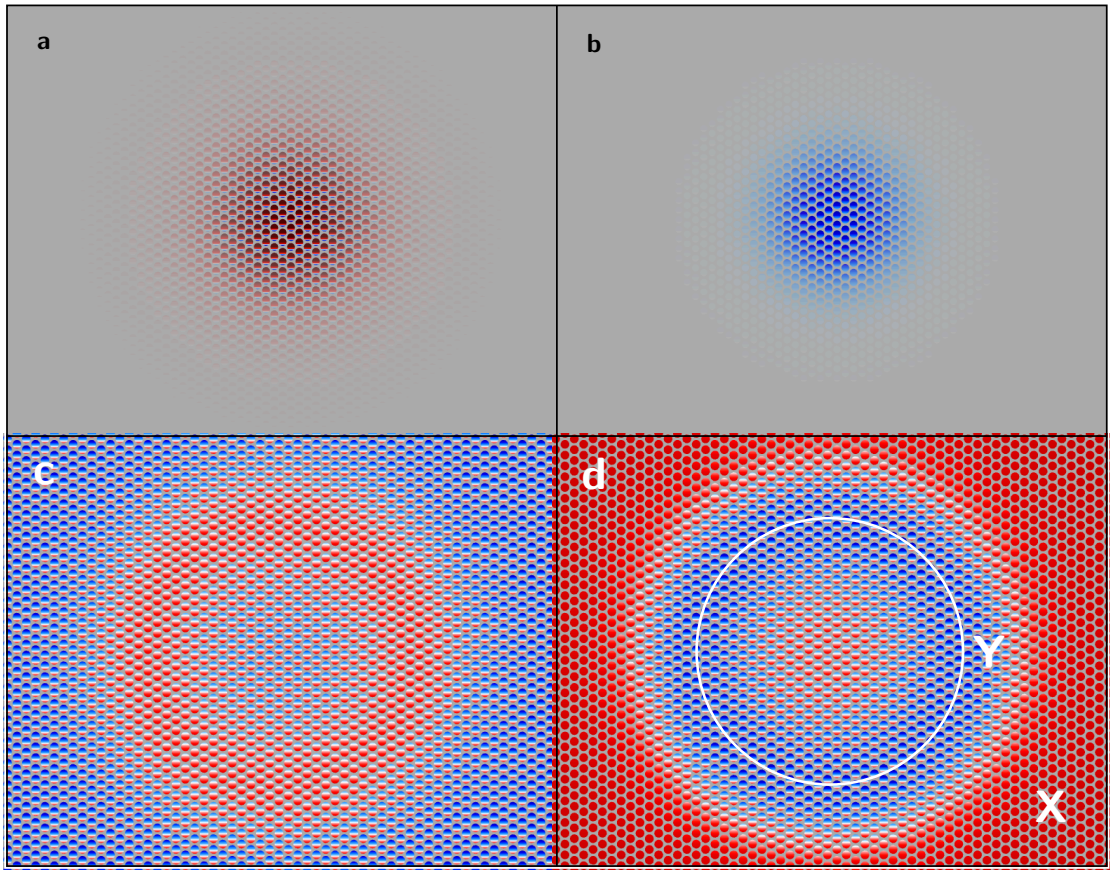

Figure 3.16: This is a selection of slices for the three-electron atom, lithium, that display a set of different features. The images here are again on different scale to previous images to account for the $2s$ orbital. As before, the transparency is an indication of the probability density function and all momentum degrees of freedom have been integrated out. The full states visualized are presented in the main text along with an important reconstruction of the state through inspection. The key features of each image are that (a) shows the overall spin state of the atom. (b) allows the electron spin density to be determined, indicating that there is an overall magnetic moment. (c) and (d) do not have the transparency turned on, so there is no direct visualization of the probability density function, but the more complex aspects of entanglement can be explored. Together they allow a determination to be made about the structure of the three-electron atom and is explored fully in the main body. Note that white is zero, blue is positive and red is negative. Further, the point X and ring Y are included for discussions in the main body. Image taken from [90].

of freedom and all spin degrees of freedom. The feature that is most prominent in this image is that the spin state matches that in Fig. 3.15 (b), *i.e.*, it is a three-spin entangled state. The reduced Wigner function plotted in Fig. 3.16 (b) is one set of spatial degrees of freedom and one set of spin degrees of freedom. This shows the overall electron spin density of the state. This indicates an overall magnetic moment in the positive z-direction, due to the preponderance of blue in that direction.

The remaining two images are plotted without the transparency turned on. This means that the visualization is being used to deduce structure and spin information only. Having removed the transparency, it is easy to see that the quantum correlations in this state are not as trivial as they appear in the first two images. Figure 3.16 (c) and (d) both show a reduced Wigner function for one set of spatial degrees of freedom and two spin degrees of freedom. The spin degrees of freedom are what are most important in these images. In Fig. 3.16 (c), the spin degrees of freedom consist of the ones that match the same label as the spatial component of the reduced Wigner function and one other set, due to indistinguishability it does not matter which. Essentially, the reduced Wigner function is $W_{\text{Red.}}(\boldsymbol{q}_1, \theta_1, \phi_1, \theta_2, \phi_2)$. In Fig. 3.16 (d), neither set of the remaining spin degrees of freedom correspond to the spatial degrees of freedom.

Considering the two together, at point X in Fig. 3.16 (d), when the electron associated with the spatial degrees of freedom is likely to be in the $2s$ orbital, the spin state of the other two electrons is the singlet state. At a similar point in Fig. 3.16 (d), the state is similar to the spin-up state. This would suggest that an electron found in the region dominated by the $2s$ orbital, is likely to be in the $|\uparrow\rangle$ state with the other two electrons forming a singlet state. This is consistent with the spin state $|\uparrow\rangle\left(|\uparrow\downarrow\rangle - |\downarrow\uparrow\rangle\right)$ as shown in Fig. 3.15 (b).

The node of the $2s$ orbital is clearly represented in these images. The ring Y in Fig. 3.15 (d) sits in the node over a set of spin states that are similar to the spin-up state. This would imply that if the electron associated with the spatial degrees of freedom is found there, it cannot be in the $2s$ orbital and one of the

other electrons is likely to be in the $|\uparrow\rangle$ state. Given the shape of the probability density function, it is reasonable to suggest that it is a combination of s-orbitals, so when the electron is not in the $2s$ it is reasonable to suggest it is instead in the $1s$. Therefore we can deduce that when an electron is found in the $1s$ orbital, one of the other electrons is in the spin-up state. Also, using Fig. 3.15 (c), an electron found in the $1s$ is likely to be in the singlet state. Collecting all of this together, these two pictures produce a state of the form $|2s1s1s\rangle\left(|\uparrow\downarrow\rangle - |\downarrow\uparrow\rangle\right)|\uparrow\rangle$. However, using Pauli's exclusion principle, the pictures must be invariant under cyclic permutation of the indices and so the state for this three-electron system must be

$$\begin{aligned}|\psi\rangle = \frac{1}{\sqrt{6}}\big[\,&|1s(1)1s(2)2s(3)\rangle\left(|\uparrow_1\downarrow_2\rangle - |\downarrow_1\uparrow_2\rangle\right)|\uparrow_3\rangle + \\ &|1s(1)2s(2)1s(3)\rangle\left(|\downarrow_1\uparrow_3\rangle - |\uparrow_1\downarrow_3\rangle\right)|\uparrow_2\rangle + \\ &|2s(1)1s(2)1s(3)\rangle\left(|\uparrow_2\downarrow_3\rangle - |\downarrow_2\uparrow_3\rangle\right)|\uparrow_1\rangle\,\big],\end{aligned} \tag{3.127}$$

taking account of normalization.

This state has a variety of different correlations that are usually lost. The spin-spin correlations immediately evident in the spin states as well as spin-spatial correlations which are evident from the way the spin state changes dependent on where an electron is found. All these correlations are visible in a simple set of pictures using this visualization technique. Given that, using only the visualization, the state has been deduced, it will now be analyzed from the theoretical framework to ensure all information has been noted.

3.5.1 Slater Determinants

The three-electron atom, as was the case with helium, is often introduced with an element of simplified logic. The electrons are added one-by-one, the first goes into the $1s$ orbital as spin-up, the second into the same orbital but with opposite spin as dictated by the Pauli exclusion principle. The third can no longer go into the $1s$ orbital as it is fully occupied and so it must go into the next energy level. a natural

choice is for this electron to go into the $2s$ orbital as spin-up for example. The real configuration, as for helium, is not quite as simple for lithium.

The tedious process that was followed in order to obtain the wavefunction for helium could be followed, however there is a simpler way. It is the use of Slater determinants which allow the formation of an antisymmetric wavefunction in conformance with the Pauli exclusion principle. In order to demonstrate that it work, the state of helium shall first be reproduced using this method.

For the ground state of helium, the Slater determinant gives the wavefunction

$$\psi^{\text{He}}_{\text{Grd.}} = \frac{1}{\sqrt{2}} \begin{vmatrix} |1s\rangle_1 |\uparrow\rangle_1 & |1s_1\rangle_1 |\downarrow\rangle_1 \\ |1s\rangle_2 |\uparrow\rangle_2 & |1s_1\rangle_2 |\downarrow\rangle_2 \end{vmatrix} \tag{3.128}$$

$$= \frac{1}{\sqrt{2}} \left[|1s\rangle_1 |\uparrow\rangle_1 |1s_1\rangle_2 |\downarrow\rangle_2 - |1s_1\rangle_1 |\downarrow\rangle_1 |1s\rangle_2 |\uparrow\rangle_2 \right] \tag{3.129}$$

$$= \frac{1}{\sqrt{2}} 1s(1)\, 1s(2) \left(|\uparrow_1 \downarrow_2\rangle - |\downarrow_1 \uparrow_2\rangle \right), \tag{3.130}$$

as expected, separable into a symmetric spatial state and a singlet spin state [98]. This determinant has been constructed by placing all the states for one electron's co-ordinates on each row in the same order.

This can be generalized to the n-electron system. That is, n orthogonal basis states $\psi_i(j)$ are available, where $i = 1, \ldots, n$ labels the orbital (including spin) and $(j) = (1), \ldots, (n)$ are the electron with which the spatial and spin coordinates are associated. The Slater determinant is then

$$\psi(1, \ldots, n) = \frac{1}{\sqrt{n!}} \begin{vmatrix} \psi_1(1) & \psi_1(2) & \cdots & \psi_1(n) \\ \psi_2(1) & \psi_2(2) & \cdots & \psi_2(n) \\ \vdots & \vdots & \ddots & \vdots \\ \psi_n(1) & \psi_n(2) & \cdots & \psi_n(n) \end{vmatrix}. \tag{3.131}$$

The following discussion has been adapted from Ref. [90]. Using this generalization the Slater determinant, and thus a physical wavefunction, for the ground state

of lithium is

$$\left|\psi^{\text{Li}}_{\text{Grd.}}\right\rangle = \frac{1}{\sqrt{3!}}\begin{vmatrix} |1s(1)\rangle\,|\uparrow_1\rangle & |1s(1)\rangle\,|\downarrow_1\rangle & |2s(1)\rangle\,|\uparrow_1\rangle \\ |1s(2)\rangle\,|\uparrow_2\rangle & |1s(2)\rangle\,|\downarrow_2\rangle & |2s(2)\rangle\,|\uparrow_2\rangle \\ |1s(3)\rangle\,|\uparrow_3\rangle & |1s(3)\rangle\,|\downarrow_3\rangle & |2s(3)\rangle\,|\uparrow_3\rangle \end{vmatrix}, \tag{3.132}$$

yielding,

$$\begin{aligned} \left|\psi^{\text{Li}}_{\text{Grd.}}\right\rangle = \frac{1}{\sqrt{6}}[&|1s(1)1s(2)2s(3)\rangle\,(|\uparrow_1\downarrow_2\rangle - |\downarrow_1\uparrow_2\rangle)\,|\uparrow_3\rangle \\ &+ |1s(1)2s(2)1s(3)\rangle\,(|\downarrow_1\uparrow_3\rangle - |\uparrow_1\downarrow_3\rangle)\,|\uparrow_2\rangle \\ &+ |2s(1)1s(2)1s(3)\rangle\,(|\uparrow_2\downarrow_3\rangle - |\downarrow_2\uparrow_3\rangle)\,|\uparrow_1\rangle] \end{aligned} \tag{3.133}$$

or

$$\begin{aligned} = \frac{1}{\sqrt{6}}[&|\uparrow_1\uparrow_2\downarrow_3\rangle\,(|2s(1)1s(2)\rangle - |1s(1)2s(2)\rangle)\,|1s(3)\rangle \\ &+ |\uparrow_1\downarrow_2\uparrow_3\rangle\,(|1s(1)2s(3)\rangle - |2s(1)1s(3)\rangle)\,|1s(2)\rangle \\ &+ |\downarrow_1\uparrow_2\uparrow_3\rangle\,(|2s(2)1s(3)\rangle - |1s(2)2s(3)\rangle)\,|1s(1)\rangle]. \end{aligned} \tag{3.134}$$

Although in a truly physical system the ground state of lithium is the linear superposition of Slater determinants, only this one shall be considered. Note the difference in the Slater determinants is the spin orientation of the final allowed state, *i.e.*, it goes from $|\uparrow\rangle$ to $|\downarrow\rangle$. From Eq. (3.133), it is clear that there is bipartite entanglement between the spin degrees of freedom; the spins are in the singlet state. However, there is also a non-trivial amount of spin-spatial entanglement in the combining of these spin states. Entanglement such as this could be an important factor in determining physical and chemical properties [17, 95–97, 101]. Therefore, being able to get a grasp of such phenomena without necessarily analyzing the full mathematics would be of tremendous value.

To do this the technique is considered once again. Lithium's Wigner function is 24-dimensional, the usual eight dimensions for each electron, but this time there also needs to be a certain amount of slicing. When the momentum degrees of freedom

have been integrated out there are still 15 dimensions left. This means that to get a clear, and understandable, set of images different slices must be taken in order to create the full picture. Slices with multiple spin degrees of freedom, use the equal angle slice for plotting. Note that other slices can be chosen to pull out other features of the state.

In Fig. 3.16 (a), the spatial degrees of freedom $\boldsymbol{q}_2$, and $\boldsymbol{q}_3$ have been integrated out. This leaves the reduced Wigner function $W^{\mathrm{Li}}_{\mathrm{Grd.}}(\boldsymbol{q}_1, \theta_1, \phi_1, \theta_2, \phi_2, \theta_3, \phi_3)$. The function behaviour at the origin of this image is similar to that displayed in Fig. 3.15 (b). It is important to note that the state differs from Fig. 3.15 (b) because what is shown is not itself pure. The reason for it being mixed (not pure) is that this is a single slice of the full Wigner function with entangled degrees of freedom integrated out. Points far from the origin tend towards the pure variation of Fig. 3.15 (b), where an electron is in the up state and likely to be found in the $2s$ orbital. This slice is consistent with the description of lithium as a singlet state in the $1s$ orbital coupled with a spin up in the $2s$ orbital. Emphasis should be placed upon the fact that state is not the one in Fig. 3.15 (a) which is the spin state that would be obtained from a simplified introduction. As with the ground state of helium, this visualization forces a departure from the standard discussion about atomic states.

Figure 3.16 (a) is a plot of the reduced Wigner function $W^{\mathrm{Li}}_{\mathrm{Grd.}}(\boldsymbol{q}_1, \theta_1, \phi_1)$. This slice gives insight into the electron spin density, revealing the magnetization of lithium. There are no negative values in this plot as a sufficient amount of entanglement information has been integrated out. This is consistent with the analysis before any theory was considered, but is compatible with all the theory discussed.

Figure 3.16 (c) shows the equal-angle slice for the reduced Wigner function given as $W^{\mathrm{Li}}_{\mathrm{Grd.}}(\boldsymbol{q}_1, \theta_1, \phi_1, \theta_2, \phi_2)$. The region dominated by red is the node of the $2s$ orbital and implies that if the electron associated with $\boldsymbol{q}_1$ is found here it is likely to be in a singlet state. Figure 3.16 (d) is the equal-angle slice of the reduced Wigner function $W^{\mathrm{Li}}_{\mathrm{Grd.}}(\boldsymbol{q}_1, \theta_2, \phi_2, \theta_3, \phi_3)$. It is seen that if the electron associated with $\boldsymbol{q}_1$

is far from the origin, the other two electrons are likely to form a singlet. By forming a singlet the electrons have high probability of being in the same orbital, the $1s$ orbital. Furthermore, where the $2s$ contribution is close to zero, there is little contribution from the singlet state indicated by the lack of negative values in the Wigner function. Hence, the electrons associated with $\boldsymbol{q}_2$ and $\boldsymbol{q}_3$ are not likely to be in the same orbital at these points.

Putting all this together the state is consistent with the Slater determinant found above. Further, the discussion is identical in some ways to the one carried out prior to theoretical discussion of the state. The complex entanglement that exists between the spatial-spin and spin-spin degrees of freedom in the three-electron atom can all be extracted from these slices.

3.6 Conclusions

This chapter has laid out the basic technique that this visualization relies upon. It has demonstrated that it is possible to visualize various forms of atomic entanglement in an accessible way. Beginning with the standard textbook visualization, the technique has built slowly up to explore how each of these features manifests. The hydrogen system allowed exploration of the visualization in a standard spin state before addressing spin-orbit coupling. In the ground state and excited states of helium, spin-spin entanglement was explored to demonstrate how easy pulling out such information is. Finally, a complex hybrid of spin-spin and spin-spatial entanglement was explored in lithium. Although the number of slices increased, the logical process of analyzing these pictures allowed recovery of the state with little more than some reference states.

Chapter 4

Simulated Atoms

Having established that the visualization that has been developed can display the quantum aspects of atomic states, the technique is adapted to interface with another software. The theoretical underpinnings of much of what is in the previous chapter is a crude approximation in comparison with the sophistication of quantum chemistry simulations. This is highlighted so as to assure the reader that the chapter was more a proof of concept than a realistic demonstration of utility. That being said, the correlations that were exposed using the technique should not be underestimated. The visualization has proven to be highly useful at portraying spin-spin and spin-spatial correlations. Such correlations are then highlighted and assessed such that full recovery of the original states was observed.

In this chapter, the technique is applied to a variety of states that are the result of quantum chemistry simulations. Such states are very good approximations to realistic systems and are the current standard of chemistry simulations. This means that the energies of these states are very close to those found in experiment. However, due to the constraints of computational approaches, the spin information is often not properly assessed. This is because most approximations do not include all electron-electron interactions which is necessary for the subsequent consideration of spin-spin entanglement. An overview of the software that can be used to create such states is presented followed by a proper assessment of the resultant states in the chosen software. The results of chemistry simulations are then plotted and analyzed.

These models may still seem crude, but the technique exposes certain features of the models. It also suggests potential problems with such simulations when trying to understand states that depend upon spin-spin and spin-spatial correlations for their energies.

4.1 Software

The software used for running quantum chemistry simulations in this thesis is COLUMBUS quantum chemistry software. Although originally developed in the 1980s at Ohio State University, it has been much expanded and adapted to deal with modern techniques. One key feature is that this system has been developed to communicate *via* files, which means that adding in extra functionality is trivial if they share, or can communicate *via*, the same data. With this in mind, the idea of creating a visualization tool that can automatically adapt the output of a COLUMBUS simulation is what has driven much of this chapter. COLUMBUS is used in a variety of fields to simulate chemical systems. The main purpose of many of these systems is to calculate the energy states of particular systems to inform experiment or to be able to model the evolution of a system. The output is a collection of data which can be used to analyze the behaviours in a system and compared to other simulations.

The basic use of COLUMBUS here is to calculate atomic orbitals, or molecular orbitals, as a basis for constructing more complex systems. Another key feature, is the ability to include spin-orbit coupling as well as other spin degrees of freedom into the calculations. The software achieves simulation of systems *via* a number of different techniques, such as standard Hartree-Fock methods of calculating atomic energies to high-order perturbation theories for modelling atoms, which could be compared using the final visualization. Within this thesis each simulation has been done using the same technique; a multi-configurational self-consistent field method with subsequent spin-orbit considerations. The details of this method is beyond the scope of this thesis.

The key motivation for using COLUMBUS is that it is highly adaptable and extendable but provides very simple basis states from which to test the utility of a visualization tool. Given the simplicity of the systems in this thesis, the real outcome of this chapter will be to determine the accuracy of a quantum chemistry simulation with regards to correlations between spin and other degrees of freedom. This level of detail will be necessary for understanding how to create materials atom-by-atom, the creation of bonds or any fundamental chemical process which depends upon energy levels heavily related to spin degrees of freedom. It is only with the current advances in quantum chemistry that such issues have begun to arise. For instance, the use of quantum techniques within the area of drug creation is now being held back by the inaccuracies of chemical simulations is a problem that could begin to be addressed with this visualization tool [121]. This is because a visualization tool would allow probing of spin correlations in different parts of the system to ensure the correlations are properly calculated.

4.1.1 Output

Although a full exploration of the technique used in the software is not appropriate here, consideration of the output is. A number of different mechanisms for producing output could be used but the one used here seems to be the simplest method for obtaining data from the simulations. Although, in practice, these may not be the forms that are used and deeper more high-level simulations would replace them, they are a sufficient example of the level of detail that these simulations achieve.

If we take one of the spin-orbit coupled states, then the output of the simulation for one particular state is the following:

```
total energy(6) = -0.1244261891

                            level       1   2    3
                            orbital     37  43   44
                            symmetry    au  bu   bu
 path   s  ms  csf#  c(i)       ext. orb.(sym)
```

```
z*     3  2  1     -0.214513          +                +
z*     3  3  2      0.536020          +                +
z*     1  1  3      0.214513             +             -
z*     3  1  4     -0.536020             +             +
z*     1  1  5      0.536020                   +       -
z*     3  1  6      0.214513                   +       +
```

This file describes the coefficients associated with a basis of Gaussian orbitals. Superposing these orbitals with the coefficients create the final result of the simulation. However, there are a number of rules contained within the documentation for Columbus to explain how this should be interpreted. For instance the state indicated by 1 1 (the `s` and `ms` values respectively), is what we will replace with the spin down state, $|\downarrow\rangle$. Similarly, for the remaining states $3\,1 \rightarrow \mathrm{i}\,|\downarrow\rangle$, $3\,2 \rightarrow |\uparrow\rangle$ and $3\,3 \rightarrow \mathrm{i}\,|\uparrow\rangle$. These correspondences are to ensure that the state matches the convention already established, *i.e.*, the $|1/2, 1/2\rangle$ p-orbital is spin-up along the z-axis. The levels indicate which energy we are dealing with whilst the orbital indicates which should be selected from the Molden file.

Although the simulation produces this data, which tells us how to construct the state that we have asked for, this state is formed of the series of molecular orbitals which are contained within the Molden file. The Molden file contains a series of Gaussian orbitals, determined to an accuracy set by the user, and forms the basis states for the simulation. These Gaussians are then superposed and multiplied by a relevant spherical harmonic to produce the same effective distribution as a real atomic orbital. This process is a standard way of modelling atomic systems and is analogous to the creation of the Fock basis in the previous chapter.

This series of atomic orbitals are then combined in a variety of ways to produce the effective state in the main simulation. For instance, the orbital 37 corresponds to the p_z-orbital, 43 corresponds to p_x and 44 corresponds to p_y. These could be denoted as any combination of the three p-orbitals, as it depends only the orientation of the axis of the system. But for our purposes, this was the convention used so that

the state matched the axis of the visualization. The code for converting the Molden files into orbitals is presented in Appendix A along with applications to this data.

It is worth noting that COLUMBUS produces twice as many states as needed. In fact, it produces states in pairs with one being i times the other. This is not of particular use, or of interest here, however the reason we therefore only have three unique states, instead of six in the case of the p-spin-orbit coupled states, is due to the symmetry in the space, so it only calculates half of the space. It is also worth noting, that the state produced from the data above, is simply the corresponding spin-orbit coupled state that we would expect multiplied by some global phase factor. This makes no difference to the visualization, but would make some differences in the case that phase were important. This is true for all the states that we calculated, they are simply multiplied by some global phase factor but are essentially the same states. This is worth noting because it demonstrates how good the approximation we initially used is.

4.2 Visualisation of Spin-Orbit States

Each of the basis states can be plotted from the Molden file using the code in Appendix A. These are not particularly insightful, but demonstrate that they exactly match the basis states that you would expect. Their orientation has been adapted to match the visualization that is being used throughout the rest of this thesis. The s-orbitals for hydrogen are also uninteresting, in as much as they map exactly onto the states from the approximation and are exactly what you would expect. Interestingly, the first states that are not what you would expect, are the p spin-orbit coupled states. Although these are well understood, the simulation produces states which are noticeably different from the approximation.

This is mainly due to the fact that the states are superpositions of the spin-orbit coupled states one would normally work with. In itself this is not a problem, the states are perfectly acceptable for describing the system due to the fact they are simply superpositions of eigenstates of all of the relevant operators. For hydrogen,

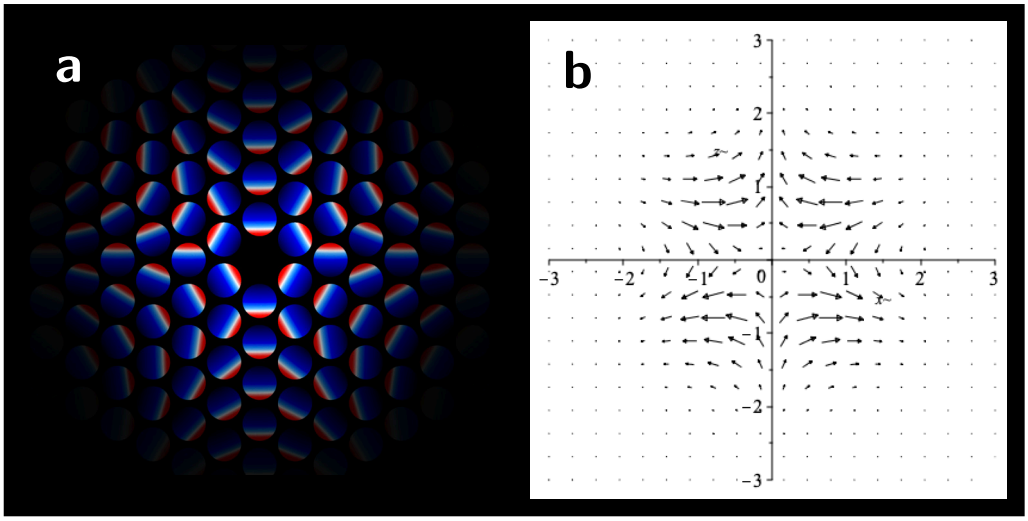

Figure 4.1: The zero orbital-angular momentum state that is produced from COLUMBUS. It is a spin-orbit coupled p-orbital and has spin-spatial correlations. Panel (a) shows the method developed within this thesis whilst panel (b) shows the same state but using arrows to represent the spin direction. From the visualization it can be identified as identical to a state from the previous chapter, the $|1/2, 1/2\rangle$ p-orbital for hydrogen. Closer analysis of the data for the state determines that it has been scaled by a complex global factor and thereby not making the state substantially different. This confirms that the simulation can deal well with single electron spin-spatial entanglement. Note that white is the zero colour, blue positive and red negative.

the single electron atom, of course this is rather easy to draw comparisons. The outcome of the p spin-orbit coupled states are presented in subsequent figures. As before, note the fact that there are only three unique states in this situation because only half of the space is covered due to symmetries.

The most relevant point to take note of is the fact that the zero angular momentum state is scaled by some global factor. In this case,

$$\psi_1 = (0.2 - 0.5\,\mathrm{i}) \left|\frac{1}{2}, \frac{1}{2}\right\rangle, \tag{4.1}$$

where ψ_1 is the state that is the result of the simulation. Looking at the spinor accompaniment to the visualization picture in Fig. 4.1 (b), it is clear that the two states are equivalent. Direct comparison with the images in the previous chapter demonstrate that the only thing that could have changed is the global phase. This has no effect on the visualization and does not change the state in a way in which

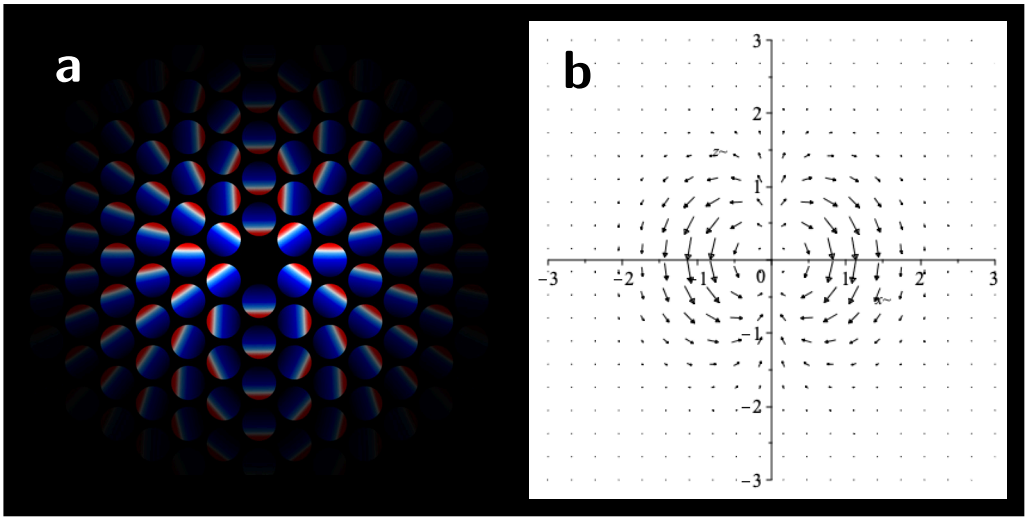

Figure 4.2: One of the non-zero orbital-angular momentum states that is produced from the chemistry simulation. Breaking this state down into its constituent parts is much more difficult. However, knowing the type of state the simulation was supposed to produce we can use the p-orbitals as a starting point. These would indicate that this state is a combination of a state that has spins in many orientations and one in which the spins are in one direction so as to rotate all of the spins. After careful analysis these can be determined as $|3/2, -3, 2\rangle$ and $|3/2, 1/2\rangle$. Panel (a) shows the method developed within this thesis whilst panel (b) shows the same state but using arrows to represent the spin direction. Note that white is the zero colour, blue positive and red negative.

we need be concerned. Due to the fact that this state is scaled it is easy to find the factor; the remaining two states do not break down quite so nicely.

First, we obtain the state

$$\psi_2 = 0.9 \left|\frac{3}{2}, \frac{1}{2}\right\rangle - 0.5 \left|\frac{3}{2}, -\frac{3}{2}\right\rangle, \tag{4.2}$$

in Fig. 4.2. Comparing Fig. 4.2 (a) with its spinor representation in Fig. 4.2 (b) is again clear that the two match. Although slightly more difficult to spot, this is also in line with the spin-orbit coupled states in Eq. (3.67) to Eq. (3.72). The state $|3/2, -3, 2\rangle$ is spin-down everywhere. This means that the addition of this state to $|3/2, 1/2\rangle$ will be to rotate the spins in plane. Effectively, it will cause spins to be tended toward down where they were previously tending towards up. Along the axis there is no change as there is no contribution in the vertical axis from $|3/2, -3, 2\rangle$ and the states are equivalent along the horizontal.

A different way of considering how this state must breakdown is to consider how it compares with the pictures in Fig. 3.10. Given that the spins point in different directions away from the axis then it makes sense that one of the constituent states in the superposition is also of this form. Considering that the spin states are easily rotated, *cf.* the spin states that appear in the single electron examples (see Fig. 3.5), it could be determined that one of the states is one in which all of the spins point in a specific direction. Of course the way in which we break this down, due to the symmetries of the problem, is a matter of choice rather than a definitive solution. In this case, the choice was to identify the state with non-aligned spins first and then attempt to rotate the spins into the configuration seen in Fig. 4.2. This also leads to the same state, *i.e.*, that $|3/2, 1/2\rangle$ is superposed with $|3/2, -3, 2\rangle$ rotating the spins into the orientation above.

The reason that this is important, is that we have been able to use the output of the quantum chemistry simulation, the internals of which we have very little knowledge of, and are able to decompose it into states that we recognize directly from the visualization. This means that the tool that has been created, is not just about determining correlations within states. It can also be used to identify key features and break down complex states into simpler basis states. This is important when verifying that the output of a simulation matches the expectation of reality. Although the main focus is on being able to visualize the correlations easily, being able to check the output of the simulation in this way could prove valuable. The key advantage of course, being in the fact that studying the visualization is much easier than the output data files. For instance, it would be easy to spot any out-of-plane rotation that would bring the validity of the state into question.

Similarly, the final state is

$$\psi_3 = 0.5 \left| \frac{3}{2}, \frac{1}{2} \right\rangle - 0.9 \left| \frac{3}{2}, \frac{3}{2} \right\rangle , \tag{4.3}$$

which can be compared to the spinor representation in Fig. 4.3(b). As before, this state can be analyzed in a number of ways. Directly from the picture we can

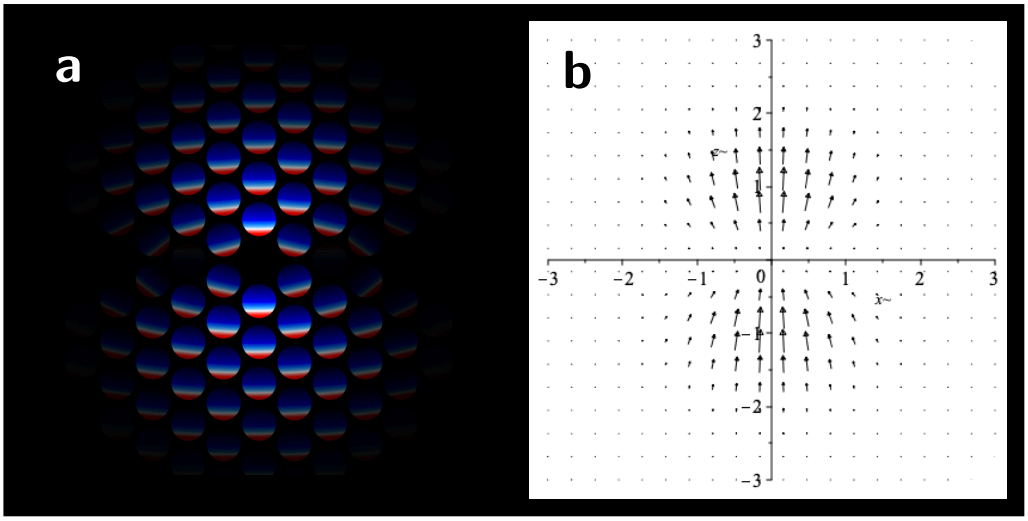

Figure 4.3: One of the non-zero orbital-angular momentum states that is produced from the chemistry simulation. Considering how this state breaks up is slightly more complicated than the previous state. This time we begin with the state that has spins predominantly in the up-state. Perhaps the easiest way of understanding this state is to consider it as having all spins pointing up and then being superpose with a state that rotates the spins differing amounts. These states are found to be $|3/2, 3, 2\rangle$ and $|3/2, 1/2\rangle$. The state disappearing along the horizontal axis although may be counterintuitive, is verified in the spinor representation of this superposition. Panel (a) shows the method developed within this thesis whilst panel (b) shows the same state but using arrows to represent the spin direction. Note that white is the zero colour, blue positive and red negative.

see a predominance of spin in the up-direction suggesting that it would be sensible to begin with a state in which all the spins are $|\uparrow\rangle$. The most obvious candidate, using Fig. 3.10, is the $|3/2, 3, 2\rangle$ state. It is also clear that the spins must be rotated away from the axis by a different amount. Therefore, the state with which we should form a superposition must be one in which the off-axis spins are not aligned. Given the form of the previous state, it could be quickly determined that this is likely to be $|3/2, 1/2\rangle$. The check this time, is less intuitive but can be verified as the state presented in Eq. (4.3).

As discussed before, the software only produces half the states needed due to symmetry. This also suggests that each superposition presented above is one way of creating each state and that they will have another form due to the symmetry within this space. That is to say that the simulation does calculate a complete set of states but given the symmetries each state shown here has an opposite one which differs

only in phase. Although states different to the theoretical approach used last time were produced, we have also demonstrates the ability of the visualization tool to be used to verify the output of the simulation. Each of these states can be decomposed into the p spin-orbit coupled states that were presented earlier. This gives some insight into how the simulation obtains a good approximation to the real world. As long as it takes superpositions of states with a similar energy, and then does not select or prefer one over the other, then the final state will be close to reality.

Moving up to the d spin-orbit coupled states the exact same features occur. For hydrogen, the states maintain this superposition feature, although the coefficient differ of course. This means that the simulation appears to be consistent for higher energy levels. It also means that the states that were explored previously, are a good attempt for modelling realistic systems. At this point, everything that was done for hydrogen has been recovered using a full quantum chemistry simulation with very little effort or adaptation. The Molden file is used to produce a set of Gaussian type orbitals which are then combined to produce molecular orbitals which are then combined to produce the state desired, in this case the spin-orbit coupled state of hydrogen. Therefore, this visualization tool is already at the stage that it could be integrated with such a piece of software and prove to be useful in explaining the details behind the calculation.

An interesting factor in modelling higher level systems, *i.e.*, systems with more electrons, is the fact that in order to keep the calculations reasonable, certain approximations are made. One such approximation, is the modelling of the inner electrons of an atom as a reduction of the electric charge of the nucleus [59]. In effect, this means that an atom with a single electron in the outer shell is modelled in an equivalent way to the hydrogen atom. The simulation takes account of the differences in energy, as well as the difference in size of such an atom. However, in the visualization the difference between the two pictures is not significant. That is to say, that unless a spatial scale is added to such figures, the two pictures, *i.e.*, that of the hydrogen atom in a d spin-orbit coupled state and that of an atom with a

single outer electron in an equivalent state, are indistinguishable.

Such an example is the yttrium atom, where the outer electron is considered to be in a d-orbital. The visualization produced from such a simulation is equivalent to the d-orbitals produced for the hydrogen simulation. This means that the approximation of simplifying the inner electron correlations, loses the detail needed for our visualization. In most cases, the concern of such a simulation is the energy of the final state and the orientation of the outer electron such that an understanding of how a bond could be formed is found. However, to fully explain the process by which such a bond may be formed, a full understanding of the internal correlations is needed. It is this that motivated the original consideration of the lithium atom in its full extent. That is to say the attempt to visualize the state with full spin-spin and spin-spatial entanglement information. To see how this extends to the quantum simulations this procedure is repeated.

4.3 Visualisation of Lithium

The data output for lithium is equivalent to that presented earlier, although of course due to the increase of electrons the '+' and '−' have extended forms. This time each '+' and '−' combination must indicate a three-spin state rather than a two-spin state as before. Again a simple substitution rule is used to create full state which is a linear combination of Slater determinants. This means that the state of lithium is analogous to the approximation made in the previous chapter. Although, given the inclusion of spin-orbit coupling within the simulation and the fact that it works to obtain atomic lithium rather than a model atom makes it much more realistic.

Given the intended application of this visualization, it is important that the data file could be used directly. Significant work has been put into producing a piece of software which could be added to the output of simulation software with this specific data format. The visualization produced from this software for the lithium spin-orbit coupled ground state is presented in Fig. 4.4. Choosing this state is intentional

because it is the easiest comparison with the state discussed in the previous chapter.

The first two reduced Wigner functions are only different in size to those found in the case of the earlier approximation. This reduction in size is simply due to the accuracy of the basis states being used to model the system. The omission of hydrogenic wavefunctions in the previous model, was accompanied with the acknowledgement that such differences would be subsequently found. However, this difference in size is not remarkable for our discussion. Instead, the focus is largely upon the states that form the state.

In Fig. 4.4 (a), the reduced Wigner function $W^{\mathrm{Li}}_{\mathrm{Grd.}}(\boldsymbol{q}_1, \theta_1, \phi_1, \theta_2, \phi_2, \theta_3, \phi_3)$ is presented. This again integrates out all momentum degrees of freedom, all position degrees of freedom but leaves everything else alone. Because of the nature of the data produced from the simulation, it uses the position representation, integrating out the momentum degrees of freedom has already been achieved. This figure shows the spin state of a single electron wherever it is found within the system. That is to say, that this tells us the overall correlation between all the electrons in the system. Interestingly, the correlation found is exactly the same as in the approximation indicating that these electrons have been treated in the same way and no entanglement information has been lost.

This is distinctly different to the model in which high-level atoms are treated, where the internal electrons are approximated as a shielding effect. In the case that such an approximation were made for lithium, a noticeable difference in this figure would be that the entanglement between all the electrons would not be equivalent to a state permutation of the total number of electrons in the system. Essentially, the fact that we have a spin state that is identical to the spin state for a specific three spin system is indicative of full spin-spin correlations being maintained.

In Fig. 4.4 (b), the reduced Wigner function $W^{\mathrm{Li}}_{\mathrm{Grd.}}(\boldsymbol{q}_1, \theta_1)$ is presented. This slice gives insight into the spin density of the system and demonstrates an overall magnetic moment in the up-direction. This again is consistent with what was found in the previous chapter. No difference in these two figures is of significant note.

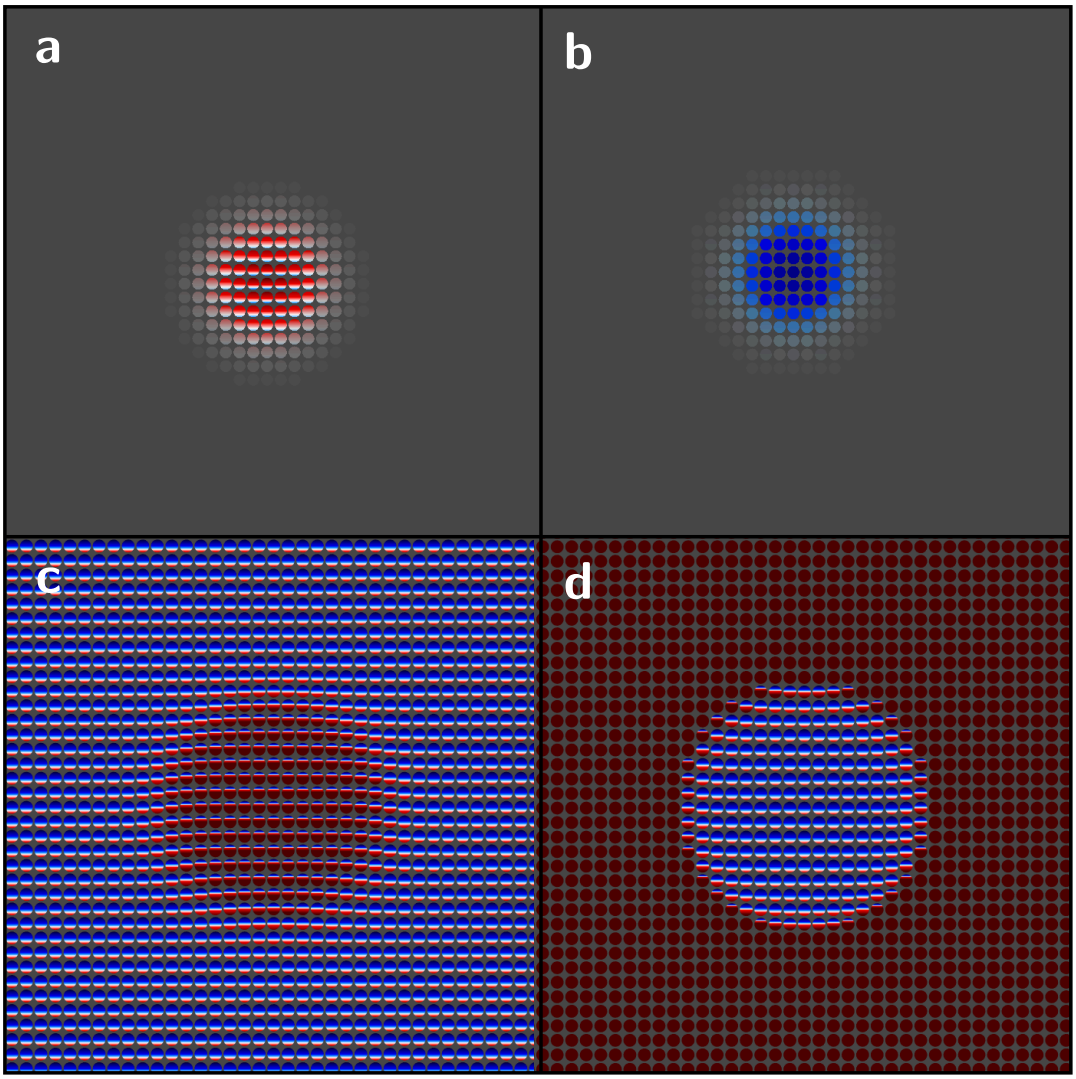

Figure 4.4: This is the set of images that can be produced for the spin-orbit coupled ground state of lithium that is outputted from the quantum chemistry simulation. It is immediately obvious that there are great similarities between these and those in Fig. 3.16. (a) is the reduced Wigner function for the position of one electron and all other spins $W^{\mathrm{Li}}_{\mathrm{Grd.}}(\boldsymbol{q}_1, \theta_1, \phi_1, \theta_2, \phi_2, \theta_3, \phi_3)$ and is consistent with the approximation in the previous chapter. (b) is the reduced Wigner function for the position and spin of a single electron $W^{\mathrm{Li}}_{\mathrm{Grd.}}(\boldsymbol{q}_1, \theta_1, \phi_1)$. As in the previous chapter, this demonstrates the magnetic moment of lithium and is in full agreement with the approximation. The state is somewhat smaller than in the previous chapter but this is due to the more accurate simulation. Note that the size of significant probability is smaller than previously due to the higher level of accuracy in this simulation. As before, (c) and (d) are $W^{\mathrm{Li}}_{\mathrm{Grd.}}(\boldsymbol{q}_1, \theta_1, \phi_1, \theta_2, \phi_2)$ and $W^{\mathrm{Li}}_{\mathrm{Grd.}}(\boldsymbol{q}_1, \theta_2, \phi_2, \theta_3, \phi_3)$ respectively. The overall form of these states is similar to before but is lacking the ring formation. This is because the model used earlier produces un-physically sized $1s$- and $2s$-orbitals. In this case, the node of the $2s$ means that instead of the ring, there is a circle which almost entirely indicates that the electron is in the $1s$-orbital. The circles in (c) and (d) Match the same state found inside the ring of previous approximation. Note that white is the zero point, blue is positive and red is negative.

These figures also demonstrates how spin-spin correlations can be determined from quantum chemistry simulation data files in an accessible way. As well as this, we also see the ability to pull out key physical properties of the system again using only the data files produced from the chemistry simulation. Having the ability to explore these visualizations at the end of a simulation, could easily provide information that is necessary for understanding the outcome of a particular reaction. All of this has been done using a relatively small number of example states and, once familiar, is very accessible.

As before, the remaining two figures must be discussed together. The first obvious difference in these two figures is the disappearance of the ring structure seen previously. This is simply an artefact of the approximation used for modelling the orbitals. Essentially, the previous model overestimated the significance of the $2s$ - orbital inside the node and underestimated, therefore, the dominance of the $1s$ in this region. There can be case put forward for the advantage of both of these overestimations but, crucially, this visualization can highlight the differences. Instead, here we find a dominating circle indicating the presence of the electron in the $1s$-orbital anywhere inside the node of the $2s$, *i.e.*, a negligible probability of being in the $2s$ at all points close to the origin.

Although this is a distinctive difference, it does not have a particularly large impact on the rest of the analysis. In Fig. 4.4 (c), far from the origin the state still tends towards spin-up. This indicates that if the electron is found in the $2s$-orbital it is likely that it is also in the spin-up state. Further, if it is found close to the origin, *i.e.*, inside the node of the $2s$, then the state tends toward a singlet state, though some element of spin-up remains. Contrastingly, in Fig. 4.4 (d), far from the origin the state tends towards the singlet state and internal to the node of the $2s$ tends towards spin-up. This indicates that if an electron is measured far from the origin, then the spin state of the other two electrons is likely to be the singlet. Further, if an electron is measured close to the origin then the spin state of the other electrons is likely to be spin-up. Similarly, from (c) if the electron is found far from the origin

then its spin state is likely to be spin-up and if the electron is found close to the origin then its spin state is likely to be in the singlet.

Due to the lack of nodal structure, this is as much as can be determined from these two figures. Notice, this is significantly less than in the approximation case and more readily suggests a state of the form $|2s1s1s\rangle\left(|\uparrow\downarrow\rangle - |\downarrow\uparrow\rangle\right)|\uparrow\rangle$. Accounting for Pauli's exclusion principle, the superposition state obtained from the Slater determinant is recovered. Interestingly, this argument is made much simpler by the removal of the nodal structure in the centre. However, we have again recovered the full state that is being observed simply by assessing the visualization produced from the data of the simulation. This is a clear benefit when the outcome of the simulation is unknown. There is no suggestion that in all cases you will be able to fully reconstruct the state, however being able to identify key physical features and then collate this information together could be helpful for describing the state.

The first image, (a), also reinforces the full spin-spin correlations that exist within the state. The subsequent images suggest the spin-spatial correlations that exist within the state. This visualization, prevents the omission of correlation information from being considered when trying to understand the properties of a state. It would be very easy, if given only two of these images, to assume that the state is two electrons in the $1s$-orbital in a singlet state and the other electron in a $2s$-orbital in a spin-up state as a rudimentary textbook explanation would have it. Collectively, this cannot be the state because of the spin-spin correlations in other images. This forces the final state as described above to be the only reasonable description. Given the potential use for explaining reactions and given the difference in energies for differently entangled state, maintaining these correlations is necessary. Looking directly at the data this information is sometimes lost because it is clear that there is a singlet and a spin-up, whereas using the visualization this information cannot be avoided.

4.4 Conclusions

The application of the visualization technique developed in the previous chapter should be of significant benefit to quantum chemistry simulations for the identification of states. The technique has been applied in different ways to verify the basis states with the system, to check for the reliability of spin orbit coupled simulations, to highlight differences when using approximations with regards to inner electrons and finally to do a full assessment of the lithium ground state. Each of these is important in the examination of the utility of such a technique.

The basis states used are far more accurate than in the previous model but the visualization is largely unaffected by such changes. The spin-orbit coupled states were reduced in number due to the symmetries used by the simulation, as well as being superpositions instead of the elegant theoretical states previously seen. It was, however, demonstrated that each of the states could be broken down into the theoretical states previously described. Further analysis was undertaken on the formation of the visualization to ensure that these superpositions made sense. It was also indicated that such a technique could be used in future to deconstruct states from the visualization alone.

The problem encountered with the yttrium atom, is one that is concerning when considering the applicability to high level atoms. The fact that the d-orbital is indistinguishable from the d-orbital of a hydrogen atom, due to the approximations made in the simulation, means that identifying this state is impossible. It is noted however, that this was a simplified simulation in order to verify the ability of the software to cope with atoms of a significant number of electrons. If spin-orbit coupling were included, and if a full analysis given, this problem may disappear. However, it highlights the importance of verifying approximations in quantum chemistry simulations with regards to spin and spatial correlations that exist within a system.

Finally, the lithium atom was re-examined using a spin-orbit coupled simulation. The accuracy did reduce the size of the reduced Wigner function, in terms of the

region of significant probability, but this had little effect on the visualization. It also removed some of the artefacts of the simplified model which did not consider hydrogenic functions. The four images produced from the visualization for this state, were again sufficient to fully reconstruct the state with all spin and spatial correlations being considered. It was demonstrated how, with little effort, physical features can be derived from these pictures even if the full state were not to be then reconstructed. Coupled with the inclusion of all correlations, the utility of such a visualization at the end of a simulation is embodied in the ability to pull out the features discussed.

Overall, the visualization technique that was developed in the previous chapter has now been extended as a tool for analyzing the output of quantum chemistry simulations. Although currently rather crude, its ability to reconstruct various states as well as identify physical features should not be underestimated. Extending this to dealing with more complicated states, as well as considering how to account for certain similarities is the subject of the next chapter.

Chapter 5

More Complex Systems

The development of the visualization technique from model systems to the output of quantum chemistry simulations was the focus of the previous chapters. Although concentrating on relatively simple systems, it has been demonstrated that the reconstruction of a complex state with many correlations is achievable. The reliability of this tool and the accessibility of the visualizations is necessary for its success. Further, the ability of this tool to be applied to more complex systems and demonstrate different physical effects, or chemical processes, is the future aspiration.

Given the future direction, one area of interest is quantum simulation. Modelling atomic interactions and examining how bonds are formed is a problem that may find a solution in quantum simulation [121]. Methods for designing drugs, and modelling their effects are highly complex due to the quantum nature of the systems. However, an analogous quantum system can sometimes be used to demonstrate evolution, resolving many issues. It is this fact that means extending this visualization to the domain of quantum information is necessary.

As quantum simulation is only useful when the technique is reliable and the verification simple, emphasis should be devoted to identifying key signatures of quantum correlations as well as the area of state verification. However, common tools like the reduced Wigner function suffer from a loss of entanglement information in the atomic simulations, such a tool removes information which could give deeper insight because of the removal of correlated degrees of freedom. In the case of the

simulations in the previous chapter, the loss of information meant that visualizations of different states are non-distinguishable. Here, the issue is that the reduced Wigner function loses correlations resulting in mixed states which are indistinguishable from the visualization.

Attempts to resolve this issue have led to a number of innovative approaches, for instance Ref. [43] used reduced CV Wigner functions in different Pauli bases to show Bell's inequality. Equally, adaptation to tomography methods for entangled hybrid systems that take account of these problems have been used [122]. Although approaches such as these give a better appreciation of the quantum correlations, they still only provide glimpses of the nature of the full quantum state. It is shown here how the visualization technique created can now be extended to provide insight to this area.

Exploring these issues and providing some solutions as well as exploring some of the other aspects of the visualization tool is the focus of this chapter. The subsequent extension of this tool to visualize molecules both from a theoretical and a simulated viewpoint is explored. A simple modification is shown to bring the visualization in line with the expectations of chemistry visualizations. To address the reliability and indistinguishability issues, it is necessary to develop slice selection and new techniques for exploring reduced Wigner functions more easily. Finally, the application of this visualization tool in the area of quantum information with regards to state verification is discussed.

5.1 Molecules

Beyond the case of high electron atoms, is the characterization of molecules and the way in which the bonds that hold them together form. Being able to predict the physical process of a chemical reaction, the simplest case being the process by which a bond forms, would be highly beneficial to areas within quantum chemistry such as drug simulation. To achieve this, full consideration of the quantum state of the molecule must be included in the model. This means that visualizing spin degrees

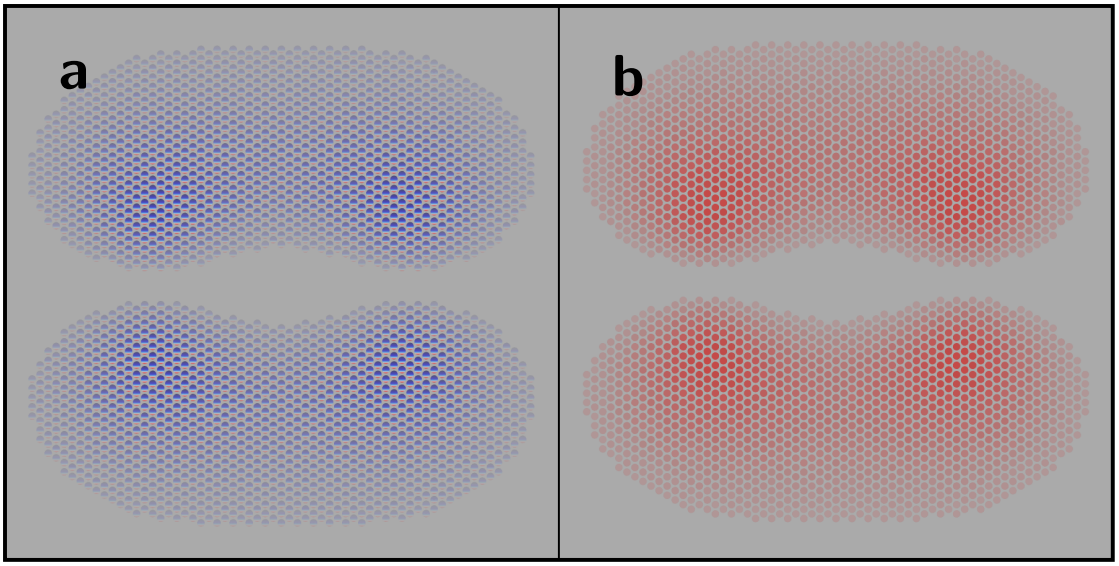

Figure 5.1: Simplified versions of single electron, (a), and double electron, (b), $\pi-$bonds in a p-bonded pseudo-molecule. Note that in the linear combination of atomic orbitals approximation the spatial components are identical, the states can only be visually distinguished through spin degrees of freedom – this difference is clearly seen in the Wigner functions displayed above. States where this distinction is important will arise often in organic chemistry. It should be noted that a full quantum mechanical calculation of real molecular bonds including terms from spin-spin, spin-orbit, electron-electron, nuclear interaction, other relativistic effects *etc.*, will have a substantial effect on the forms of these Wigner functions.

of freedom within the molecules is key to being able to analyze the process. Such an important case is illustrated in Fig. 5.1 which shows simplified versions of single electron, Fig. 5.1 (a), and double electron, Fig. 5.1 (b), $\pi-$bonds.

The spatial distribution of these two pseudo molecules are identical in the linear combination of atomic orbitals approximation [93]. The spin uniquely identifies them. The problem is that this type of bond, without the spin degrees of freedom, would appear identical but have different chemical properties. The distinction between these two states is highly important in many areas such as organic chemistry. The ability of each of these bonds to interact with other molecules and atoms is different and therefore their presence or absence in a system will affect the reactions. Being able to visually distinguish the two within a process would help provide explanations of where correlations exist at a specific point in time. This in turn could provide understanding for the underlying physical process. Furthermore, as quantum correlations may determine how certain parts of a molecule will

react [17, 94–96], such a visualization will aid understanding of such processes.

This example demonstrates the ability, as well as the necessity, for a visualization technique that is able to distinguish all correlations in a system. Being able to consider the evolution of states is more complex and the ability of this technique to identify correlations needs careful consideration. It is therefore necessary to explore whether this technique can adequately be used to analyze more complex states as well as an evolving process. However, the suitability of already established techniques such as the use of the reduced Wigner function, must also be examined. The purpose of the rest of this chapter is to address both of these concerns. Firstly, the inadequacies for displaying such information by use of the reduced Wigner function shall be demonstrated and, secondly, the ability of the signatures to identify complex quantum behaviour shall be presented.

5.2 State Verification

The ability to extend current simulation software with this visualization technique was demonstrated in the previous chapter. Throughout this thesis, a number of issues with the simulation of chemical systems have been highlighted as areas in which such a visualization could help. For example, as quantum chemistry needs greater insight to how information is shared across a large molecule in the development of drugs the use of quantum simulation becomes more appealing [121]. However, for quantum simulations to be useful, a reliable method of verifying and characterizing states is needed. Therefore, having established how the visualization can demonstrate correlations between the internal systems of an atom, or molecule, we now turn attention to the problem of verifying and characterizing states. This demonstrates how the visualization tool could provide insight for problems where the mechanism by which information is exchanged between systems is unknown such as the modelling of bond creation, avian compasses, photosynthesis process (PSI and PSII) and oxygen transport *via* haemoglobin in blood [65–70].

The following is joint work with Russell Rundle[1], and largely follows the work set out in Ref. [123]. It uses the same framework in Refs. [11, 76] and the visualization technique created in Ref. [90], as introduced earlier in this thesis. The visualization is adapted so as to better deal with the problem at hand, namely state verification in quantum systems. By use of the visualization it will be shown that this method reveals how quantum information is shared through correlations in light-matter type interactions. The purpose for this is that quantum correlations are important to many quantum technologies, such as hybrid two-qubit gates for quantum computers [124–127]. This is true regardless of whether these quantum correlations are found between macroscopically distinct superpositions of states, also known as Schrödinger's cat states, or in the entanglement between multiple systems. Currently, such technologies can be broadly categorized as being based on either continuous-variable (CV) or discrete-variable (DV) quantum systems.

A key feature of verification, will be to distinguish between both quantum and classical correlations, as discussed with the introduction of coherent Schrödinger's cat states in Chapter 2. Understanding the difference between their signatures is paramount to the efficacy of quantum technologies. Since what gives quantum technologies this advantage is the manifestation of quantum correlations. It is also shown that this method can characterize signatures that arise due to both quantum and classical correlations. The spatial side of the states so far considered, constitute a continuous-variable (CV) system and, as shown in Ref. [128], the Wigner function is particularly good at revealing correlations within such systems.

The spin side of the states so far considered, constitute a discrete-variable (DV) system, this is easily analogous to a qubit [125, 129, 130]. Little work has been developed for dealing with such systems but the two common approaches use informationally complete DV Wigner functions. Whereas the approach developed in Refs. [48, 49], use discrete degrees of freedom and has proven useful for quantum information. As discussed with the introduction of the visualization for spins, the

[1]Russell modelled and produced the states of interest and led the analysis. I developed the visualization tool and assisted in subsequent analysis.

approach used in this thesis uses continuous degrees of freedom analogous to the Bloch sphere [11, 53, 57, 60–62, 87]. Interest in DV systems has grown and the methods exploring such systems have been able to reveal correlations in a variety of situations, including the validation of atomic Schrödinger's cat states of up to 20 superconducting qubits [57, 73, 76, 131–134]. However, what has not been explored is the hybrid CV-DV systems. This is what is now addressed; the unexplored visualization of CV-DV systems and the way in which quantum information is shared between the two as an analogy of molecular information exchange.

The hybridization of CV-DV systems (referred to as hybrid states[2] in this thesis) is seen in the application of many quantum technologies, the key example being in quantum gate models for performing quantum computation [135–137]. Quantum correlations arising from this hybridization are commonly modelled within the framework of cavity quantum electrodynamics, describing it by two level quantum systems interaction with a single mode of a microwave field. Analyzing these interactions, within the framework of the Jaynes-Cummings model, allows a route to understanding the quantum information shared between the CV and DV system [138]. Therefore, the visualization method is further used to display the interaction within the Jaynes-Cummings model, giving new visual insight into how information is transferred between an atom and a field mode. Being able to understand these will be especially helpful for the advancement of quantum technologies, in particular quantum communication where CV-DV hybridization is used for teleportation entanglement distillation [136, 139–147].

5.2.1 Lambert Azimuthal Projection

A concern found throughout the previous analysis is the difficulty in observing the full DV state. So far this has not been a problem as the focus has not been on state verification but simply identification of the state. However, it should be noted that half of the function is hidden on the other side of the sphere in the images so

[2] This is not in the chemical sense of hybridization.

far produced. Of course, it should also be noted that the image produced on the computer is rotatable and so the production of the image is not limited to this view. The focus of state verification though, requires that all quantum correlations in a DV system be visible and it is therefore important that the entirety of the sphere is easily accessible. There are a number of ways of doing this, the easiest for paper format is to use a projection of the sphere onto a circle. Again, there are a number of ways of performing such a projection but an important feature of the one chosen is the fact that it is area preserving. The reason this is important is because we are dealing with a probability distribution function where, by definition, the integral over volume determines the probability; area preserving therefore translates into probability preserving. The projection used, therefore, is the Lambert azimuthal projection [148].

The Lambert azimuthal projection allows the entire surface of the sphere to be displayed as a circle. This projection maps the north pole to the centre of the disk and the south pole to the outer boundary. The equator of the sphere is projected onto a concentric circle with radius $1/\sqrt{2}$ times the radius of the entire circle. To make this more clear, some simple spin states have been presented in Fig. 5.2. The first thing to note is that, on the sphere, all of the states are rotations of each other but the outcome of the projection is that some regions of phase space have become warped. They are the same standard two-level quantum states displayed earlier in Fig. 3.5, where Fig. 5.2 (a) is spin up for the atom, Fig. 5.2 (b) is spin down for the atom and Fig. 5.2 (c) is the equal superposition of spin-up and spin-down.

This adaptation to the visualization of the spin Wigner function helps to make more information visually accessible. However, as before, the states considered here for verification will have a dimensionality higher than is convenient to plot. A similar approach to that used earlier, that is reducing the Wigner function in a suitable way, is used to give a full picture of the quantum correlations. For simplicity, the ground state of the CV system and the excited state of the DV system along with their product state is plotted in Fig. 5.3. In the context of quantum information, this is

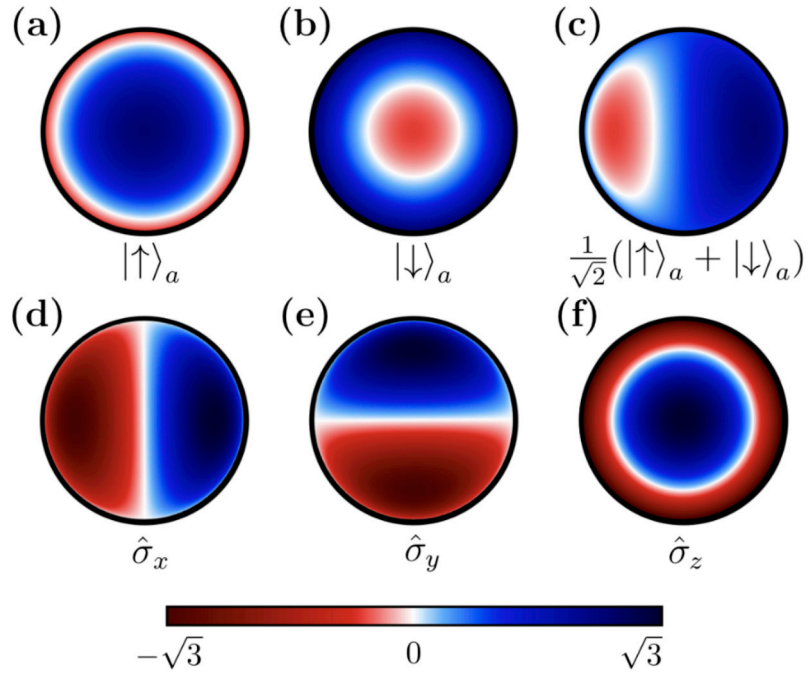

Figure 5.2: A replication of Fig. 3.5 is shown using the Lambert azimuthal projection where the sphere is mapped onto a circle with the north pole becoming the centre and the south pole the perimeter. Further, the projection is area preserving so that the probabilities are also preserving. The pure states are shown in (a) – (c), where (a) and (b) are the eigenstates of $\hat{\sigma}_z$, $|\uparrow\rangle_a$ and $|\downarrow\rangle_a$ corresponding previously to the electron spin, with eigenvalues ± 1 respectively. (c) is the equal superposition of the states in (a) and (b), $(|\uparrow\rangle_a + |\downarrow\rangle_a)/\sqrt{2}$. Also shown in (d) – (f) are the qubit Wigner functions of the three Pauli matrices, $\hat{\sigma}_x$, $\hat{\sigma}_y$, and $\hat{\sigma}_z$ respectively. These are shown for the benefit of future analysis.

a completely separable state formed of the vacuum state $|0\rangle_f$ (subscript indicates field) for the CV system and the $|\uparrow\rangle_a$ (subscript indicates atom) for the DV system.

The reduced Wigner function for the CV and DV systems are recognizable from previous images and provide little insight. The composite visualization, *i.e.*, the visualization of the full state $|0\rangle_f |\uparrow\rangle_a$, is created by dividing the CV phase space into discrete points on a rectangular map at which the DV Wigner function is produced and plotted using the Lambert azimuthal projection. The transparency of each disk is then set proportional to the maximum absolute value in the phase space at that point, $\max_{\theta,\phi} |W_{\hat{\rho}}(\alpha, \theta, \phi)|$. Note, this is a deviation from the previous chapters where the transparency was set proportional to the absolute value of the CV Wigner function. The reason for this is that the states subsequently considered require a more detailed visualization to be able to see the correlations that manifest. If the

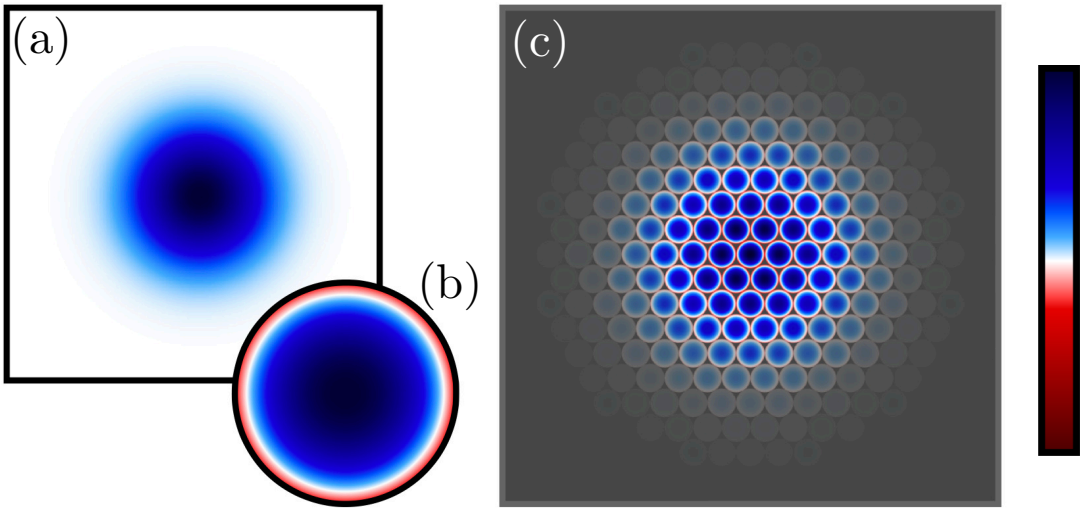

Figure 5.3: This is the vacuum state coupled with a two-level system using the Lambert azimuthal projection, *e.g.*, the vacuum state coupled to an electron. The constituent states that form the full state are shown in (a) and (b). The full state is equivalent in form to the product of the CV vacuum state and a DV excited state, $|0\rangle_f |\uparrow\rangle_a$. The full Wigner function of the hybrid system, where the CV phase space is split up as a discrete grid, is shown in (c). As before, each point has the DV Wigner function for that point plotted but this time the transparency set proportional to the maximum quasi-probability at that point in CV phase space. The colour bar is white at 0 with limits ± 2 for (a), $\pm(1+\sqrt{3})/2$ for (b), and $\pm(1+\sqrt{3})$ for (c).

previous method had been used, then the transparency would be determined after the DV system's degrees of freedom have been integrated out losing the quantum correlations associated with these components.

5.2.2 Fock State Qubits

Being able to provide a measure, or quantify, the quantum correlations within a system is not something that this visualization aims to provide. Instead, attempts are made to highlight key features of different systems that give insight to their overall state. With this in mind, our approach is to identify a number of signatures within the visualization which characterize the quantum correlations and identify classical correlations. In the case of atoms and molecules the quantum correlations between two electrons is important when considering energy levels; entanglement in a system can affect the overall energy. In the case of quantum information the correlations between two spins is equally important but the distinction between

classical and quantum correlations is somewhat more important. The standard simple state in quantum information is the *qubit*; a two-level system that can be in two distinct states or in some superposition of them both [125, 129, 130].

Using the electron, whose spin is a two-level system, a qubit can be imagined where the qubit states are associated with spin orientation. These states have been reproduced in Fig. 5.2 using the Lambert azimuthal projection. Note that the addition of states (σ_x, σ_y, σ_z) associated with the Pauli matrices is for the benefit of future analysis. Having developed an understanding of the DV Wigner function for these states, the same idea must be extended to the CV states. For simplicity, the bit states 0 and 1 are associated with the vacuum and one-photon Fock states, $|0\rangle_f$ and $|1\rangle_f$ respectively, for the CV case. Figure 5.3, compares the DV and CV qubit representations and emphasizes the fact that the DV qubit basis state may be considered to be simply a discrete analog of the Fock state. Considering the different states that can now be produced, the excited CV-DV state, the equal superposition state and a Bell Fock state are analyzed in Fig. 5.4.

To begin with the state $|1\rangle_f |\downarrow\rangle_a$ is shown in Fig. 5.4(c) with the CV system shown in Fig. 5.4(a) and the analogous DV system in Fig. 5.4(b). It is clear how these two states are analogues of each other and the hybrid state that they produce is not unexpected given what has been previously seen. Taking this further, the state $(|0\rangle_f + |1\rangle_f)/\sqrt{2}$, shown Fig. 5.4(d), and $(|\uparrow\rangle_a + |\downarrow\rangle_a)/\sqrt{2}$, shown in Fig. 5.4(e), are also analogous. In the DV system, it was discussed how the equal superposition of the two states produced a rotation of the sphere. Similarly, the equal superposition of the CV system has produced a similar rotation in phase space. The product of both of the states is shown in Fig. 5.4(f) and given the separability, similarities with the state shown in Fig. 5.3 are clear. As in the case of the hydrogen atom, and also seen in helium, the separability is evident by the existence of the same DV Wigner function at every point in CV phase space with an amplitude modulated by the CV Wigner function at that point.

Both of the previous cases demonstrate the reliability of distinguishing local

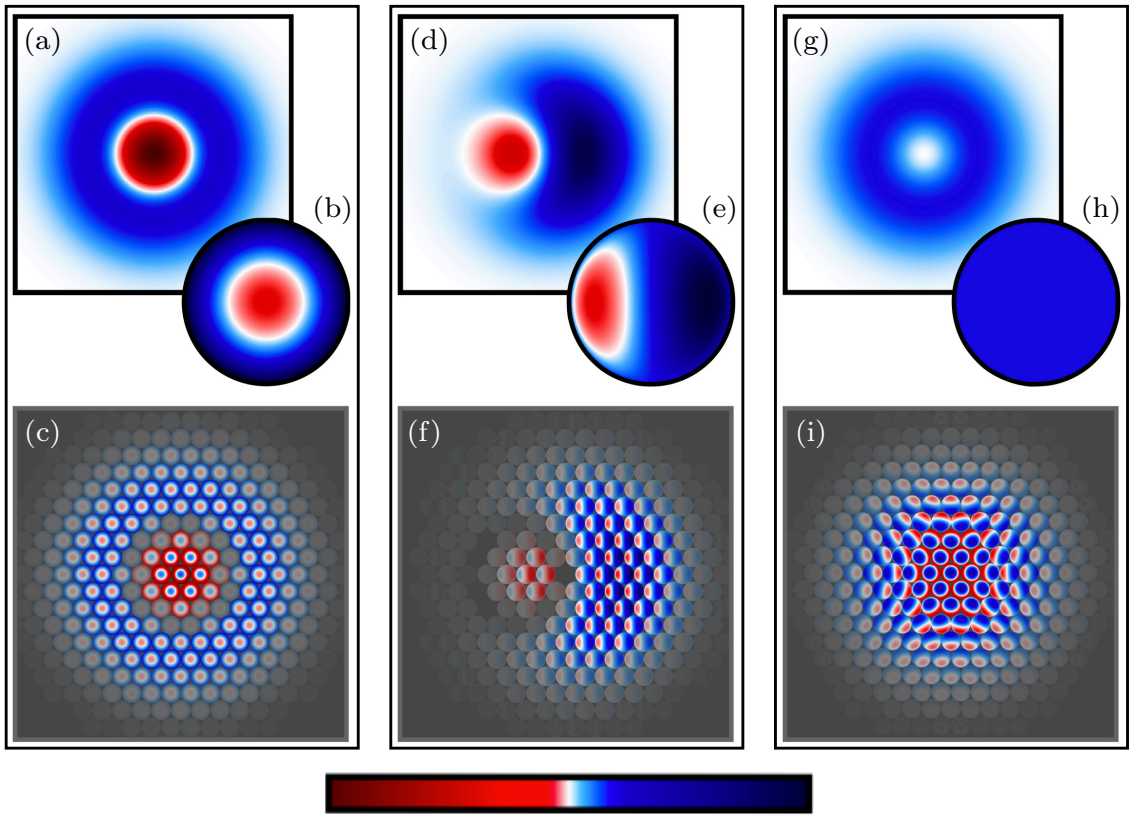

Figure 5.4: Here is shown some example states of a Fock state qubit, *i.e.*, Fock states coupled to DV qubits such as an electron spin. (a) – (c) show the state $|1\rangle_f |\downarrow\rangle_a$ and the corresponding reduced Wigner functions for the CV and DV systems. (d) – (f) show the corresponding Wigner functions for the state $(|0\rangle_f + |1\rangle_f)(|\uparrow\rangle_a + |\downarrow\rangle_a)/2$. Similarly, (g) – (i) show the results for the entangled state $(|0\rangle_f |\uparrow\rangle_a + |1\rangle_f |\downarrow\rangle_a)/2$. (a), (d), and (g) show the reduced CV Wigner functions for each of the states whilst (b), (e), and (h) show the reduced DV Wigner functions. (c), (f), and (i) are the full hybrid state Wigner functions. The colour bar is white at 0 with limits ± 2 for the reduced CV Wigner function, $\pm(1+\sqrt{3})/2$ for reduced DV Wigner function, and $\pm(1+\sqrt{3})$ for hybrid Wigner function.

correlations from this visualization. The final state considered here, the state $(|0\rangle_f |\uparrow\rangle_a + |1\rangle_f |\downarrow\rangle_a)/\sqrt{2}$ shown in Fig. 5.4 (i), demonstrate the ability to see entanglement. As in the case of the spin-orbit coupled hydrogen atom, the entanglement is seen by the twisting of the DV Wigner function at each point in CV phase space. This dependence, as discussed earlier, removes the ability for this state to be separable as the DV Wigner function is not simply modulated by the CV Wigner function at that point. Since the state is pure, this indicates that there must be coupling between the two subsystems. This is what can now be characterized as a signature of this type of quantum correlation in this type of hybrid state. It should

also be pointed out that Fig. 5.4 (i) highlights the importance of considering the full phase space for entangled states. As can be seen from the constituent states, had the full phase space not been considered, the correlations would have been lost and a statistical mixture would have been all that remained.

5.2.3 Coherent State Qubits

Given the complexities of quantum simulation, other ways of encoding information are equally valid. One example uses coherent states for the CV system to encode its information [149, 150]. Due to the over-complete basis the separation of the two coherent states must be sufficiently large so as to render the overlap negligible. Assuming this has been done, the bit values can be assigned; for instance $0 \to \beta_1$ and $1 \to \beta_2$ where $\beta_1 = -\beta_2 = \beta$ and the general state being some superposition of the two analogous to the case of the DV system. The equal superposition of these two states (for $\beta = 3$) is shown in Fig. 5.5 (a) which when coupled with the equal superposition for the DV system, Fig. 5.5 (b), produces the state in Fig. 5.5 (c). This state is given as

$$\frac{1}{2}\left(|\beta\rangle_f + |-\beta\rangle_f\right)\left(|\uparrow\rangle_a + |\downarrow\rangle_a\right); \tag{5.1}$$

a simple coherent state qubit formed of a Schrödinger cat state coupled to a qubit.

Qualitatively from Fig. 5.5 (c) we can see that at each point in phase space the dominant DV Wigner function colour is pointing in the same direction, *i.e.*, to the right. At first it may appear that there are two different DV states in this picture suggesting a quantum correlation is present. However, by looking at the reduced Wigner function in Fig. 5.5 (a) we can see that the interference terms oscillate between negative and positive values. If we take the product of a negative oscillation and the reduced Wigner function in Fig. 5.5 (b) we can see we will simply flip the red and blue colours. This means that the DV state shown in Fig. 5.5 (b) will have a small blue region on the left and a large red region on the right. This is consistent

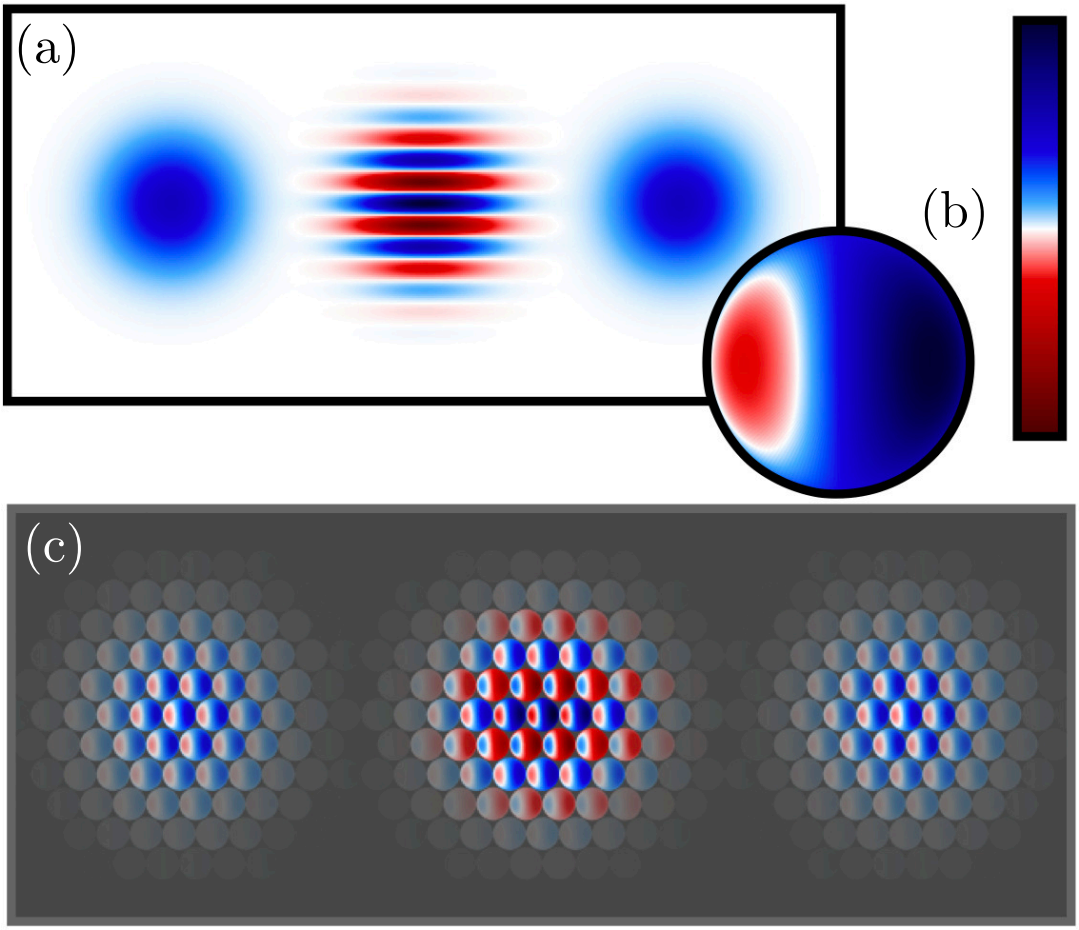

Figure 5.5: A simple coherent state qubit formed of a Schrödinger cat state coupled to a qubit; $(|\beta\rangle_f + |-\beta\rangle_f)(|\uparrow\rangle_a + |\downarrow\rangle_a)/2$. In this case $|\beta\rangle$ is a coherent state centred at β for $\beta = 3$. (a) shows the reduced CV Wigner function and (b) shows the reduced DV Wigner function whilst the hybrid state is shown in (c). The colour bar is white at 0 with limits ± 2 for (a), $\pm(1+\sqrt{3})/2$ for (b), and $\pm(1+\sqrt{3})$ for (c).

with the DV Wigner functions found in the interference region in Fig. 5.5 (c). This means that we do not have different DV states at different points in phase space, just sign modulated DV states, and so there cannot be any CV-DV entanglement, *i.e.*, the state is separable. In summary, because the full Wigner function in Fig. 5.5 (c) is the product of the reduced Wigner functions in Figs. 5.5 (a) and (b) the state is separable.

The hybrid state corresponding to the equal superpositions of the CV and DV systems is

$$\frac{1}{2}\left(|\beta\rangle_f + |-\beta\rangle_f\right)\left(|\uparrow\rangle_a + |\downarrow\rangle_a\right). \tag{5.2}$$

Due to the full system being a simple tensor product of the constituent subsystems, the state is fully separable and follows the same visual signature as Figs. 5.4 (c) and (f), as well as the atomic states noted earlier: each point of the CV phase space has the same DV spin Wigner function modulated by the CV system.

As in the case of the Fock state qubit in the previous section, signatures for local correlations were found and contrasted with those for the non-local correlations. Using a similar Bell state as in Fig. 5.4,

$$\frac{1}{\sqrt{2}}\left(|\beta\rangle_f|\uparrow\rangle_a + |-\beta\rangle_f|\downarrow\rangle_a\right), \tag{5.3}$$

a correlation signature can be found. For the Fock state qubit, the full Wigner function had to be used due to the loss of correlation information in the reduced Wigner function. Similarly, the key identifier was the twisting in the DV Wigner function for each point of CV phase space. Figure 5.6 explores this state and demonstrates several features.

As expected, neither reduced Wigner function, Figs. 5.6 (a) and (b), has visible quantum correlations, yielding two mixed states. However, by utilizing this method of visualization all the correlations are visible in the hybrid state image, Fig. 5.6 (c). The first thing to note is that the interference terms between the two coherent states demonstrate quantum correlations which arise from the superposition. Being able to see these immediately tells us more about the state than the reduced Wigner function. As in the case of spin in atoms, such a visualization ensures any analysis does not omit correlations that exist with the system. This therefore means the full consideration of correlations within the system is always adhered to. Furthermore, the state of the DV system is a traceless state, compare with the Pauli matrices qubit state, with the state at the very centre being the $\hat{\sigma}_x$ Pauli matrix. This is yet another signature of quantum correlations; the manifestation of traceless states is indicative of quantum correlations. Without this visualization tool quantum and classical correlations are indistinguishable. Being able to determine the difference gives more insight into the suitability of the state for quantum information processing.

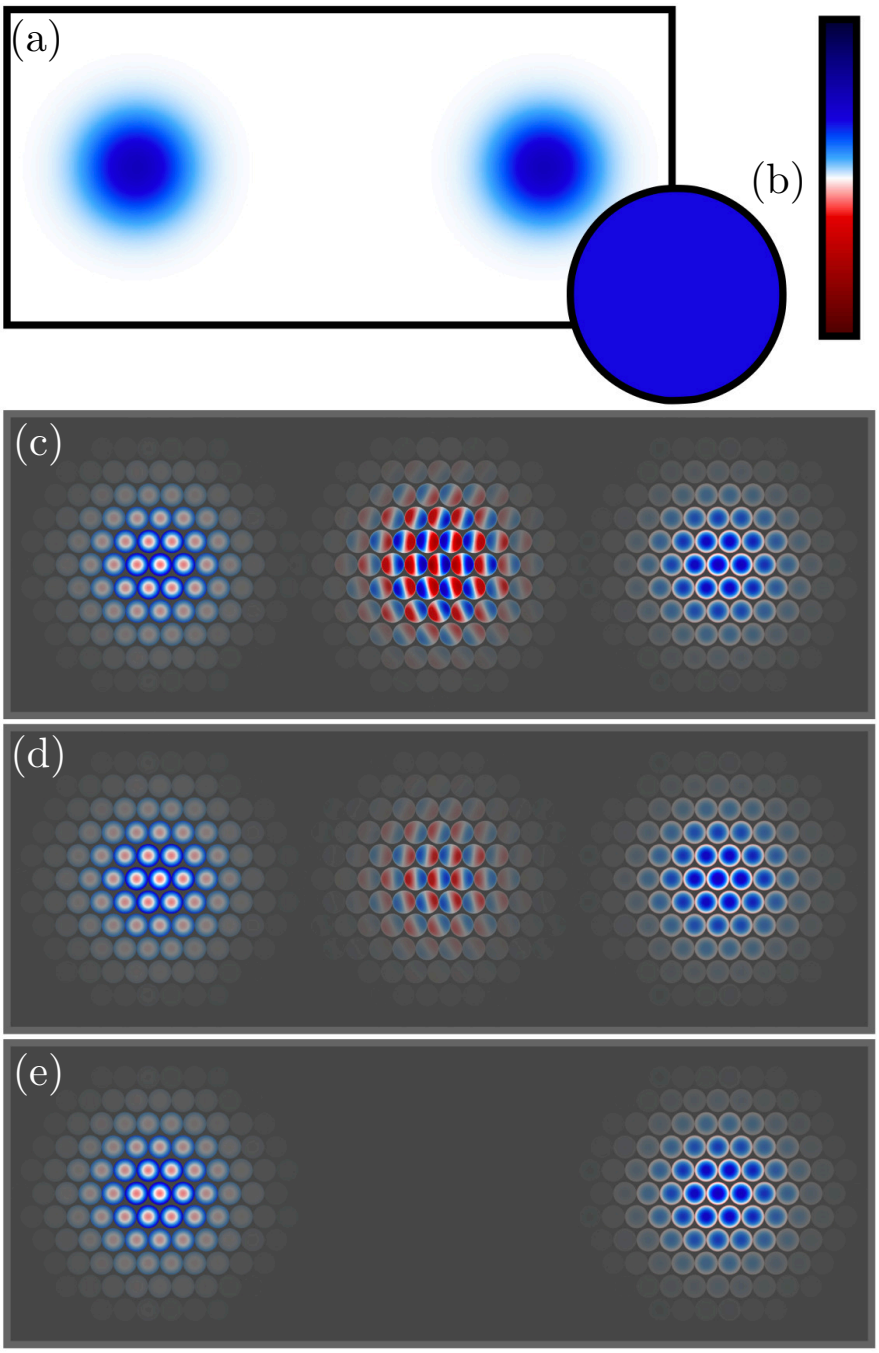

Figure 5.6: Demonstrating the signatures and inadequacy of the reduced Wigner function, here are a number of examples of a lossy entangled Bell-cat state, with varying values of loss. (a) and (b) shows the reduced Wigner function for the CV and DV systems respectively. Key to these images is the lack of correlation information and the loss of any ability to verify the state. The reduced Wigner functions remain the same for the following three example states. (c) shows the full Wigner function for the state with no loss $(|\alpha\rangle_f |\uparrow\rangle_a + |-\alpha\rangle_f |\downarrow\rangle_a)/\sqrt{2}$. (d) shows partial loss of the quantum correlations. (e) shows a fully mixed version of the state $(|\beta\rangle\langle\beta|_f |\uparrow\rangle\langle\uparrow|_a + |-\beta\rangle\langle-\beta|_f |\downarrow\rangle\langle\downarrow|_a)/2$. The colour bar is white at 0 with limits ± 2 for (a), $\pm(1+\sqrt{3})/2$ for (b), and $\pm(1+\sqrt{3})$ for (c).

States formed of the same CV and DV systems but with a different amount of loss can be created from the general state (a 'lossy' cat state)

$$\frac{1}{2}\left(|\beta\rangle\langle\beta|_f|\uparrow\rangle\langle\uparrow|_a+\eta|\beta\rangle\langle-\beta|_f|\uparrow\rangle\langle\downarrow|_a+\eta|-\beta\rangle\langle\beta|_f|\downarrow\rangle\langle\uparrow|_a+|-\beta\rangle\langle-\beta|_f|\downarrow\rangle\langle\downarrow|_a\right). \tag{5.4}$$

If $\eta = 1$ then the equal superposition is formed presented in Fig. 5.6 (c) whilst the states corresponding to $\eta = 0.5$ and $\eta = 0$ are presented in Fig. 5.6 (d) and Fig. 5.6 (e) respectively. The degree of quantum correlations is different for all three cases as the amount of correlations lost to the environment is dependent on the coupling. Each of these is called a lossy cat state with η being their respective coupling to the environment. The lower the value of η the greater the information loss. If the only tool for analyzing the state was the reduced Wigner function, then no useful insight would be found with regards to this loss. This because the very nature of the reduced Wigner function loses this information as seen in Fig. 5.6 (a) and (b). Given that this loss of correlation makes the state less useful for quantum information purposes, being unable to visualize this has been a problem.

However, each state is clearly different using our visualization technique. Not only is it possible to distinguish the strength of quantum correlations, by comparing the transparency of the states, but it also reveals a signature of classical correlations. This is because the final state is the classical mixture where the $|\beta\rangle_f$ coherent state is correlated with $|\uparrow\rangle_a$ states and the $|-\beta\rangle_f$ with $|\downarrow\rangle_a$ states. The absence of interference terms, including the traceless states, between the two coherent states indicates both that the form of this state is a signature of classical correlations and also that traceless states form as a result of quantum correlations in the hybrid state.

Unlike in Fig. 5.5 we can see that in Fig. 5.6 we no longer have the same DV Wigner function at each point in phase space. The first comparison is to consider the DV Wigner function in the region of the coherent state on the left. This has a red circle in the middle surrounded by blue at the edge. Conversely, in the coherent state on the right we have a large blue circle in the middle with a small red region

around the outside. These are clearly DV states that point in orthogonal directions and, due to the difference in size of the middle circle, are not the same state with the sign flipped. Equally, we could consider the fact that the DV Wigner function in the interference pattern is different to the state found in either coherent state region. This alone is sufficient to indicate that the state is not separable.

As in the case of the Fock state qubit, the coherent state qubit has been examined allowing a number of correlations and signatures to be extracted. The ability to analyze the quantum state and verify the correlations that exist within it is important for quantum information to ensure the correct states are used for processing. However, not only can this visualization technique be used to verify the output of a chemical simulation, as shown in Chapter 4, but could also be used in the state preparation and verification of a quantum simulation. The necessity for this within future applications of quantum simulation, such as drug modelling, is key to ensuring a good understanding of information exchange within systems and this visualization provides access to such a tool. Again, the insight that this simple visualization technique provides could provide greater abilities in this area, such as exploiting quantum correlations during a chemical process.

5.2.4 Jaynes-Cummings Model

A large focus of this thesis has been on the use of a visualization tool to explore the interaction and correlations within atomic systems. Moving forward, this would have to be applied to larger systems including molecules as outlined at the end of the previous chapter. However, questions may still remain about the ability of such a visualization tool to be able to display how information is transferred around the system. For instance, when molecules interact and create bonds then it is important that the quantum information that is shared between the two molecules is clear within the visualization. A good example of how this visualization can track quantum information is seen within the Jaynes-Cummings model [138].

This model has great interest within atomic physics and other areas and was

originally developed to explore how light and atoms interact. Consequently, it has been used experimentally and theoretically to understand the details of quantum effects. During the evolution, quantum information is transferred back and forth between the CV and DV systems as well as across the system as a whole. By use of this visualization technique, this transfer can be seen swapping between the field and the atom; manifesting as Schrödinger's cat states or Bell pairs of the sort shown in Fig. 5.4. In order to demonstrate how the signatures previously highlighted enable this transfer to be seen, the interaction picture of the James Cummings model shall be used [138];

$$\hat{H}_{\mathrm{JC}} = \omega(\hat{a}^{\dagger}\hat{\sigma}_{-} + \hat{a}\hat{\sigma}_{+}). \tag{5.5}$$

Here ω is the field-qubit coupling constant and the operators $\hat{\sigma}_{\pm} = (\hat{\sigma}_x \pm \mathrm{i}\,\hat{\sigma}_y)/2$ are the qubit raising and lowering operators that transition the state between eigenstates of $\hat{\sigma}_z$.

The motivation for such analysis is to demonstrate that signatures from small simple states may be extended to describe the complex dynamics of other systems, indicating how adaptable this technique can be. Previously in this thesis, signatures within atomic systems have been identified and it has been suggested that such signatures could be used in more complex state. Here, we have begun with finding signatures in simple CV and DV systems, which we shall now use to explain complex behaviour within a system. Once an efficient mechanism of modelling atomic/molecular systems in this way is found, applying such visualization techniques should be very similar. To begin the analysis, we consider a Fock state basis within the Jaynes-Cummings model. The evolution model uses a density matrix of 80 states in the Fock basis which is obtained numerically by integrating the von Neumann equation using a 6^{th} order Runge-Kutta integration method. The Wigner function is then obtained by taking $\mathrm{Tr}\left[\hat{\rho}\hat{\Pi}\right]$ where $\hat{\rho}$ is the density matrix obtained via this method and $\hat{\Pi}$ is the parity. The Wigner function could instead be found by integrating the Moyal function, though this is not done here. Only the interaction terms of the Hamiltonian are modelled.

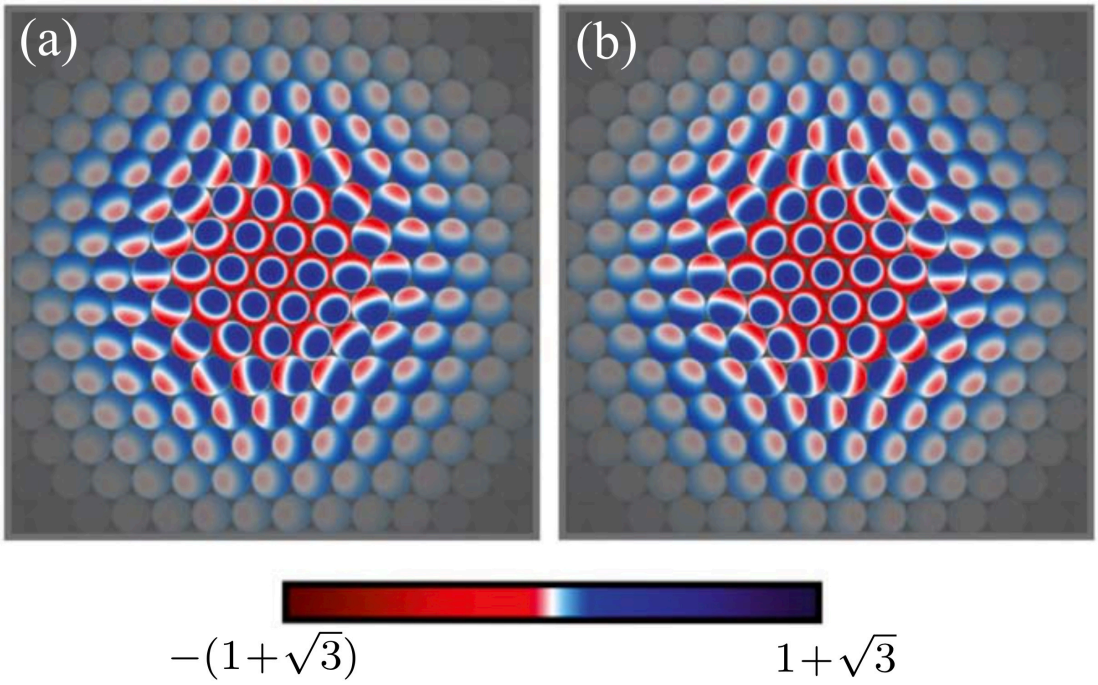

Figure 5.7: The Wigner function of two points in the evolution of the James Cummings model with the initial state $|0\rangle_f|\uparrow\rangle_a$ is shown. During this evolution two entangled Bell-Fock states are generated before returning to the initial state. Both states are shown here with (a) showing the state $(|0\rangle_f|\uparrow\rangle_a - \mathrm{i}\,|1\rangle_f|\downarrow\rangle_a)/\sqrt{2}$ and with (b) showing $(|0\rangle_f|\uparrow\rangle_a + \mathrm{i}\,|1\rangle_f|\downarrow\rangle_a)/\sqrt{2}$. Using both the signatures found when discussing atomic states and the signatures highlighted earlier in the chapter, entanglement is visible through the dependence of the DV Wigner function upon the CV position in phase space; the twisting of the balls.

If the initial state, in the Fock basis, is the vacuum state of the field and the excited, spin-up, state of the DV qubit, then the evolution fluctuates between the two states $|0\rangle_f|\uparrow\rangle_a$ and $|1\rangle_f|\downarrow\rangle_a$ [137]. Information can then be modelled as being transferred between two qubits. This is because the evolution is fully described through the use of two independent states. Given that this model has a fluctuation while continuously transferring quantum information between the two qubits, then we consider a single period of this transfer. In one period, there are two Bell-Fock States that are generated

$$\left|\Phi^{\pm}\right\rangle = \frac{1}{\sqrt{2}}\left(|0\rangle_f|\uparrow\rangle_a \pm \mathrm{i}\,|1\rangle_f|\downarrow\rangle_a\right), \tag{5.6}$$

as shown in Fig. 5.7. As in the previous analysis, Fig. 5.4, the reduced Wigner

function of these Bell-Fock states lose all correlation information. However, it is clear in the full Wigner function due to the twisting at each point in phase space that there is entanglement within this state.

The fact that the Wigner function for the DV system depends upon the point in CV phase space is a signature earlier highlighted of entanglement. This visualization technique has allowed such entanglement correlations to be visible throughout the evolution of this system. Further, although the reduced Wigner function for both Bell states are identical, the role that the phase plays in the state is clear in the ability to distinguish of the hybrid full Wigner function shown using this visualization. The ability not just to identify entanglement through use of signatures, but to also separately distinguish similar states that differ only in phase is where the strength of this visualization lies. Such application could be found in the modelling of bond creation because of the necessity to distinguish the internal quantum correlations between otherwise identical states.

Finally, if the initial state is replaced by a coherent state, $|\beta\rangle_f |\uparrow\rangle_a$ (where $\beta = 3$ in this case), a very different effect is produced. A key distinction between this and the previous case is the collapse and revival of Rabi oscillations, where the Rabi oscillation revival time is t_r [138]. In order to understand this evolution three key points have been focused upon and are indicated by the solid vertical lines in Fig. 5.8 (a). Figure 5.8 (a) shows the qubit inversion, $\langle\hat{\sigma}_z\rangle$, in red and the von Neumann entropy in cyan for each point in the evolution. The first key point is early in the evolution, at $t \approx t_r/9$, which shows a high degree of coupling between the CV and DV systems. The reduced Wigner functions are shown in Figs. 5.8 (b) and (c) from which it can be seen that the DV system is in a highly mixed state. This is from the fact that there is an absence of negativity and the sphere is almost uniformly blue. The CV system, is in a state approaching a Schrödinger's cat state with the interference terms between the two coherent states almost being fully formed as in the example states featured in Chapter 2. Together, these pictures show that there are correlations between the qubit and the field mode but the nature of the quantum

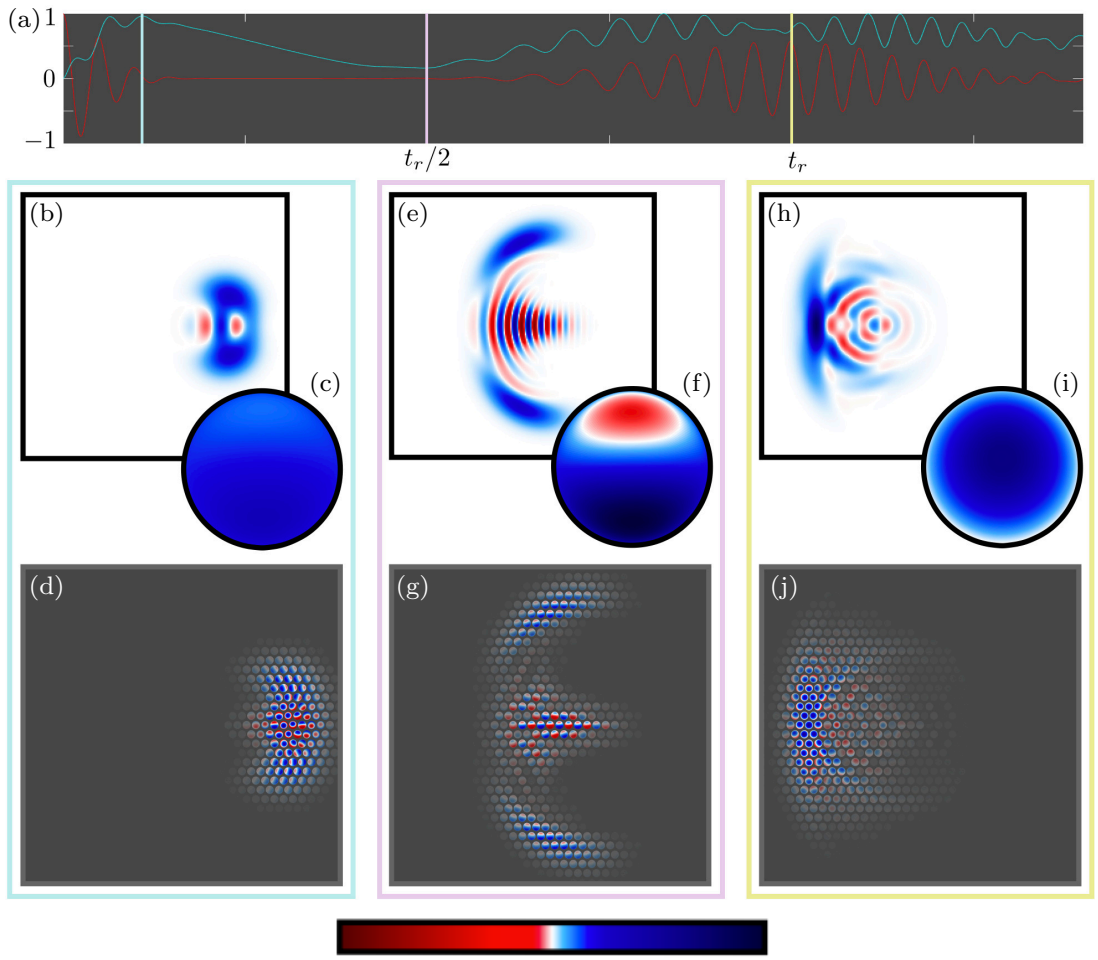

Figure 5.8: The evolution of the Jaynes-Cummings model with initial coherent state qubit $|3\rangle_f |\uparrow\rangle_a$ is shown by use of the Wigner function. Plotted in (a) is the qubit inversion, $\langle\hat{\sigma}_z\rangle$, in red and the von Neumann entropy in cyan over time. Highlighted by solid lines, are three key points in this evolution where t_r is the revival time of the Rabi oscillations. Both the reduced Wigner functions and the hybrid Wigner functions are plotted for each key point. The reduced Wigner functions for the CV system is displayed in (b), (e), and (h) with the related DV Wigner function in (c), (f), and (i). The hybrid Wigner functions for the coupled system are in (d), (g), and (j). The values for the colours correspond to the same values in Fig. 5.6.

correlations between the two is not clear.

Given that the reduced Wigner function is unable to demonstrate the quantum correlations between the CV and DV system it would be possible to conclude that there are no correlations. The Wigner function for the full hybrid state is shown in Fig. 5.8 (d) where a signature of entanglement is immediately obvious through the twisting of the DV state. Without further analysis, it is easily deducible that entanglement, *i.e.*, quantum correlations, exist between the field mode and the qubit.

The direction in which the DV state is oriented, using the terminology of spin, changes for each point in CV phase space. Noticeably, the spin direction at the top of the image of the CV Wigner function is orthogonal to the direction at the bottom; the spin points in the direction of the negative eigenstate of $\hat{\sigma}_x$ at the top and the reverse at the bottom. For the two emerging coherent states, the interference between them is the signature for identifying the correlations due to the traceless states. As this is not an exact coherent state qubit, the interference terms are not fully formed and therefore, although identifiably similar to this signature, they are not yet identical. It is suggested that all of this analysis can be achieved by the use of only the pictures, and the signatures discussed, presented within this chapter. This again highlights the power of a visualization tool for analyzing complex states.

The point at which the field and the qubit start to disentangle is half the Rabi oscillation revival time $t_r/2$ and is displayed in Figs. 5.8 (e) – (g). At this point the quantum correlations have been transferred into the field forming a CV Schrödinger's cat state. Using the reduced Wigner functions, Figs. 5.8 (e) and (f), this Schrödinger's cat state can be easily seen and the coherence of the DV qubit indicates a lack of correlation between the two systems. Whereas, in the previous key point, the interference terms between the two coherent states had not fully formed, the reduced CV Wigner function now demonstrates significant interference between them. Further, the reduced DV Wigner function has increased in both positive and negative amplitudes moving out of a mixed state into the eigenstate of $\hat{\sigma}_y$ with eigenvalue -1. As in the previous case, where it was possible to determine the correlations between the two systems, now it is possible to demonstrate the lack of correlation between the two systems. However, as before the reduced Wigner function lacks any correlation information.

Figure 5.5 shows the initial coherent state qubit, which was itself approximately separable and to a certain degree is analogous to this current state. This means that not only is there a lack of correlation between the two systems, but this state may be approximately separable in the same way. The full hybrid system confirms that

this state should be approximately separable. However, although there are very few correlations between the two systems, some residual quantum correlation remains between the two. Close examination of the interference terms demonstrates a slight twisting for various points in CV phase space. This signature yet again indicates some entanglement remaining within the system. This is expected as the state never truly becomes separable, but the ability to see these correlations reinforces the fact that the quantum correlations never fully disappear.

The final key point, shown in Figs. 5.8 (h) – (j), occurs at $t \approx t_r$, the revival of the Rabi oscillations when the state is closest to the initial state. The reduced Wigner function of the DV system indicates an average total spin-up, using spin terminology, but also demonstrates a loss of coherence seen through the decrease in amplitude of positive values and the lack of negative values. The hybrid Wigner function has a number of rotated DV states indicating residual quantum correlations, as in the previous key point, but at most points is consistent with spin-up. The strongest example of this is the left-hand side of the image where the state is most consistent with the initial coherent state qubit. The choice of CV qubit produces different effects which are easily seen in the signatures arising in their hybrid Wigner functions. It has been shown how each of these qubits can be easily distinguished and how they arise from correlations within and between the CV and DV systems.

5.3 Conclusions

Having laid the foundation for the examination of atomic and molecular states using this Wigner function visualization technique, it is necessary to explore the ability of such a technique. To do this, the role of this visualization technique in state verification for quantum information purposes has been examined. Beginning with the DV qubit coupled to two different CV systems, signatures similar to those found for atomic states were identified. Being able to then characterize the correlations in the states allowed further examination of the evolution of the states in the Jaynes-Cummings model.

Motivating this approach, is the fact that traditional methods such as the reduced Wigner function have been demonstrated to lack the full nature of quantum correlations in CV-DV hybrid systems. Often, this produces mixed states with little ability to characterize any quantum correlations. Using the technique introduced in this thesis, this loss of information has been overcome and has been able to portray these correlations. A slight adaptation to the technique is the consideration of the transparency. This is because in the case of the atomic states the transparency was set according to the reduced Wigner function for the CV system. However, this method loses information when the CV and DV systems share quantum information. To account for this, the transparency is instead proportionally set to $\max_{\theta,\phi} |W_{\hat{\rho}}(\alpha, \theta, \phi)|$ at each point in CV phase space.

By making a slight adjustment, visualizing the quantum correlations in CV-DV hybrid states, such as those that manifest between two coherent states in a hybrid Schrödinger's cat state, becomes possible. It is suggested that when considering bond formation, quantum correlations between the two atoms/molecules may manifest in a similar way to such Schrödinger's cat states. Being able to see these correlations is therefore necessary to understanding the underlying physical process. By characterizing the signatures of quantum correlations, being able to pull out the way in which states evolve becomes a much simpler process. These signatures also provide the ability to analyze the correlations in previously more difficult states to characterize in quantum information; maximally entangled states or squeezed states that produce entanglement.

To demonstrate the ability of the signatures to describe evolution, the Jaynes-Cummings model was used where information was exchanged continuously between the subsystems. The observation, in a visual way, of the transfer of quantum information between the CV and DV systems was made using only the signatures found earlier in the chapter. The ease with which entanglement or a reduction of correlation could be identified, enabled a description of the evolution to be produced. This method could prove to be very useful in the identification of key points of bond

formation. However, it could also prove to be highly useful in areas such as quantum simulation, when it is applied to chemical systems, due to the ability to see information exchange across and between systems. Extending these methods would allow for a more intuitive picture of the exchange of quantum information within coupled systems and provide insight on how systems become correlated. An adaptation of the methods in Ref. [122] along with the method presented here could become an experimental technique considered to be a form of quantum state spectroscopy.

Chapter 6

Conclusions

In this thesis, the power of phase-space as a visualization tool has been developed and demonstrated. After introducing the formulation of the Wigner function, a simple catalogue of states is produced. This catalogue enables the study of more complex states to become a simple task. The methods for both representing spatial Wigner functions, as well as spin Wigner functions, are explored along with the concept of representing these functions with reduced dimensionality.

With the aim of creating a technique to visualize quantum states, an example case of visualizing states in quantum chemistry is developed. Similar to the early development of intracules, we begin by considering simple atomic states and then begin to include spin. The theory needed in order to discuss the states with a common language is provided and a standard model adopted. This model is used in a variety of situations and replaces the full hydrogenic atomic state with the eigenstates of the 3D SHO. Although this is a compromise, the final states are not too dissimilar to what would be expected from a full chemical consideration. Further, as the focus is upon developing a technique for considering any quantum state, then the more important factor is the ability for the technique to demonstrate quantum correlations within a system.

After developing the model, the visualization technique is described using very simple hydrogen states. The technique is used to demonstrate the ease with which spin degrees of freedom can be portrayed. Most significantly, a state with spin-

orbit coupling is explored and the entanglement, not usually visible, is seen by the twisting of spheres. This first example of how easy it becomes to pull out correlations between spin and spatial degrees of freedom is an indication of how powerful this tool can be. The ability to portray these correlations goes beyond anything that has been seen in the visualization of atomic states even at this simple level. For instance, the method of visualizing states in the form of intracules was unable to unify these correlations into a simple picture.

The consideration of helium requires the introduction of models which deal with two electrons. Again, these models are simple enough for them to be modelled easily but are also good representatives of the true states. A feature of the spin Wigner function, as used in this thesis, is its ability to identify the singlet state where other techniques fail. This is first shown in the ground state of helium where, although it has the same spatial distribution as the ground state of hydrogen, it is distinguished by the spin Wigner function seen in the visualization. The consideration of the first excited states of helium allows a variety of spin relationships to be explored. Each spin combination is identifiable using the catalogue developed. This shows the next important correlations, spin-spin, that this technique can identify with little effort. The ability to distinguish between the triplet states is an important feature that could prove vital in quantum chemistry due to the consequences of such states on bond formation. Once more, this technique has gone further than previous attempts to visualize the states by making it clear and easy to distinguish between similar states. At this point the ability to see spin-spatial correlations as well as spin-spin correlations is beyond other methods.

Finally, this chapter deals with lithium demonstrating how all of this information can be put together to recover the full state. For a visualization tool to be particularly useful when considering quantum states, it is important that the technique allows the reader to recover the full quantum state. Identifying features within a state is a useful tool however attempting to go beyond this involves having the ability to use these features to recreate the state. As an example of how this can be

done, the lithium section follows both lines of argument. It is shown how the images can be used to reconstruct the full quantum state using a small catalogue of example Wigner functions and a little bit of knowledge about the exclusion principle. It turns out that this state, which has significant spin-spin and spin-spatial correlations, can be fully reconstructed. It is true that in order to do this the number of slices had to be increased and this is likely to happen again as states become more complex. However, it is also true that using models to simplify the states and using slices to specifically target particular degrees of freedom will enable this technique to be used in a variety of circumstances.

At this point, the basic technique that is used in the visualization has been developed, and has been demonstrated to work for a variety of different atomic states. It has been shown that entanglement can be visualized in accessible way and complex states have been fully recovered from the visualization. The next important consideration is the usability of this technique with specific software. Being able to visualize quantum states in a very particular setting is not useful to people outside of that field. Chapter 4 demonstrates how this technique can be used as an add-on to software that outputs quantum states. The point here is to emphasize how this technique can be added to existing software packages as an output of simulations. Carrying on the case already considered, the states already explored are re-formulated using quantum chemistry simulation software. Although, this simulation also uses certain simplifications it is the standard in the field for modelling atomic and molecular systems.

Here it is seen how the basic physics model differs from simulation. This is in part due to the fact that the main consideration of quantum chemistry simulations is to reproduce energy levels given certain constraints. This means that rather than producing the same states produced by theoretical models, they produce superpositions of those states which minimize the energies within the simulation framework. However, due to the simplicity of this visualization it is easy to spot that these states still represent the same forms of spin-spatial entanglement. The ability to

easily describe and characterize this spin-spatial entanglement is what could make this technique useful for exploring problems such as the effect of spin-orbit coupling within catalyst reactions.

The first example of significant differences between the two models is in the visualization of lithium. The disappearance of the spatial structures, in comparison to the earlier model, means that examining this system is slightly more difficult. Fortunately, the impact on the analysis is minimized by the use of all four slices to discuss the features. This would suggest that when systems are more complex in their form, the more dependent on a variety of slices the analysis becomes. This is not a surprising consequence, and further emphasizes the need to integrate this technique with the output of software. Not only has this technique now been demonstrated to recover features previously lost, it has now been extended as a tool for standard software used within the field.

The final chapter focuses on why such a technique is important for exploring quantum states. At this point, the ability to find correlations within the system has been exemplified in both a theoretical and a practical way. It is easy to see how such tools would become useful when designing quantum technologies for instance. This chapter explores how this visualization, or rather an adaptation of this visualization, can be used to characterize quantum states. Importantly, traditional techniques lack the ability to portray the full quantum correlations within the system considered. Being able to see these correlations is important in a variety of fields in order to understand the underlying physical process. By considering Schrödinger's cat states, it is shown how this technique does portray the necessary quantum information needed in order to characterize the state.

Finally, due to the importance of dynamics in physical processes, the ability to identify signatures describing the evolution is demonstrated through this technique. Again, the ability to do this is based upon constructing a simple catalogue of signatures and known states and then applying scrutiny to more complex images. The Jaynes-Cummings model of continuous information exchange between subsystems is

used as an example and it is readily demonstarted how this technique can be applied to other quantum simulations. This provides a stable platform from which different quantum states in different contexts can be explored.

The ability to identify, characterize and reconstruct quantum state in a variety of circumstances has been explored using the Wigner function. Introducing a specific way of visualizing the Wigner function allows a number of correlations to be easily deduced from the output. This visualization tool goes beyond methods that exist within the field of quantum chemistry, our first consideration, such as intracules, by reducing the overhead on analysis. Further, it goes beyond traditional methods of characterizing quantum states, such as the reduced Wigner function, by revealing information that is normally lost. This will not just be invaluable as a tool when developing systems dependent upon quantum correlations, but also has the potential of being used in an experimental setting.

Bibliography

[1] Georgescu I M, Ashhab S, and Nori F, 'Quantum simulation', *Rev Mod Phys*, **86**(1), 2014, 1308.6253.

[2] Vidal G, 'Efficient simulation of one-dimensional quantum many-body systems', *Phys Rev Lett*, **93**(4), 2004, pp. 040502–1, 0310089.

[3] Richerme P, 'Two-dimensional ion crystals in radio-frequency traps for quantum simulation', *Phys Rev A*, **94**, 2016, p. 032320.

[4] Marty O, Cramer M, and Plenio M B, 'Practical Entanglement Estimation for Spin-System Quantum Simulators', *Phys Rev Lett*, **116**, 2016, p. 105301.

[5] Percival I, *Quantum State Diffusion*, Cambridge University Press, 1999.

[6] Cook R J, 'What are Quantum Jumps?', *Phys Scr*, **T21**, 1988, pp. 49–51.

[7] Jacob C R, and Reiher M, 'Spin in density-functional theory', *Int J Quantum Chem*, **112**(23), 2012, pp. 3661–3684.

[8] Capelle K, and Gross E K U, 'Spin-density functionals from current-density functional theory and vice versa: A road towards new approximations', *Phys Rev Lett*, **78**(10), 1997, pp. 1872–1875.

[9] Wittbrodt J M, and Schlegel H B, 'Some reasons not to use spin projected density functional theory', *J Chem Phys*, **105**(15), 1996, p. 6574.

[10] Ye S, and Neese F, 'Accurate modeling of spin-state energetics in spin-crossover systems with modern density functional theory', *Inorg Chem*, **49**(3), 2010, pp. 772–774.

[11] Tilma T, Everitt M J, Samson J H, *et al.*, 'Wigner Functions for Arbitrary Quantum Systems', *Phys Rev Lett*, **117**(18), 2016, p. 180401.

[12] Wigner E P, 'On the quantum correction for thermodynamic equilibrium', *Phys Rev*, **40**, 1932, pp. 749–759.

[13] Dahl J P, 'The Wigner function', *Physica A*, **114**(1-3), 1982, pp. 439–444.

[14] Dahl J P, 'On the Group of Translations and Inversions of Phase Space and the Wigner Functions', *Phys Scr*, **25**(4), 1982, pp. 499–503.

[15] Schleich W, *Quantum Optics in Phase Space*, Wiley, 2011.

[16] Molina-Espíritu M, Esquivel R O, López-Rosa S, and Dehesa J S, 'Quantum Entanglement and Chemical Reactivity', *Journal of Chemical Theory and Computation*, **11**(11), 2015, pp. 5144–5151, `https://doi.org/10.1021/acs.jctc.5b00390`.

[17] Boguslawski K, and Tecmer P, 'Orbital entanglement in quantum chemistry', *Int J Quantum Chem*, **115**(19), 2015, pp. 1289–1295.

[18] Gill P M, O'Neill D P, and Besley N A, 'Two-electron distribution functions and intracules', *Theor Chem Acc*, **109**(5), 2003, pp. 241–250.

[19] Besley N A, and Gill P M W, 'Atomic and molecular intracules for excited states', *J Chem Phys*, **120**(16), 2004, pp. 7290–7297.

[20] Besley N A, 'Computation of Husimi intracules', *Chem Phys Lett*, **409**(1–3), 2005, pp. 63–69.

[21] Besley N A, O'Neill D P, and Gill P M W, 'Computation of molecular Hartree-Fock Wigner intracules', *J Chem Phys*, **118**(5), 2003, pp. 2033–2038.

[22] Gill P M W, Crittenden D L, O'Neill D P, and Besley N A, 'A family of intracules, a conjecture and the electron correlation problem.', *Phys Chem Chem Phys*, **8**(1), 2006, pp. 15–25.

[23] Springborg M, 'Wigner's phase space function and the bond in LiH', *Theor Chem Acc*, **63**(4), 1983, pp. 349–356.

[24] Blanchard P, Gracia-Bondiacutea J M, and Várilly J C, 'Density functional theory on phase space', *Int J Quantum Chem*, **112**(4), 2012, pp. 1134–1164.

[25] Hillery M, O'Connell R F, Scully M O, and Wigner E P, 'Distribution functions in physics: Fundamentals', *Phys Rep*, **106**(3), 1984, pp. 121–167.

[26] Wallentowitz S, de Matos Filho R L, and Vogel W, 'Determination of entangled quantum states of a trapped atom', *Phys Rev A*, **56**(2), 1997, pp. 1205–1211.

[27] Sperling J, Agudelo E, Walmsley I A, and Vogel W, 'Quantum correlations in composite systems', *J Phys B*, **50**(13), 2017, p. 134003.

[28] Sperling J, and Walmsley I A, 'Quasiprobability representation of quantum coherence', *Phys Rev A*, **97**(6), 2018, p. 062327.

[29] Sundar B, Wang K C, and Hazzard K R, 'Analysis of continuous and discrete Wigner approximations for spin dynamics', *Phys Rev A*, **99**(4), 2019, p. 43627.

[30] Kenfack A, and Zyczkowski K, 'Negativity of the Wigner function as an indicator of non-classicality', *J Opt B*, **6**(10), 2004, pp. 396–404.

[31] Taghiabadi R, Akhtarshenas S J, and Sarbishaei M, 'Revealing quantum correlation by negativity of the Wigner function', *Quant Inf Process*, **15**(5), 2016, pp. 1999–2020.

[32] Siyouri F, El Baz M, and Hassouni Y, 'The negativity of Wigner function as a measure of quantum correlations', *Quant Inf Process*, **15**(10), 2016, pp. 4237–4252.

[33] Moyal J E, 'Quantum mechanics as a statistical theory', *Proc Cambridge Phil Soc*, **45**(1), 1949, pp. 99–124.

[34] Groenewold H J, 'On the principles of elementary quantum mechanics', *Physica*, **12**(7), 1946, pp. 405–460.

[35] Hudson R, 'When is the wigner quasi-probability density non-negative?', *Rep Math Phys*, **6**(2), 1974, pp. 249–252.

[36] Arkhipov I I, Barasiński A, and Svozilík J, 'Negativity volume of the generalized Wigner function as an entanglement witness for hybrid bipartite states', *Sci Rep*, **8**(1), 2018, p. 16955.

[37] Glauber R J, 'Coherent and Incoherent States of the Radiation Field', *Phys Rev*, **131**(6), 1963, p. 2766.

[38] Cahill K E, and Glauber R J, 'Density Operators and Quasiprobability Distributions', *Phys Rev*, **177**(5), 1969, pp. 1882–1902.

[39] Royer A, 'Wigner function as the expectation value of a parity operator', *Phys Rev A*, **15**(2), 1977, pp. 449–450.

[40] Breinig M, 'The Wigner-Eckart Theorem', The University of Tennessee Web-Based Quantum Mechanics Course, 2001.

[41] Brune M, Haroche S, Raimond J M, *et al.*, 'Manipulation of photons in a cavity by dispersive atom-field coupling: Quantum-nondemolition measurements and generation of Schrödinger cat states', *Phys Rev A*, **45**(7), 1992, pp. 5193–5214.

[42] Deléglise S, Dotsenko I, Sayrin C, *et al.*, 'Reconstruction of non-classical cavity field states with snapshots of their decoherence', *Nature*, **455**(7212), 2008, pp. 510–514.

[43] Vlastakis B, Petrenko A, Ofek N, *et al.*, 'Characterizing entanglement of an artificial atom and a cavity cat state with Bell's inequality', *Nat Comms*, **6**, 2015, pp. 1–8.

[44] Scully M O, and Zubairy M S, *Quantum Optics*, Cambridge University Press, 5 edition, 2006.

[45] Rungta P, Munro W J, Nemoto K, *et al.*, 'Qudit Entanglement', in *Directions in Quantum Optics: A Collection of Papers Dedicated to the Memory of Dan Walls*, H J Carmichael, R J Glauber, and M O Scully (eds.), Springer-Verlag, Berlin, 2001, pp. 149–164, `arXiv:quant-ph/0001075`.

[46] Husimi K, 'Some Formal Properties of the Density Matrix', *Proc Phys Math Soc Jpn*, **22**(4), 1940, pp. 264–314.

[47] Stratonovich R L, 'On distributions in representation space', *J Exp Theor Phys*, **4**(6), 1957, pp. 891–898.

[48] Wootters W K, 'A Wigner-function formulation of finite-state quantum mechanics', *Ann Phys (N Y)*, **176**(1), 1987, pp. 1–21.

[49] Gibbons K S, Hoffman M J, and Wootters W K, 'Discrete phase space based on finite fields', *Phys Rev A*, **70**(6), 2004, p. 062101.

[50] Howard M, Wallman J, Veitch V, and Emerson J, 'Contextuality supplies the 'magic' for quantum computation', *Nature*, **510**(7505), 2014, pp. 351–355.

[51] Delfosse N, Guerin P A, Bian J, and Raussendorf R, 'Wigner function negativity and contextuality in quantum computation on rebits', *Phys Rev X*, **5**(2), 2015, p. 021003.

[52] Raussendorf R, Browne D E, Delfosse N, *et al.*, 'Contextuality and Wigner-function negativity in qubit quantum computation', *Phys Rev A*, **95**(5), 2017, pp. 1–22.

[53] Várilly J C, and Gracia-Bondía J M, 'The moyal representation for spin', *Ann Phys (N Y)*, **190**(1), 1989, pp. 107–148.

[54] Arecchi F T, Courtens E, Gilmore R, and Thomas H, 'Atomic Coherent States in Quantum Optics', *Phys Rev A*, **6**(6), 1972, pp. 2211–2237.

[55] Perelomov A, *Generalized Coherent States and Their Applications*, Springer-Verlag, Berlin, 1986.

[56] Klimov A B, and Espinoza P, 'Moyal-like form of the star product for generalized SU(2) Stratonovich-Weyl symbols', *J Phys A*, **35**(40), 2002, pp. 8435–8447.

[57] Garon A, Zeier R, and Glaser S J, 'Visualizing operators of coupled spin systems', *Phys Rev A*, **91**(4), 2015, pp. 1–28.

[58] Luis A, 'Quantum phase space points for Wigner functions in finite-dimensional spaces', *Phys Rev A*, **69**(5), 2004, p. 052112.

[59] Harland D, Everitt M J, Nemoto K, *et al.*, 'Towards a complete and continuous Wigner function for an ensemble of spins or qubits', *Phys Rev A*, **86**(6), 2012, p. 062117.

[60] Brif C, and Mann A, 'Phase-space formulation of quantum mechanics and quantum-state reconstruction for physical systems with Lie-group symmetries', *Phys Rev A*, **59**(2), 1999, pp. 971–987.

[61] Dowling J P, Agarwal G S, and Schleich W P, 'Wigner distribution of a general angular-momentum state: Applications to a collection of two-level atoms', *Phys Rev A*, **49**(5), 1994, pp. 4101–4109.

[62] Rundle R P, Tilma T, Samson J H, *et al.*, 'General approach to quantum mechanics as a statistical theory', *Phys Rev A*, **99**(1), 2019, p. 012115.

[63] Minaev B F, and Ågren H, 'Spin-catalysis phenomena', *International Journal of Quantum Chemistry*, **57**(3), 1996, pp. 519–532.

[64] Wang Y, Zhu X, and Li Y, 'Spin–Orbit Coupling-Dominated Catalytic Activity of Two-Dimensional Bismuth toward CO2 Electroreduction: Not the Thinner the Better', *The Journal of Physical Chemistry Letters*, **10**(16), 2019,

pp. 4663–4667, pMID: 31314533, https://doi.org/10.1021/acs.jpclett.9b01406.

[65] Brádler K, Wilde M M, Vinjanampathy S, and Uskov D B, 'Identifying the quantum correlations in light-harvesting complexes', *Phys Rev A*, **82**(6), 2010, p. 062310.

[66] Cai J, Guerreschi G G, and Briegel H J, 'Quantum Control and Entanglement in a Chemical Compass', *Phys Rev Lett*, **104**(22), 2010, p. 220502.

[67] Cai J, Popescu S, and Briegel H J, 'Dynamic entanglement in oscillating molecules and potential biological implications', *Phys Rev E*, **82**(2), 2010, p. 021921.

[68] Caruso F, Chin A W, Datta A, *et al.*, 'Entanglement and entangling power of the dynamics in light-harvesting complexes', *Phys Rev A*, **81**(6), 2010, p. 062346.

[69] Novoselov D, Korotin D M, and Anisimov V I, 'Quantum states entanglement in hemoglobin molecule active center', 2016, arXiv:1602.02963.

[70] Sarovar M, Ishizaki A, Fleming G R, and Whaley K B, 'Quantum entanglement in photosynthetic light-harvesting complexes', *Nature Physics*, **6**, 2010, pp. 462–467.

[71] Agudelo E, Sperling J, Costanzo L S, *et al.*, 'Conditional Hybrid Nonclassicality', *Phys Rev Lett*, **119**(12), 2017, pp. 1–6.

[72] Polkovnikov A, 'Phase space representation of quantum dynamics', *Ann Phys (N Y)*, **325**(8), 2010, pp. 1790–1852.

[73] Leiner D, Zeier R, and Glaser S J, 'Wigner tomography of multispin quantum states', *Phys Rev A*, **96**(6), 2017, pp. 1–14, arXiv:1707.08465.

[74] Kakofengitis D, Oliva M, and Steuernagel O, 'Wigner's representation of quantum mechanics in integral form and its applications', *Phys Rev A*, **95**, 2017, p. 022127.

[75] Steuernagel O, Kakofengitis D, and Ritter G, 'Wigner Flow Reveals Topological Order in Quantum Phase Space Dynamics', *Phys Rev Lett*, **110**, 2013, p. 030401.

[76] Rundle R P, Mills P W, Tilma T, *et al.*, 'Simple procedure for phase-space measurement and entanglement validation', *Phys Rev A*, **96**(2), 2017, p. 022117.

[77] Weyl H, 'Quantenmechanik und Gruppentheorie', *Z Phys*, **46**(1), 1927, pp. 1–46, republished 1931 Gruppentheorie and Quantcnmechanik (Leipzig: S. Hirzel Verlag) English reprint 1950 (New York: Dover Publications).

[78] Sudarshan E C G, 'Equivalence of Semiclassical and Quantum Mechanical Descriptions of Statistical Light Beams', *Phys Rev Lett*, **10**(7), 1963, pp. 277–279.

[79] Goldstein H, *Classical Mechanics*, Pearson India, 2011.

[80] Schwabl F, and Brewer W, *Statistical Mechanics*, Advanced Texts in Physics, Springer Berlin Heidelberg, 2002.

[81] Sakurai J J, and Napolitano J, *Modern Quantum Mechanics*, Cambridge University Press, 2 edition, 2017.

[82] Cohen-Tannoudji C, Diu B, and Laloë F, *Quantum Mechanics Vol. 1*, Quantum Mechanics, Wiley, 1977.

[83] Rozema L A, Darabi A, Mahler D H, *et al.*, 'Violation of Heisenberg's Measurement-Disturbance Relationship by Weak Measurements', *Phys Rev Lett*, **109**, 2012, p. 100404.

[84] Curtright T L, and Zachos C K, 'Quantum Mechanics in Phase Space', *Asia Pac Phys Newsl*, **01**(01), 2012, pp. 37–46.

[85] Patra M K, and Braunstein S L, 'Quantum Fourier transform, Heisenberg groups and quasiprobability distributions', *New J Phys*, **13**, 2011, p. 063013.

[86] Vourdas A, 'Phase space methods for finite quantum systems', *Rep Math Phys*, **40**(2), 1997, pp. 367–371.

[87] Klimov A B, and Romero J L, 'A generalized Wigner function for quantum systems with the SU(2) dynamical symmetry group', *J Phys A*, **41**(5), 2008, p. 055303.

[88] Tilma T, and Nemoto K, 'SU(N)-symmetric quasi-probability distribution functions', *J Phys A*, **45**(1), 2012, p. 015302.

[89] Bondar D I, Cabrera R, Zhdanov D V, and Rabitz H A, 'Wigner phase-space distribution as a wave function', *Phys Rev A*, **88**(5), 2013, 1202.3628.

[90] Davies B I, Rundle R P, Dwyer V M, *et al.*, 'Visualizing spin degrees of freedom in atoms and molecules', *Phys Rev A*, **100**, 2019, p. 042102.

[91] Cohen-Tannoudji C, Diu B, and Laloë F, *Quantum Mechanics Vol. 2*, Quantum Mechanics, Wiley, 1977.

[92] Mills P W, Rundle R P, Samson J H, *et al.*, 'Quantum invariants and the graph isomorphism problem', *Phys Rev A*, **100**, 2019, p. 052317.

[93] Haaland A, *Molecules and Models: The molecular structures of main group element compounds*, OUP Oxford, 2008.

[94] Roos B O, and Malmqvist P, 'Relativistic quantum chemistry: the multiconfigurational approach', *Phys Chem Chem Phys*, **6**(11), 2004, pp. 2919–2927.

[95] Dehesa J S, Koga T, Yáñez R J, *et al.*, 'Quantum entanglement in helium', *J Phys B*, **45**(1), 2012, p. 015504.

[96] Esquivel R O, Flores-Gallegos N, Molina-Espíritu M, *et al.*, 'Quantum entanglement and the dissociation process of diatomic molecules', *J Phys B*, **44**(17), 2011, p. 175101.

[97] Tichy M C, Mintert F, and Buchleitner A, 'Essential entanglement for atomic and molecular physics', *J Phys B*, **44**(19), 2011, p. 192001.

[98] Lowe J, and Peterson K, *Quantum Chemistry*, Elsevier Science, 2011.

[99] Amovilli C, and March N H, 'Quantum information: Jaynes and Shannon entropies in a two-electron entangled artificial atom', *Phys Rev A*, **69**(5), 2004, p. 054302.

[100] Coe J P, Sudbery A, and D'Amico I, 'Entanglement and density-functional theory: Testing approximations on Hooke's atom', *Phys Rev B*, **77**(20), 2008, p. 205122.

[101] Osenda O, and Serra P, 'Scaling of the von Neumann entropy in a two-electron system near the ionization threshold', *Phys Rev A*, **75**(4), 2007, p. 042331.

[102] Pipek J, and Nagy I, 'Measures of spatial entanglement in a two-electron model atom', *Phys Rev A*, **79**(5), 2009, p. 052501.

[103] Miller J L, 'An unexpected spin flip alters the course of a chemical reaction', *Physics Today*, **72**(2), 2019, pp. 14–16.

[104] Zobel J P, Nogueira J J, and González L, 'Mechanism of Ultrafast Intersystem Crossing in 2-Nitronaphthalene', *Chem: Eur J*, **24**(20), 2018, pp. 5379–5387.

[105] Li H, Kamasah A, Matsika S, and Suits A G, 'Intersystem crossing in the exit channel', *Nat Chem*, **11**(2), 2019, pp. 123–128.

[106] Condon E, and Odabasi H, *Atomic Structure*, Cambridge University Press, 1980.

[107] Szabo A, and Ostlund N, *Modern Quantum Chemistry: Introduction to Advanced Electronic Structure Theory*, Dover Books on Chemistry, Dover Publications, 2012.

[108] Levine I, *Quantum Chemistry*, Pearson advanced chemistry series, Pearson, 2014.

[109] McArdle S, Endo S, Aspuru-Guzik A, *et al.*, 'Quantum computational chemistry', *Rev Mod Phys*, **92**, 2020, p. 015003.

[110] García-Castelán R M G, Choe W S, and Lee Y C, 'Correlation energies for two interacting electrons in a harmonic quantum dot', *Phys Rev B*, **57**(16), 1998, pp. 9792–9806.

[111] Laguna H G, and Sagar R P, 'Position-momentum correlations in the Moshinsky atom', *J Phys A*, **45**(2), 2012, p. 025307.

[112] Yañez R J, Plastino A R, and Dehesa J S, 'Quantum entanglement in a soluble two-electron model atom', *Eur Phys J D*, **56**(1), 2009, pp. 141–150.

[113] Boys S F, and Egerton A C, 'Electronic wave functions - I. A general method of calculation for the stationary states of any molecular system', *Proceedings of the Royal Society of London Series A Mathematical and Physical Sciences*, **200**(1063), 1950, pp. 542–554.

[114] Wulfman C E, 'Approximate Electronic Energy Surfaces from Cuspless Wave Functions', *The Journal of Chemical Physics*, **33**(5), 1960, pp. 1567–1576.

[115] Harris F E, 'Gaussian Wave Functions for Polyatomic Molecules', *Rev Mod Phys*, **35**, 1963, pp. 558–568.

[116] Moshinsky M, and Novaro O, 'Harmonic Oscillator in Atomic and Molecular Physics', *The Journal of Chemical Physics*, **48**(9), 1968, pp. 4162–4180.

[117] Moshinsky M, Novaro O, and Calles A, 'The Pseudo-Atom: A Soluble Many Body Problem', *J Phys Colloques*, **31**(C4), 1970, pp. 125–140.

[118] Cooper M J, 'Compton scattering and electron momentum determination', *Rep Prog Phys*, **48**(4), 1985, pp. 415–481.

[119] Singru R M, and Mishra R R, 'Transformation from metallic electron charge density to electron momentum density', *J Phys Condens Matter*, **1**, 1989, pp. SA21–SA25.

[120] Brandao F G S L, Christandl M, Harrow A W, and Walter M, 'The Mathematics of Entanglement', 2016, `1604.01790`.

[121] Cao Y, Romero J, and Aspuru-Guzik A, 'Potential of Quantum Computing for Drug Discovery', *IBM J Res Dev*, **62**(6), 2018.

[122] Eichler C, Lang C, Fink J M, *et al.*, 'Observation of Entanglement between Itinerant Microwave Photons and a Superconducting Qubit', *Phys Rev Lett*, **109**(24), 2012, p. 240501.

[123] Rundle R P, Davies B I, Dwyer V M, *et al.*, 'Visualization of correlations in hybrid discrete-continuous variable quantum systems', *Journal of Physics Communications*, **4**(2), 2020, p. 025002.

[124] Gerry C, and Knight P L, *Introductory Quantum Optics*, Cambridge University Press, 2005.

[125] Nielson M A, and Chuang I L, *Quantum Computation and Quantum Information*, Cambridge University Press, Cambridge, 2000.

[126] Wheeler J A, and Zurek W H, *Quantum Theory and Measurement*, Princeton University Press, Princeton, NJ, 1983.

[127] Wiseman H M, and Milburn G J, *Quantum Measurement and Control*, Cambridge University Press, 2009.

[128] Breitenbach G, Schiller S, and Mlynek J, 'Measurement of the quantum states of squeezed light', *Nature*, **387**(6632), 1997, pp. 471–475.

[129] Ladd T D, Jelezko F, Laflamme R, *et al.*, 'Quantum Computing', *Nature*, **464**, 2010, pp. 45–53.

[130] Schumacher B, 'Quantum coding', *Phys Rev A*, **51**(4), 1995, pp. 2738–2747.

[131] Song C, Xu K, Li H, *et al.*, 'Generation of multicomponent atomic Schrödinger cat states of up to 20 qubits', *Science*, **365**(6453), 2019, pp. 574–577.

[132] Tian Y, Wang Z, Zhang P, *et al.*, 'Measurement of complete and continuous Wigner functions for discrete atomic systems', *Phys Rev A*, **97**(1), 2018, p. 013840.

[133] Mukherjee R, Mirasola A E, Hollingsworth J, *et al.*, 'Geometric representation of spin correlations and applications to ultracold systems', *Phys Rev A*, **97**(4), 2018, pp. 1–13.

[134] Chen B, Geng J, Zhou F, *et al.*, 'Quantum state tomography of a single electron spin in diamond with Wigner function reconstruction', *Appl Phys Lett*, **114**(4), 2019, p. 041102.

[135] Reiserer A, Kalb N, Rempe G, and Ritter S, 'A quantum gate between a flying optical photon and a single trapped atom', *Nature*, **508**(7495), 2014, pp. 237–240.

[136] Hacker B, Welte S, Daiss A Severin Shaukat, *et al.*, 'Deterministic creation of entangled atom–light Schrödinger-cat states', *Nat Photonics*, **13**(2), 2019, pp. 110–115.

[137] Haroche S, and Raimond J M, *Exploring the Quantum: Atoms, Cavities, and Photons*, Oxford: Oxford Univ. Press, 2006.

[138] Jaynes E T, and Cummings F W, 'Comparison of Quantum and Semiclassical Radiation Theories with Application to the Beam Maser', *Proc IEEE*, **51**(1), 1963, pp. 89–109.

[139] Andersen U L, and Ralph T C, 'High-fidelity teleportation of continuous-variable quantum states using delocalized single photons', *Phys Rev Lett*, **111**(5), 2013, pp. 1–5.

[140] Andersen U L, Neergaard-Nielsen J S, Van Loock P, and Furusawa A, 'Hybrid discrete- and continuous-variable quantum information', *Nat Phys*, **11**(9), 2015, pp. 713–719.

[141] Morin O, Huang K, Liu J, *et al.*, 'Remote creation of hybrid entanglement between particle-like and wave-like optical qubits', *Nat Photonics*, **8**, 2014, pp. 570–574.

[142] Gottesman D, Kitaev A, and Preskill J, 'Encoding a qubit in an oscillator', *Phys Rev A*, **64**(1), 2001, pp. 123101–1231021.

[143] Lee N, Benichi H, Takeno Y, *et al.*, 'Teleportation of nonclassical wave packets of light', *Science*, **332**(6027), 2011, pp. 330–333.

[144] Takeda S, Mizuta T, Fuwa M, *et al.*, 'Deterministic quantum teleportation of photonic quantum bits by a hybrid technique', *Nature*, **500**(7462), 2013, pp. 315–318.

[145] Van Loock P, Ladd T D, Sanaka K, *et al.*, 'Hybrid quantum repeater using bright coherent light', *Phys Rev Lett*, **96**(24), 2006, pp. 1–4.

[146] Ourjoumtsev A, Jeong H, Tualle-Brouri R, and Grangier P, 'Generation of optical "Schrödinger cats" from photon number states', *Nature*, **448**(7155), 2007, pp. 784–786.

[147] Datta A, Zhang L, Nunn J, *et al.*, 'Compact continuous-variable entanglement distillation', *Phys Rev Lett*, **108**(6), 2012, pp. 1–5.

[148] Lambert J H, 'Beiträge zum Gebrauch der Mathematik und deren Anwendungen', *Berlin, Verlag der Buchhandlung der Relschule*, 1772.

[149] Ralph T C, Gilchrist A, Milburn G J, *et al.*, 'Quantum computation with optical coherent states', *Phys Rev A*, **68**(4), 2003, p. 042319.

[150] Gilchrist A, Nemoto K, Munro W J, *et al.*, 'Schrödinger cats and their power for quantum information processing', *J Opt B*, **6**(8), 2004, pp. S828–S833.

Appendix A

Main Sections of Relevant Code

The Swift programming language is a protocol-oriented general purpose language that is strongly typed. Its use of data types and hardware acceleration mean that it has the potential for executing linear algebra routines very efficiently with minimal chance of variable overwrite. Further, given the creation of the language primarily for dealing with App development, its ability to produce fast visualizations with high functionality meant that it became an interesting candidate as the language of choice for this work. The following contains a few examples of the Swift code used for this work.

```
1  public protocol Contents {
2          func getPrimary() -> Array<Any>
3          func getSecondary() -> Array<Any>
4  }
5
6  Here is the Swift code used to convert the output data files from
       COLUMBUS into useable functions for plotting Wigner functions.
7
8  public struct File {
9      public private(set) var fileArray: [String] = [String]()
10         public var line: Int
11
12         public init(_ file: String, _ separator: String, _ lineIn:
       Int = 0) {
13                 line = lineIn
14         readFileToArray(file, separator)
15     }
16
17     private mutating func readFileToArray(_ file: String, _
       separator: String) {
18         do {
19             let fileContents = try String(contentsOfFile: file)
20
```

```
21              fileArray = fileContents.components(separatedBy:
    separator)
22          } catch {
23              print("something went wrong reading file: " + file)
24          }
25      }
26  }
27
28  public struct FileSection {
29          public let name: String
30          public private(set) var checked: Bool
31          public private(set) var contents: Contents
32          public private(set) var parse: (File) -> Contents
33
34          public init(name nameIn: String, checked checkedIn: Bool =
    false, contents contentsIn: Contents, parse parseIn: @escaping
    (File) -> Contents) {
35                  name = nameIn
36                  checked = checkedIn
37                  contents = contentsIn
38                  parse = parseIn
39          }
40
41          public mutating func addContents(file: File) {
42                  checked = true
43                  contents = parse(file)
44          }
45  }
46
47  public struct MoldenFile {
48      public private(set) var file: File
49          private var line: Int { get { return file.line } }
50          private var fileContent: [String] { get { return
    file.fileArray } }
51      public var sections: MoldenSections
52
53      public init(_ fileIn: String, separator: String = "\n") {
54                  file = File(fileIn, separator)
55          sections = MoldenSections()
56                  checkFormat()
57                  parse()
58      }
59
60      private mutating func checkFormat() {
61          if !sections.fileFormat.checked {
62              sections.fileFormat.checked = true
63
64              if
    (sections.fileFormat.type).localizedCaseInsensitiveContains(
    file.fileArray[file.line].trimmingCharacters(in: .whitespaces))
    {
65                  file.line += 1
66              } else {
67                  print("Incorrect Format: This file must be Molden
    file.")
68              }
69          }
70      }
```

```
71
72      private mutating func parse() {
73                  var sectionNumber = 0
74
75          while sectionNumber != -1 {
76              if sectionExists(sectionNumber) {
77                  file.line += 1
78                  sections.list[sectionNumber].addContents(file:
    file)
79                  sectionNumber = -1
80              }
81
82              sectionNumber += 1
83
84              if sectionNumber == sections.list.count {
85                  file.line += 1
86                  sectionNumber = -1
87              }
88          }
89
90          if line < fileContent.count {
91                          parse()
92          }
93
94          while line < fileContent.count {
95                          parse()
96          }
97      }
98
99          private func sectionExists(_ entry: Int) -> Bool {
100                 return fileContent[line].trimmingCharacters(in:
    .whitespaces).contains(sections.list[entry].name)
101         }
102 }
103
104 public struct MoldenParsers {
105         public static func atoms(_ file: File) -> [String] {
106                 let currentLine =
    file.fileArray[file.line].split(separator: " ")
107                 var contents = [String]()
108
109                 for bit in currentLine {
110                         contents.append(String(bit))
111                 }
112
113                 return contents
114         }
115
116         public static func GaussianTypeOrbital(_ fileIn: File) ->
    GaussianTypeOrbital {
117                 var file = fileIn
118                 var handler = GaussianTypeOrbitalHandler()
119
120                 file.line += 1
121                 handler.continueGaussianTypeOrbitalParse(file:
    &file)
122
123                 return handler.contents
```

```
124         }
125
126         public static func molecularOrbitals(_ fileIn: File) ->
    MolecularOrbitals {
127                 var file = fileIn
128                 var handler = MolecularOrbitalsHandler()
129
130                 handler.continueMolecularOrbitalsParse(file: &file)
131
132                 return handler.contents
133         }
134 }
135
136 public struct MoldenSections {
137     public var fileFormat = (type: "[MOLDEN FORMAT]", checked:
    false)
138     public var list = [FileSection(name: "[MO]",        contents:
    MolecularOrbitals(),  parse: MoldenParsers.molecularOrbitals),
139                        FileSection(name: "[GTO]",       contents:
    [[Double]](),                 parse:
    MoldenParsers.GaussianTypeOrbital),
140                        FileSection(name: "[ATOMS]", contents:
    [String](),                       parse: MoldenParsers.atoms)]
141 }
142
143 public struct GaussianTypeOrbitalBasis {
144         public private(set) var chis: [(Point) -> Double]
145         public private(set) var gaussians: [[(Point) -> Double]]
146
147         private let file: MoldenFile
148
149         public init(from fileIn: MoldenFile) {
150                 file = fileIn
151                 gaussians = [[(Point) -> Double]]()
152                 chis = [(Point) -> Double]()
153
154                 createGaussians()
155                 createChis()
156         }
157
158         private mutating func createGaussians() {
159                 let GaussianTypeOrbitalContent =
    file.sections.list[1].contents.getPrimary() as! [[Double]]
160
161                 for state in GaussianTypeOrbitalContent {
162                         var current = [(Point) -> Double]()
163
164                         for i in 0..<state.count/2 {
165                                 func gaussian(_ point: Point) ->
    Double {
166                                         return state[i*2] *
    exp(-1.0*state[i*2 + 1]*point.r*point.r)
167                                 }
168
169                                 current.append(gaussian)
170                         }
171
172                         gaussians.append(current)
```

```
173                 }
174         }
175
176         private mutating func createChis() {
177                 let chiList =
    file.sections.list[1].contents.getSecondary() as! [[(Point) ->
    Double]]
178                 let GaussianTypeOrbitalContent =
    file.sections.list[1].contents.getPrimary() as! [[Double]]
179
180                 for i in chiList.indices {
181                         for j in chiList[i].indices {
182                                 func chi(_ point: Point)
    -> Double {
183                                         var result = 0.0
184
185                                         for k in
    0..<GaussianTypeOrbitalContent[i].count/2 {
186                                                 result +=
    GaussianTypeOrbitalContent[i][k*2] *
    exp(-1.0*GaussianTypeOrbitalContent[i][k*2 + 1]*point.r*point.r)
187                                         }
188
189                                         return result *
    chiList[i][j](point)
190                                 }
191
192                                 chis.append(chi)
193                         }
194                 }
195         }
196 }
197
198 public struct MolecularOrbitalBasis {
199         public private(set) var phis: [(Point) -> Double]
200
201         private let file: MoldenFile
202
203         public init(from fileIn: MoldenFile) {
204                 file = fileIn
205                 phis = [(Point) -> Double]()
206
207                 createPhis()
208         }
209
210         private mutating func createPhis() {
211                 let molecularOrbitalCoefficients =
    file.sections.list[0].contents.getPrimary() as! [[Double]]
212                 let chis = GaussianTypeOrbitalBasis(from:
    file).chis
213
214                 for phiCoefficient in molecularOrbitalCoefficients
    {
215                         func phi(_ point: Point) -> Double {
216                                 var result = 0.0
217
218                                 for i in phiCoefficient.indices {
```

```
219                                             result +=
    phiCoefficient[i] * chis[i](point)
220                                     }
221
222                                     return result
223                             }
224
225                             phis.append(phi)
226                     }
227             }
228     }
229
230     public struct GaussianTypeOrbital: Contents {
231             public var orbitalCoefficients = [[Double]]()
232             public var orbitalHarmonic = [[(Point) -> Double]]()
233
234             public func getPrimary() -> Array<Any> {
235                     return orbitalCoefficients
236             }
237
238             public func getSecondary() -> Array<Any> {
239                     return orbitalHarmonic
240             }
241     }
242
243     public struct MolecularOrbitals: Contents {
244             public var coefficients = [[Double]]()
245             public var symmetries = [String]()
246             public var energies = [Double]()
247             public var spin = [String]()
248             public var occupation = [Double]()
249
250             public func getPrimary() -> Array<Any> {
251                     return coefficients
252             }
253
254             public func getSecondary() -> Array<Any> {
255                     return energies
256             }
257     }
258
259     public struct GaussianTypeOrbitalHandler {
260             public private(set) var orbital: Int
261             public var contents = GaussianTypeOrbital()
262
263             public init(_ orbitalIn: Int = -1, _
    orbitalCoefficientsIn: [[Double]] = [[Double]]()) {
264                     orbital = orbitalIn
265                     contents.orbitalCoefficients =
    orbitalCoefficientsIn
266                     contents.orbitalHarmonic = []
267             }
268
269             public mutating func
    continueGaussianTypeOrbitalParse(file: inout File) {
270                     let fileLine = file.fileArray[file.line]
271                     let currentTrimmedLine =
    fileLine.trimmingCharacters(in: .whitespaces)
```

```
272
273                 if currentTrimmedLine.contains("s") ||
    currentTrimmedLine.contains("p") ||
    currentTrimmedLine.contains("d") ||
    currentTrimmedLine.contains("f") {
274                         file.line += 1
275                         newOrbital()
276
    dealWithSphericalHarmonic(currentTrimmedLine)
277                         continueGaussianTypeOrbitalParse(file:
    &file)
278                 } else if currentTrimmedLine != "" {
279                         var currentLine =
    fileLine.split(separator: " ")
280
281                         currentLine.reverse()
282
283                         for bit in currentLine {
284                                 newCoefficient(bit)
285                         }
286
287                         file.line += 1
288                         continueGaussianTypeOrbitalParse(file:
    &file)
289                 }
290         }
291
292         private mutating func newOrbital() {
293                 orbital += 1
294                 contents.orbitalCoefficients.append([])
295         }
296
297         private mutating func newCoefficient(_ value: Substring) {
298
    contents.orbitalCoefficients[orbital].append(Double(value)!)
299         }
300
301         private mutating func dealWithSphericalHarmonic(_ symbol:
    String) {
302                 if symbol.contains("s") {
303
    contents.orbitalHarmonic.append([RealSphericalHarmonics.Y00])
304                 } else if symbol.contains("p") {
305                         dealWithPOrbital()
306                 } else if symbol.contains("d") {
307                         dealWithDOrbital()
308                 } else if symbol.contains("f") {
309                         dealWithFOrbital()
310                 }
311         }
312
313         private mutating func dealWithPOrbital() {
314
    contents.orbitalHarmonic.append([RealSphericalHarmonics.Y11,
315
                                 RealSphericalHarmonics.Y1m1,
316
                                 RealSphericalHarmonics.Y10])
```

```
317         }
318
319         private mutating func dealWithDOrbital() {
320
    contents.orbitalHarmonic.append([RealSphericalHarmonics.Y20,
321
                                RealSphericalHarmonics.Y21,
322
                                RealSphericalHarmonics.Y2m1,
323
                                RealSphericalHarmonics.Y22,
324
                                RealSphericalHarmonics.Y2m2])
325         }
326
327         private mutating func dealWithFOrbital() {
328
    contents.orbitalHarmonic.append([RealSphericalHarmonics.Y30,
329
                        RealSphericalHarmonics.Y31,
330
                        RealSphericalHarmonics.Y3m1,
331
                        RealSphericalHarmonics.Y32,
332
                        RealSphericalHarmonics.Y3m2,
333
                        RealSphericalHarmonics.Y33,
334
                        RealSphericalHarmonics.Y3m3])
335         }
336 }
337
338 public struct MolecularOrbitalsHandler {
339         public private(set) var orbital: Int
340         public private(set) var contents = MolecularOrbitals()
341
342         public init(_ orbitalIn: Int = -1) {
343                 orbital = orbitalIn
344         }
345
346         public mutating func continueMolecularOrbitalsParse(file:
    inout File) {
347                 let fileLine = file.fileArray[file.line]
348                 let trimmedLine = fileLine.trimmingCharacters(in:
    .whitespaces)
349
350                 if trimmedLine.contains("Sym") {
351                         let currentLine =
    fileLine.split(separator: " ")
352
353                         newOrbital()
354
    contents.symmetries.append(String(currentLine[1]))
355                         file.line += 1
356                         continueMolecularOrbitalsParse(file: &file)
357                 } else if trimmedLine.contains("Ene") {
```

```
358                         let currentLine =
    fileLine.split(separator: " ")
359
360
    contents.energies.append(Double(currentLine[1])!)
361                         file.line += 1
362                         continueMolecularOrbitalsParse(file: &file)
363                 } else if trimmedLine.contains("Spin") {
364                         let currentLine =
    fileLine.split(separator: " ")
365
366
    contents.spin.append(String(currentLine[1]))
367                         file.line += 1
368                         continueMolecularOrbitalsParse(file: &file)
369                 } else if trimmedLine.contains("Occup") {
370                         let currentLine =
    fileLine.split(separator: " ")
371
372
    contents.occupation.append(Double(currentLine[1])!)
373                         file.line += 1
374                         continueMolecularOrbitalsParse(file: &file)
375                 } else if trimmedLine != "" {
376                         let currentLine =
    fileLine.split(separator: " ")
377
378
    contents.coefficients[orbital].append(Double(currentLine[1])!)
379                         file.line += 1
380                         continueMolecularOrbitalsParse(file: &file)
381                 }
382         }
383
384         private mutating func newOrbital() {
385                 orbital += 1
386                 contents.coefficients.append([])
387         }
388 }
```

Presented also is the main code for producing a spin Wigner function in Swift which is then done for each point in phase space to construct the visualizations within this thesis.

```
1  public class Scene: SCNScene {
2          public init(plot: [[Double]], spinMatrix:
    ComplexSquareMatrix) {
3                         super.init()
4
5                         let texture =
    createWignerFunctionVisualisationRotated(state: spinMatrix,
    resolution: 100)
6                         let radius: CGFloat = 0.1
7                         let spheres = SCNNode()
8                         let normalisedData = normalise(data: plot,
    element: 3)
```

```
9                       let colourMap =
    RedBlueColourMap(magnitudes: texture, maximumValue: 0.5)
10
11                      for i in normalisedData.indices {
12                              let x = normalisedData[i][0]
13                              let y = normalisedData[i][1]
14                              let z = normalisedData[i][2]
15                              let value =
    CGFloat(abs(normalisedData[i][3]))
16
17                              if value > 0.01 {
18                                      let sphereGeometry =
    SCNSphere(radius: radius)
19                                      let sphereNode =
    SCNNode(geometry: sphereGeometry)
20
21
    sphereGeometry.firstMaterial?.diffuse.contents =
    colourMap.texture().cgImage()
22
    sphereGeometry.firstMaterial?.specular.contents = NSColor.white
23                                      sphereNode.position =
    SCNVector3(x: CGFloat(x), y: CGFloat(y), z: CGFloat(z))
24
    sphereGeometry.firstMaterial?.transparency = value
25
    spheres.addChildNode(sphereNode)
26                              }
27                      }
28
29                      self.rootNode.addChildNode(spheres)
30              }
31
32      public func
    createWignerFunctionVisualisationRotated(state:
    ComplexSquareMatrix, resolution: Int, wignerValue: Double =
    1.0) -> [Double] {
33              let harrMeasure = sqrt(3.0)
34              var zero = 0.0
35              var thetaIncrement =
    Double.pi/(2.0*Double(resolution))
36              var phiIncrement = Double.pi/Double(resolution)
37              var densityMatrix = ComplexSquareMatrix(dimension:
    0)
38              var wignerColorDensity =
    [Double](repeatElement(0.0, count: resolution*resolution))
39              var thetas = [Double](repeatElement(0.0, count:
    resolution))
40              var phis = [Double](repeatElement(0.0, count:
    resolution))
41              var kernelSU2 = ComplexSquareMatrix(dimension: 2)
42
43              densityMatrix = state
44              vDSP_vrampD(&zero, &thetaIncrement, &thetas, 1,
    UInt(thetas.count))
45              vDSP_vrampD(&zero, &phiIncrement, &phis, 1,
    UInt(phis.count))
46
```

```
47                  for thetaIndex in thetas.indices {
48                          let theta = thetas[thetaIndex]
49                          let cosTheta =
    harrMeasure*0.5*cos(2.0*theta)
50                          let sinTheta =
    harrMeasure*0.5*sin(2.0*theta)
51
52                          for phiIndex in phis.indices {
53                                  let phi = phis[phiIndex]
54
55                                  kernelSU2.setValue(0, 0, to: (0.5
    - (sinTheta*cos(2.0*phi)).r))
56                                  kernelSU2.setValue(0, 1, to:
    cosTheta - sinTheta*sin(2.0*phi).i)
57                                  kernelSU2.setValue(1, 0, to:
    cosTheta + sinTheta*sin(2.0*phi).i)
58                                  kernelSU2.setValue(1, 1, to: (0.5
    + sinTheta*cos(2.0*phi)).r)
59
60                                  var kernel = kernelSU2
61
62                                  for _ in
    1..<Int(log2(Double(densityMatrix.dimension))) {
63                                          kernel =
    kernel.kron(kernelSU2)
64                                  }
65
66                                  let wignerColorValue =
    kernel.trace(product: densityMatrix).realPart * wignerValue
67
68
    wignerColorDensity[thetaIndex*resolution + phiIndex] =
    wignerColorValue / Double.pi
69                          }
70                  }
71
72                  return wignerColorDensity
73          }
74  }
```

Appendix B

Visualizing spin degrees of freedom in atoms and molecules

Visualizing spin degrees of freedom in atoms and molecules

B. I. Davies,[1] R. P. Rundle,[1,2] V. M. Dwyer,[1,2] J. H. Samson,[1] Todd Tilma,[3,4,1] and M. J. Everitt[1,*]

[1]*Quantum Systems Engineering Research Group, Department of Physics, Loughborough University, Loughborough LE11 3TU, United Kingdom*

[2]*The Wolfson School, Loughborough University, Loughborough LE11 3TU, United Kingdom*

[3]*Department of Physics, College of Science, Tokyo Institute of Technology, H-63, 2-12-1 Ōokayama, Meguro-ku, Tokyo 152-8550, Japan*

[4]*Quantum Computing Unit, Institute of Innovative Research, Tokyo Institute of Technology, S1-16, 4259 Nagatsuta-cho, Midori-ku, Yokohama 226-8503, Japan*

(Received 30 April 2019; published 1 October 2019)

In this work we show how constructing Wigner functions of heterogeneous quantum systems leads to new capability in the visualization of quantum states of atoms and molecules. This method allows us to display quantum correlations (entanglement) between spin and spatial degrees of freedom (spin-orbit coupling) and between spin degrees of freedom, as well as more complex combinations of spin and spatial entanglement. This is important as there is growing recognition that such properties affect the physical characteristics, and chemistry, of atoms and molecules. Our visualizations are sufficiently accessible that, with some preparation, those with a nontechnical background can gain an appreciation of subtle quantum properties of atomic and other systems. By providing insights and modeling capability, our phase-space representation will be of great utility in understanding aspects of atomic physics and chemistry not available with current techniques.

DOI: 10.1103/PhysRevA.100.042102

I. INTRODUCTION

Despite its fundamental flaws, the Rutherford description of the atom as electrons orbiting a nucleus is an established icon of the physical sciences. This provides a familiar image with which to start a discussion of matter at the subatomic level. In such discussions one rapidly moves towards a more sophisticated view of a set of atomic and molecular orbitals, generally displayed as the 90th percentile of the probability density of the associated quantum-mechanical energy eigenstate. These images represent a much more accurate view; however, some simplifications remain. For example, they are unable to display the entanglement of spin and spatial degrees of freedom due to coupling between the spin of an electron and its orbital angular momentum. This spin-orbit coupling contains key features that change the shape of an energy eigenstate as well as affecting chemical properties such as dissociation energy [1–4]. Given the growing recognition that phenomena such as spin-orbit coupling play an important role in some chemical reactions [5–7], there is a need for tools to help better understand these processes.

In this work we bring insight to atomic systems by presenting a framework for visualizing states such as those found using modern quantum-chemistry numerical simulations (which include both spin and entanglement [8–11]). To do this we extend the standard picture of the probability density to the full atomic phase space, including spin degrees of freedom. While there have been a number of previous attempts to visualize atoms using these techniques, none have so far included spin [12–16]. Representing atoms and molecules in phase space (via Wigner functions) allows for a complete description of the quantum state as a quasiprobability density function. While Refs. [17,18] lay down the necessary framework for heterogeneous systems (by which we mean systems combining differing continuous phase-space representations), we are aware of only two other examples considering the Wigner functions of heterogeneous quantum systems completely within phase space. Reference [19] considers using the Wigner function as an entanglement witness for hybrid bipartite states. Reference [20] investigates the phase-space representation of one or more two-level systems coupled to a cavity mode in the Jaynes- and Tavis-Cummings models. Our simple procedure however, allows for the construction of Wigner functions of composite heterogeneous systems.

We demonstrate below how such methods can be used to visualize spin-orbital, spin-spin, and other more complex entanglement combinations of spin and spatial degrees of freedom. We expect that this capability will find great utility in understanding important electronic transfer processes such as photosynthesis (PSI and PSII), the avian compasses, and oxygen transport via hemoglobin in blood [21–26]. Having said this, spin-orbital entanglement is not trivial, particularly for many-electron systems which often have many internal correlations between electrons. It is with these future applications in mind that we demonstrate a more accurate visualization of the atom: one that is familiar, yet at the same time offers more insight into the internal entanglement effects that determine many atomic properties [2–4,10,27].

*m.j.everitt@physics.org

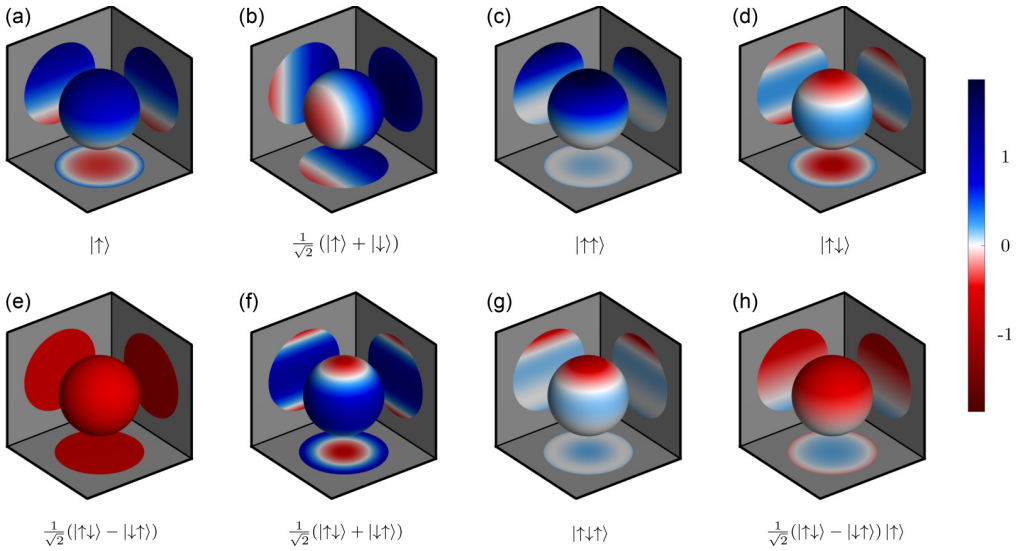

FIG. 1. A set of reference plots of spin Wigner functions to aid interpretation of the results presented later in this work. The state vectors for each Wigner function are given under each image. Multispin states have been plotted on the equal-angle slice, $\theta_i = \theta$ and $\phi_i = \phi$ for all i. Note that panel (c) is the product of two states which individually are the same as those in panel (a), panel (g) is the product of panels (a) and (d), and panel (h) is the product of panels (a) and (e). See Ref. [28] for a full discussion. For those in black and white, note that the top of the sphere in panel (a) is positive and blue and that panel (e) is uniformly red and negative. The top of the color bar is blue and the bottom is red.

II. PARTICLES IN PHASE SPACE

It is possible to write the state of any system as a quasiprobability distribution over the system's degrees of freedom [17,18,28]. This is termed the Wigner function and can be calculated by taking the expectation value of a suitably displaced parity operator over all its possible configurations (the phase space). For the electron this generalized parity is the tensor product of the displaced spatial parity $\hat{\Pi}_i(\mathbf{q}_i, \mathbf{p}_i)$ and the generalized displaced spin-parity $\hat{\pi}_i(\theta_i, \phi_i)$:

$$\hat{\Pi}_i^{e^-}(\mathbf{q}_i, \mathbf{p}_i, \theta_i, \phi_i) = \hat{\Pi}_i(\mathbf{q}_i, \mathbf{p}_i) \otimes \hat{\pi}_i(\theta_i, \phi_i). \tag{1}$$

The spatial parity $\hat{\Pi}$ is the operator that reflects states through the origin in phase space, displaced by the displacement operator $\hat{D}_i(\mathbf{q}_i, \mathbf{p}_i) = \exp(i[\mathbf{p}_i \cdot \hat{\mathbf{q}}_i - \mathbf{q}_i \cdot \hat{\mathbf{p}}_i]/\hbar)$ so that $\hat{\Pi}_i(\mathbf{q}_i, \mathbf{p}_i) = \hat{D}_i(\mathbf{q}_i, \mathbf{p}_i)\hat{\Pi}\hat{D}_i^\dagger(\mathbf{q}_i, \mathbf{p}_i)$ [29]. The generalized spin-parity is $\hat{\pi} = (\mathbb{1} + \sqrt{3}\sigma_z)/2$ and is chosen over a parity operator with eigenvalues ± 1 so that it satisfies Stratonovich-Weyl conditions [28]. The displacement operator for spin is $\hat{U}(\theta, \phi, \Phi) = \exp(i\hat{\sigma}_z\phi)\exp(i\hat{\sigma}_y\theta)\exp(i\hat{\sigma}_z\Phi)$ so that $\hat{\pi}_i(\theta_i, \phi_i) = \hat{U}_i(\theta_i, \phi_i, \Phi_i)\hat{\pi}\hat{U}_i^\dagger(\theta_i, \phi_i, \Phi_i)$ for Euler angles θ_i and ϕ_i (note that the third angle Φ_i cancels and plays no part in the Wigner function). Given our focus on atomic physics and chemistry applications rather than quantum information, a sign convention is used for $\hat{U}(\theta, \phi, \Phi)$ and $\hat{\pi}$ that is different from that used in Refs. [17,18,28] so that the Wigner function for $\sigma_z = +1$, i.e., spin up, points up. Note that the negative values in the Wigner function have manifested due to spin-half systems not being classical [30,31]; a full discussion of this approach can be found in Ref. [28] with exploration of other spin systems. There have been a number of other attempts to describe spin systems, such as Refs. [17,18,28,31–37]. However, none of these have also included the spatial degrees of freedom needed to fully describe the quantum state of atoms and molecules.

The Wigner function for a composite system is found by taking expectation values of the tensor product of the displaced parity for each of the constituent parts. The examples shown in Fig. 1 provide a visual index of some important spin Wigner functions that will be used to inform later discussions, where the total spin-parity is $\bigotimes_i \hat{\pi}_i(\theta_i, \phi_i)$ over the appropriate set of spins. Note that throughout the paper, blue is positive, red is negative, and white always corresponds to 0 (see colorbar in Fig. 1).

For an N-electron atom, ignoring the nucleus, with density matrix $\hat{\rho}$ the Wigner function will be

$$W(\mathbf{q}_1, \mathbf{p}_1, \theta_1, \phi_1, \ldots) = \mathrm{Tr}[\hat{\rho}\,\hat{\Pi}(\mathbf{q}_1, \mathbf{p}_1, \theta_1, \phi_1, \ldots)], \tag{2}$$

where

$$\hat{\Pi}(\mathbf{q}_1, \mathbf{p}_1, \theta_1, \phi_1, \ldots) = \bigotimes_{i=1}^{N} \hat{\Pi}_i^{e^-}(\mathbf{q}_i, \mathbf{p}_i, \theta_i, \phi_i). \tag{3}$$

The generalized displaced parity for each electron has eight dimensions of which three are the spatial degrees of freedom, x_i, y_i, and z_i; three are the concomitant momentum degrees of freedom; and two are the spin degrees of freedom, θ_i and ϕ_i. The Wigner function is therefore an $8N$-dimensional function—distilling from this function meaningful visualizations of atomic states is the subject of the next section.

How we choose to visualize the Wigner function depends very much on the application at hand. If, for example, the system is an electron in a periodic lattice, where momentum states are well defined, we might start by integrating out position degrees of freedom. This would yield a function that combines the probability density in the momentum representation with the spin Wigner function. If instead the system

is an electron exposed to a potential that is periodic in one dimension and quadratic in perpendicular directions (such as a quantum wire or ion trap) it seems appropriate to integrate out the position degrees of freedom for the periodic component and the momentum degrees of freedom for the other components. This would yield a function that combines the probability density function in the momentum representation for the periodic dimension, the position representation of the probability density, and the spin Wigner function.

It is possible to extend our method to include the nucleus using a suitable spin-parity operator to represent the overall nuclear spin. The total atomic Wigner function is then obtained by taking expectation values of

$$\hat{\Pi}^{\mathrm{He}}_{\text{with nucleus}} = \hat{\Pi}_{\text{nucleus}} \otimes \hat{\Pi}^{e^-}_1 \otimes \hat{\Pi}^{e^-}_2, \tag{4}$$

which may be of interest for systems where the Jahn-Teller effect is important (see Refs. [17,18] for details on how to construct $\hat{\Pi}_{\text{nucleus}}$ for a given nuclear spin). If more detail is required, displaced parity operators for protons and neutrons could be used so that

$$\hat{\Pi}^{\mathrm{He}}_{\text{total}} = \hat{\Pi}^{p^+}_1 \otimes \hat{\Pi}^{p^+}_2 \otimes \hat{\Pi}^{n}_1 \otimes \hat{\Pi}^{n}_2 \otimes \hat{\Pi}^{e^-}_1 \otimes \hat{\Pi}^{e^-}_2. \tag{5}$$

If still more detail is required, it may even be possible to write the phase-space representation for each nucleon's constituent parts (see Refs. [17,18] for details on how to construct generalized displaced parity operators such as those needed for other spins and color).

In a similar way, to describe an atom interacting with a field, or indeed molecules, the total parity is the tensor product of the parities of all the system's constituent parts. This leads to a Wigner phase-space representation of the total quantum state.

III. RESULTS

In this section we obtain a Wigner function visualization for a range of atomic states. The states we consider are pure states of the atom before integration over degrees of freedom. At this stage, in order to simplify calculations, we use a model atom representation which replaces the Coulomb confining potential with that of a three-dimensional harmonic oscillator (as in Ref. [38]) and is similar in form to the Hooke and Moshinsky atoms in the noninteracting electron model [9–11,39–41]. This approximation does not alter the angular distributions of the eigenstates and provides an adequate first approximation to the radial dependence of real hydrogenic systems which is sufficient for our present purposes. It has the additional advantage of allowing the calculation of momentum-only representations, such as are required for the visualization of Compton scattering profiles (see, for example, Refs. [42,43]).

The states of hydrogen, helium, and lithium referred to below are obtained within this approximation; however, for simplicity, such states are referred to by their corresponding atomic name.

A. Hydrogen

Even though hydrogen is a one-electron system, the Wigner function is eight dimensional (with three spatial $\mathbf{q}$, three momentum $\mathbf{p}$, and two spin degrees of freedom). To produce from this a representation of hydrogen as similar as possible to existing images we integrate out the momentum degrees of freedom:

$$W^{\mathrm{H}}(\mathbf{q}, \theta, \phi) := \int d^3\mathbf{p}\, W^{\mathrm{H}}(\mathbf{q}, \mathbf{p}, \theta, \phi). \tag{6}$$

In contrast to tracing out entire components we have here reduced complexity by using marginals to integrate out individual degrees of freedom (the momentum) while still retaining others (position). This results in a reduced Wigner function of only three spatial and two spin degrees of freedom. We adopt the notation throughout this work that the degrees of freedom not in the argument list have been integrated out resulting in a reduced Wigner function. We now consider a visualization strategy that seeks to display as much of this information as possible, while being constrained by our requirement to make this as familiar as possible.

For the visualization we choose a set of points in space [44]. At each of these points a sphere is plotted with its opacity, α, obtained from the value of

$$|\psi^{\mathrm{H}}(\mathbf{q})|^2 = W^{\mathrm{H}}(\mathbf{q}) = \frac{2}{\pi}\int_0^{\pi/2} d\theta \int_0^{\pi} d\phi\, \sin(2\theta) W^{\mathrm{H}}(\mathbf{q}, \theta, \phi), \tag{7}$$

as $\alpha = W^{\mathrm{H}}(\mathbf{q})/W^{\mathrm{H}}_{\max}(\mathbf{q})$. This position marginal is simply the spatial probability density function. In order to more readily make comparison with standard orbital plots, all spheres with an opacity less than 0.1 have been omitted. On the surface of the sphere at $\mathbf{q}$ is plotted the reduced Wigner function $W^{\mathrm{H}}(\mathbf{q}, \theta, \phi)$. This means that each sphere is an indication of the probability of finding an electron at that point in space with a certain spin.

As a gentle introduction to our visualization scheme a simple state generated using the above scheme is plotted in Fig. 2. The spatial dependence conforms to standard plots of d_{z^2} orbitals of hydrogen. Comparing each sphere with Fig. 1(a), the spin Wigner function at each point is consistent with the up state, $|\uparrow\rangle$. From inspection we have been able to correctly infer that this is $|d_{z^2}, \uparrow\rangle$ [45].

Figure 3 shows a less trivial state. It is interesting to explore what can be deduced from only this figure and Fig. 1. The first observation is that the spheres are identical to that in Fig. 1(a) but pointing in different directions. The more opaque spheres are predominantly pointing in one direction suggesting there is a corresponding overall spin magnetic moment. Second, the direction of the spin varies as a function of position—this is an indication of correlation (entanglement) of the electron's spin and spatial degrees of freedom [46]. Neither of these two pieces of information are obtainable from conventional plots of atomic orbitals.

In real atomic hydrogen the total energy is more than the sum of kinetic and Coulomb potential energies. There are a number of relativistic effects that need to be taken into account in order to get an accurate model that, for example, correctly predicts the energy level structure and thus the absorption and emission spectra of hydrogen. One of the most important of these relativistic effects is the spin-orbit coupling term (proportional to $\hat{\mathbf{L}} \cdot \hat{\mathbf{S}}$). In Fig. 3 is a state that takes account

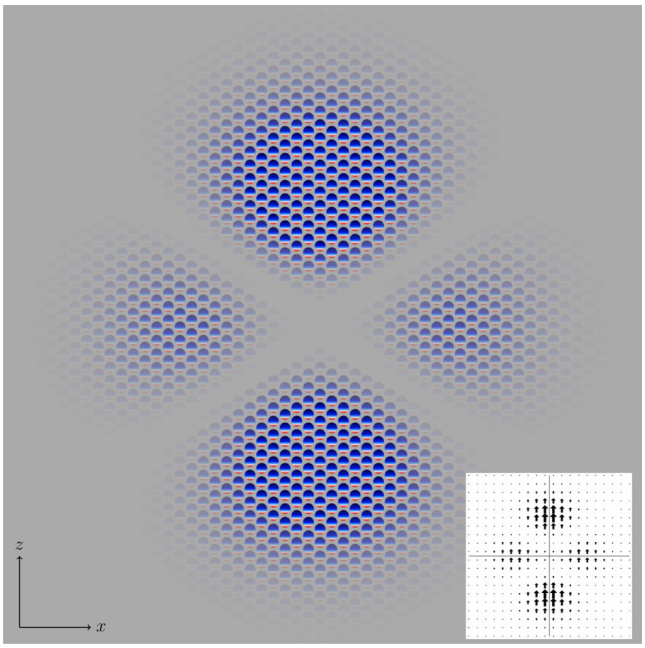

FIG. 2. This figure displays the spin-up $3d_{z^2}$ orbital for the three-dimensional harmonic oscillator. The Wigner function for this orbital has eight dimensions:at the three spatial x, y, and z degrees of freedom; the concomitant momentum degrees of freedom; and two spin degrees of freedom, θ and ϕ. To obtain the familiar orbital structure, all momentum and spin degrees of freedom are integrated out to yield the probability density function in terms of position. These values are used to set the opacity (α) of each sphere, neglecting all points where $\alpha < 0.1$. At each point $\mathbf{q}$ in the xz plane we plot the reduced Wigner function $W^{\mathrm{H}}(\mathbf{q}, \theta, \phi)$ on a sphere as in Fig. 1 [see Eq. (6)]. Each sphere can then be interpreted as an indication of the probability of finding an electron at $\mathbf{q}$ with a certain spin. In this plot, which has rotational symmetry about the z axis, the state of the system is of the same form as an $n = 3, l = 2$, and $m = 0$ d orbital of hydrogen with spin pointing up [see Fig. 1(a)]. To aid interpretation, the inset shows an equivalent plot using arrows to represent the spin; i.e., the arrows show the direction of the spin component (Bloch vector) at each point in position space.

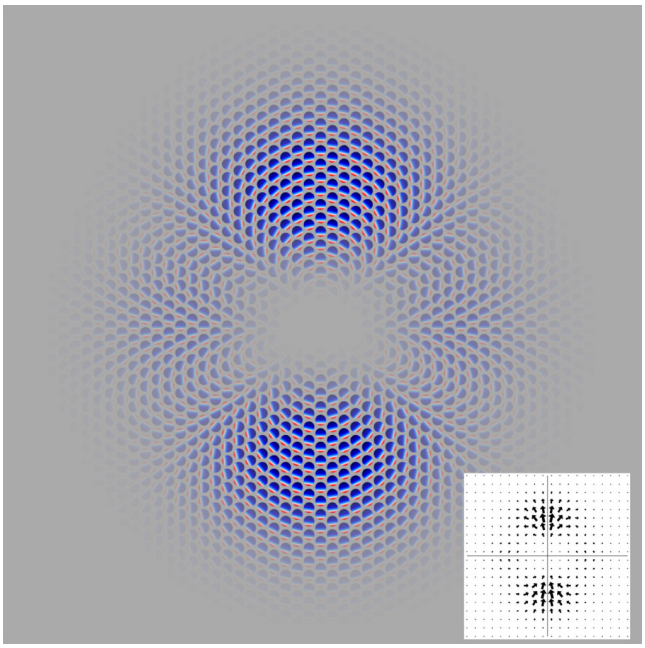

FIG. 3. Due to relativistic effects in the Hamiltonian of real atomic hydrogen, states such as the one shown in Fig. 2 are not stationary. One of the most important corrections arises due to a coupling between spin and orbital angular momentum degrees of freedom. This affects every state, other than the s orbitals, and the result is that the energy eigenstates have entangled spin and spatial degrees of freedom. Such entanglement cannot be made visible using conventional probability density plots. This figure follows the same scheme as Fig. 2 but for the $|j = 5/2, m = 1/2\rangle$ orbital; it is clear that there are correlations between the spin and spatial degrees of freedom. In this way we demonstrate how our method can visualize the entanglement of the electron's spin and orbital degrees of freedom, as the spin points in different directions at different positions. The inset shows an equivalent plot using arrows to represent the spin.

of such correlations. Specifically,

$$\left|j = \frac{5}{2}, m = \frac{1}{2}\right\rangle = \sqrt{\frac{3}{5}}|d_{z^2}\rangle|\uparrow\rangle + \sqrt{\frac{1}{5}}(|d_{xz}\rangle + i|d_{yz}\rangle)|\downarrow\rangle, \tag{8}$$

which, as we deduced in our above discussion of Fig. 3, has a nonzero magnetization (1/2), strongly entangles spin and spatial degrees of freedom and has an entropy of entanglement of 0.971 bits. We note that the eigenstates $|j, m\rangle$ are labeled by j, the quantum number associated with $\hat{J}^2 = (\hat{\mathbf{L}} + \hat{\mathbf{S}})^2$, and m, the eigenvalue of $\hat{J}_z = \hat{L}_z + \hat{S}_z$ for orbital and spin angular momenta $\hat{\mathbf{L}}$ and $\hat{\mathbf{S}}$, respectively. These two pictures then are not only able to distinguish between states with spin-orbit coupling and those without but also are able to make clear spin-spatial correlations. Figure 3 has different spin states of the electron at different positions, encapsulating the definition of pure state entanglement visually. That is, this is a direct manifestation of, and can be mapped back to, the fact that the spin of a particle cannot be described independently of its position.

B. Helium

We now begin to consider the case of multielectron atoms. Helium's Wigner function is 16 dimensional having three spatial, three momentum and two spin degrees of freedom for each electron. To obtain the graphical representation of helium we use a scheme to the one used for hydrogen, also taking account of the Wigner function's increased dimensionality. Once more a reduced Wigner function is calculated, $W^{\mathrm{He}}(\mathbf{q}_1, \theta_1, \phi_1, \theta_2, \phi_2)$, integrating out both electrons' momenta and one of the electron's spatial degrees of freedom (indistinguishability of electrons means that it will not matter which one is chosen). Here the function $W^{\mathrm{He}}(\mathbf{q}_1) = |\psi^{\mathrm{He}}(\mathbf{q}_1)|^2$, defined in the same manner as in Eq. (7), by integrating out all spin degrees of freedom, is again used to set the intensity. In plotting multielectron systems, we choose the equal-angle slice of the Wigner function for the spin degrees of freedom, where $\theta_1 = \theta_2$ and $\phi_1 = \phi_2$. Choosing this slice has the advantage of keeping the figures familiar in the context of the literature, for example, states found in Ref. [33]. It not

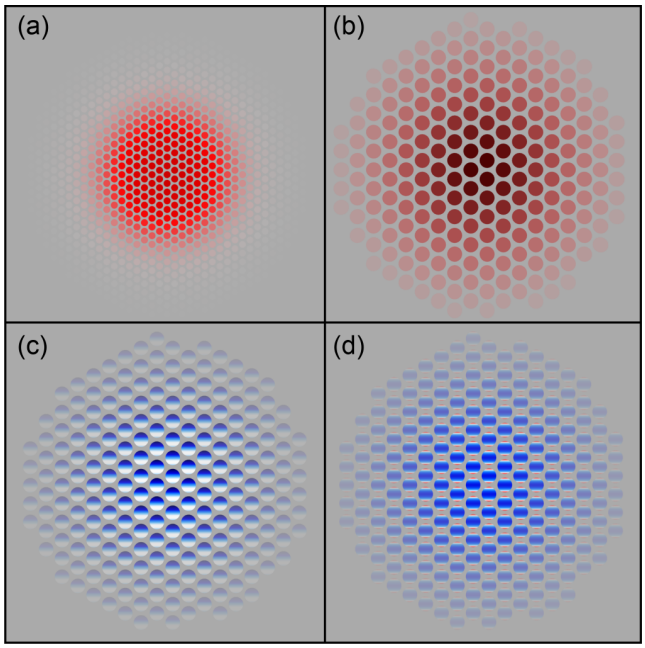

FIG. 4. This figure shows the equal-angle slice, $\theta_1 = \theta_2 = \theta$ and $\phi_1 = \phi_2 = \phi$, of the Wigner function for the following states of helium: (a) ground state, (b) first excited singlet, (c) first triplet state with magnetization quantum number $m = 1$ (note for $m = -1$ each sphere would be the antipodal version of the ones shown here), and (d) first triplet state with magnetization quantum number $m = 0$. Comparing each figure with Fig. 1 we see that panels (a) and (b) correspond to the entangled state in Fig. 1(e) and that panel (d) corresponds to the entangled state in Fig. 1(f). Panel (c) corresponds to the nonentangled state in Fig. 1(c). In this way we demonstrate how our method clearly visualizes not only spin-orbit entanglement (as in Fig. 3) but also spin-spin entanglement.

only allows us to relate certain states to other representations of the Wigner function but also allows us to pull out additional useful information (such as the ability to represent the singlet state). This slice is then plotted on the surface of each of the spheres in Fig. 4 for helium.

In Fig. 4 we have plotted the ground state [Fig. 4(a)], the first excited singlet state [Fig. 4(b)], and two of the triplet states [Figs. 4(c) and 4(d)] of helium. In the ground state we see three key features: (i) with reference to Fig. 1(d), each sphere is consistent with that of the two-spin singlet state (the antisymmetric superposition of spin up and spin down, and not $|\uparrow\downarrow\rangle$ as in Fig. 1(c), often indicated in elementary treatments of the subject); (ii) the intensity in this plot suggests the spatial component is the product of two s orbitals; and (iii) there is no dependence of spin on position, consistent with the spin and spatial degrees of freedom being separable. These observations are consistent with the ground state of helium, $|1S(1)1S(2)\rangle(|\uparrow_1\downarrow_2\rangle - |\downarrow_1\uparrow_2\rangle)/\sqrt{2}$ [47]. A comparison of the spins with Fig. 1 for the remaining states demonstrates that both Figs. 1(b) and 1(d) are in an entangled spin state, while Fig. 1(c) is not.

C. Lithium

As with helium, lithium is often introduced along the following simplified lines: two electrons are added to the $1S$ orbital with opposite spin, as dictated by the Pauli exclusion principle. It also states that the third electron cannot be in the $1S$ orbital as it is now fully occupied. This electron must therefore go into the $2S$ orbital with spin $|\uparrow\rangle$ for example. The actual configuration of electrons in lithium is not this simple.

The state of multifermionic systems can be found using the Slater determinant, which ensures that Pauli's exclusion principle is properly satisfied and for lithium is

$$|\psi^{\mathrm{Li}}\rangle = \frac{1}{\sqrt{3!}}\begin{vmatrix} |1S(1)\rangle|\uparrow_1\rangle & |1S(1)\rangle|\downarrow_1\rangle & |2S(1)\rangle|\uparrow_1\rangle \\ |1S(2)\rangle|\uparrow_2\rangle & |1S(2)\rangle|\downarrow_2\rangle & |2S(2)\rangle|\uparrow_2\rangle \\ |1S(3)\rangle|\uparrow_3\rangle & |1S(3)\rangle|\downarrow_3\rangle & |2S(3)\rangle|\uparrow_3\rangle \end{vmatrix}, \tag{9}$$

yielding

$$\begin{aligned} |\psi^{\mathrm{Li}}\rangle = \frac{1}{\sqrt{6}}[&|1S(1)1S(2)2S(3)\rangle(|\uparrow_1\downarrow_2\rangle - |\downarrow_1\uparrow_2\rangle)|\uparrow_3\rangle \\ &+ |1S(1)2S(2)1S(3)\rangle(|\downarrow_1\uparrow_3\rangle - |\uparrow_1\downarrow_3\rangle)|\uparrow_2\rangle \\ &+ |2S(1)1S(2)1S(3)\rangle(|\uparrow_2\downarrow_3\rangle - |\downarrow_2\uparrow_3)|\uparrow_1\rangle] \end{aligned} \tag{10}$$

or

$$\begin{aligned} = \frac{1}{\sqrt{6}}[&|\uparrow_1\uparrow_2\downarrow_3\rangle(|2S(1)1S(2)\rangle - |1S(1)2S(2)\rangle)|1S(3)\rangle \\ &+ |\uparrow_1\downarrow_2\uparrow_3\rangle(|1S(1)2S(3)\rangle - |2S(1)1S(3)\rangle)|1S(2)\rangle \\ &+ |\downarrow_1\uparrow_2\uparrow_3\rangle(|2S(2)1S(3)\rangle - |1S(2)2S(3)\rangle)|1S(1)\rangle]. \end{aligned} \tag{11}$$

The ground state of lithium is a superposition of Slater determinants but here we shall only consider this one. From Eq. (10), it can be seen that there is bipartite entanglement between each spin degree of freedom. There is also a nontrivial level of spin-spatial entanglement combining these bipartite entangled spin states. Entanglement such as this could be an important factor in determining physical and chemical properties [2–4,10,27]. Therefore, being able to get a grasp of such phenomena without necessarily analyzing the full mathematics would be of tremendous value. We now explore an example of how our visualization strategy can be utilized in achieving such an ambition.

Lithium has a 24-dimensional Wigner function (the usual eight dimensions for each electron). Due to the added complexity of lithium, it is now necessary to look at different slices of the Wigner function. As before all momentum degrees of freedom have been integrated out; however, spin degrees of freedom have also been integrated out, appropriate to each figure. For those slices with multiple electron spin degrees of freedom remaining, the equal-angle slice is used. We show a selection of different slices in Fig. 5. Although we have restricted this discussion to the four slices presented, other slices could be chosen to explore different features of the state.

In Fig. 5(a), the spatial degrees of freedom $\mathbf{q}_2$ and $\mathbf{q}_3$ have been integrated out. This leaves the reduced Wigner function $W^{\mathrm{Li}}(\mathbf{q}_1, \theta_1, \phi_1, \theta_2, \phi_2, \theta_3, \phi_3)$. The function behavior at the origin of Fig. 5(a) is similar to that displayed in Fig. 1(h). It is important to note that the state differs from Fig. 1(h) because what is shown is not itself pure. The reason for it being mixed is that this is a single slice of the full Wigner function with entangled degrees of freedom integrated out. Points far from

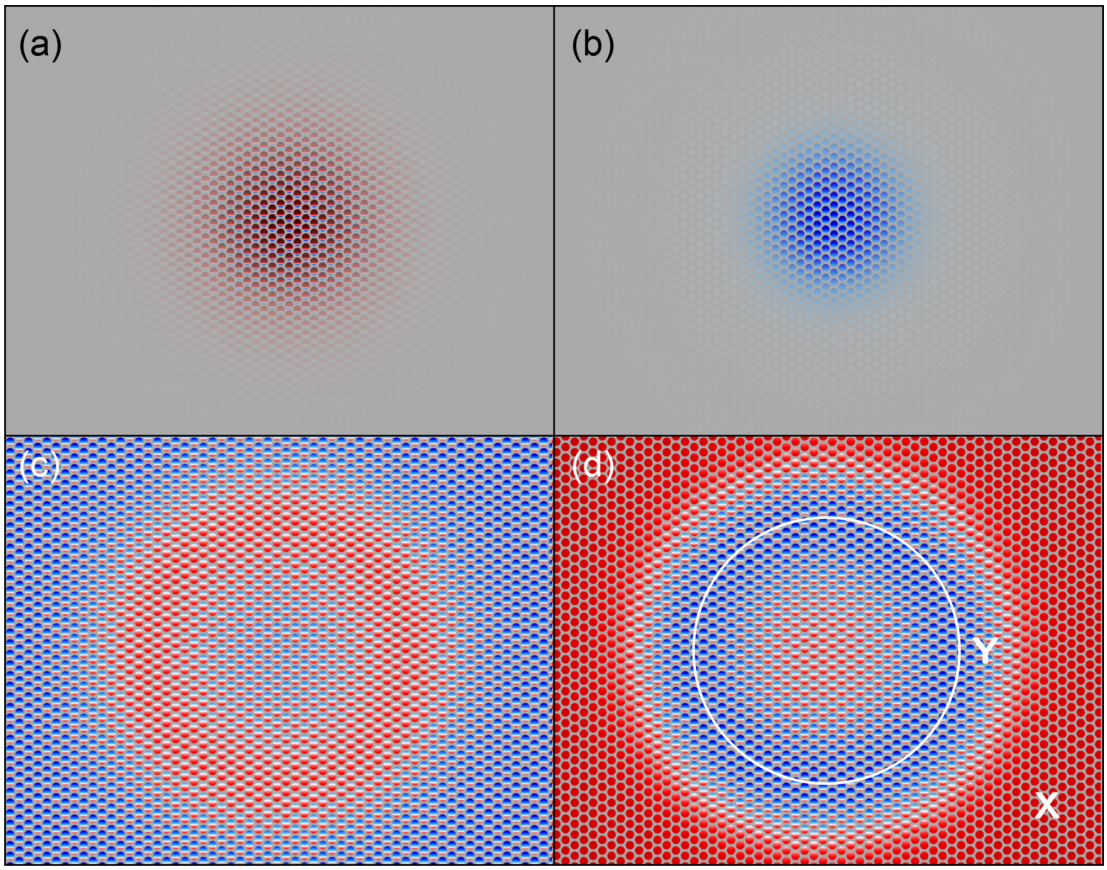

FIG. 5. Showcasing the power of the Wigner function we demonstrate how to reconstruct all the important aspects of the Slater determinant for lithium by inspection of different slices (these figures are on a different scale to others to accommodate the $2S$ orbital). We follow the same scheme as in Fig. 4, on the equal-angle slice where appropriate. In panel (a) is the reduced Wigner function $W^{\mathrm{Li}}(\mathbf{q}_1, \theta_1, \phi_1, \theta_2, \phi_2, \theta_3, \phi_3)$, which at the origin is similar to that displayed in Fig. 1(h). Importantly, this shows that the spin entanglement structure in Fig. 1(h) is part of the state. In panel (b) we extract the electron spin density, plotting the reduced Wigner function $W^{\mathrm{Li}}(\mathbf{q}_1, \theta_1, \phi_1)$. This means that lithium must have an overall magnetic moment and, by comparison with Fig. 1(a), we see this manifested as the preponderance of blue, positive values, in the positive z direction. In panels (c) and (d) we have removed the link between transparency and amplitude of the position marginal to explore some of the more complex aspects of the quantum correlations. Panel (c) shows the reduced Wigner function $W^{\mathrm{Li}}(\mathbf{q}_1, \theta_1, \phi_1, \theta_2, \phi_2)$. Note that integrating out θ_2 and ϕ_2 instead yields the same result, as the only spatial component is $\mathbf{q}_1$. Panel (d) shows the reduced Wigner function $W^{\mathrm{Li}}(\mathbf{q}_1, \theta_2, \phi_2, \theta_3, \phi_3)$. At point X, when $\mathbf{q}_1$ is likely to be in the $2S$ orbital, we find the singlet state $|\uparrow_2 \downarrow_3\rangle - |\downarrow_2\uparrow_3\rangle$. At the same point in panel (c), the state is similar to spin up. From both of these figures then, the spin state they are visualizing is consistent with $|\uparrow_1\rangle(|\uparrow_2 \downarrow_3\rangle - |\downarrow_2\uparrow_3\rangle)$. In panel (d), the node of the $2S$ orbital (indicated by the ring Y) has spin states similar to spin up. This means that when $\mathbf{q}_1$ is likely to be in the $1S$ orbital, one of the other electrons is likely to be spin up. Putting the information from panels (c) and (d) together we deduce a state consistent with $|2S(1), 1S(2), 1S(3)\rangle(|\uparrow_2 \downarrow_3\rangle - |\downarrow_2\uparrow_3\rangle)|\uparrow_1\rangle$. Coupled with the fact that the pictures must be invariant under cyclic permutation of electron indices (Pauli's exclusion principle), we infer that the state is $|\psi^{\mathrm{Li}}\rangle = \frac{1}{\sqrt{6}}[|1S(1), 1S(2), 2S(3)\rangle(|\uparrow_1 \downarrow_2\rangle - |\downarrow_1\uparrow_2\rangle)|\uparrow_3\rangle + |1S(1), 2S(2), 1S(3)\rangle(|\downarrow_1\uparrow_3\rangle - |\uparrow_1 \downarrow_3\rangle)|\uparrow_2\rangle + |2S(1), 1S(2), 1S(3)\rangle(|\uparrow_2 \downarrow_3\rangle - |\downarrow_2\uparrow_3\rangle)|\uparrow_1\rangle]$.

the origin tend towards the pure variation of Fig. 1(h), where an electron is in the up state and likely to be found in the $2S$ orbital. This slice is consistent with the description of lithium as a singlet state in the $1S$ orbital coupled with a spin up in the $2S$ orbital.

Figure 5(b) is a plot of the reduced Wigner function $W^{\mathrm{Li}}(\mathbf{q}_1, \theta_1, \phi_1)$. This slice gives us insight into the electron spin density, revealing the magnetization of lithium. Lithium has an overall magnetic moment which is manifested as the preponderance of blue in the up direction [compare with Fig. 1(a)]. There are no negative values in this plot as a sufficient amount of entanglement information has been integrated out.

Figures 5(c) and 5(d) explore some of the more complex aspects of the quantum correlations within lithium, which combine both spin-spin and spin-orbit entanglement. To study these entanglement effects in more detail, we have removed the link between transparency and amplitude of the position marginal.

Figure 5(c) is the equal-angle slice of the reduced Wigner function $W^{\mathrm{Li}}(\mathbf{q}_1, \theta_1, \phi_1, \theta_2, \phi_2)$. We note that integrating out θ_2 and ϕ_2 instead of θ_3 and ϕ_3 yields the same result, as the only spatial component is $\mathbf{q}_1$. The region dominated by red, the same region ring Y indicates in panel (d), is the node of the $2S$ orbital and implies that if the electron associated with $\mathbf{q}_1$ is found here it is likely to be in a singlet state.

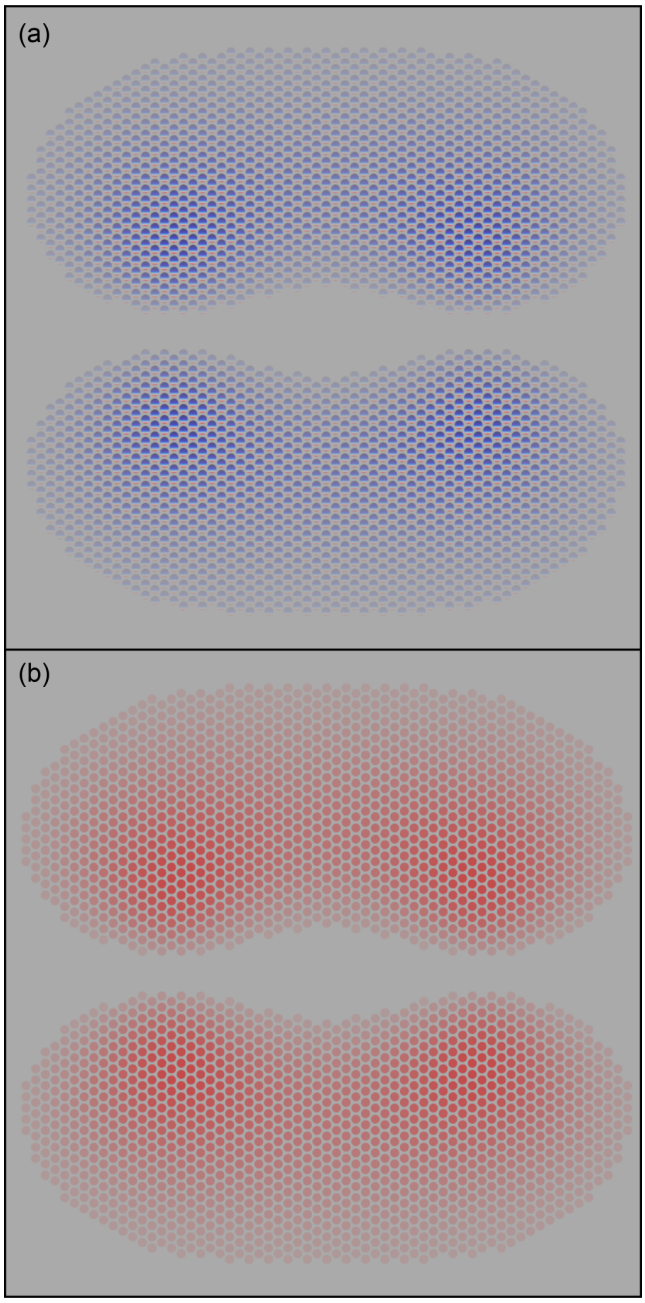

FIG. 6. Simplified versions of (a) single electron and (b) double electron π bonds in a p-bonded pseudomolecule. Note that in the linear combination of atomic orbitals approximation the spatial components are identical; the states can only be visually distinguished through spin degrees of freedom—this difference is clearly seen in the Wigner functions displayed above. States where this distinction is important will arise often in organic chemistry.

Figure 5(d) is the equal-angle slice of the reduced Wigner function $W^{\mathrm{Li}}(\mathbf{q}_1, \theta_2, \phi_2, \theta_3, \phi_3)$. Here we see that if the electron associated with $\mathbf{q}_1$ is far from the origin, the other two electrons are likely to form a singlet. By forming a singlet the electrons have high probability of being in the same orbital, the $1S$ orbital. Furthermore, where the $2S$ contribution is close to zero, there is little contribution from the singlet state indicated by the lack of negative values in the Wigner function (comparatively less red, compare with Fig. 1(d)). Hence, the electrons associated with $\mathbf{q}_2$ and $\mathbf{q}_3$ are not likely to be in the same orbital at these points.

Putting all this together, and taking recognition of the permutations, we see from Fig. 5 that we can infer the Slater determinant and get substantial insight into advanced aspects of the quantum nature of lithium. This analysis is performed purely on the basis of the supporting table of spin Wigner function reference states (Fig. 1).

IV. MOLECULES

The importance of including spin degrees of freedom in the visualization of atoms and molecules is clearly illustrated in Fig. 6, which shows simplified versions of single electron [panel (a)] and double electron [panel (b)] π bonds. The spatial distributions of these two pseudomolecules are identical in the linear combination of atomic orbitals approximation [48]. However the spin provides a distinguishing feature in the visualization for each state. Such situations will naturally be important in organic chemistry.

As the number of degrees of freedom grows, more reduced Wigner functions become available for plotting. The key to utilizing our technique will be in selecting plots that display the relevant information of important aspects of the quantum state. As quantum correlations may determine how certain parts of a molecule will react [1–4], correctly chosen slices will provide a visualization that will aid the understanding of such processes.

We note that a full quantum mechanical calculation of real molecular bonds, including terms from spin-spin, spin-orbit, electron-electron, nuclear interaction, and other relativistic effects, will have a substantial effect on the forms of these Wigner functions. As such Figs. 6(a) and 6(b) provide only a glimpse of the potential that Wigner functions have for understanding the role of spin and entanglement in chemical processes. However, such analysis is beyond the scope of this paper and will be considered in future work.

V. CONCLUDING REMARKS

In this work we have shown that it is possible to visualize various forms of atomic entanglement in an accessible way. Specifically, we have considered spin-orbit coupling (in hydrogen), spin-only entanglement (in helium), and more complex hybrid entanglement (in lithium). Importantly, we have been able to infer each of the states from the visualization alone. We believe that this visualization technique will be of great utility in communicating the more complex and subtle aspects of the quantum mechanics of atoms and molecules, not just within the professional scientific community but also beyond. We note that the Wigner function is found by taking expectation values of displaced parity operators, each of which commute with one another and are observables. Should simultaneous measurement of these quantities be possible, then the direct measurement of the system's Wigner function could be considered a form of quantum state spectroscopy.

ACKNOWLEDGMENTS

T.T. notes that this work was supported in part by JSPS KAKENHI (C) Grant No. JP17K05569. R.P.R. is funded by the EPSRC (Grant No. EP/N509516/1). M.J.E. and T.T. thank Gergely Juhasz and Steve Christie for interesting and informative discussions. The authors thank Pooja Goddard (née Panchmatia) for informative discussions.

[1] B. O. Roos and P. Malmqvist, Phys. Chem. Chem. Phys. **6**, 2919 (2004).
[2] K. Boguslawski and P. Tecmer, Int. J. Quantum Chem. **115**, 1289 (2015).
[3] J. S. Dehesa, T. Koga, R. J. Yáñez, A. R. Plastino, and R. O. Esquivel, J. Phys. B **45**, 015504 (2012).
[4] R. O. Esquivel, N. Flores-Gallegos, M. Molina-Espíritu, A. R. Plastino, J. C. Angulo, J. Antolín, and J. S. Dehesa, J. Phys. B **44**, 175101 (2011).
[5] J. L. Miller, Phys. Today **72**(1), 14 (2019).
[6] J. P. Zobel, J. J. Nogueira, and L. González, Chem. - Eur. J. **24**, 5379 (2018).
[7] H. Li, A. Kamasah, S. Matsika, and A. G. Suits, Nat. Chem. **11**, 123 (2019).
[8] C. Amovilli and N. H. March, Phys. Rev. A **69**, 054302 (2004).
[9] J. P. Coe, A. Sudbery, and I. D'Amico, Phys. Rev. B **77**, 205122 (2008).
[10] O. Osenda and P. Serra, Phys. Rev. A **75**, 042331 (2007).
[11] J. Pipek and I. Nagy, Phys. Rev. A **79**, 052501 (2009).
[12] N. A. Besley, D. P. O'Neill, and P. M. W. Gill, J. Chem. Phys. **118**, 2033 (2003).
[13] N. A. Besley and P. M. W. Gill, J. Chem. Phys. **120**, 7290 (2004).
[14] N. A. Besley, Chem. Phys. Lett. **409**, 63 (2005).
[15] P. M. Gill, D. P. O'Neill, and N. A. Besley, Theor. Chem. Acc. **109**, 241 (2003).
[16] P. M. W. Gill, D. L. Crittenden, D. P. O'Neill, and N. A. Besley, Phys. Chem. Chem. Phys. **8**, 15 (2006).
[17] T. Tilma, M. J. Everitt, J. H. Samson, W. J. Munro, and K. Nemoto, Phys. Rev. Lett. **117**, 180401 (2016).
[18] R. P. Rundle, T. Tilma, J. H. Samson, V. M. Dwyer, R. F. Bishop, and M. J. Everitt, Phys. Rev. A **99**, 012115 (2019).
[19] I. I. Arkhipov, A. Barasiński, and J. Svozilík, Sci. Rep. **8**, 16955 (2018).
[20] R. P. Rundle, B. I. Davies, V. M. Dwyer, T. Tilma, and M. J. Everitt, arXiv:1809.10564.
[21] K. Brádler, M. M. Wilde, S. Vinjanampathy, and D. B. Uskov, Phys. Rev. A **82**, 062310 (2010).
[22] J. Cai, S. Popescu, and H. J. Briegel, Phys. Rev. E **82**, 021921 (2010).
[23] J. Cai, G. G. Guerreschi, and H. J. Briegel, Phys. Rev. Lett. **104**, 220502 (2010).
[24] F. Caruso, A. W. Chin, A. Datta, S. F. Huelga, and M. B. Plenio, Phys. Rev. A **81**, 062346 (2010).
[25] D. Novoselov, D. M. Korotin, and V. I. Anisimov, arXiv:1602.02963.
[26] M. Sarovar, A. Ishizaki, G. R. Fleming, and K. B. Whaley, Nat. Phys. **6**, 462 (2010).
[27] M. C. Tichy, F. Mintert, and A. Buchleitner, J. Phys. B **44**, 192001 (2011).
[28] R. P. Rundle, P. W. Mills, T. Tilma, J. H. Samson, and M. J. Everitt, Phys. Rev. A **96**, 022117 (2017).
[29] For completeness, and given the importance of coherent states in atomic physics and quantum chemistry, we note that the displacement operator can also be written as $\hat{D}_i(\alpha) = \exp(\boldsymbol{\alpha}\cdot\hat{\boldsymbol{a}}^\dagger - \boldsymbol{\alpha}^* - \cdot\hat{\boldsymbol{a}})$ with parity $\hat{\Pi} = \exp(i\pi\hat{\boldsymbol{a}}^\dagger - \cdot\hat{\boldsymbol{a}})$.
[30] R. Hudson, Rep. Math. Phys. **6**, 249 (1974).
[31] J. C. Várilly and J. Gracia-Bondía, Ann. Phys. **190**, 107 (1989).
[32] W. K. Wootters, Ann. Phys. **176**, 1 (1987).
[33] J. P. Dowling, G. S. Agarwal, and W. P. Schleich, Phys. Rev. A **49**, 4101 (1994).
[34] C. Brif and A. Mann, Phys. Rev. A **59**, 971 (1999).
[35] A. Garon, R. Zeier, and S. J. Glaser, Phys. Rev. A **91**, 042122 (2015).
[36] D. Leiner, R. Zeier, and S. J. Glaser, Phys. Rev. A **96**, 063413 (2017).
[37] A. B. Klimov and J. L. Romero, J. Phys. A.: Math. Theor. **41**, 055303 (2008).
[38] C. Cohen-Tannoudji, B. Diu, and F. Laloë, *Quantum Mechanics* (Wiley, New York, 1977).
[39] R. M. G. García-Castelán, W. S. Choe, and Y. C. Lee, Phys. Rev. B **57**, 9792 (1998).
[40] H. G. Laguna and R. P. Sagar, J. Phys. A: Math. Theor. **45**, 025307 (2012).
[41] R. J. Yáñez, A. R. Plastino, and J. S. Dehesa, Eur. Phys. J. D **56**, 141 (2010).
[42] M. J. Cooper, Rep. Prog. Phys. **48**, 415 (1985).
[43] R. M. Singru and R. R. Mishra, J. Phys.: Condens. Matter **1**, SA21 (1989).
[44] For simplicity, and with respect to symmetry, we have chosen a plane grid but this method can be extended to the three spatial dimensions .
[45] The basis states in this paper are represented as Fock states, where $|n_x, n_y, n_z\rangle$ are eigenstates of the three-dimensional harmonic oscillator and n_i indicates the number of photons in the x, y, or z component, see Ref. [38] for details). The forms of the relevant states are $|d_{xz}\rangle = |101\rangle$, $|d_{yz}\rangle = |011\rangle$, and $|d_{z^2},\uparrow\rangle = \sqrt{1/6}(2|002\rangle - |200\rangle - |020\rangle)|\uparrow\rangle$.
[46] As the displaced parity is formed via tensor products, a pure separable state with the density operator

$$\hat{\rho} = \hat{\rho}_{\text{spatial}} \otimes \hat{\rho}_{\text{spin}}$$

has the Wigner function

$$\begin{aligned} W(\mathbf{q},\mathbf{p},\theta,\phi) &= \text{Tr}[\hat{\rho}\,\Pi(\mathbf{q},\mathbf{p},\theta,\phi)], \\ &= \text{Tr}[(\hat{\rho}_{\text{spatial}} \otimes \hat{\rho}_{\text{spin}})(\Pi_{\text{spatial}} \otimes \Pi_{\text{spin}})], \\ &= \text{Tr}[(\hat{\rho}_{\text{spatial}}\Pi_{\text{spatial}}) \otimes (\hat{\rho}_{\text{spin}}\Pi_{\text{spin}})], \\ &= \text{Tr}[\hat{\rho}_{\text{spatial}}\Pi_{\text{spatial}}]\text{Tr}[\hat{\rho}_{\text{spin}}\Pi_{\text{spin}}], \\ &= W(\mathbf{q},\mathbf{p})W(\theta,\phi). \end{aligned}$$

This means that the Wigner function, when visualized at different points, will have only scaled versions of the same state. When this separability is not there the spin pointing in different directions becomes possible, as seen in Fig. 3. Thus, as the state is pure, the rotation in the spin state can only have arisen from the lack of separability, i.e., entanglement.

[47] This work has adopted the notation that the number before the S (or P, D, …) indicates the principal quantum number with the electron index in parentheses.

[48] A. Haaland, *Molecules and Models: The Molecular Structures of Main Group Element Compounds* (Oxford University Press, Oxford, England, 2008).

Appendix C

Visualization of correlations in hybrid discrete-continuous variable quantum systems

Journal of Physics Communications

PAPER

Visualization of correlations in hybrid discrete–continuous variable quantum systems

R P Rundle[1,2], B I Davies[1], V M Dwyer[1,2], Todd Tilma[1,3,4] and M J Everitt[1]

[1] Quantum Systems Engineering Research Group, Department of Physics, Loughborough University, Leicestershire LE11 3TU, United Kingdom
[2] The Wolfson School, Loughborough University, United Kingdom
[3] Department of Physics, College of Science, Tokyo Institute of Technology, H-63, 2-12-1 Ōokayama, Meguro-ku, Tokyo 152-8550, Japan
[4] Quantum Computing Unit, Institute of Innovative Research, Tokyo Institute of Technology, S1-16, 4259 Nagatsuta-cho, Midori-ku, Yokohama 226-8503, Japan

E-mail: m.j.everitt@physics.org

Keywords: Wigner function, phase space, quantum Mechanics, hybrid Systems, correlations

OPEN ACCESS

RECEIVED
10 October 2019

REVISED
24 January 2020

ACCEPTED FOR PUBLICATION
24 January 2020

PUBLISHED
4 February 2020

Abstract

In this work we construct Wigner functions for hybrid continuous and discrete variable quantum systems. We demonstrate new capabilities in the visualization of the interactions and correlations between discrete and continuous variable quantum systems, where visualizing the full phase space has proven difficult in the past due to the high number of degrees of freedom. Specifically, we show how to clearly distinguish signatures that arise due to quantum and classical correlations in an entangled Bell-cat state. We further show how correlations are manifested in different types of interaction, leading to a deeper understanding of how quantum information is shared between two subsystems. Understanding the nature of the correlations between systems is central to harnessing quantum effects for information processing; the methods presented here reveal the nature of these correlations, allowing a clear visualization of the quantum information present in these hybrid discrete-continuous variable quantum systems. The methods presented here could be viewed as a form of quantum state spectroscopy.

1. Introduction

Quantum correlations have become central to the design and manufacture of various quantum technologies [1–4]. Whether these quantum correlations are found between macroscopically distinct superpositions of states, also known as Schrödinger cat states, or in the entanglement between multiple systems. Currently, such technologies can be broadly categorized as being based on either continuous-variable (CV) or discrete-variable (DV) quantum systems.

For CV systems, the primary focus has been on quantum optical systems; manipulating coherent states of light for various quantum information processing applications [5–8]. In such systems, the Wigner function [9, 10] is commonly used due to its ability to display an intuitive representation of a quantum state. Furthermore, the Wigner function is particularly good at revealing coherences and correlations, such as squeezing and superposition [11]. For these reasons, it has become a fundamental tool in the 'search' for Schrödingers cats [12], readily identified by the iconic interference patterns arising from its quantum correlations.

By contrast the focus for DV systems has been on exploiting two-level quantum systems—*qubits*—in order to generate a quantum analogue of the classical bit [2, 13, 14]. Here, the Wigner function has received little attention as a means of visualization. Unlike the case of CV systems, there are two common approaches for generating informationally complete DV Wigner functions, both of which have found application. The approach developed in [15, 16] uses discrete degrees of freedom and has proven useful for quantum information purposes, particularly in the case of contextuality and Wigner function negativity [17–19]. The second approach (and the one used in this work) uses a DV Wigner function with continuous degrees of freedom, similar to the

Bloch sphere [20–26]. For example, there have been various proposals put forward that use a continuous Wigner function to reveal correlations between DV systems [26–28]. These methods have further been validated through the direct measurement of phase-space to reveal quantum correlations [28–31]. Recently this has been extended to experiments validating atomic Schrödinger cat states of up to 20 superconducting qubits [32].

A case that has not been explored in much detail is the phase-space representation of CV-DV hybridization. This hybridisation is seen in many applications of quantum technologies, including simple gate models for quantum computers, such as hybrid two-qubit gates [33, 34], and CV microwave pulse control of DV qubits [35]. The generation of hybrid quantum correlations within CV-DV hybrid[5] systems commonly takes place within the framework of cavity quantum electrodynamics, that describes the interaction between a two-level quantum system and a single mode of a microwave field. These models can be further used to describe the effect of circuit quantum electrodynamics, and to consider the interaction of the microwave field with an artificial atom. Analyzing these interactions within the framework of the Jaynes–Cummings model [36] allows us to display how quantum information is shared between the CV and DV systems.

A number of papers [23, 24, 37] have shown the mathematical construction of hybrid states within the phase space, these have been constructed without giving a way to visually display the degrees of freedom of such composite systems. A method for displaying states with heterogeneous degrees of freedom, using the Wigner function, came from the application of composite phase-space methods to quantum chemistry [38]. The technique presented here is based on this approach, however in [38], reduced Wigner functions are used and an envelope is further applied, potentially losing many of the non-local correlations that arise due to entanglement. Other methods for combining CV Wigner function tomography with other representations of DV systems have been created [39–41], however, only the CV system was treated using the Wigner function formulation. The visualization technique used in [38] displays heterogeneous degrees of freedom, highlighting the power of a hybrid Wigner function approach for visualizing correlations. This approach also demonstrates how many of the correlations are lost when using standard phase-space methods, such as the reduced Wigner function. A hybrid phase-space representation, of all the information within these hybrid systems, is crucial for a more complete understanding of CV-DV hybridization, and its physical properties [42–44]. This understanding will be especially helpful for advancing quantum technologies [34, 45–48], in particular quantum communication where CV-DV hybridization has been used for teleportation [49–51] and entanglement distillation [52–54].

Using the procedure laid out in [24] to generate any quantum state in phase space, and adapting the visualization method from [38], we show how the Wigner function of a hybrid system can be intuitively represented. We begin by presenting examples of important states for CV and DV systems, illustrating how our representation makes correlation information clear. We extend our analysis using the Jaynes–Cummings model to show how intuitive this representation can be. The results open new directions for the use of phase-space methods in hybrid quantum systems.

2. The Wigner function

The Wigner function is traditionally introduced as the Fourier transform of an autocorrelation function [9, 55]. Here it is more suitable to consider a general Wigner function of some arbitrary operator $\hat{A}$, defined as [56]

$$W_{\hat{A}}(\Omega) = \mathrm{Tr}\left[\hat{A}\ \hat{\Pi}(\Omega)\right], \tag{1}$$

where $\hat{\Pi}(\Omega)$ is the displaced parity operator for some parameterization of phase space Ω. The displaced parity operator is defined through displacing a generalized parity operator [24], and for the CV Wigner function is [57]

$$\hat{\Pi}_f(\alpha) = 2\hat{D}(\alpha)\hat{\Pi}_f\hat{D}^{\dagger}(\alpha), \tag{2}$$

where $\hat{\Pi}_f = \sum_{i=0}^{\infty}(-1)^i|i\rangle\langle i|$, written here as an operator in the Fock basis, is the usual parity operator that reflects a point through the origin and

$$\hat{D}(\alpha) = \exp\left(\alpha\hat{a}^{\dagger} - \alpha^{*}\hat{a}\right) \tag{3}$$

is the standard CV displacement operator written using the annihilation and creation operators, $\hat{a}$ and $\hat{a}^{\dagger}$, respectively. Note that we have introduced the subscript *f*, for 'field', to indicate CV systems. The displacement operator can be used to define a coherent state [57]

$$|\beta\rangle_f = \hat{D}(\beta)|0\rangle_f, \tag{4}$$

as the displacement of the vacuum state, $|0\rangle_f$, generating a new coherent state $|\beta\rangle_f$.

As shown in [23, 24], a similar approach to (2) can be used to generate Wigner functions for arbitrary quantum systems. For two-level DV systems, for example,

[5] From now on, we shall refer to CV-DV hybrid states as simply 'hybrid states', dropping 'CV-DV'.

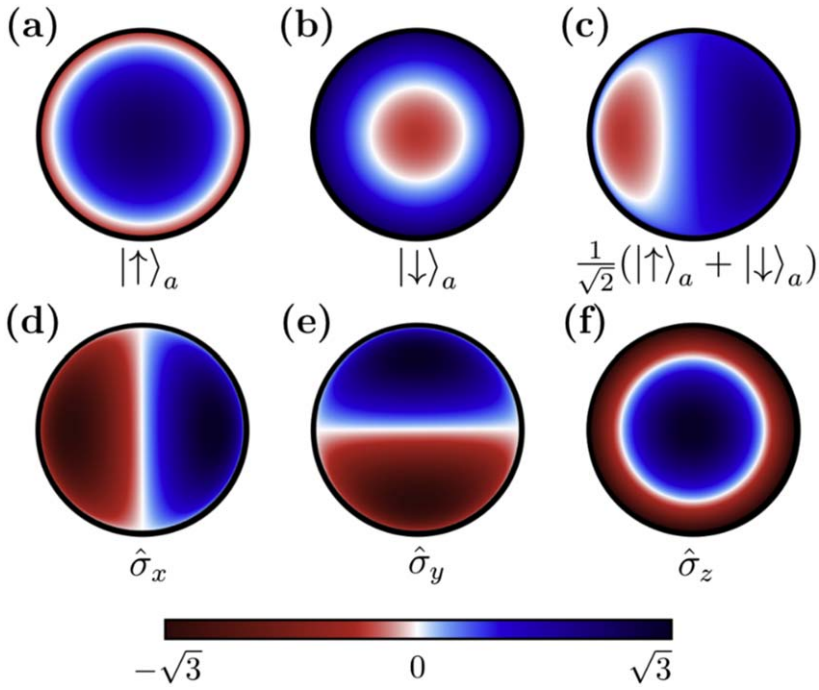

Figure 1. Shown here are six example qubit Wigner functions using the Lambert azimuthal equal-area projection, that maps a sphere onto a circle where the north pole is mapped to the centre and the south pole is on the perimeter. Three single-qubit pure states are shown in (a)–(c), where (a) and (b) are the eigenstates of $\hat{\sigma}_z$, $|\uparrow\rangle_a$ and $|\downarrow\rangle_a$, with eigenvalues ± 1 respectively. (c) is the equal superposition of the states in (a) and (b), $(|\uparrow\rangle_a + |\downarrow\rangle_a)/\sqrt{2}$. (d)–(f) show the qubit Wigner functions of the three Pauli matrices, $\hat{\sigma}_x$, $\hat{\sigma}_y$, and $\hat{\sigma}_z$ respectively.

$$\hat{\Pi}_a(\theta, \phi) = \hat{U}(\theta, \phi, \Phi)\hat{\Pi}_a\hat{U}^{\dagger}(\theta, \phi, \Phi), \tag{5}$$

where the generalized parity, $\hat{\Pi}_a$, for a single, two-level, system is $\hat{\Pi}_a = (\hat{\mathbb{1}} + \sqrt{3}\,\hat{\sigma}_z)/2$ [23, 24, 28], for a full derivation of the kernel see [58]. Note that the subscript a here indicates that this is a state for the 'atom', or DV system. The analogue of the displacement operator, $\hat{U}(\theta, \phi, \Phi)$, given in terms of Euler angles, is

$$\hat{U}(\theta, \phi, \Phi) = \exp(\mathrm{i}\hat{\sigma}_z\phi)\exp(\mathrm{i}\hat{\sigma}_y\theta)\exp(\mathrm{i}\hat{\sigma}_z\Phi) \tag{6}$$

for the standard Pauli matrices $\hat{\sigma}_y$ and $\hat{\sigma}_z$. Note as the parity operator commutes with $\hat{\sigma}_z$, the Φ term does not contribute, and the DV Wigner function depends only on θ and ϕ, allowing it to be plotted on the surface of a sphere. Note that by DV Wigner function, we mean the Wigner function for DV systems; the Wigner function used here is however parameterized over the continuous variables θ and ϕ.

figure 1 shows examples of the DV Wigner function generated by (5) for some simple qubit states. Each of the DV Wigner functions presented in figure 1 is plotted following [59], using the Lambert azimuthal equal-area projection [60]. This projection is area preserving and maps the surface of a sphere to polar coordinates, with the north pole mapped to the centre of the disc and the south pole to the outer boundary. The equator of the sphere is projected onto a concentric circle, with a radius $1/\sqrt{2}$ times the radius of the entire circle, this is explicitly seen as the white circle in figure 1(f). This means that the Lambert azimuthal equal-area projection allows us to view the entire surface of the sphere as a circle. The reason for using this area-preserving mapping, rather than an angle-preserving mapping, is because we are dealing with a probability distribution function. By definition, the integral over a volume determines the probability; area-preserving therefore translates into probability-preserving. A consequence of this mapping is that in some regions of phase space, the quasi-probability distribution appears warped. For instance, the first three states in figures 1(a)–(c) are all rotations of one another on a sphere.

The DV Wigner functions presented in figures 1(a)–(c) are standard two-level quantum states, where figures 1(a) and (b) are the ± 1 eigenstates of the $\hat{\sigma}_z$ operator, $|\uparrow\rangle_a$ and $|\downarrow\rangle_a$ respectively. The state in figure 1(c) is the equal superposition of $|\uparrow\rangle_a$ and $|\downarrow\rangle_a$, or the positive eigenstate of $\hat{\sigma}_x$. In all the presented states, there are negative values in the DV Wigner function. Importantly, in the DV Wigner function for qubits, negative volume, as well as being an indicator of non-classicality, is also a measure of purity [37]. This is because discrete system coherent states are fundamentally quantum; regardless of whether the system is the polarization of a photon or the direction of spin in an electron.

More generally, in both CV and DV Wigner functions, negative values arise as a consequence of self-interference. In the CV Wigner function this arises from non-Gaussianity [61], and can be seen in the Fock states

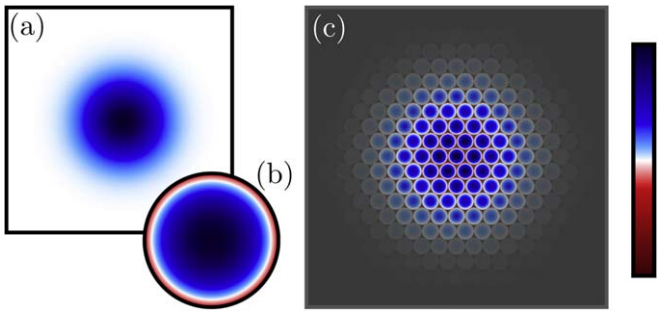

Figure 2. Example Wigner function for the product of the CV vacuum state and a DV excited state, $|0\rangle_f|\uparrow\rangle_a$, where (a) and (b) show the reduced Wigner functions for the continuous-variable (CV) and discrete-variable (DV) Wigner functions respectively. In (c) is the full Wigner function of the hybrid system, where the CV phase space is split up as a discrete grid. At each of these discrete points the DV Wigner function at that point in phase space is plotted. The transparency of each of the DV Wigner functions is proportional to the maximum quasi-probability at that point in CV phase space. The colour bar is white at 0 with limits ± 2 for (a), $\pm(1+\sqrt{3})/2$ for (b), and $\pm(1+\sqrt{3})$ for (c).

(excluding the vacuum state) or in superpositions of Gaussian states, see figure 3 for an example, discussed later in the paper. This explains why negative values have been used as a measure of quantumness, however there is one notable exception, the non-negative, entangled, Gaussian CV two-mode squeezed state.

Since the Gaussian states of a DV Wigner function can be visualized on a sphere, the emergence of self-interference is now inevitable, due to the inherent geometry of the sphere. For example, the Wigner function for the state $|\uparrow\rangle_a$ has a Gaussian distribution centred at the north pole; as this Gaussian distribution tends towards zero, near the south pole, there is an emergence of negative quasi-probabilities. This negativity in the Wigner function is manifested as a result of self-interference, as the quantum coherences interfere with each other at the south pole. As the number of levels is increased (from the two-level system) in the DV Wigner function and take the infinite limit[6], the $SU(2)$ DV Wigner function tends towards the Heisenberg-Weyl group, returning to the standard CV Wigner function. This is because the effective size of the sphere increases, decreasing the relative size of the Gaussian. In the infinite limit, the negativity in the Wigner function is completely eliminated, since the Gaussian can no longer interact with itself on the opposite side of the sphere.

Although the example states so far have been density operators for pure states, the general formalism in (1) allows for the Wigner function to be generated for any arbitrary operator. To emphasize this, in figures 1(d)–(f) are the DV Wigner representation of each of the three Pauli operators. In general, Wigner function exhibit the normalization condition

$$\int_{\Omega} \mathrm{d}\Omega\ W_{\hat{A}}(\Omega) = \mathrm{Tr}[\hat{A}]. \tag{7}$$

For normal density operators, this yields unity, as would be expected for any probability distribution function. For the Pauli operators however, $\mathrm{Tr}[\hat{\sigma}_i] = 0$, where $i = \{x, y, z\}$, therefore $\int_{\Omega} \mathrm{d}\Omega\ W_{\hat{\sigma}_i}(\Omega) = 0$. The tracelessness of these matrices can be seen in figures 1(d)–(f) by noting that the negative and positive volumes are equivalent and therefore cancel. This feature will be key to several of our observations later in this work.

For a CV-DV hybrid system, the total displaced parity operator is simply the tensor product of the displaced parity operator for each subsystem [23, 24, 28]

$$\hat{\Pi}(\alpha, \theta, \phi) = \hat{\Pi}_f(\alpha) \otimes \hat{\Pi}_a(\theta, \phi), \tag{8}$$

yielding a hybrid Wigner function for a density matrix $\hat{\rho}$

$$W_{\hat{\rho}}(\alpha, \theta, \phi) = \mathrm{Tr}[\hat{\rho}\ \hat{\Pi}(\alpha, \theta, \phi)]. \tag{9}$$

Hybrid systems generated with (9) usually have more degrees of freedom than is convenient to plot. For this reason, many approaches that use phase-space methods to treat hybrid systems use reduced Wigner functions, rather than considering the full phase space of the composite system. To give a full picture of the quantum correlations found between the two systems, a method similar to that introduced in [38] can be used. As an example of the utility of this method, the fully separable state, $|0\rangle_f|\uparrow\rangle_a$, is shown in figure 2. The reduced Wigner functions for CV and DV degrees of freedom are presented in figures 2(a) and (b) respectively. In figure 2(c) we apply the method first presented in [38] to plot the phase-space representation of this state.

Specifically, figure 2(c) was created by first dividing the CV phase space into discrete points on a rectangular map. Each of these discrete points is then associated with a discrete complex value α, equally spaced across the

[6] The general Wigner function for any system in the displaced parity formalism can be found in [24].

phase space grid. For each set point α, the values of the Wigner function for θ and ϕ degrees of freedom are calculated, with the Wigner function at that point plotted using the Lambert projection. This produces a DV Wigner function at each α in CV phase space. The transparency of each disc is then set proportional to the absolute maximal value of the phase space at that point, $\max_{\theta,\phi}|W_{\hat{\rho}}(\alpha,\ \theta,\ \phi)|$. For example, to generate the disc at the centre of figure 2(c), we calculate $W_{\hat{\rho}}(\alpha = 0,\ \theta,\ \phi)$, resulting in a DV Wigner function for $|\uparrow\rangle_a$, and then modify the amplitudes of the quasi-probabilities using the value of α. This is then repeated for every α. Note that a main difference between the plots presented here and in [38] is that the transparency of the DV Wigner functions in [38] is set proportional to $|W_f(\alpha)|$. Using the method presented here allows for a clearer view of the quantum correlations that manifest.

Since the state being plotted here is a pure separable state, the Wigner function can be expressed as

$$W_{\hat{\rho}}(\alpha,\ \theta,\ \phi) = W_{\hat{\rho}_f}(\alpha)\, W_{\hat{\rho}_a}(\theta,\ \phi), \tag{10}$$

where $\hat{\rho}_f$ and $\hat{\rho}_a$ are the reduced density matrices for the CV and DV systems respectively. As a result, figure 2(c) has the same form as a coherent state, dictated by the CV Wigner function, with every point in phase space having an $|\uparrow\rangle_a$ DV Wigner function. The difference in this method, in comparison to [38], is that here the transparency is not set by integrating out the qubit degrees of freedom; such an approach leads to a loss of quantum correlations in the systems of interest.

3. Visualizing correlations in hybrid quantum systems

Quantifying different types of correlations in quantum systems is a key area of research that has received a great deal of attention [62–69]. In parallel, phase-space methods have been utilized as a tool to identify and categorize quantum correlations [41, 70–73]. Further, these methods have been used to generate measures based on the emergence of negative quasi-probabilities in the Wigner function [37, 74–76]. However, due to the higher number of degrees of freedom, visually representing correlations in composite systems is more difficult. We now show how our technique produces definite signatures of both quantum and classical correlations, that can be discerned for hybrid quantum systems. When dealing with quantum information processing with two coupled qubits, the distinction between these two types of correlations is important. Beginning with how correlations that arise from superposition appear, we will describe our choices of DV and CV qubits and how the encoding of quantum information is represented on these qubits.

Certain similarities are seen between DV and CV systems, whether in structure, choice in qubit, or in appearance of the quantum correlations that manifest. These similarities will be demonstrated here, by showing how quantum information can be encoded onto different types of state. Encoding quantum information onto quantum states can be done in various ways, including a variety of approaches even within the same system [45]. We will therefore begin by using the simplest case of a DV qubit for quantum information processing. Since the DV systems used here are two-level systems, the encoding of quantum information is straightforward; a bit value 0 or 1 is simply assigned to each of the two levels, $|\uparrow\rangle_a$ and $|\downarrow\rangle_a$ respectively. The DV 0bit is now represented visually by figure 1(a), likewise the 1 bit value is represented by figure 1(b). Furthermore, a general pure superposition state

$$a_a\,|\uparrow\rangle_a + b_a\,|\downarrow\rangle_a, \tag{11}$$

where $|a_a|^2 + |b_a|^2 = 1$, allowing any weighted superposition between 0 and 1. When $a_a = b_a = 1/\sqrt{2}$, an equal superposition is yielded and is represented visually by figure 1(c).

This binary choice becomes more complicated when assigning bit values to a CV qubit. Although, there are various ways to encode quantum information onto a CV system creating similarities between CV and DV systems. Since the Hilbert space is infinite, there are different constraints on assigning qubit values. We will now demonstrate two examples of CV qubits, comparing the results with the DV qubits

3.1. Fock state qubits

Fock states are orthogonal and therefore a natural choice for quantum information processing. For simplicity we consider the vacuum and one-photon Fock states, $|0\rangle_f$ and $|1\rangle_f$ respectively. We can now form the analogy with the DV qubit state by assigning bit values to these states $0 \rightarrow |0\rangle_f$ and $1 \rightarrow |1\rangle_f$.

Comparison of the Wigner functions for the DV and the CV Fock qubits can be found in figures 2(a) and (b); where in the Lambert projection, the DV qubit in figure 2(b) has a similar Gaussian form as the vacuum state in figure 2(a). In fact, the DV qubit basis states are discrete analogues of the Fock states. Therefore, the presence of the negative values in the DV qubit states becomes more apparent by considering the one-photon Fock state $|1\rangle_f$ and the DV qubit state $|\downarrow\rangle_a$ (in figures 3(a) and (b) respectively). The orientation of the DV qubit is somewhat arbitrary, the $|\uparrow\rangle_a$ and $|\downarrow\rangle_a$ states are orthogonal rotations of one another; therefore, the DV qubit states share

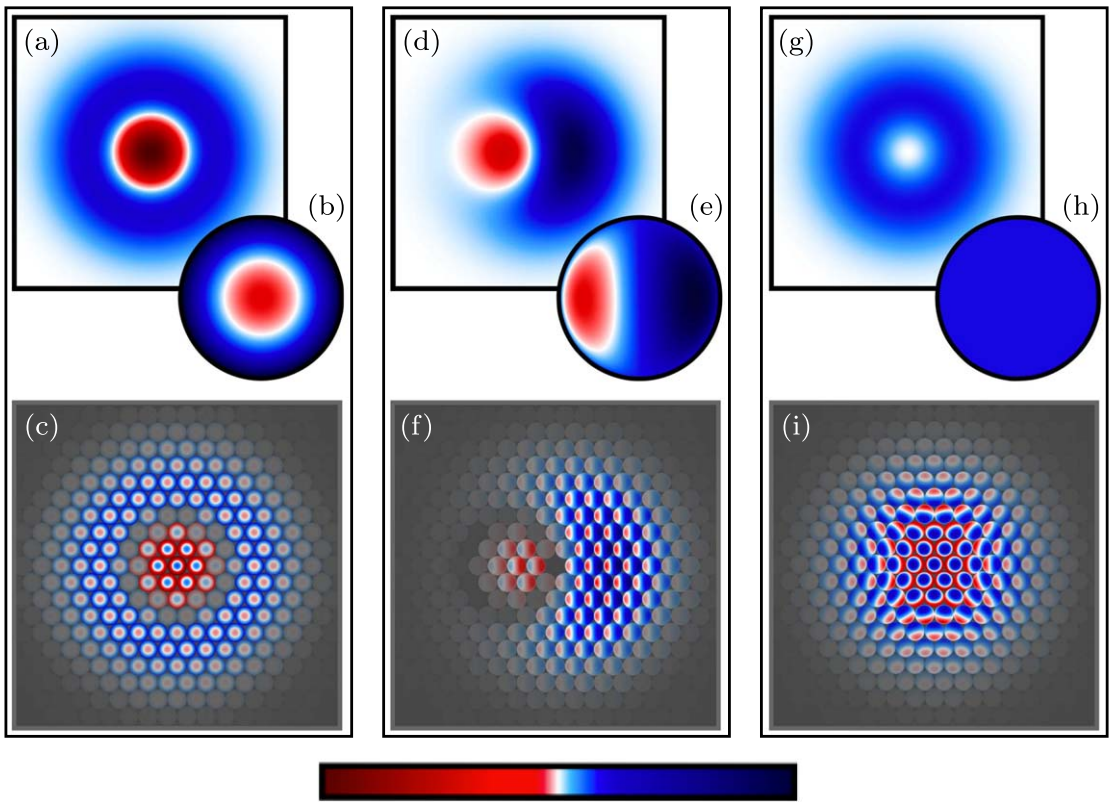

Figure 3. Examples of Fock states coupled to DV qubits. (a) - (c) show the state $|1\rangle_f|\downarrow\rangle_a$. (d)–(f) are the state $(|0\rangle_f + |1\rangle_f)(|\uparrow\rangle_a + |\downarrow\rangle_a)/2$. (g)–(i) are the entangled state $(|0\rangle_f|\uparrow\rangle_a + |1\rangle_f|\downarrow\rangle_a)/2$. (a), (d), and (g) show the reduced CV Wigner functions, (b), (e), and (h) are the reduced DV Wigner functions and (c), (f), and (i) are the full hybrid Wigner functions. The colour bar is white at 0 with limits ± 2 for the reduced CV Wigner function, $\pm(1+\sqrt{3})/2$ for reduced DV Wigner function, and $\pm(1+\sqrt{3})$ for hybrid Wigner function.

properties of both the $|0\rangle_f$ and $|1\rangle_f$ Fock states. This analogy can be seen further in figures 3(d) and (e), where the Wigner functions for the states $(|0\rangle_f + |1\rangle_f)/\sqrt{2}$ and $(|\uparrow\rangle_a + |\downarrow\rangle_a)/\sqrt{2}$ are shown respectively.

Also in figure 3, we show the hybrid Wigner functions for these states. In figure 3(c) we show the product of figures 3(a) and (b). The product of figures 3(d) and (e) is shown in figure 3(f). Since in both cases the CV and DV qubits are separable and therefore follow (10), the pattern of the hybrid phase space is similar to that found in figure 2. The separability is evident by the existence of a DV Wigner function at every point in CV phase space, with the amplitude modulated by the CV Wigner function at that point. For both of the hybrid Wigner functions in figures 3(c) and (f), the negative regions in the CV Wigner functions affect the sign of the DV Wigner function, causing there to be a negative prefactor whenever $W_{\hat{\rho}_f}(\alpha) < 0$, inverting the positive and negative quasi-probabilities at those points in CV phase space.

Having established that the hybrid Wigner function allows local correlations to be discerned reliably, we now demonstrate how quantum correlations arising between subsystems in this type of hybrid system manifest. Entanglement in Fock hybrid states, a Bell-Fock state[7], $(|0\rangle_f|\uparrow\rangle_a + |1\rangle_f|\downarrow\rangle_a)/\sqrt{2}$, is shown in figure 3(i). The full Wigner functions for bipartite Bell-Fock states have a distinctive pattern, reminiscent of the spin-orbit coupled state from [38], where there is a twisting of the DV Wigner functions dependent on the point in CV phase space. This DV dependence on the CV Wigner function is indicative that (10) does not hold for this state. This means that the state in question is not separable, and since this state is a pure state this indicates coupling between the two subsystems. This is a signature one should look for when investigating quantum correlations in this type of hybrid state.

Comparing the hybrid Wigner function in figure 3(i) to the reduced Wigner function for the CV and DV qubits in figures 3(g) and (h) respectively, we see the importance in considering the full phase space for entangled states such as this. It can be seen in figures 3(g) and (h) how correlations between the two systems are lost when considering the reduced Wigner functions, leaving only statistical mixtures of the basis states in each case.

[7] Bell state for an entangled DV qubit with a CV Fock qubit.

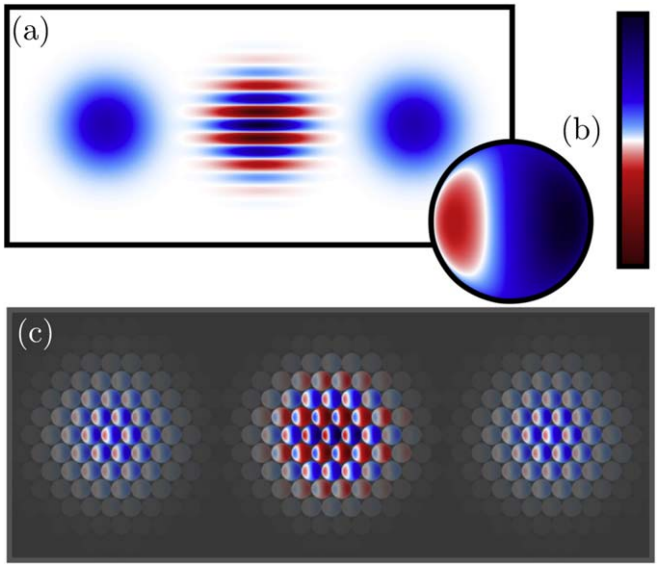

Figure 4. Here is an example of the Wigner representation of a Schrödinger cat state coupled to a qubit, $(|\beta\rangle_f + |-\beta\rangle_f)(|\uparrow\rangle_a + |\downarrow\rangle_a)/2$, where $|\beta\rangle$ is a coherent state centred at β for $\beta = 3$. (a) shows the reduced CV Wigner function and (b) shows the reduced DV Wigner function. (c) shows the hybrid Wigner function. The colour bar is white at 0 with limits ± 2 for (a), $\pm(1 + \sqrt{3})/2$ for (b), and $\pm(1 + \sqrt{3})$ for (c).

3.2. Coherent state qubits

Another choice in creating a CV qubit is to encode quantum information onto coherent states [5, 6]. Unlike with the Fock CV qubit, the coherent state basis is an overcomplete basis where there is some degree of overlap between any two coherent states. However with sufficient distance between two coherent states, this overlap is negligible. For simplicity, our example states will be real values of β, where the two levels are set to the values $\beta_1 = -\beta_2 = \beta$.

We then label each of the coherent states as a certain bit value; for instance $0 \rightarrow \beta_1$ and $1 \rightarrow \beta_2$. This creates a qubit in the form of a Schrödinger cat state [6], with the general qubit state being

$$a_f\,|\beta\rangle_f + b_f\,|-\beta\rangle_f, \tag{12}$$

as in (11). This means that there is a coherent state at β when $a_f = 1$ and a coherent state at $-\beta$ when $b_f = 1$. The superposition state $a_f = b_f = 1/\sqrt{2}$ produces the Schrödinger cat state shown (for $\beta = 3$) in figure 4(a).

Coupling the CV and DV qubits in figgures 4(a) and (b) generates the full Wigner function in figure 4(c). Explicitly, this is the state

$$\frac{1}{2}(|\beta\rangle_f + |-\beta\rangle_f)(|\uparrow\rangle_a + |\downarrow\rangle_a). \tag{13}$$

Since the full system is a simple tensor product of the two qubits, the subsystems are separable, resulting in a full Wigner function that obeys (10). The separability between these states is seen in the full Wigner function in figure 4(c). The image of the CV Schrödinger cat state is visible as a discrete grid, with the DV Wigner function for the state at every point.

Given the difference in the local correlations between the two choices of CV qubit, it is now worthwhile to demonstrate how the signature of the non-local correlations differ for the coherent state CV qubits. The hybrid analogue of a Bell state for coherent states, the Bell-cat state, is

$$\frac{1}{\sqrt{2}}(|\beta\rangle_f|\uparrow\rangle_a + |-\beta\rangle_f|\downarrow\rangle_a). \tag{14}$$

Since many of the correlations in this state are due to entanglement, the standard approach of using reduced Wigner functions is insufficient, as seen in figures 5(a) and (b). Neither reduced Wigner function has visible quantum correlations, yielding two mixed states. This issue motivated other approaches to tomography and state verification for such states, for instance [40] used reduced CV Wigner functions in different Pauli bases to show Bell's inequality. Other tomography methods for entangled hybrid systems, such as [47], also take into consideration the problems of a reduced phase-space representation of a hybrid entangled state. Although approaches such as these give a better appreciation of the quantum correlations, they still only provide glimpses of the nature of the full quantum state.

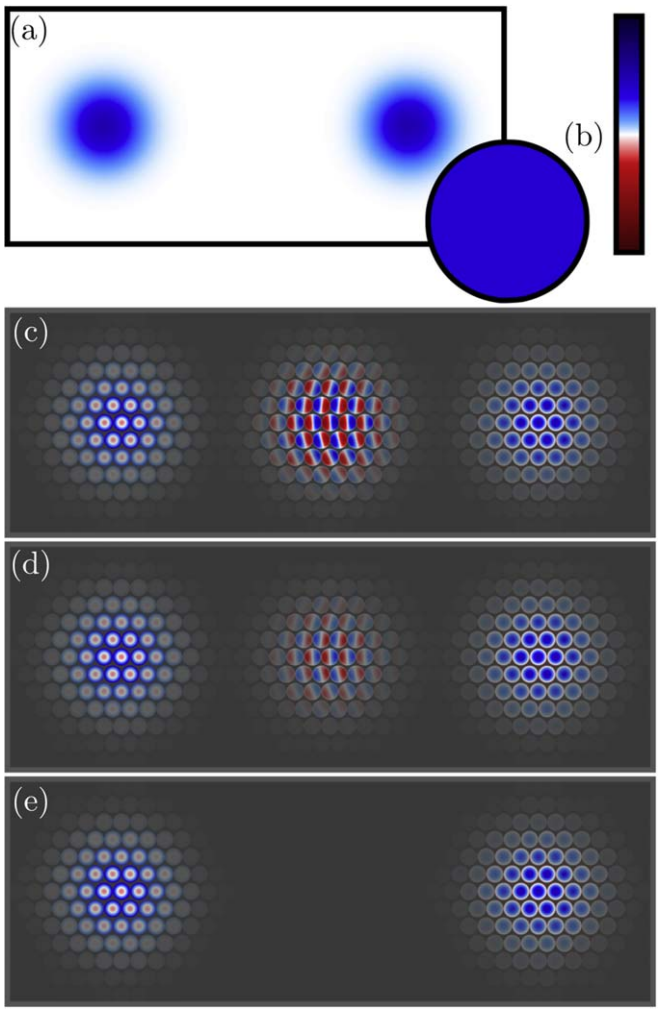

Figure 5. Here are examples of the Wigner representation of a lossy entangled Bell-cat state, with varying values of loss. (a) shows the reduced CV Wigner function and (b) shows the reduced DV Wigner function. The reduced Wigner functions remain the same for the following three example states. (c) shows the full Wigner function for the state with no loss $(|\alpha\rangle_f|\uparrow\rangle_a + |-\alpha\rangle_f|\downarrow\rangle_a)/\sqrt{2}$. (d) shows partial loss of the quantum correlations. (e) shows a fully mixed version of the state $(|\beta\rangle\langle\beta|_f|e\rangle\langle e|_a + |-\beta\rangle\langle-\beta|_f|g\rangle\langle g|_a)/2$. The colour bar is white at 0 with limits ± 2 for (a), $\pm(1+\sqrt{3})/2$ for (b), and $\pm(1+\sqrt{3})$ for (c).

The hybrid Wigner function for (14) is shown in figure 5(c). Comparing our representation with the reduced Wigner function treatment, the quantum correlations are now visible, manifesting as interference terms between the two coherent states. The nature of these quantum correlations is completely lost when the full Wigner function is not generated. Further, within the quantum correlations, the qubit states approach traceless states, as in figures 1(d)–(f), where the state at the very centre, $\alpha = 0$, is in fact the $\hat{\sigma}_x$ Pauli matrix. It is important to note at this point that the manifestation of traceless here, found only in the hybrid phase-space picture, are a signature of quantum correlations. Some existing tomography methods can pick up these correlations, however their full nature is not captured. For example, measuring the reduced Wigner functions results in a loss of quantum and classical correlations, as demonstrated in figures 5(a) and (b). This makes classical and quantum correlations, for this kind of state, indistinguishable. The ability to obtain signatures to distinguish between classical and quantum correlations is important in determining the suitability of states in quantum information processing.

To highlight this, we now consider two further examples of states that have the same reduced CV and DV Wigner functions. Though the degree of quantum correlations differ for each state. The general state is

$$\frac{1}{2}(|\beta\rangle\langle\beta|_f|e\rangle\langle e|_a + \eta|\beta\rangle\langle-\beta|_f|e\rangle\langle g|_a + \eta|-\beta\rangle\langle\beta|_f|g\rangle\langle e|_a + |-\beta\rangle\langle-\beta|_f|g\rangle\langle g|_a), \tag{15}$$

where η determines the purity of the state. When $\eta = 1$ (15) reduces to (14). Changing the value of the loss to $\eta = 0.5$ and then to $\eta = 0$, figures 5(d) and (e) are, respectively, generated. In both, it is clear that the quantum correlations are slowly lost. The loss of quantum correlations means these states are less useful for quantum information purposes, and analyzing the reduced Wigner functions, unlike our approach, does not provide any

insight to this loss. By using our method to represent the full Wigner function, it is not only possible to distinguish the strength of the quantum correlations but, the signature of classical correlations is revealed.

In figure 5(e) is the state

$$\frac{1}{2}(|\beta\rangle\langle\beta|_f|e\rangle\langle e|_a + |-\beta\rangle\langle-\beta|_f|g\rangle\langle g|_a) \tag{16}$$

that describes the equal classical probability of finding an excited state at β and a ground state at $-\beta$. The classical correlations that correspond to this probability is shown in our full picture of the Wigner function, where the $|\beta\rangle_f$ coherent state is correlated with $|\uparrow\rangle_a$ states, likewise the $|-\beta\rangle_f$ coherent state is correlated with $|\downarrow\rangle_a$ states. This process not only reveals that this is the signature of classical correlations, it verifies the case that the traceless states between the two states are a result of the quantum correlations within the hybrid system.

4. The Jaynes-Cummings model

Light-matter interaction in the form of quantum electrodynamics (QED) has been an experimental cornerstone in understanding quantum effects. It has also given a helping hand in the development of quantum information applications, such as single-photon quantum non-demolition measurements acting as two-qubit gates between microwaves and atoms [35]. The standard example of a QED interaction between a two-level DV system and a CV field is the Jaynes–Cummings model [36]. Jaynes–Cummings type interactions are the basis for the generation of non-Gaussian states and are well known for showing the collapse and revival of Rabi oscillations [66, 77, 78] throughout its evolution. During this evolution, quantum information is transferred back and forth between the CV and DV systems; through this process, quantum information can then manifest as a Schrödinger cat state or generate Bell pairs of the sort shown in figure 3(i). By using our methods, the transfer of quantum information can be visualized as is swaps between the microwave field and the atom.

The interaction picture of the Jaynes–Cummings model

$$\hat{H}_{\rm JC} = \omega(\hat{a}^\dagger\hat{\sigma}_- + \hat{a}\hat{\sigma}_+), \tag{17}$$

will be used, where ω is the field-qubit coupling constant, and the operators $\hat{\sigma}_\pm = (\hat{\sigma}_x \pm i\hat{\sigma}_y)/2$ are the qubit raising and lowering operators that transition the state between eigenstates of $\hat{\sigma}_z$.

Following the example given in section 3, we consider a Fock state basis to model the Jaynes-Cumming model. Choosing the initial state in the field to be a vacuum state and coupling it to an excited DV qubit results in an evolution that fluctuates between $|0\rangle_f|\uparrow\rangle_a$ and $|1\rangle_f|\downarrow\rangle_a$ [35], as shown in figures 2 and 3(d)–(g) respectively. This means that the evolution can be fully described with the two levels of the Fock state qubit and the DV qubit, allowing us to consider this as an exchange between two qubits.

The fluctuation as part of this model results in the system continuously transferring quantum information between the two qubits, where the state at time t is

$$|\Psi(t)\rangle = \cos(\omega t)|0\rangle_f|\uparrow\rangle_a - i\sin(\omega t)|1\rangle_f|\downarrow\rangle_a, \tag{18}$$

returning to the initial state at $t = \pi/\omega$. A video of this evolution is given in supplementary material. As the information transfers between these two states, throughout one period, two entangled Bell-Fock states are generated

$$|\Phi^\pm\rangle = \frac{1}{\sqrt{2}}(|0\rangle_f|\uparrow\rangle_a \pm i\,|1\rangle_f|\downarrow\rangle_a), \tag{19}$$

where the full Wigner functions for these states are shown in figure 6. Both of these states have the same reduced Wigner functions, which are not shown here since all Bell-Fock states have the same reduced Wigner functions, shown in figures 3(g) and (h).

During Jaynes–Cummings evolution, the first of the Bell-Fock states appears at $t = \omega^{-1}\pi/4$, where the state $|\Psi(\omega^{-1}\pi/4)\rangle = |\Phi^-\rangle$. This first Bell-Fock state is shown in figure 6(a), the second $|\Psi(3\omega^{-1}\pi/4)\rangle = |\Phi^+\rangle$ is given in figure 6(b). Comparing these two states to figure 3(i), even though the reduced Wigner functions are identical, the difference the phase plays in the full hybrid Wigner functions is apparent. Extrapolating to another choice of phase, for example $(|0\rangle_f|\uparrow\rangle_a - |1\rangle_f|\downarrow\rangle_a)/\sqrt{2}$, the full hybrid Wigner function is similar to figure 3(i) with each of the DV Wigner functions pointing in the orthogonal directions. The quantum correlations that arise in this form of hybrid system have a unique signature which can best be described as a twisting of the DV Wigner function at points in CV phase space.

We now consider the JCM evolution with a different initial state. The vacuum state is replaced by a coherent state, giving the initial state $|\beta\rangle_f|\uparrow\rangle_a$, where again $\beta = 3$. This choice of initial state produces very different effects in the Jaynes-Cumming model, such as the collapse and revival of the Rabi oscillations, where the revival of the Rabi oscillations happen at time t_r. Three noteworthy snapshots, points within the evolution, of the Jaynes–Cummings model are shown in figure 7, indicated by the three vertical lines in figure 7(a), showing the value of

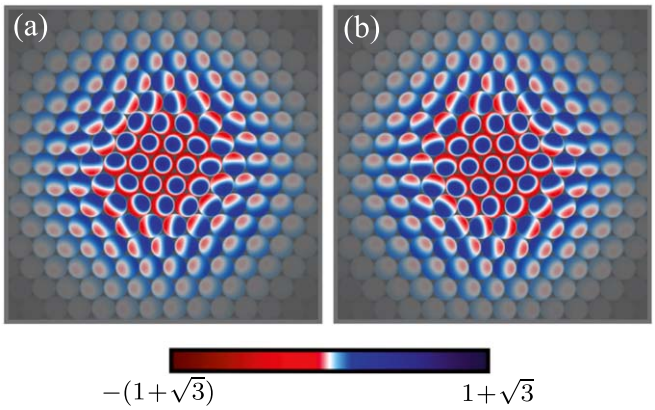

Figure 6. Here we show the Wigner functions for two points in the evolution of the Jaynes–Cummings model with initial state $|0\rangle_f|\uparrow\rangle_a$. During the evolution of the Jaynes–Cummings model with this excited state, two entangled Bell-Fock states are generates before returning to the initial state again. The two entangled Fock-States are shown here, where the first one in (a) is the state $(|0\rangle_f|\uparrow\rangle_a - \mathrm{i}\,|1\rangle_f|\downarrow\rangle_a)/\sqrt{2}$. The second entangled Bell-Fock state in the evolution is shown in (b), where the state is $(|0\rangle_f|\uparrow\rangle_a + \mathrm{i}\,|1\rangle_f|\downarrow\rangle_a)/\sqrt{2}$. The signature of entanglement in these states can be seen in the DV Wigner function dependence on the value of the CV Wigner function, similarly to the example state in figure 3(i).

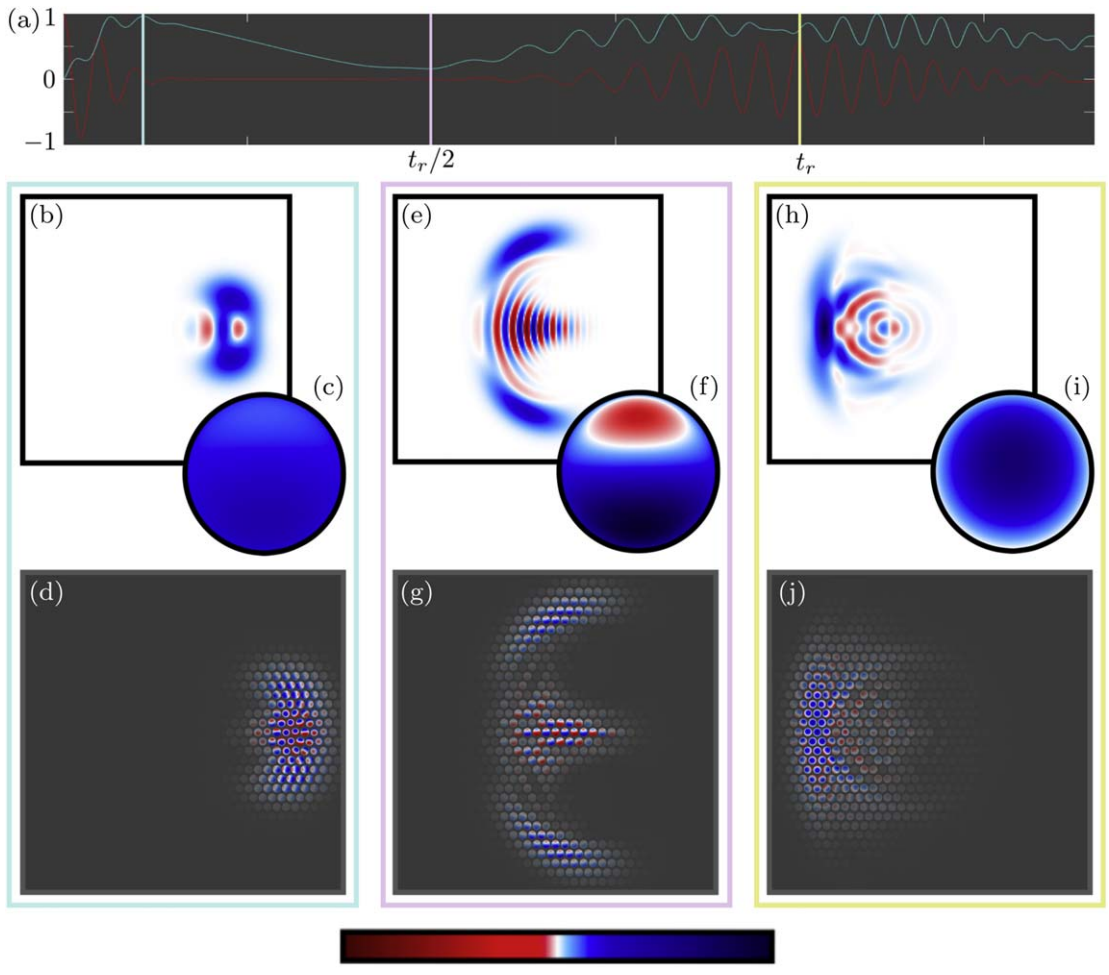

Figure 7. Here we show the Wigner functions for three points in the evolution of the Jaynes–Cummings model with initial state $|\beta\rangle_f|\uparrow\rangle_a$, where $\beta = 3$. (a) shows the qubit inversion, $\langle\hat{\sigma}_z\rangle$, in red and the von Neumann entropy in cyan over time. t_r is the revival time of the Rabi oscillations. Three solid lines are shown in (a) that indicate the different point in the evolution where we have displayed the Wigner functions. The reduced Wigner functions are then given below (a), where the reduced CV Wigner functions are in (b), (e), and (h). The reduced DV Wigner functions are in (c), (f), and (i). The hybrid Wigner functions for the coupled system are in (d), (g), and (j). The values for the colours correspond to the same values in figures 4 and 5.

the von Neumann entropy (cyan) and qubit inversion, $\langle\hat{\sigma}_z\rangle$, (red) at each point in the evolution. For each of the snapshots the reduced Wigner functions are figures 7(b), (e), and (h) for the CV system, and figures 7(c), (f), and (i) for the DV qubit. In figures 7(d), (g), and (j) are the full Wigner function for each of these snapshots.

The first snapshot is early on in the evolution, $t \approx t_r/9$, where there is a high degree of coupling between the two systems. The reduced Wigner functions in figures 7(b) and (c), indicate that something approaching a Schrödinger cat state forming in the CV system; where the DV qubit is in a highly mixed state. All that can be deduced from the reduced Wigner functions then is that there are correlations between the qubit and the field mode; the nature of the quantum correlations remains hidden.

Evaluating the full Wigner function in figure 7(d), a better appreciation of the quantum correlations at this point in the evolution can be obtained. The DV spin direction at the top of the CV Wigner functions are orthogonal to those in the bottom of the CV Wigner function. Where at the top, the spins point in the direction of the negative eigenstate of $\hat{\sigma}_x$; at the bottom they point in the positive eigenstate of $\hat{\sigma}_x$. The correlations found in the middle in figure 7(d) match the quantum correlation signature for a coherent state qubit, as they are of a form similar to the traceless states in figure 1.

The second snapshot of the Jaynes–Cummings model, $t \approx t_r/2$, is where the field mode and the qubit disentangle, transferring the quantum correlations to form a CV Schrödinger cat state. Presence of this Schrödinger cat state is immediately visible in the reduced CV Wigner function in figure 7(e). The reduced DV Wigner function in figure 7(f) has now increased in both negative and positive amplitudes, rotating to the eigenstate of $\hat{\sigma}_y$ with eigenvalue -1. The return of coherence of the DV qubit is a good indication that the correlations between the two systems have decreased.

Both of the reduced Wigner functions in figures 7(e) and (f) suggest that this state is similar to the example state in figure 4, which is approximately separable. Observation of figure 7(g) confirms this suggestion, but more detail can still be found. Although very few correlations appear between the two subsystems, some residual quantum correlation has remained between the two. These correlations are found in the slight twisting of the qubits around the two cats and within the quantum correlations in between.

The final snapshot occurs at the revival of the Rabi oscillations, $t \approx t_r$, where the qubit state is closest to the initial state within the revival. In figure 7(i) the average spin is pointing in the direction of an excited state $|\uparrow\rangle_a$, however, there is a loss of coherence associated with the decrease in amplitudes and no negative values. The full Wigner function reveals why the coherences in the reduced DV Wigner function have formed. At most points in the full Wigner function, the DV Wigner function is in the excited state, however at many points there are rotations in the qubit Wigner functions, indicating some residual quantum correlations. The strongest coherent states are found on the left-hand side, where it appears the state is returning to the initial state of a coherent state coupled to $|\uparrow\rangle_a$.

The quantum correlations that accompany the two choices of CV qubits have a somewhat different nature however their signatures are distinguishable when considering the full Wigner function. The correlations for the Fock state qubits show a dependence on each other, arising due to the non-separability of the state. This closely resembles the pattern found in spin-orbit coupled states [38], and is comparable to spin texture images. The fundamental signatures come from the behaviour of the coherences and correlations within and between the systems. The form of the Wigner function of a two-mode squeezed state, although lacking negative values due to it being Gaussian, resembles the signature identified for the Bell-Fock states; the spatial dependence of one system affecting the state in the other system.

5. Conclusions

By plotting the information generated by calculating the Wigner function for a CV-DV hybrid system, we have shown that the usual techniques for visualizing these systems misses the full nature of the quantum correlations that arise. For example, the most common technique of generating the reduced Wigner function causes the correlations that arise between the systems to be traced out. Tracing out a system results in a loss of correlations that can be found between the two systems. A method to overcome this loss of information was presented in [38], but an envelope was applied setting the transparency of the points in phase space according to the reduced Wigner function for the CV degrees of freedom $W_f(\alpha)$. Here this method has been developed, changing the envelope to instead be proportional to $\max_{\theta,\phi}|W_{\hat{\rho}}(\alpha, \theta, \phi)|$ at each point in CV phase space. This adjustment further allows us to visualize the quantum correlations present in CV-DV hybrid states, such as those that manifest between the two coherent states in a hybrid Schrödinger cat state. Doing this means it is possible to gain a more full picture of the correlations that arise in the interaction between CV and DV systems. As well as allowing us to characterize signatures of quantum correlations found in certain systems; a result that promises potential usefulness in analyzing the correlations in maximally entangled states and entanglement as a result of squeezing. Being able to visually determine the level of quantum correlations, not always clear in coupled

systems, gives significant advantage over reduced Wigner function methods that do not always detect the purity of Bell-cat like entanglement.

By demonstrating these methods within the Jaynes–Cummings model, we show how excitations are shared and swapped, demonstrating a visual representation of the transfer of quantum information between systems. Extending these methods to different systems, will allow for a more intuitive picture of how quantum information moved around coupled systems, providing further insight into the inner process of quantum processes and algorithms.

There have been previous experimental examples which have used phase space to investigate the types of state considered in this paper. One notable example is [47], from a sequence of measurements of the expectation values of the qubit in different bases, they have been able to recreate the CV Wigner function. Using a similar procedure with our generalized displaced parity operator, it should be possible to extend this to produce experimental results equivalent to those in this paper. This technique could be considered to be a form of quantum state spectroscopy.

Acknowledgments

RPR is funded by the EPSRC [grant number EP/N509516/1]. TT notes that this work was supported in part by JSPS KAKENHI (C) Grant Number JP17K05569. The authors would like to thank Kae Nemoto, William Munro and T D Clark for interesting and informative discussions.

ORCID iDs

M J Everitt https://orcid.org/0000-0002-4542-3918

References

[1] Wheeler J A and Zurek W H 1983 *Quantum Theory and Measurement* (Princeton, NJ: Princeton University Press))
[2] Nielson M A and Chuang I L 2000 *Quantum Computation and Quantum Information* (Cambridge: Cambridge University Press))
[3] Wiseman H M and Milburn G J 2009 *Quantum Measurement and Control* (Cambridge: Cambridge University Press))
[4] Gerry C and Knight P L 2005 *Introductory Quantum Optics* (Cambridge: Cambridge University Press))
[5] Ralph T C, Gilchrist A, Milburn G J, Munro W J and Glancy S 2003 Quantum computation with optical coherent states *Phys. Rev.* A **68** 042319
[6] Gilchrist A, Nemoto K, Munro W J, Ralph T C, Glancy S, Braunstein S L and Milburn G J 2004 Schrödinger cats and their power for quantum information processing *J. Opt.* B **6** S828–33
[7] Braunstein S L and van Loock P 2005 Quantum information with continuous variables *Rev. Mod. Phys.* **77** 513–77
[8] Neergaard-Nielsen J S, Takeuchi M, Wakui K, Takahashi H, Hayasaka K, Takeoka M and Sasaki M 2010 Optical continuous-variable qubit *Phys. Rev. Lett.* **105** 1–4
[9] Hillery M, O'Connell R F, Scully M O and Wigner E P 1984 Distribution functions in physics: Fundamentals *Phys. Rep.* **106** 121
[10] Scully M O and Zubairy M S 2006 *Quantum Optics* 5 edn. (Cambridge: Cambridge University Press))
[11] Breitenbach G, Schiller S and Mlynek J 1997 Measurement of the quantum states of squeezed light *Nature* **387** 471–5
[12] Brune M, Haroche S, Raimond J M, Davidovich L and Zagury N 1992 Manipulation of photons in a cavity by dispersive atom-field coupling: Quantum-nondemolition measurements and generation of Schrödinger cat states *Phys. Rev.* A **45** 5193–214
[13] Schumacher B 1995 Quantum coding *Phys. Rev.* A **51** 2738–47
[14] Ladd T D, Jelezko F, Laflamme R, Nakamura Y, Monroe C and O'Brien J L 2010 Quantum computing *Nature* **464** 45–53
[15] Wootters W K 1987 A wigner-function formulation of finite-state quantum mechanics *Ann. Phys. (N.Y.)* **176** 1–21
[16] Gibbons K S, Hoffman M J and Wootters W K 2004 Discrete phase space based on finite fields *Phys. Rev.* A **70** 062101
[17] Howard M, Wallman J, Veitch V and Emerson J 2014 Contextuality supplies the 'magic' for quantum computation *Nature* **510** 351–5
[18] Delfosse N, Guerin P A, Bian J and Raussendorf R 2015 Wigner function negativity and contextuality in quantum computation on rebits *Phys. Rev.* X **5** 021003
[19] Raussendorf R, Browne D E, Delfosse N, Okay C and Bermejo-Vega J 2017 Contextuality and Wigner-function negativity in qubit quantum computation *Phys. Rev.* A **95** 1–22
[20] Dowling J P, Agarwal G S and Schleich W P 1994 Wigner distribution of a general angular-momentum state: Applications to a collection of two-level atoms *Phys. Rev.* A **49** 4101
[21] Várilly J C and Gracia-Bondía J M 1989 The moyal representation for spin *Ann. Phys. (N.Y.)* **190** 107–48
[22] Brif C and Mann A 1999 Phase-space formulation of quantum mechanics and quantum-state reconstruction for physical systems with lie-group symmetries *Phys. Rev.* A **59** 971–87
[23] Tilma T, Everitt M J, Samson J H, Munro W J and Nemoto K 2016 Wigner functions for arbitrary quantum systems *Phys. Rev. Lett.* **117** 180401
[24] Rundle R P, Tilma T, Samson J H, Dwyer V M, Bishop R F and Everitt M J 2019 General approach to quantum mechanics as a statistical theory *Phys. Rev.* A **99** 012115
[25] Klimov A B and Romero J L 2008 A generalized wigner function for quantum systems with the su (2) dynamical symmetry group *J. Phys. A.: Math. Theor.* **41** 055303
[26] Garon A, Zeier R and Glaser S J 2015 Visualizing operators of coupled spin systems *Phys. Rev.* A **91** 1–28
[27] Mukherjee R, Mirasola A E, Hollingsworth J, White I G and Hazzard K R A 2018 Geometric representation of spin correlations and applications to ultracold systems *Phys. Rev.* A **97** 1–13

[28] Rundle R P, Mills P W, Tilma T, Samson J H and Everitt M J 2017 Simple procedure for phase-space measurement and entanglement validation *Phys. Rev.* A **96** 022117
[29] Leiner D, Zeier R and Glaser S J 2017 Wigner tomography of multispin quantum states *Phys. Rev.* A **96** 1–14
[30] Tian Y, Wang Z, Zhang P, Li G, Li J and Zhang T 2018 Measurement of complete and continuous Wigner functions for discrete atomic systems *Phys. Rev.* A **013840** 1–6
[31] Chen B, Geng J, Zhou F, Song L, Shen H and Xu N 2019 Quantum state tomography of a single electron spin in diamond with wigner function reconstruction *Appl. Phys. Lett.* **114** 041102
[32] Song C *et al* 2019 Generation of multicomponent atomic schrödinger cat states of up to 20 qubits *Science* **365** 574–7
[33] Reiserer A, Kalb N, Rempe G and Ritter S 2014 A quantum gate between a flying optical photon and a single trapped atom *Nature* **508** 237–40
[34] Hacker B, Welte S, Daiss S, Shaukat A, Ritter S, Li L and Rempe G 2019 Deterministic creation of entangled atom–light Schrödinger-cat states *Nat. Photonics* **13** 110–5
[35] Haroche S and Raimond J M 2006 *Exploring the Quantum: Atoms, Cavities, and Photons.* (Oxford: Oxford Univ. Press))
[36] Jaynes E T and Cummings F W 1963 Comparison of quantum and semiclassical radiation theories with application to the beam maser *Proc. IEEE* **51** 89–109
[37] Arkhipov I I, Barasiński A and Svozilík J 2018 Negativity volume of the generalized Wigner function as an entanglement witness for hybrid bipartite states *Sci. Rep.* **8** 16955
[38] Davies B I, Rundle R P, Dwyer V M, Samson J H, Todd Tilma and Everitt M J 2018 Visualising entanglement in atoms *Phys. Rev.* A **100** 042102
[39] Jeong H, Zavatta A, Kang M, Lee S-W, Costanzo L S, Grandi S, Ralph T C and Bellini M 2014 Generation of hybrid entanglement of light *Nat. Photonics* **8** 564
[40] Vlastakis B *et al* 2015 Characterizing entanglement of an artificial atom and a cavity cat state with Bell's inequality *Nat. Commun.* **6** 1–8
[41] Sperling J, Agudelo E, Walmsley I A and Vogel W 2017 Quantum correlations in composite systems *J. Phys.* B **50** 134003
[42] Monroe C, Meekhof D M, King B E and Wineland D J 1996 A schrödinger cat superposition state of an atom *Science* **272** 1131–6
[43] Brune M, Hagley E, Dreyer J, Maître X, Maali A, Wunderlich C, Raimond J M and Haroche S 1996 Observing the progressive decoherence of the 'meter' in a quantum measurement *Phys. Rev. Lett.* **77** 4887–90
[44] Deléglise S, Dotsenko I, Sayrin C, Bernu J, Brune M, Raimond J M and Haroche S 2008 Reconstruction of non-classical cavity field states with snapshots of their decoherence *Nature* **455** 510–4
[45] Andersen U L, Neergaard-Nielsen J S, Van Loock P and Furusawa A 2015 Hybrid discrete- and continuous-variable quantum information *Nat. Phys.* **11** 713–9
[46] Morin O, Huang K, Liu J, Le Jeannic H, Fabre C and Laurat J 2014 Remote creation of hybrid entanglement between particle-like and wave-like optical qubits *Nat. Photonics* **8** 570
[47] Eichler C, Lang C, Fink J M, Govenius J, Filipp S and Wallraff A 2012 Observation of entanglement between itinerant microwave photons and a superconducting qubit *Phys. Rev. Lett.* **109** 240501
[48] Gottesman D, Kitaev A and Preskill J 2001 Encoding a qubit in an oscillator *Physical Review A. Atomic, Molecular, and Optical Physics* **64** 123101123101–21
[49] Lee N, Benichi H, Takeno Y, Takeda S, Webb J, Huntington E and Furusawa A 2011 Teleportation of nonclassical wave packets of light *Science* **332** 330–3
[50] Andersen U L and Ralph T C 2013 High-fidelity teleportation of continuous-variable quantum states using delocalized single photons *Phys. Rev. Lett.* **111** 1–5
[51] Takeda S, Mizuta T, Fuwa M, Van Loock P and Furusawa A 2013 Deterministic quantum teleportation of photonic quantum bits by a hybrid technique *Nature* **500** 315–8
[52] Van Loock P, Ladd T D, Sanaka K, Yamaguchi F, Nemoto K, Munro W J and Yamamoto Y 2006 Hybrid quantum repeater using bright coherent light *Phys. Rev. Lett.* **96** 1–4
[53] Ourjoumtsev A, Dantan A, Tualle-Brouri R and Grangier P 2007 Increasing entanglement between Gaussian states by coherent photon subtraction *Phys. Rev. Lett.* **98** 1–4
[54] Datta A, Zhang L, Nunn J, Langford N K, Feito A, Plenio M B and Walmsley I A 2012 Compact continuous-variable entanglement distillation *Phys. Rev. Lett.* **108** 1–5
[55] Wigner E P 1932 On the quantum correction for thermodynamic equilibrium *Phys. Rev.* **40** 749
[56] Groenewold H J 1946 On the principles of elementary quantum mechanics *Physica* **12** 405–60
[57] Cahill K E and Glauber R J 1969 Density operators and quasiprobability distributions *Phys. Rev.* **177** 1882
[58] Stratonovich R L 1956 On distributions in representation space *Sov. Phys—JETP* **31** 1012
[59] Everitt M J, Munro W J and Spiller T P 2012 Overcoming decoherence in the collapse and revival of spin schrödinger-cat states *Phys. Rev.* A **85** 022113
[60] Lambert J H 1772 *Beiträge zum gebrauch der mathematik und deren anwendungen* (Berlin: Verlag der Buchhandlung der Relschule)
[61] Hudson R L 1974 When is the wigner quasi-probability density non-negative? *Rep. Math. Phys.* **6** 249–52
[62] Bennett C H, DiVincenzo D P, Smolin J A and Wootters W K 1996 Mixed-state entanglement and quantum error correction *Phys. Rev.* A **54** 3824–51
[63] Vedral V, Plenio M B, Rippin M A and Knight P L 1997 Quantifying entanglement *Phys. Rev. Lett.* **78** 2275–9
[64] Wootters W K 1998 Entanglement of formation of an arbitrary state of two qubits *Phys. Rev. Lett.* **80** 2245–8
[65] Vedral V and Plenio M B 1998 Entanglement measures and purification procedures *Phys. Rev.* A **57** 1619–33
[66] Narozhny N B, Sanchez-Mondragon J J and Eberly J H 1981 Coherence versus incoherence: Collapse and revival in a simple quantum model *Phys. Rev.* A **23** 236–47
[67] Eisert J and Plenio M B 1999 A comparison of entanglement measures *J. Mod. Opt.* **46** 145–54
[68] Henderson L and Vedral V 2001 Classical, quantum and total correlations *J. Phys. A. : Math. Gen.* **34** 6899–905
[69] Adesso G, Bromley T R and Cianciaruso M 2016 Measures and applications of quantum correlations *J. Phys. A.: Math. Theor.* **49** 1–82
[70] Wallentowitz S, de Matos Filho R L and Vogel W 1997 Determination of entangled quantum states of a trapped atom *Phys. Rev.* A **56** 1205–11
[71] Agudelo E, Sperling J, Costanzo L S, Bellini M, Zavatta A and Vogel W 2017 Conditional hybrid nonclassicality *Phys. Rev. Lett.* **119** 1–6
[72] Sperling J and Walmsley I A 2018 Quasiprobability representation of quantum coherence *Phys. Rev.* A **062327** 1–14
[73] Sundar B, Wang K C and Hazzard K R A 2019 Analysis of continuous and discrete Wigner approximations for spin dynamics *Phys. Rev.* A **99** 43627
[74] Kenfack A and Zyczkowski K 2004 Negativity of the wigner function as an indicator of non-classicality *J. Opt. B: Quant. Semi. Opt.* **6** 396

[75] Taghiabadi R, Akhtarshenas S J and Sarbishaei M 2016 Revealing quantum correlation by negativity of the Wigner function *Quant. Inf. Process.* **15** 1999–2020
[76] Siyouri F, El Baz M and Hassouni Y 2016 The negativity of Wigner function as a measure of quantum correlations *Quant. Inf. Process.* **15** 4237–52
[77] Cummings F W 1965 Stimulated emission of radiation in a single mode *Phys. Rev.* **140** A1051–6
[78] Eberly J H, Narozhny N B and Sanchez-Mondragon J J 1980 Periodic spontaneous collapse and revival in a simple quantum model *Phys. Rev. Lett.* **44** 1323–6